Ultrasound-triggered drug release from vibrating microbubbles

Ying Luan

Financial support for the printing of this thesis is kindly provided by:

ISBN: 978-94-6108-809-3
Cover designed by: Ying Luan
Printed by: Gildeprint Drukkerijen B.V., Enschede, the Netherlands

Ultrasound-triggered drug release from vibrating microbubbles

Ultrageluid geïnitieerde medicijn-afgifte van trillende microbellen

Thesis

to obtain the degree of Doctor from the
Erasmus University Rotterdam
by command of the Rector Magnificus

Prof.dr. H.A.P. Pols

and in accordance with the decision of the Doctorate Board

The public defense shall be held on
Wednesday 19th of November at 11.30 hours
by

Ying Luan
born in Nanjing, China

ERASMUS UNIVERSITEIT ROTTERDAM

Doctoral Committee

Promotors:	Prof.dr.ir. N. de Jong
	Prof.dr.ir. A.F.W. van der Steen
	Prof.dr. A.M. Versluis
Other members:	Prof.dr. D.W. J. Dippel
	Dr. T.L.M. ten Hagen
	Prof.dr. C.T.W. Moonen

This study was performed at Biomedical Engineering, Thorax Center, Erasmus MC Rotterdam, the Netherlands. A strong collaboration with the Physics of Fluid group, University of Twente, Enschede, the Netherlands is acknowledged. The study was supported by the EU FP7 collaborative projects SONODRUGS and NanonextNL, a micro and nanotechnology consortium of the Government of the Netherlands and 130 partners.
Financial support by the Dutch Heart Foundation for the publication of this thesis is gratefully acknowledged.

"It would be impossible to tell of all the good these years brought to me. Unknown in Paris, I was lost in the great city, but the feeling of living there alone, taking care of myself without any aid, did not at all depress me. All that I saw and learned that was new delighted me. If sometimes I felt lonesome, my usual state of mind was one of calm and great moral satisfaction. Undistracted by any outside occupation, I was entirely absorbed in the joy of learning and understanding. It was like a new world opened to me, the world of science, which I was at last permitted to know in all liberty."

— from *Autobiographical Notes,* by Marie Curie

Contents

1 Introduction 1
2 Acoustical properties of individual liposome-loaded microbubbles 9
3 An impulse response method for characterization of echogenic liposomes 25
4 Segmented high speed imaging of vibrating microbubbles during long ultrasound pulses 43
5 Nonlinear dynamics of single freely-floating microbubbles by combined optical and ultrafast acoustical characterization 51
6 Lipid shedding from single oscillating microbubbles 69
7 Liposomes release from a vibrating microbubble on nanoseconds timescale 91
8 Investigations on the liposomes release relative to the microbubble dissolution 101
9 The mechanism for lipid shedding from microbubbles near a boundary lies in their non-spherical oscillations 119
10 SPIO labeling of endothelial cells using ultrasound and targeted microbubbles at low mechanical index 141
11 Targeted microbubble mediated sonoporation of endothelial cells *in vivo* 157
12 Discussion and conclusions 167
Bibliography 175
Summary 191
Sammenvatting 195
Acknowledgements 199
List of publication 203
PhD portfolio 207
A note about the author 211

1
Introduction

The moment two bubbles are united, they both vanish.
A lotus blooms.

— *Murakami Kijo*

1.1 DIAGNOSTIC ULTRASOUND AND CONTRAST AGENTS

Diagnostic medical ultrasound may have a slightly longer history than what you expected. Its root dates back to 1930s and 1940s, when Theodore Dussik, a psychiatrist and neurologist, and his brother Friederich used a 1.5 MHz source to record signal variations after transmitting the wave through the human brain. Although these images were later shown to measure the skull bone attenuation instead of brain ventricles as the Dussik brothers had believed, it was one of the earliest attempts to scan an *in vivo* organ (White 1988). The real developments of medical ultrasound imaging initiated after Second World War, since 1950s, when the "pulse echo" technique was adapted from military sonar and radar. For the practicality to position the setup for medical imaging, only a single transducer was used to measure the reflected wave from the target sample in contrast to transmission, which measures the wave transmitted through the medium by a sending transducer and a separate receiving transducer. In early 1950s, John Wild and John Reid developed the first hand-held imaging device which was applied to image breast cancer tumors (Newman and Rozycki 1998). However, it was not until 1960s and 1970s, with the development of electronics, these pioneering works truly came to fruition. The static B-mode imaging was replaced by real-time imaging modalities thanks to new techniques such as phased linear arrays (Seibert 1995). One of the major breakthroughs (which is also of special meaning to the author) is the multi-element linear arrays developed by the group headed by Professor Nicolaas Bom at Thoraxcenter, Erasmus medical center Rotterdam. The probe face consists of 20 crystals which can produce 20 scan lines in total. Figure 1.1 shows the design of the probe and the real-time cardiac image it produced. This early simple concept has later evolved into the more complicate real-time scanners that are widely available today. The later combination of real-time imaging with pulsed wave Doppler technique enabled accurate measurements of the blood flow, which greatly benefited diagnostic echocardiography.

In echocardiography, the ability to image vessels (e.g., arteries, veins, arterioles, and capillaries) and their blood supply has high diagnostic value (Vos 2010). For example, direct visualization of arterial vasa vasorum, networks of small blood vessels formed on the surface of arteries, can assist in early detection of atherosclerotic cardiovascular disease (Feinstein 2006; Biedermann et al. 2008). However, the scattering strength of blood is lower than that of the surrounding tissue at typical imaging frequencies (2-10 MHz), which becomes even more critical to image small blood vessels. The necessity of increasing image contrast to discriminate blood and tissue motivated Raymond Gramiak and Pravin Shah's pioneering work on ultrasound contrast agents (UCAs) in 1968 (Nanda 1997). When preforming an echocardiogram,

they observed "a cloud of reflectors" from the aortic root after injecting saline through an intra-aortic catheter. These "microbubbles" (< 10 μm in diameter) were a result of individual droplets of dye formed at the end of the injecting catheter. The gas cores of microbubbles have much higher compressibility than the surrounding liquid and tissue, thus bubbles undergo sequential compression and expansion due to pressure variations in the surrounding medium and act as strong nonlinear scatterers in an ultrasound field (de Jong et al. 2002).

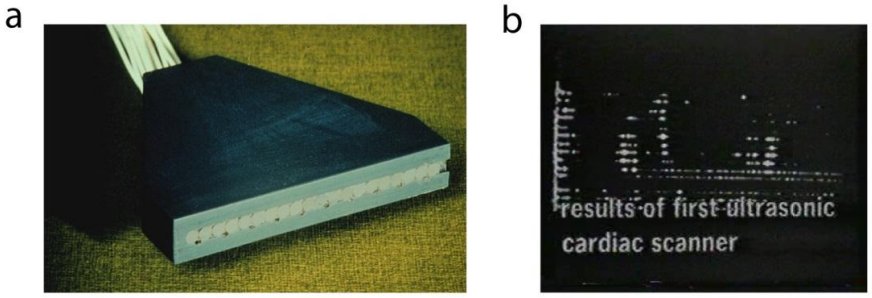

Figure 1.1. (a) The design of multi-element linear arrays with 20 elements (each 4 mm x 10 mm). The axial resolution was 1.25 mm while the beam width at 6 cm was 10 mm. (b) The real-time cardiac image produced by the probe.

Early contrast agents were usually agitated saline and they suffered from a range of issues such as a short bubble life, unknown bubble size, and they were too large to pass through the pulmonary circulation (Nanda 1997). Later, commercial products developed since 1990s, e.g., Albunex (Mallinckrodt, St. Louis, USA) were standardized, and a stabilization shell (e.g., denatured albumin for Albunex) was utilized to decrease the bubble surface tension (Borden and Longo 2002) and resist gas diffusion so that they persist for several minutes after injection (Cosgrove 2006). Soon afterwards, the air filled bubbles were replaced by less diffusible high-molecular weight gases (usually a perfluro gas), and more varieties of encapsulations were developed (e.g., phospholipids, surfactants). This forms the most prevalent contrast agents for clinical use nowadays such as Sonovue (Bracco, Milan, Italy) and Definity (Lantheus Medical Imaging, North Billerica, USA).

1.2 CONTRAST AGENTS AS DRUG DELIVERY VEHICLES

1.2.1 Sonoporation

Besides being widely applied for diagnostic imaging, contrast agents microbubbles have been recently proposed as a therapeutic tool for, e.g., thrombolysis (Cohen et al. 2003), gene therapy and drug delivery (Lindner and Kaul 2001; Porter and Xie 2001;

Unger et al. 2002). Applied as cavitation nucleus, microbubbles were shown to increase the capillary permeability and delivery of materials to the interstitial tissue (Price et al. 1998). This was explained as a phenomenon called sonoporation, when reversible or non-reversible openings of the cell membrane were generated upon microbubble oscillations or violent collapses (Klibanov 2006; Lentacker et al. 2009; Kooiman 2011). Recently, real-time confocal microscopy has revealed that most of the small pores (typically < 30 μm^2) were observed to reseal within 1 minute, while larger pores (> 100 μm^2) tend to fail in resealing (Hu et al. 2013). Although the mechanism of sonoporation has not been fully elucidated, the general consensus ascribes the cell perforation to the high shear stress caused by bubble vibrations, microjets or violent bubble collapses (Mukherjee et al. 2000; Prentice et al. 2005; Vos 2010).

1.2.2 Drug-loaded microbubbles

Early drug delivery studies involved the systemic co-injection of microbubbles and drug molecules (dissolved in a solution or incorporated in a particle) followed by the local application of ultrasound (Newman et al. 2001; Lentacker et al. 2009). Despite the successful reports in enhancing drug delivery, a more advantageous approach is to bind gene or drug molecules to microbubbles (Lentacker et al. 2007; Vandenbroucke et al. 2008; Geers et al. 2010). In this way, cavitation events can be associated intimately with the drug application. The cavitation of the microbubble can locally release the drugs and optimally deliver the drugs into the target tissue. Additionally, drug delivery may be monitored by an ultrasound scanner in parallel due to the echogenicity of the contrast agents (Unger et al. 2002). As shown in figure 1.2, there are different configurations of a drug-loaded microbubble: drugs can be imbedded within, surrounding or attached to the bubble membrane (Lentacker et al. 2009).

One of the most recent and innovative designs was to conjugate liposomes to the microbubble surface by biotin-avidin links (Kheirolomoom et al. 2007) or covalent thiol-maleimide linkages (Geers et al. 2011). Liposomes are membrane-enclosed vesicles composed of a lipid bilayer shell surrounding an aqueous core. Therefore it can trap both hydrophobic or amphipathic drugs and encapsulate hydrophilic drugs (Figure 1.2) (Heyes et al. 2005; Yoshina-Ishii et al. 2005). This liposome-loaded microbubble can serve as an efficient drug-delivery vehicle, especially to deliver highly active drugs, e.g., proteins (cytokines and growth factors), and chemotherapeutic agents (paclitaxel and doxorubicin). These highly active drugs can be carried by liposome vesicles with a minimum influence of the healthy tissue during transport, and be administered effectively achieving higher concentrations in the target area. Echogenic liposomes (ELIP), another novel drug delivery vehicle, are thought to contain an aqueous core, allowing drug-loading, and also encapsulate a gas bubble, making them sensitive to ultrasound (Alkan-Onyuksel et al. 1996).

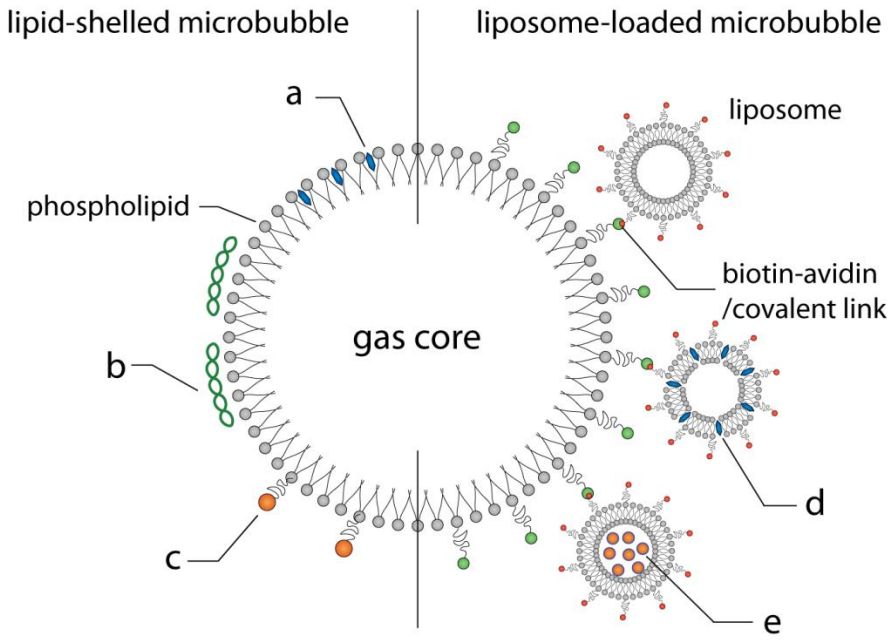

Figure 1.2. Schematic plot of several examples of drug loading configurations on a lipid-shelled microbubble and on a liposome-loaded microbubble: (a) drugs imbedded within the lipid membrane; (b) hydrophobic drugs incorporated into a layer of oily material that forms a film surrounding the microbubble; (c) drugs attached to the lipid membrane; (d) drugs incorporated within the lipid membrane of liposomes; (e) drugs encapsulated within the aqueous core of the liposome.

1.2.3 Drug release

In an ultrasound-triggered drug delivery system, drug-loaded microbubbles can respond to insonation by releasing the drugs from the carrier directly via mechanical effects, or indirectly, via thermal effects of ultrasound (e.g., for temperature-sensitive liposomes) (Hauck et al. 2006; Klibanov et al. 2010). It is essential to understand the drug release process as a function of ultrasound parameters (e.g., the pressure and the pulse length) for the success of future drug delivery applications. This thesis focuses on the investigation of the mechanical release from both lipid-coated microbubbles and liposome-loaded microbubbles. Specifically, drug carriers (the lipid membrane or liposome vesicles) were labeled with a fluorescent probe, which was excited by a continuous wave laser, so that sufficient optical contrast could be achieved to resolve the small particles (several hundreds of nanometers). The time scale of the lipids/liposomes detachment can be comparable to that of bubble vibrations, which is

tens of nanoseconds to microseconds. However, the subsequent transport of released materials by the surrounding flow field can be several orders of magnitude slower, which is tens to hundreds of milliseconds (Elder 1959; Gelderblom 2012). Therefore, to monitor the dynamics of shell material release and transport, high-speed fluorescence imaging at microseconds time scale with the recording length of milliseconds was utilized.

1.3 MICROBUBBLE CHARACTERIZATION TECHNIQUES

For both imaging and therapeutic purposes, the acoustic response of microbubbles to ultrasound excitation is of key importance. For diagnostic imaging, the bubble signal should be enhanced to the largest extent while the surrounding tissue signal should be suppressed. The stability of bubbles is essential for preset ultrasound parameters. On the other hand, controllable drug delivery requires manipulating bubble vibrations which lead to local drug release and transport to the target tissue. Moreover, bubble destruction may be inevitable or even preferable here for efficient drug delivery. In contrast to lipid-shelled bubbles used in diagnostic imaging, loading drugs onto the microbubble surface may change the acoustic characteristics of bubbles. Therefore, it is necessary to characterize microbubbles for a thorough knowledge of the bubble response (i.e., amplitude of oscillations, nonlinear properties, stability) is crucial for both imaging and drug delivery strategies (e.g., to design the pulse sequence and new contrast agents). This section provides a brief overview of the characterization techniques of microbubbles.

1.3.1 Acoustic approach

For acoustic characterization, either a population of microbubbles is measured or single isolated bubbles are investigated. In the population study, the attenuation or scattered signals from bubbles are recorded and properties of the bubble shell (i.e., stiffness, viscosity) are estimated from the characteristic response (de Jong et al. 1992; Hoff et al. 2000; Emmer et al. 2009; Faez et al. 2011). This approach is straightforward and easy to perform. However, it has a major disadvantage in that a simplified model based on the acoustic scattering cross-sections is used to extract shell parameters. The lipid coating is considered as homogeneous and equal for all microbubbles, which is not the case revealed by optical characterizations later (Kooiman et al. 2010). Moreover, effects which are not predicted by the model are masked. For example, compression-only behavior, which is an important nonlinear response shown already at comparatively low pressures, was not recognized with this method (Vos 2010).

The single bubble measurement requires microbubbles being isolated by using capillary tubes, focused flow, high dilution or radiation force (Morgan et al. 2000; Palanchon et al. 2005; Vos et al. 2007; Maresca et al. 2010; Mannaris and Averkiou 2012; Renaud et al. 2013). Shell properties can be estimated based on matching the simulation with the experimental data, and the size of the bubbles is either optically measured or estimated based on simulations. This method requires a high sensitivity of the setup to receive the echo signal and an accurate calibration of the setup. Bubbles are normally floating against a wall, which may influence the acoustic behavior of the bubble (Garbin et al. 2006). Another challenge here is to record large amounts of bubbles covering different sizes to produce statistical results.

1.3.2 Optical approach

The optical characterization approach involves recording instantaneous microbubble vibrations on the nanosecond time scale. Light scattering from a laser beam, or by a high speed streak and framing camera systems are examples of optical imaging techniques (Chomas et al. 2001; Chin et al. 2003; Guan and Matula 2004). The radius-time curve can be obtained by tracking the bubble oscillations. The optical method is direct and intuitive, providing new insights into bubble vibrational dynamics. For example, since the introductionon of an ultra-high speed camera system Brandaris 128 (0.5-25 Mfps) (Chin et al. 2003), which consists of a rotating mirror mounted on a helium-driven turbine, a series of interesting phenomena have been observed, including: thresholding behavior (Emmer et al. 2007), compression-only response (de Jong et al. 2007) and surface mode oscillations (Versluis et al. 2010). The destruction of microbubbles (i.e., dissolution, fragmentation) relative to bubble vibrations under burst excitations was also revealed (Bouakaz et al. 2005; Viti et al. 2012; Thomas et al. 2013). Similar to single bubble acoustic characterization techniques, bubbles studied here were mostly floating against a wall. However, by using an optical tweezer to manipulate the bubble position, the wall effect was able to be investigated (Garbin et al. 2007). Additionally, biotinylated microbubbles were targeted to avidin-coated surface *in vitro*, and the interaction between two single bubbles driven by the secondary acoustic radiation force was able to be studied (Garbin et al. 2009; Kokhuis et al. 2013). The limitations of the optical characterization method can be the restricted exposure time, which is a trade-off with the frame rate. Moreover, the setup might be difficult and expensive to build.

1.4 OVERVIEW OF THIS THESIS

This thesis will take you into a microscopic world, where events taking place on the time scale of nanoseconds to milliseconds will be uncovered. This world is

challenging but exciting. You will be amazed by the beautiful events created by those tiny microbubbles in an ultrasound field. In this thesis, progresses from different perspectives have been made by interpreting the micro-world in light of our observations. Technically innovative methods and systems have been developed and optimized for in-depth investigations. New physical phenomena were observed and theoretical explanations have been exploited.

The major goal of this thesis is to optically and acoustically characterize single (loaded) microbubbles *in vitro* to achieve controlled drug-delivery. Liposomes were selected as a major type of drug carrier due to the loading scheme, by either conjugating to microbubbles or encapsulating gas pockets. The acoustic response and the dynamics of lipid shedding were characterized for a number of single lipid-coated bubbles and/or liposome-loaded bubbles through high-speed (fluorescence) imaging. **Chapter 2** describes optical characterization of single liposome-loaded microbubbles based on a spectroscopy technique by Brandaris camera (van der Meer et al. 2007). Lipid-shelled microbubbles without loading were used as reference. In **Chapter 3** the newly-developed echogenic-liposome agent was characterized by impulse response, which provides a novel optical characterization approach. **Chapter 4 and 5** introduce innovative technical progresses**.** In **Chapter 4**, we developed a "segmented" mode in Brandaris camera which largely extended the recording time. Therefore bubble dynamics exposed to a prolonged ultrasound burst could be studied. In **Chapter 5** an acoustic characterization system was developed for the first time to optically size and acoustically measure single freely-floating microbubbles simultaneously. Through **Chapter 6** to **Chapter 9**, ultrasound triggered bubble shell materials release was the focus of study. Lipid shedding and/or liposome release from single oscillating microbubbles were monitored in real-time from both the top and the side to obtain a 3D view. In **Chapter 10,** a parametric study *in vitro* of the cell labeling for MRI tracking using targeted microbubbles was performed. Finally an *in vivo* study of sonoporation with a chicken embryo model is presented in **Chapter 11**. The outcomes of this thesis are discussed and summarized in **Chapter 12**.

2

Acoustical properties of individual liposome-loaded microbubbles

Abstract — A comparison between phospholipid-coated microbubbles with and without liposomes attached to the microbubble surface was performed using the ultra-high speed imaging camera (Brandaris 128). We investigated 73 liposome-loaded microbubbles (loaded microbubbles) and 41 microbubbles without liposome loading (unloaded microbubbles) with a diameter ranging from 3 µm to 10 µm at frequencies ranging from 0.6 to 3.8 MHz, and acoustic pressures from 5 to 100 kPa. The experimental data showed nearly the same shell elasticity for the loaded and unloaded bubbles but the shell viscosity was higher for loaded bubbles compared to unloaded bubbles. For loaded bubbles a higher pressure threshold for the bubble vibrations was noticed. Finally, fluorescence imaging showed heterogeneity of liposome distributions of the loaded bubbles.

Appeared in *Ultrasound in Medicine & Biology*, by Y. Luan, T. Faez, E.C. Gelderblom, I. Skachkov, B. Geers, I. Lentacker, A.F.W. van der Steen, M. Versluis, N. de Jong, Vol. 38, Issue 12, pp. 685-688, December 2012. The authors acknowledge valuable discussions with Marlies Overvelde (University of Twente, Enschede, the Netherlands) and Benjamin Dollet (University of Rennes, Rennes, France).

2.1 INTRODUCTION

The applications of ultrasound-mediated drug delivery systems and their underlying physical mechanisms are nowadays under extensive investigations due to their enormous clinical potential, especially in oncology and cardiovascular applications (Ferrara et al. 2007; Newman and Bettinger 2007; Hernot and Klibanov 2008). The general goal of drug delivery is to improve the efficiency of drug uptake in the region of interest while reducing undesired side effects, such as toxicity in healthy tissue (Hernot and Klibanov 2008). It has been shown that the oscillations of co-administered contrast agent microbubbles are capable of greatly enhancing the drug transfer efficiency (Frinking et al. 1998; van Wamel et al. 2006; Kooiman et al. 2010). Microbubbles are also designed to be preloaded with pharmaceutical agent, which is locally released by an ultrasound pulse (Unger et al. 1998; Lentacker et al. 2009; Tinkov et al. 2010).

An even more advanced drug loading system consists of nanoparticles containing drugs, attached to the shell of the microbubble. This ensures a higher drug playload and a higher drug transportation safety. Liposome nanoparticles, composed of an aqueous core entrapped by one or more lipid bilayers, are investigated as functional micro-particulate drug carriers for both hydrophobic and hydrophilic drugs (Sharma and Sharma 1997; Kheirolomoom et al. 2007). To combine the advantages of the acoustical properties of the microbubbles and the fusogenicity of the liposomes, Kheirolomoom et al. (2007) introduced novel liposome-loaded microbubbles (loaded microbubbles) by mounting liposomes to the microbubble shell via avidin-biotin conjugation. Based on this formulation, Lentacker et al. (2007) presented PEGylated lipoplex-loaded microbubbles, which showed strongly improved gene transfer efficiency. Recently, Geers et al. (2011) further improved the system by covalent thiol-maleimide linkages between liposomes and microbubbles through a single step self-assembly process. The size distribution of lipid-shelled microbubbles (unloaded microbubbles) and loaded microbubbles was measured by a Multisizer™ 4 Coulter Counter, with a measurement range of 0.4-12 μm. Results indicated an average volume diameter of 4 μm for loaded bubbles, which is approximately 400 nm larger than the diameter of the unloaded microbubbles (Geers et al. 2011). This is in agreement with the liposome layer thickness of 200 nm. The drug loading capacity of the loaded bubbles was also evaluated by flow cytometry. The number of liposomes attached to each microbubble surface is about 600 to 1300. *In vitro* and *in vivo* characterizations evaluated the biological efficiency of drug-containing loaded bubbles and the results indicated a great enhancement in the cellular uptake (Lentacker et al. 2009; Geers et al. 2011).

Optimal use of loaded bubbles for drug delivery in (pre-) clinical research requires a thorough characterization of the loaded bubble, to get the optimal ultrasonic parameters for bubble activation and feedback for bubble preparation. Extensive work has been performed in recent years on the characterization of the acoustical behavior of unloaded microbubbles both experimentally and theoretically. Examples of experimental work have been presented (Dayton et al. 1999; van der Meer et al. 2007; Emmer et al. 2009; Overvelde et al. 2010; Sijl et al. 2010; Faez et al. 2011). They showed the nonlinear bubble dynamics in response to ultrasound and their experimental results were compared with theoretical models introduced by for instance de Jong et al. (1994), Church (1995) and Marmottant et al. (2005). Shell properties of the unloaded bubbles were also investigated through acoustic attenuation and scattering measurements (Pi Hsien et al. 1995; Morgan et al. 2000; Faez et al. 2011), atomic force microscopy (Sboros et al. 2006), and light scattering (Tu et al. 2009).

Van der Meer et al. (2007) estimated the shell properties of BR14 phospholipid-coated microbubbles (Bracco Research S.A., Geneva, Switzerland) by performing microbubble spectroscopy, i.e. insonifying a single bubble sequentially by sweeping the transmit frequency. They reported that for coated bubbles the resonance frequency increases due to the shell elasticity and that the shell viscosity decreases with dilatation rate, from which they postulate a rheological thinning behavior of the microbubble shell. In 2007, two phenomena were reported: a “compression-only” behavior in which the radial oscillations of microbubbles are asymmetric and compression outweighs expansion (de Jong et al. 2007) and a thresholding behavior (Emmer et al. 2007), which indicates that if the acoustic pressure is lower than a certain threshold, no bubble oscillations could be observed. Sijl et al. (2010) demonstrated that the mechanism of “compression-only” behavior can be explained with the Marmottant et al. (2005) model. Also Overvelde et al. (2010) showed that the “thresholding” behavior can be explained and modeled by nonlinear bubble dynamics, which includes buckling and rupture of the phospholipid shell.

Experimental and theoretical investigations on unloaded bubbles have provided rich knowledge concerning microbubbles, which can be applied as a reliable reference in studying loaded bubbles. In this study, the acoustic behavior of unloaded and loaded bubbles as a function of the transmit frequency and the applied acoustic pressure were investigated, using an ultra-high speed imaging technique. The shell properties of loaded bubbles are derived and compared with unloaded bubbles. Finally, with the aid of confocal fluorescence imaging, the morphological structure of liposome attachment of loaded bubbles is studied.

2.2 MATERIALS AND METHODS

2.2.1 Microbubble sample preparation

Unloaded microbubbles were prepared by mixing 1,2-dipalmitoyl-sn-glycero-3-phosphocholine (DPPC) (Lipoid, Ludwigshafen, Germany) and 1,2-distearoyl-sn-glycero-3-phosphoethanolamine-N-[PDP(polyethylene glycol)-2000] (DSPE-PEG-SPDP) in a molar ratio of 65:35 in chloroform. After chloroform evaporation, the lipid film was dissolved in a 1:2:7 glycerine-propyleneglycol-H_2O mixture to obtain a clear solution with a final lipid concentration of 4×10^{-4} mmol/mL. This lipid solution was aliquotted in 2.5mL chromatography vials of which the headspace was filled with perfluorobutane gas (F2 chemicals, Preston, UK). Finally, bubbles were obtained by high speed shaking of the chromatography vial in a Vialmix agent activator (Bristol-Myers Squibb Medical Imaging, North Billerica, MA, USA) for 15 seconds. For loaded microbubbles, maleimide-functionalized liposomes were prepared by mixing DPPC, 1,2-distearoyl-snglycero-3-phosphoethanolamine-N-[maleimide(polyethyleneglycol)-2000] (ammonium salt) (DSPE-PEG maleimide) (Laysan Bio Inc, Arab, AL), cholesterol, all dissolved in chloroform in a round-bottom flask at a 49:15:35 molar ratio with a final lipid concentration of 16 mg/mL lipids. The chloroform was evaporated and the remaining lipid film was hydrated with distilled water. The liposomes were sized by extruding through a 200nm polycarbonate filter using a mini-extruder at 60 °C (Avanti Polar Lipids, Alabaster, AL). Then liposomes were added with a concentration of 100 mmol/mL to the lipid solution used for the preparation of unloaded microbubbles. The mechanical activation forms loaded bubbles with a liposomes layer coupled to the microbubble surface through a covalent thiol-maleimide link.

For fluorescence labeling of loaded microbubbles, the bubble samples were prepared with nearly the same procedure as described previously, only the lipid mixture used for the preparation of unloaded microbubbles was added with bodipy (Invitrogen, Merelbeke, Belgium) labeled liposomes and the lipophilic dye DiI (Sigma-Aldrich, Bornem, Belgium). High speed shaking of the vial generates loaded bubbles with DiI-labeled lipid shell and bodipy-labeled liposomes attached on the bubble shell (Geers et al. 2011). Figure 2.1 schematically depicts the structure of an unloaded bubble and a loaded bubble.

2.2.2 Experimental setup

2.2.2.a Frequency scanning experiment

Figure 2.1a shows a schematic view of the experimental setup showing the ultrasound, optical microscope and the ultra-high speed camera. An acoustically transparent cellulose capillary tube with an inner diameter of 200 μm and a wall

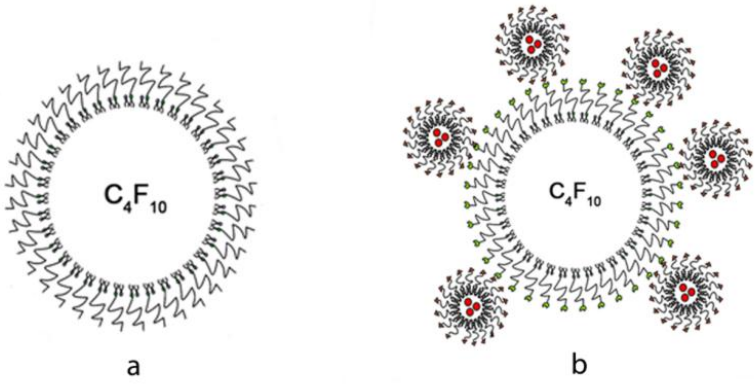

Figure 2.1. The schematic view of (a) an unloaded bubble and (b) a loaded bubble.

thickness of 20 μm (Product No. 132294 Spectrum Europe, Breda, NL) was submerged and fixed in a water tank at room temperature. A broadband transducer (PA086, 0.5-4 MHz, Precision Acoustics, Dorchester, UK) was mounted on the side of the water tank and was focused on the capillary tube. Before the experiments, the transducer was calibrated in a separate set-up with a calibrated 0.075 mm needle hydrophone (Precision Acoustic Ltd., Dorchester, UK). The transmit signal was generated by an arbitrary wave generator (8026, Tabor Electronics Ltd., Tel Hanan, Israel) and amplified with a power amplifier (150A100B Amplifier Research, Limerick, Ireland). An optical light guide (SCHOTT AG, Mainz, Germany) connected to a Xenon flash lamp (A-260 Vision Light Tech, Uden, NL) was mounted at the bottom of the water tank to illuminate the region-of-interest in the capillary tube. An Olympus microscope with a 60× water immersed objective (NA = 0.9) and a 2× magnifier was focused on the bubbles inside the capillary. Microbubbles were withdrawn from the vial and diluted in Isotone II (Coulter Electronics, Luton, UK). Then the dilution was injected with a syringe into the capillary. Bubbles with a diameter ranging from 3 to 10 μm were insonified at driving frequencies between 0.5 MHz and 3.9 MHz with a frequency step of 200 kHz and at acoustic pressures of 50 kPa and 100 kPa. Bursts of a 10 cycle sinusoidal wave, tapered with a Gaussian envelope at the first and last 2 cycles were transmitted. The dynamics of the bubbles was captured by the Brandaris 128 (Chin et al. 2003) at a frame rate of 15 million frames per second (Mfps). For each single bubble the camera was set to record 35 movies of 128 frames so that all frequencies could be acquired in a single run. For each movie the diameter of the microbubble as a function of time (DT-curve) was measured using custom-designed image analysis software (van der Meer et al. 2007).

2.2.2.b Pressure scanning experiment

In the pressure scanning measurements, in which the microbubbles should be kept in the field of view for successive insonifications with different acoustic pressures, the capillary tube was replaced by an OptiCell chamber (NUNCTM, Thermo Fisher Scientific, Wiesbaden, Germany) as depicted in figure 2.2b. The optical focal point of the objective and the acoustical focus of the transducer were aligned by a needle hydrophone (HPM02/1, Precision Acoustics, Dorchester, UK) which was positioned at the focus of the objective. The bubble solution was injected into the OptiCell chamber which was filled with Milli-Q water (Millipore, Billerica, MA). The transmitted frequency range was from 0.6 to 3.8 MHz, with frequency steps of 200 kHz. The applied acoustic pressures were 5 kPa to 50 kPa with pressure steps of 5 kPa, followed by 75 kPa and 100 kPa, leading in total to a set of 204 experiments on each single bubble.

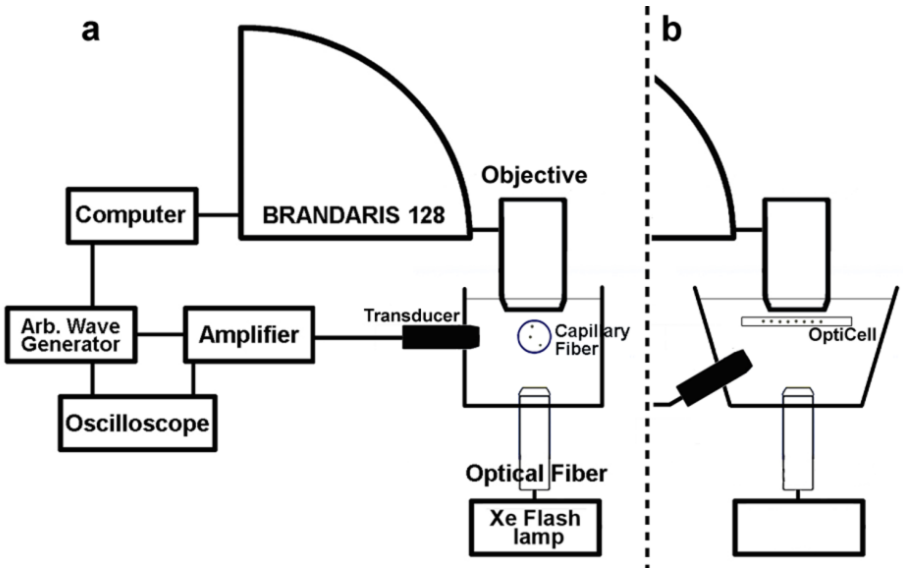

Figure 2.2. Schematic view of the experimental setups with (a) a capillary tube, and (b) an OptiCell chamber.

2.2.3 Fluorescence imaging

Confocal fluorescence microscopy (Zeiss LSM510META JNI, Jena, Germany) was performed on individual loaded bubbles with bodipy-labeled liposomes and DiI-labeled microbubble lipid shell to observe the morphological features of liposomes attachment. A 100× oil-immersed objective (Plan Apochromat, Carl Zeiss, Oberkochen, Germany) (NA = 1.4) was used. The excitation wavelengths applied for bodipy and DiI

were 488 nm and 633 nm, while the emission filters for detecting these two fluorophores were BP 505-530 nm and LP 560 nm, respectively.

2.2.4 Simulations

2.2.4.a Resonance and damping

The discrete Fourier transform of the DT-curves were calculated. The maximum amplitude of excursion at each transmitted frequency was determined and plotted as a function of the transmit frequency. The resonance curve was constructed by fitting the experimentally obtained oscillation response to the model of a harmonic oscillator by the least mean square method, defined as:

$$\mathrm{Re}(f) = \frac{\mathrm{Re}_0}{(1 - f^2 / f_0^2)^2 + (\delta f / f_0)^2} \tag{2.1}$$

Two parameters are obtained: the eigenfrequency f_0 and the total damping coefficient δ_{tot}.

An example of 4 DT-curves of a 7.5 µm loaded bubble and their power spectra are shown in figure 2.3. The driving frequency in these selected graphs increases from 1.3 MHz to 1.9 MHz and the acoustic pressure is 50 kPa.

In figure 2.4, the resonance curves of two unloaded bubbles and two loaded bubbles are displayed. Unloaded bubbles and loaded bubbles of a similar size are compared.

2.2.4.b Shell elasticity and shell viscosity

The shell viscosity (κ_s) is estimated from the total damping coefficient (δ_{tot}) as follows (Goertz et al. 2007; van der Meer et al. 2007; Faez et al. 2011):

$$\delta_{tot} = \frac{\omega_0 R_0}{c} + \frac{4\mu}{R_0^2 \rho \omega_0} + \frac{4\kappa_s}{R_0^3 \rho \omega_0} \tag{2.2}$$

δ_{tot} is the sum of the contributions of acoustic re-radiation, viscous damping of the liquid and the shell viscous damping coefficient respectively. $f_0 = 2\pi\omega_0$ is the eigenfrequency of the microbubble; R_0 is the equilibrium radius; $c=1.5\times10^3$ m/s is the speed of sound in water; $\rho=10^3$ kg/m^3 is the density of water; $\mu= 2\times10^{-3}$ Pa·s is an effective viscosity parameter, which indicates the real viscosity of the surrounding liquid and the effect of the thermal damping, as proposed by Devin (1959) and Medwin (1977).

A shell elasticity is estimated by fitting the experimentally measured resonance frequencies versus the bubble's diameter using a linear viscoelastic model (Marmottant et al. 2005), as described by**:**

$$f_0 = \frac{1}{2\pi}\sqrt{\frac{1}{\rho R_0^2}[3\gamma P_0 + \frac{2(3\gamma-1)\sigma_\omega}{R_0} + \frac{4\chi}{R_0}]} \tag{2.3}$$

The resonance frequency is where the maximum amplitude of oscillations occurs and is lower than the eigenfrequency f_0 by a factor of $\sqrt{1-\delta^2/2}$ in the presence of damping. In our case, this factor is between 1 and 1.11. $P_0 = 10^5$ Pa is the ambient pressure; we assume adiabatic behavior and take the ratio of specific heats of C_4F_{10} (1.07) as the value of polytropic gas exponent γ (Marmottant et al. 2005); $\sigma_\omega = 0.072$ N/m is the surface tension and χ is the shell elasticity.

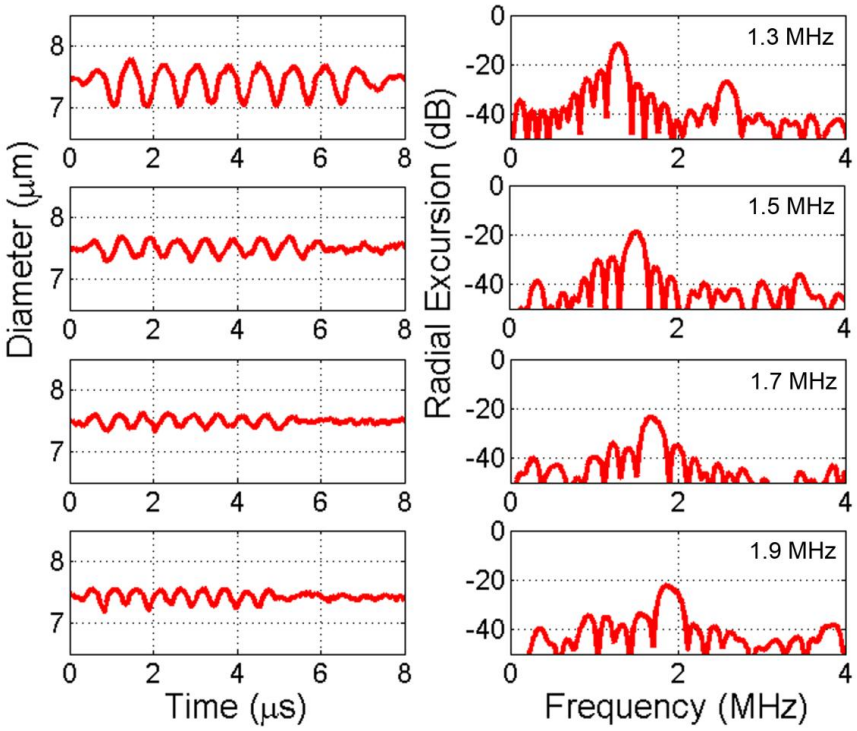

Figure 2.3. Selected DT-curves and corresponding radial excursion of a loaded bubble with a diameter of 7.5 μm. The selection has been done between 1.3 MHz to 1.9 MHz with the step frequency of 200 kHz. The applied acoustic pressure is 50 kPa.

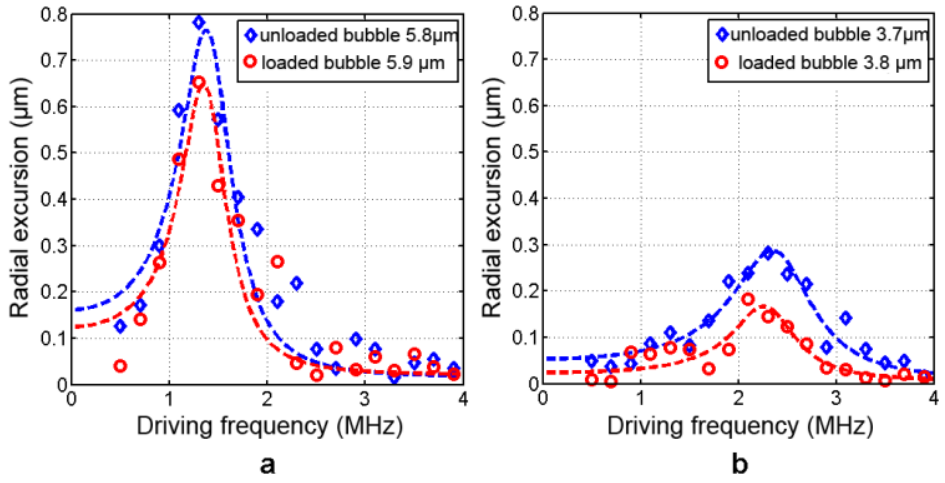

Figure 2.4. Resonance curve and the fit on the data of two pairs of unloaded bubbles and loaded bubbles with similar size of about (a) 5.9 μm and (b) 3.8 μm respectively. The applied acoustic pressure is 50 kPa.

2.3 RESULTS

2.3.1 Shell properties

The responses of 38 loaded bubbles and 27 unloaded bubbles were recorded in the frequency scanning measurement. Figure 2.5 depicts the total damping coefficient of the studied bubbles as a function of the bubbles' diameter. The estimated shell viscosity of the unloaded bubbles and loaded bubbles as a function of the bubble diameter and the dilatation rate as described by van der Meer et al. (2007) are depicted in figure 2.6a and b respectively. An apparent difference of the shell viscosity between the loaded and the unloaded bubble is found for bubbles larger than 6 μm in diameter. The averaged shell viscosity among the loaded bubbles larger than 6 μm in diameter is 4.0×10^{-8} kg/s, which is almost twice that of unloaded bubbles within the same size range (2.3×10^{-8} kg/s). In figure 2.6b the shell viscosity is plotted against the dilatation rate showing shear thinning especially for the loaded bubble.

Figure 2.7 shows plot of the experimentally measured resonance frequencies versus the bubble's diameter. At 50 kPa, a shell elasticity of $\chi = 0.17 \pm 0.09$ N/m was found for loaded bubbles, which is very similar to the value found for unloaded bubbles ($\chi = 0.19 \pm 0.07$ N/m).

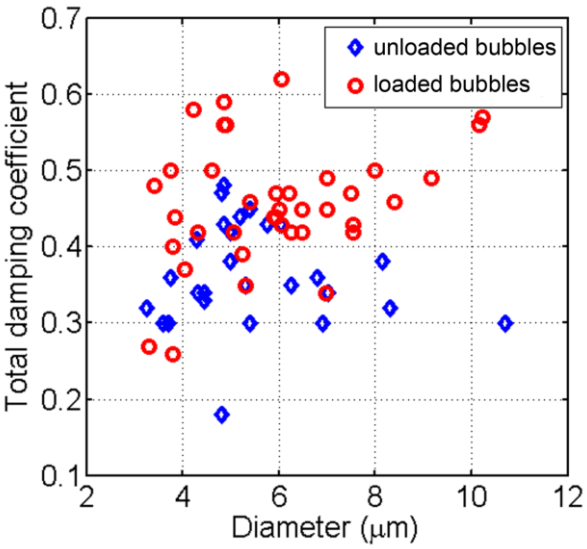

Figure. 2.5. The total damping coefficient of unloaded bubbles and loaded bubbles as a function of bubble size.

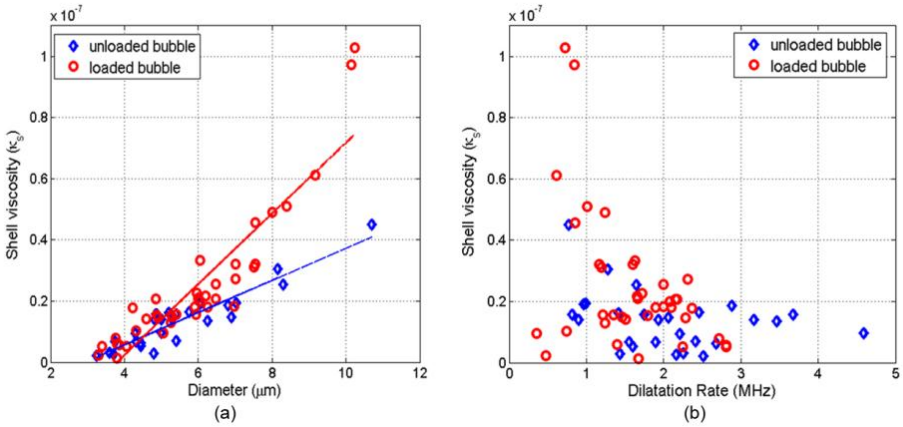

Figure 2.6. The shell viscosity of unloaded bubbles and loaded bubbles as a function of (a) bubble size and (b) the dilatation rate. Dashed lines are the linear fit on the data with coefficients of 5.3×10^{-9} for unloaded bubbles and 1.2×10^{-8} for loaded bubbles.

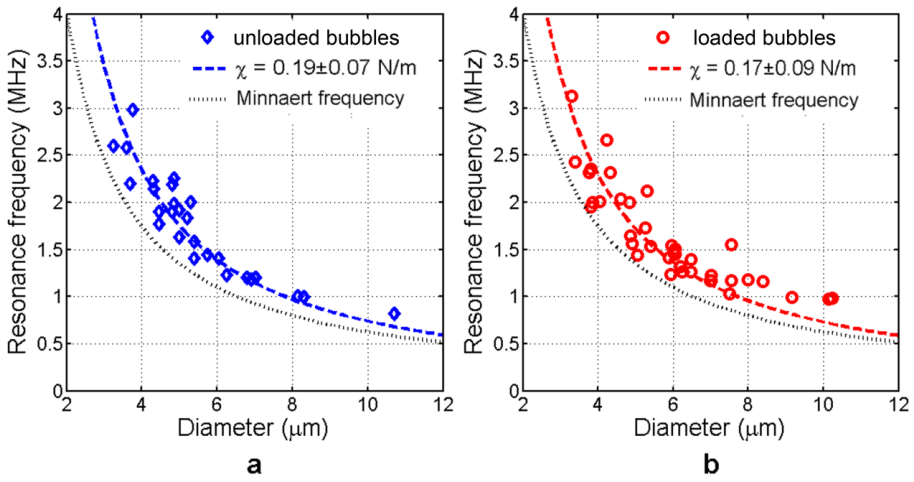

Figure 2.7. The resonance frequency of (a) unloaded bubbles and (b) loaded bubbles as a function of the bubble diameter at an acoustic pressure of 50 kPa. A fit on the data was performed using Eq. (2.2).

2.3.2 Pressure dependent resonance

Figure 2.8 shows the experimentally obtained amplitude of oscillations of an unloaded bubble and a loaded bubble, with the diameter of 4.5 μm and 4.3 μm respectively, for the full driving frequency and pressure scan. The color indicates the amplitude of the vibration. A total of 204 DT-curves have been measured at 12 different acoustic pressures in the range of 10 to 100 kPa. For each pressure, 17 different frequencies were applied. It can be seen that by increasing the acoustic pressure, the resonance frequencies of the unloaded and loaded bubbles slightly decrease. However, at the same acoustic pressure, unloaded bubbles have higher amplitude of oscillation compared to the loaded bubbles. Also the threshold pressure, that is the pressure below which no vibration amplitude can be noticed, differs between loaded and unloaded bubbles. To better demonstrate this effect we plot the amplitude of oscillation of the same bubbles presented in figure 2.8 as a function of the acoustic pressure at three driving frequencies: 2.2 MHz, which is the frequency of maximum response (FMR) of the two microbubbles at 100 kPa, and 2.6 MHz and 1.8 MHz, which are 400 kHz above and below the indicated FMR, respectively. The results are shown in figure 2.9.

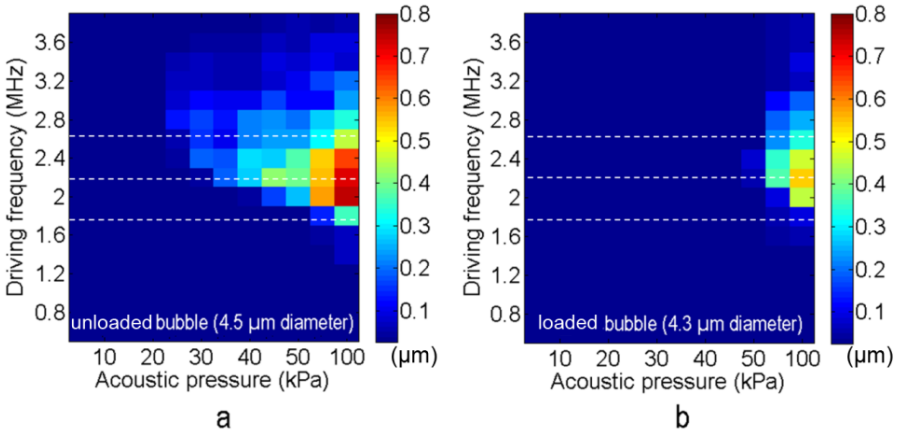

Figure 2.8. Amplitude of oscillation as functions of acoustic pressure and driving frequency for (a) an unloaded bubble with 4.5 µm diameter and (b) a loaded bubble with 4.3 µm diameter. Dashed lines indicate the experimental data obtained at 2.6 MHz, 2.2 MHz and 1.8 MHz, which are plotted in Fig.2.9.

Figures 2.9a, b and c show the thresholding behavior for both microbubbles below the resonance, at the resonance and above the resonance, respectively. The threshold pressure for the initiation of bubble oscillations is in general higher for the loaded bubble compared with the unloaded bubble with a similar size. Moreover, the threshold pressure for the unloaded bubble is higher with decreasing driving frequency (Fig. 2.8a). In other words, the thresholding behavior of unloaded bubbles is driving frequency dependent. The noise level of the amplitude of oscillation was estimated by the discrete Fourier transform of the D-t curves if no ultrasound was applied.

Figure 2.10 shows the threshold pressure for all the unloaded and loaded bubbles investigated in the pressure scanning experiment as a function of the bubble size. Similar to figure 2.9, the threshold pressure of the bubbles was derived at the resonance frequency of the bubbles (Fig. 2.10b) and at 400 kHz above and below their resonance frequencies (Fig. 2.10a and c respectively). The threshold pressures decrease with increasing bubble size, and decrease by increasing the driving frequency, as indicated before (Fig. 2.9). The increase of the pressure threshold are estimated by comparing loaded bubbles to unloaded bubbles of similar size range ($\Delta d < 0.5$ µm, Δd is the size difference). For frequencies above resonance, the pressure thresholds of the loaded bubbles are estimated to be 110% to 500% of unloaded bubbles within a similar size range. For frequencies near resonance, the value is in the range of 108% to 375%. In case of frequencies below resonance, the range is 94% to

250%, with an average value of 200%. In general, loaded bubbles show a higher pressure threshold values than unloaded bubbles of a similar size.

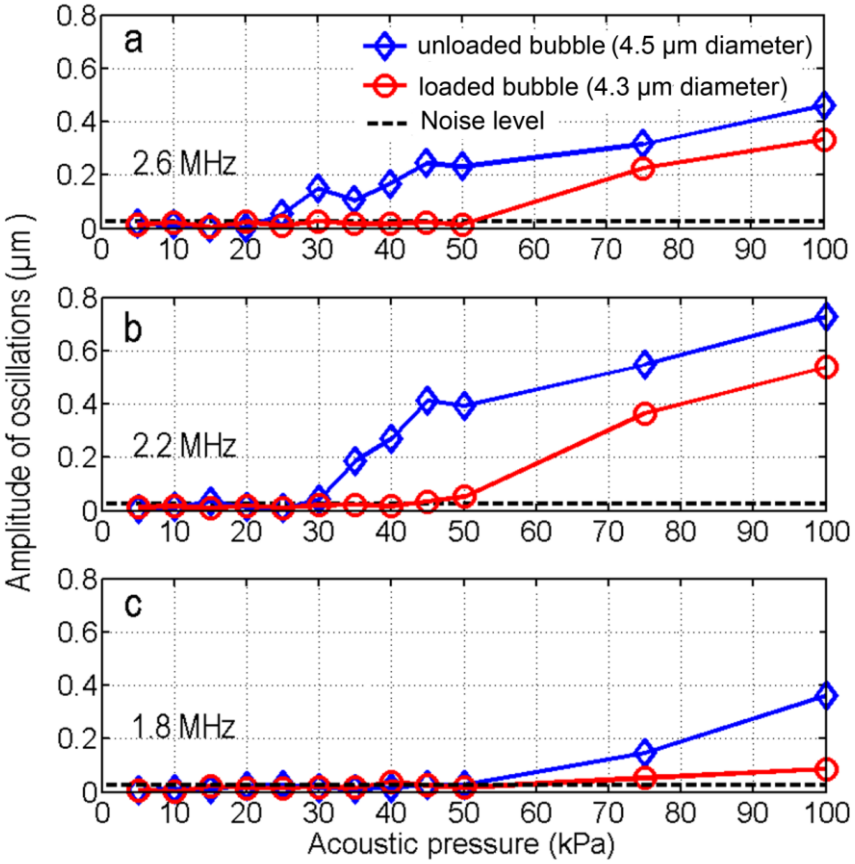

Figure 2.9. Amplitude of oscillation as a function of the acoustic pressure (a) at 400 kHz above the resonance (2.6 MHz) (b) at the resonance (2.2 MHz) and (c) at 400 kHz below the resonance (1.8 MHz). Dashed lines indicate the noise level in the experiments.

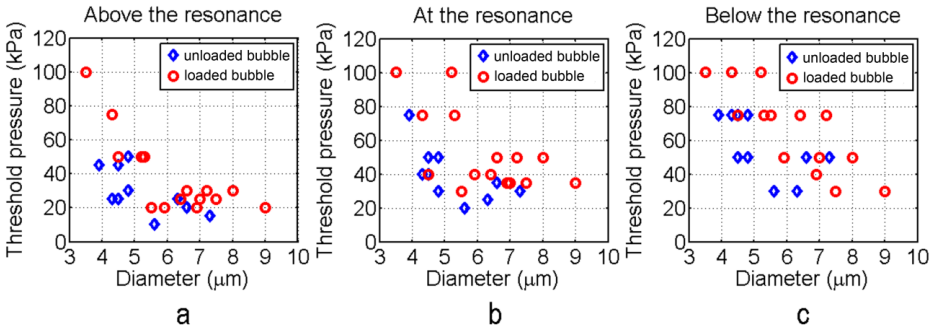

Figure 2.10. Threshold pressure for the initiation of bubble oscillations for unloaded and loaded bubbles at (a) 400 kHz above the resonance, (b) the resonance and (c) 400 kHz below the resonance.

2.3.3 Liposome attachment

Figure 2.11 shows the bright-field and fluorescence images of a loaded bubble taken with a confocal microscope. The liposome (Fig. 2.11b) and the lipid shell of the microbubbles (Fig. 2.11c) were both fluorescently labeled and showed to have a heterogeneous distribution of the shell coating (Fig. 2.11d). This is in agreement with observations of Kooiman et al. (2010) by 4Pi microscopy, in which they reported inhomogeneous distributions of phospholipids on the microbubble shell.

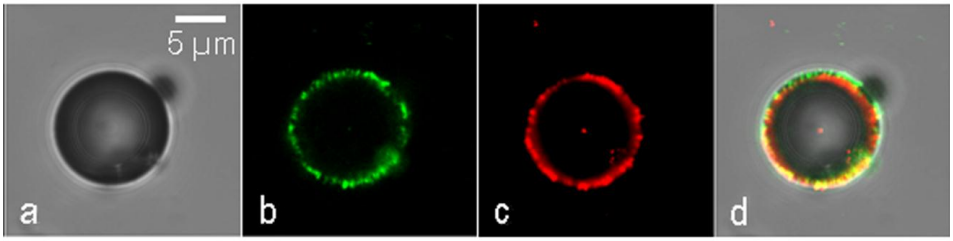

Figure 2.11. (a) bright-field image of a loaded bubble and the fluorescent images with (b) bodipy-labeled liposomes and (c) DiI-labeled lipid shell. (d) The combined image of both layers on the bright field image.

2.4 DISCUSSION

2.4.1 Shell properties

The effective shell properties (elasticity and viscosity) of the 27 unloaded bubbles and the 38 loaded microbubbles were derived experimentally. For unloaded bubbles, an elasticity of 0.19 ± 0.07 N/m was calculated (Fig. 2.7). Also it was observed that the

shell dilatational viscosity increases with the bubble size, and a typical viscosity of 4.0×10^{-8} kg/s was derived for loaded bubbles larger than 6 μm (Fig. 2.6a). The shell elasticity of unloaded bubbles derived from this study is lower than the value (0.54 ± 0.1 N/m) reported in previous experimental observations for phospholipid-coated microbubbles (BR14), while the shell viscosity values are compatible with previously reported values of 0.72×10^{-8} kg/s and 1.5×10^{-8} kg/s (Gorce et al. 2000; Marmottant et al. 2005; van der Meer et al. 2007). As shown previously in figure 2.8a, with the increase of the applied acoustic pressures, the frequency of maximum response decreases, leading to lower effective shell elasticity. Therefore, one possible reason of the lower shell elasticity may be due to the higher applied acoustical pressure (50 kPa), compared to pressures used in previous studies with the same setup (van der Meer et al. 2007; Overvelde et al. 2010). By comparing unloaded bubbles with loaded bubbles, we observed a slight change in the shell properties of loaded microbubbles. The averaged shell elasticity of loaded microbubbles (0.17 ± 0.09 N/m) was comparable to that of unloaded bubbles but the values of shell viscosities (2.5×10^{-8} kg/s), especially for larger bubbles (≥ 6μm) were found to be almost twice the reported value for unloaded bubbles. We hypothesize that the increase in the shell viscosity of large loaded microbubbles can be due to the change of the surface morphology of the bubble coating after the attachment of liposomes by thiol-maleimide cross-links. The hypothetical dynamics of loaded microbubbles during different oscillating phases are shown in figure 2.12.

Previous studies on the rheology of particle based coatings indicate that small and anisotropic-shaped particles tend to raise suspension bulk viscosity, due to the particle-to-particle interactions favored by the acicular particle shape and higher Brownian motions which randomize the particle configurations (Hoffman 1992; Chang and Powell 1994; Weitz 2004). Fluorescent images of the loaded microbubbles revealed the inhomogeneous distribution of liposomes on the loaded microbubbles (Fig. 2.11) and a high mobility of the microbubble lipid shell (Kooiman et al. 2010). The interactions between liposomes during bubble oscillations can cause energy loss and results in a higher “internal friction” which altogether may lead to a higher shell viscosity.

Also a shear-thinning behavior was found for unloaded microbubbles (Fig. 2.6b), as was reported before (van der Meer et al. 2007; Tu et al. 2011). However, a large variation for the viscosity was found for the loaded bubbles, especially at low dilatation rate. The cause can be the liposome distribution around the lipid monolayer, which varies greatly for each

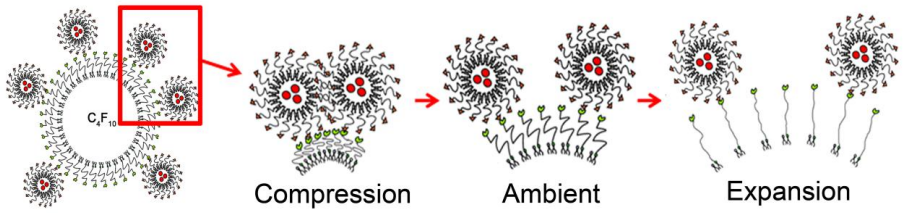

Figure 2.12. Cartoon of loaded microbubbles dynamics during compression and expansion.

individual microbubble. Similar variations in the lipids concentration for unloaded bubbles were reported by Stride et al. (2008) and by Borden (2009).

2.4.2 Thresholding behavior

Thresholding behavior was found for both unloaded bubbles and loaded bubbles, where loaded bubbles show higher pressure thresholds (Fig. 2.8-2.10). Overvelde et al. (2010) showed that this behavior is closely related to the nonlinear bubble dynamics. A bubble in the elastic regime shows a rapid decrease of the frequency of maximal response with increasing amplitude of oscillations, where the shell buckling and rupture are likely to occur, leading to a pronounced skewing of the resonance curves. On the other hand, bubble oscillation amplitude is greatly influenced by the shell viscosity. The experimental data showed decreased bubble oscillation amplitudes for loaded bubbles compared to unloaded bubbles (Fig. 2.4). It was also observed that loaded bubbles have higher shell viscosity than unloaded bubbles (Fig. 2.6). We hypothesize that the higher shell viscosity which leads to the higher "internal friction" during loaded bubbles oscillations is the cause of higher pressures needed for stimulating bubble oscillations. However, due to the complications of nonlinear bubble dynamics for loaded bubbles, further investigations on the exact cause for higher pressure thresholds are necessary and a new theoretical model is required to describe the loaded bubble dynamics.

2.5 CONCLUSION

The shell elasticity of loaded bubbles is nearly the same as unloaded bubbles. A clear difference was found in the shell viscosity of loaded bubbles. Pressure dependent bubble resonance indicated a thresholding behavior for the initiation of bubble oscillations, and the loaded bubble showed a higher threshold pressure.

3

An impulse response method for characterization of echogenic liposomes

Abstract — An optical characterization method is presented based on the use of the impulse response to characterize the damping imparted by the shell of an air-filled ultrasound contrast agent (UCA). The interfacial shell viscosity was estimated based on the unforced decaying response of individual echogenic liposomes (ELIP) exposed to a broadband acoustic impulse excitation. Radius versus time response was measured optically based on recordings acquired using an ultra-high-speed camera. The method provided an efficient approach that enabled statistical measurements on 106 individual ELIP. A decrease in shell viscosity, from 2.3×10^{-8} kg/s to 2.1×10^{-9} kg/s, was observed with increasing dilatation rate, from 0.5×10^{6} s^{-1} to 1×10^{7} s^{-1}. This nonlinear behavior has been reported in other studies of lipid-shelled UCAs and is consistent with rheological shear-thinning. The measured shell viscosity for the ELIP formulation used in this study ($\kappa_s = (2.1 \pm 0.1)\times10^{-8}$ kg/s) was in quantitative agreement with previously reported values on a population of ELIP and is consistent with other lipid-shelled UCAs. The acoustic response of ELIP therefore is similar to other lipid-shelled UCAs, despite loading with air instead of perfluorocarbon gas. The methods described here can provide an accurate estimate of the shell viscosity and damping for individual UCA microbubbles.

Submitted to Journal of the Acoustical Society of America, by J. L. Raymond, Y. Luan, T. van Rooij, K. Kooiman, S.L. Huang, D. D. McPherson, M. Versluis, N. de Jong and C. K. Holland. The authors would like to thank Robert Beurskens and Frits Mastik from the Dept. of Biomedical Engineering, Erasmus MC for technical assistance with Brandaris experiments. The authors would also like to thank the Optical Imaging Centre of Erasmus MC for use of their facilities, and Wiggert A. van Cappellen and Alex Nigg from the Erasmus Optical Imaging Centre, Department of Pathology, Erasmus MC for technical assistance.

3.1 INTRODUCTION

Physical models for encapsulated ultrasound contrast agent (UCA) microbubbles have been developed and improved over the past two decades. The models give accurate predictions of the nonlinear radial dynamics of individual UCA microbubbles, particularly under forced, or acoustically driven, conditions (Faez et al. 2013). Such models are largely based on Rayleigh-Plesset-type equations, which describe the dynamics of a gas bubble in response to pressure variations. The effects of the shell encapsulation on the microbubble motion are incorporated by adding additional terms that describe the viscoelastic behavior of the shell (Doinikov and Bouakaz 2011). The presence of the shell increases the resonance frequency from that of a free bubble and damps the oscillations in response to the acoustic forcing (de Jong et al. 2002). The shell also affects the nonlinear response of microbubbles, a key property of UCAs which is often exploited in diagnostic imaging modes for enhanced discrimination between the contrast agent and surrounding tissue (Stride 2009).

In addition to traditional diagnostic ultrasound imaging, there has been recent interest in advancing the applications of microbubbles for molecular imaging and therapeutic applications. These applications exploit the nonlinear response for selective detection of microbubbles in a given volume for diagnosis and specific targeting of disease. Molecular imaging techniques with targeted UCAs are being used increasingly for noninvasive diagnosis of inflammation, thrombus, and neovascularization (Wen et al. 2014). Targeted microbubble agents are also being developed for controlled drug-delivery applications (Castle et al. 2013). Clinical application of these UCAs necessitates accurate prediction of the frequency-dependent response of single isolated microbubbles. A better understanding of the shell properties that can be expected for individual UCA microbubbles within a population is also critical. The acoustic response of microbubbles can depend on the morphology and viscoelastic properties of the encapsulating shell (Hosny et al. 2013), particularly if lipids are not homogeneously distributed throughout the shell (Borden et al. 2006). Therefore, single microbubble characterization techniques and physical models that accurately describe the dynamics of an encapsulated microbubble are increasingly important.

The introduction of optical methods to resolve microbubble oscillations (Chomas et al. 2000; de Jong et al. 2000) has provided new insights into the dynamic response of single microbubbles. Optical methods based on direct measurement of the bubble radius versus time can be used due to availability of ultra-high-speed imaging systems (de Jong et al. 2000; Chetty et al. 2008; Chen et al. 2013) such as the Brandaris 128 fast-framing (0.5-25 Mfps) camera (Chin et al. 2003). This system enables optical characterization studies by imaging single microbubble dynamical phenomena

occurring at multiple time-scales (Gelderblom et al. 2012). Acoustic measurements of the scattered echo from an isolated microbubble have been simultaneously recorded and compared to the optically measured radial dynamics to verify the effectiveness of this approach (Sijl et al. 2011).

Optical studies of the radial dynamics of UCAs typically rely on measuring the steady-state forced response of a microbubble to a narrow-band burst excitation. For example, the amplitude response of a microbubble exposed to multiple-cycle, low amplitude ultrasound bursts at various frequencies can be analyzed to build up a resonance curve and fit to a linearized model to derive the viscoelastic shell parameters (van der Meer et al. 2007). Such a method requires multiple recordings to characterize the frequency-dependent response of an individual microbubble. In addition, the shell morphology can be altered or destroyed due to multiple burst excitations (Thomas et al. 2012; Viti et al. 2012).

In this study, we investigated the use of the impulse response to characterize the damping imparted by the encapsulation of a microbubble stabilized by a lipid shell, or echogenic liposomes (ELIP). The shell viscosity is the dominant mechanism affecting the damping of microbubble response to acoustic excitation and most directly influences the onset of nonlinear oscillations. An understanding of this physical property of the shell encapsulation can be exploited for optimization of contrast-enhanced imaging and therapeutic applications. Through this technique, we aim to acquire a better understanding of the transient dynamics of ELIP in response to short-pulse excitations for both diagnostic and therapeutic applications. This method is also of particular interest to improve the efficiency of UCA characterization techniques in general as it requires only a single acoustic excitation when the impulse response is recorded using an ultra-high-speed camera.

ELIP are under development as theragnostic ultrasound contrast agents and differ from other commercially available ultrasound contrast agents primarily in shell material and gas content. ELIP formulations include a small amount of cholesterol to increase membrane rigidity, and are echogenic due to the presence of air, which is entrapped and stabilized by the lipid during the rehydration process (Huang 2010). The exact location of the entrapped air pockets, morphology of the encapsulation, and amount of air in each carrier has not been fully ascertained (Huang 2010; Paul et al. 2014; Raymond et al. 2014). The objective of the present study was to measure the damping due to the encapsulation and to estimate the shell viscosity based on the unforced response of individual ELIP exposed to a broadband acoustic impulse excitation.

An ultra-high-speed camera was used to capture the radius versus time response. During each recording, an isolated ELIP was excited using two ultrasound pulses with a phase difference of 180°. Following each pulse, the bubble oscillated at its natural

frequency with diminishing amplitude determined by the damping, and eventually returned to its resting radius. A generic model was developed to estimate the shell viscosity based on the amplitude decay time constant, which was determined from the experimentally measured radius versus time curve for an individual ELIP. Gas diffusion was neglected in our model, and this approach was verified experimentally by comparing the resting radius before and after the impulse excitation. The shell viscosity of individual ELIP obtained using the optical method presented here is compared to our previously reported value obtained for a population of ELIP using a broadband acoustic attenuation spectroscopy technique (Raymond et al. 2014).

3.2 MATERIALS AND METHODS

3.2.1 Experimental setup

Freeze-dried ELIP dispersions consisting of EggPC/DPPC/DPPE/DPPG/Cholesterol (27:42:8:8:15, mol %) were prepared as previously described (Buchanan et al. 2008). ELIP suspensions were prepared by reconstituting 10 mg/mL lyophilized lipid powder using air-saturated, filtered (Type I) water at room temperature as described by Huang (2010). The suspension was diluted (~100×) into air-saturated phosphate-buffered saline (PBS) mixed with 0.5% (wt./vol.) bovine serum albumin (BSA) solution (Sigma Chemical Co., St. Louis, USA), loaded into an OptiCell® (Nunc/Thermo Scientific, Wiesbaden, Germany), and placed on an optical stage in a 37 °C water bath. A microscope with a 60× water-immersion objective and 2× magnifier was used to image the bubble dynamics at approximately 17 Mfps using the Brandaris 128 fast-framing camera (Chin et al. 2003; Gelderblom 2012). A diagram of the ultra-high-speed optical imaging setup is presented in figure 3.1.

Figure 3.2(a) shows an optical image of a dilute suspension of ELIP suspended in an OptiCell® using a 40× objective to obtain a larger field of view. A single frame from a Brandaris 128 recording using the 60× objective and 2× magnifier is shown in figure 3.2(b). Figures 3.2(c) and 3.2(d) show super-resolution fluorescence microscope images of fluorescently-labeled ELIP obtained using the methods outlined by Kooiman et al. (2014). Briefly, a 4Pi confocal laser-scanning microscope (Leica TCS 4Pi) with two opposing objective lenses (100×, HCX PL APO, 1.35 NA) was used to generate super-resolution 3-D image stacks. For this supporting study, 2 mol % fluorescently-labeled rhodamine-DPPE was substituted into the ELIP formulation and the reconstituted liposomes were suspended in 87% (vol./vol.) glycerol between quartz cover slips at room temperature. The images show the distribution of the lipid molecules in the shell encapsulation of the ELIP. The size distribution of the microbubbles deduced from optical images presented in Figs. 3.2(a) and 3.2(c) is consistent with Coulter-counter measurements of the particle size distribution for this

ELIP formulation, which indicated a volume-weighted mean diameter of 2 μm (Raymond et al. 2014). Previously published transmission electron microscopy images have shown liposomes on the order of 2 μm diameter (Paul et al. 2012) as well as vesicles in the nanometer size range that could not be resolved using the optical methods described here.(Kopechek et al. 2011; Nahire et al. 2012) Atomic force microscopy (Paul et al. 2014) and fluorescence microscopy studies (Nahire et al. 2012) also indicate a broad size distribution, with particle sizes ranging over three orders of magnitude from tens of nanometers to microns.

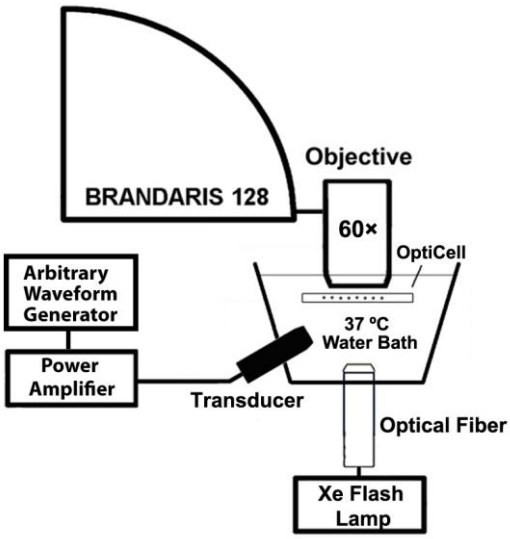

Figure 3.1. Schematic of the setup used to optically record the microbubble oscillation.

3.2.2 Acoustic excitation pulse

A focused, broadband PVDF transducer (25 mm focal distance, PA275; Precision Acoustics, Dorchester, United Kingdom) was positioned in the water bath at a 45° angle below the sample and the acoustic focus aligned with the optical field of view. For each optical recording, a sequence of two phase-inverted acoustic pulses, temporally separated by 3 μs, was used to excite each ELIP impulsively. The pulses had a phase difference of 180° but were otherwise identical with center frequency of 4 MHz and pulse duration of ~0.33 μs (1.5 cycles). Pulse excitations with peak pressure amplitude of 125, 250, or 500 kPa (210, 420, or 840 kPa peak-to-peak acoustic pressure, respectively) were used. During calibration, a 0.2-μm needle-type hydrophone (Precision Acoustics) was positioned approximately 2 mm from the sample holder membrane (a modified OptiCell® with one membrane removed), such

that the hydrophone location corresponded to the location of the ELIP during the optical measurement. The transmitted acoustic pressure amplitude *in situ* was attenuated by a factor of 3 dB relative to the free-field pressure due to the presence of the membrane and the 45° angle of incidence of the acoustic wave. The *in situ* pressure waveform and power spectrum for a 250 kPa peak pressure amplitude excitation pulse are shown in figure 3.3.

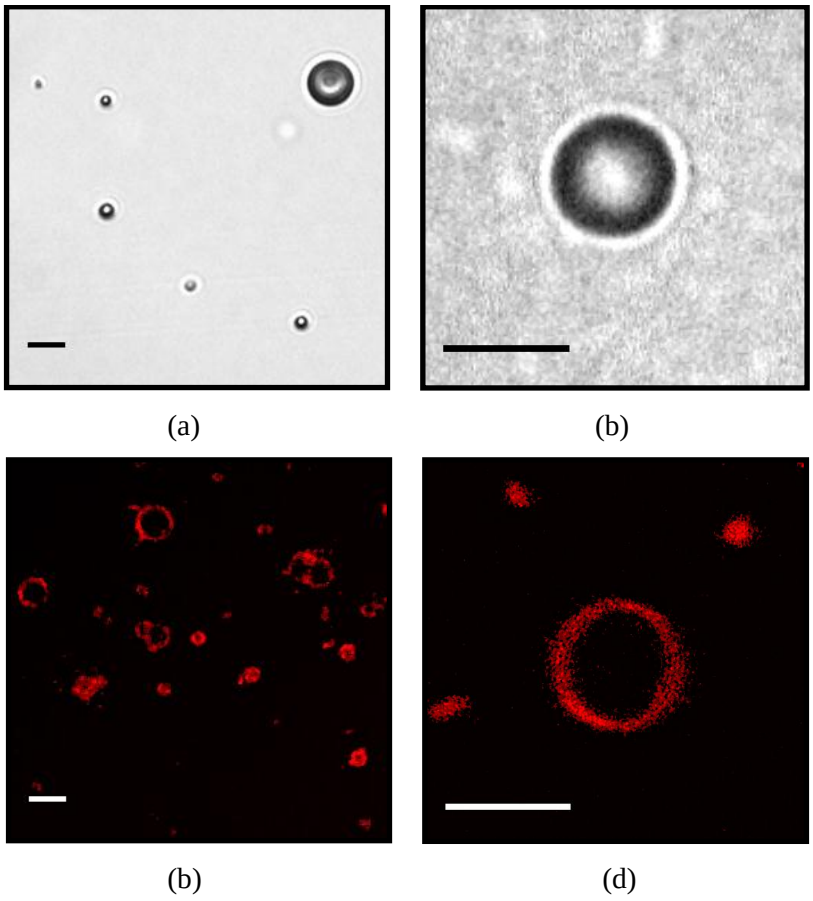

Figure 3.2. (a) Optical image of a dilute suspension of ELIP suspended in an OptiCell® (40× magnification) (b) Single frame of a Brandaris 128 recording (120× magnification) (c,d) Super-resolution confocal microscope images of fluorescently-labeled (2 mol % rhodamine-DPPE) ELIP in glycerol (Leica TCS 4Pi, 100× magnification). Scale bars represent 5 μm in all images.

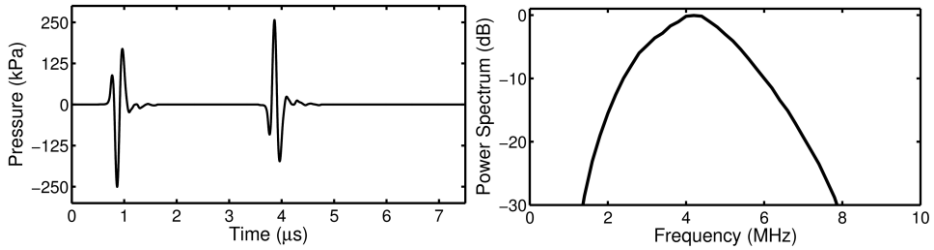

Figure 3.3. Measured pressure waveform and corresponding spectrum of the acoustic excitation pulses.

3.2.3 Estimation of the shell viscosity

Linearizion of a Rayleigh-Plesset-type bubble dynamics equation yields the equation of motion for a damped harmonic oscillator (Leighton 1994). The eigenfrequency, ω_0, is given by the Minnaert relation (Ainslie and Leighton 2011) for a free gas bubble, and for an encapsulated bubble this expression can be modified to include an additional term which depends on the elasticity of the shell (Paul et al. 2014). The damped natural frequency for unforced oscillations, ω_d, is related to the eigenfrequency of the system by the damping coefficient, $\omega_d = \omega_0\sqrt{(1-\delta^2/4)}$, where δ represents the total damping of the system (Ainslie and Leighton 2011). If the system is modeled as a linearized, single degree-of-freedom system which is underdamped ($\delta < 2$), the solution can be written in terms of an oscillatory signal with a decaying exponential envelope characterized by the time constant, $\tau = 2/(\delta\omega_0)$.

Analysis of the experimental data consists of calculating the envelope signal, A(t), from the measured radius versus time curves using the Hilbert transform. The time constant can be readily determined by fitting a line to the natural logarithm of the envelope signal (Agneni and Balis-Crema 1989), with a slope given by:

$$\frac{d(\ln|A(t)|)}{dt} = \frac{\delta\omega_0}{2} = \frac{1}{\tau} \tag{3.1}$$

In general, the total damping consists of contributions from all of the dissipative loss mechanisms, including: acoustic radiation (δ_{rad}), thermal diffusion and conduction (δ_{th}), viscosity of the surrounding liquid (δ_{vis}), and viscosity of the shell (δ_{sh}), such that $\delta = \delta_{rad} + \delta_{th} + \delta_{vis} + \delta_{sh}$ (Ainslie and Leighton 2011). For an encapsulated bubble the last term represents the damping imparted by the shell (de Jong et al. 2002), and for an unencapsulated bubble $\delta_{sh} = 0$. Assuming a Newtonian rheology, the expression for δ_{sh} in terms of the total non-dimensional damping coefficient can be written (Chatterjee and Sarkar 2003),

$$\delta_{sh} = \delta - \delta_0 = \frac{4\kappa_s}{\rho\omega_0 R_0^3} \tag{3.2}$$

where $\delta_0 = \delta_{rad} + \delta_{th} + \delta_{vis}$ represents the total damping coefficient for an unencapsulated gas bubble with the same radius and eigenfrequency as the encapsulated bubble. The shell viscosity in dimensional units, κ_s, can be estimated as a function of the time constants, τ and τ_0:

$$\kappa_s = \frac{\rho R_0^3}{2}\left(\frac{1}{\tau} - \frac{1}{\tau_0}\right) \tag{3.3}$$

where τ and τ_0 are the time constants for an encapsulated bubble (measured) and unencapsulated bubble with the same initial radius (calculated), respectively.

The expression given in Eq. 3.2 for the interfacial shell viscosity is consistent with the Rayleigh-Plesset-type model for phospholipid-encapsulated bubbles developed by Marmottant et al. (2005). In this model, the effective surface tension is described by three regimes of shell behavior: buckled, elastic, or ruptured. In the elastic regime, the shell contributes an additional restoring force, characterized by the elasticity χ, which shifts the resonance for small amplitude oscillations of an encapsulated bubble to higher frequencies. Oscillations in the purely elastic regime occur only at exceedingly low vibrational amplitudes (e.g. $R/R_0 < 1.01$ for $\chi = 2.5$ N/m (Overvelde et al. 2010)). Above a threshold radius, the shell is in the ruptured regime and the interfacial dynamics are also controlled by the free air-water surface tension. We estimate the rupture radius for ELIP to be $R/R_0 = 1.02$ based on the elasticity determined previously ($\chi = 1.55$ N/m (Raymond et al. 2014)). Overvelde et al. (2010) demonstrated that for oscillations exceeding this amplitude, the bubble is no longer oscillating in the purely elastic regime and the damped natural frequency for a encapsulated bubble approaches a value that is only slightly greater (~10%) than would be predicted for an unencapsulated bubble. For simplicity, we consider ω_0 to be the same for both encapsulated and unencapsulated bubbles and use the eigenfrequency of an unencapsulated bubble to calculate τ_0 in Eq. 3.3 (for the explicit expression see, e.g. Eq. (5) in Overvelde et al. (2010)). An example of the damping analysis is shown in figure 3.4.

3.2.4 Simulations

In order to evaluate the validity of the shell viscosity estimates obtained for individual ELIP, radius versus time curves were simulated using the dynamical model for lipid-encapsulated microbubbles developed by Marmottant et al. (2005). The

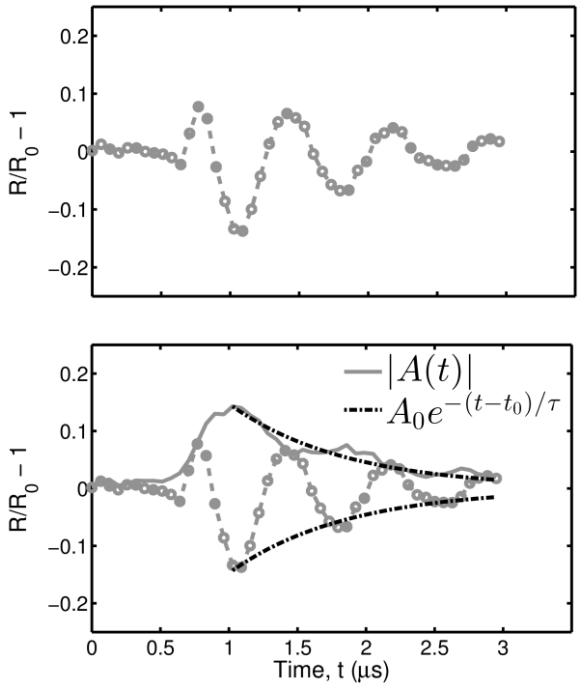

Figure 3.4. Schematic of the damping analysis. (Top) Radius versus time curve measured in response to 0° impulse excitation (the response due to 180° excitation is truncated for clarity). (Bottom) The amplitude decay envelope (solid line) is calculated using the discrete Hilbert transform. The time constant is obtained by fitting an exponential decay (dash-dot line) to the envelope using Eq. (1). For this example, R_0 = 2.5 μm, τ = 0.85 μs, $\kappa_s = 5.6\times10^{-9}$ kg/s.

measured acoustic pressure waveforms (see Fig. 3.3) were used as the forcing function for the bubble dynamics simulations which were compared with the experimental data. The values of the physical parameters used for the simulations were: ambient pressure P_0 = 100 kPa, density of the liquid, ρ = 1007 kg/m3, viscosity of the liquid (at 37 °C), $\mu = 0.76 \times 10^{-3}$ kg/(m•s), surface tension of the free air-water interface, σ_{water} = 0.072 N/m, and speed of sound, c = 1536 m/s. These parameters correspond to air-filled microbubbles suspended in PBS with 0.5% BSA solution at 37 °C (Raymond et al. 2014). The effective polytropic exponent was calculated from the ratio of specific heats using the expression given by (Hoff et al. 2000) following other researchers who have used similar expressions (Chapman and Plesset 1971; Prosperetti 1977; Crum 1983). The parameters used in the Marmottant model for describing the interfacial rheological properties of the shell are the elasticity, χ = 0.1 – 1.55 N/m, and the shell surface viscosity, κ_s, which was estimated based on experimental measurements as described in the previous section. Marmottant and others have demonstrated that a phospholipid shell stabilizes a quiescent gas bubble

by counteracting the Laplace pressure, therefore most microbubbles have an initial surface tension much lower than the surface tension of the free air-water interface, σ_{water} (Marmottant et al. 2005; Overvelde et al. 2010). In this study, we assume the shell encapsulation is initially in the pre-buckled state (i.e. the transition between the elastic and buckled regions) and consequently the initial surface tension was taken as $\sigma_0 = 0$ for all numerical simulations (Kwan and Borden 2012).

3.3 RESULTS

A total of 476 radius versus time curves for 106 individual ELIP were analyzed. The equilibrium radii of the individual ELIP ranged between 0.9 and 3.4 μm. Only trials for which the microbubble did not show any dissolution were analyzed in this study ($|\Delta r| < 0.1$ μm, where Δr is the difference between the bubble resting radius before and after the acoustic excitation). A small number of recordings (12 in total, < 3%) with $|\Delta r| > 0.1$ were therefore not included in the analysis.

Results of the measured shell viscosity as function of size are shown in figure 3.5(a). Due to the large number of individual data points, the mean value and standard deviation of the points within radius bins spaced by 0.2 μm are also shown for clarity. There is a considerable spread of the shell viscosity estimates among microbubbles of the same size range (indicated by vertical error bars). However, the estimated shell viscosity increases with increasing bubble size, as has been shown in other investigations of lipid-shelled agents (Morgan et al. 2000; van der Meer et al. 2007; Tu et al. 2011). The shell viscosity estimates range from 2.1×10^{-9} kg/s for microbubbles of 0.9-1.4 μm radius to 2.3×10^{-8} kg/s for microbubbles of 2.5-3.4 μm radius. These values are the same order of magnitude as values obtained in other studies based on population estimates of commercially available lipid-shelled microbubbles such as SonoVue® ($\kappa_s = 5.4\times10^{-9}$ kg/s (Gorce et al. 2000)), Sonazoid® ($\kappa_s = 1.2\times10^{-8}$ kg/s (Sarkar et al. 2005)), and Definity® ($\kappa_s = 3\times10^{-9}$ kg/s (Faez et al. 2011)).

The dependence of the shell viscosity on the maximum dilatation rate is shown in figure 3.5(b). The maximum dilatation rate $(\dot{R}/R)_{max}$ was determined directly from the experimentally measured radius-time curves by calculating the derivative with respect to time. Despite the dispersion in the individual shell viscosity estimates, this plot demonstrates a decrease of the shell viscosity with increasing dilatation rate. Assuming a power-law relation, the slope of the best-fit line through the points is -0.66. This power-law exponent is consistent with rheological shear-thinning behavior and has been reported earlier for lipid-shelled bubbles (van der Meer et al. 2007). For low dilatation rates ($< 0.50\times10^{6}$ s^{-1}), the mean value and standard deviation of the shell viscosity estimates in this study was $\kappa_s = (2.1 \pm 0.1)\times10^{-8}$ kg/s (n = 23).

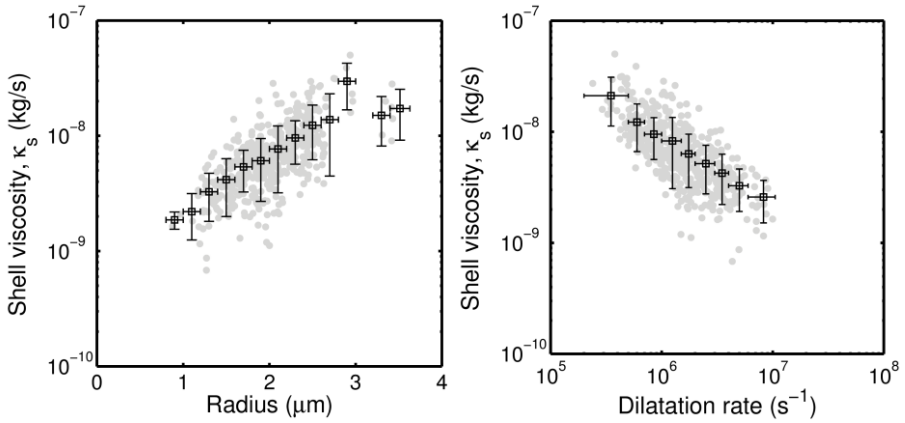

Figure 3.5. Shell viscosity versus (a) radius and (b) dilatation rate. Horizontal bars represent the bin width and vertical error bars represent one standard deviation of the points within each radius bin.

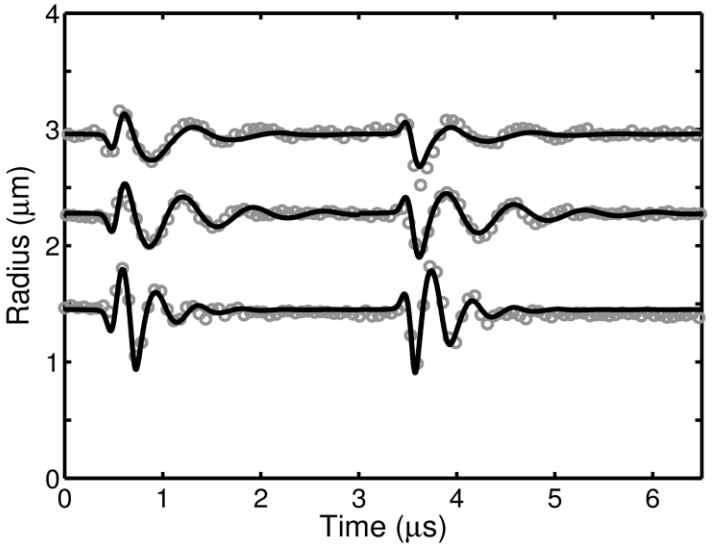

Figure 3.6. Example of simulated and experimentally measured radius versus time curves for ELIP with equilibrium radii of 1.5, 2.3, and 3.0 μm. The excitation peak pressure amplitude for all cases was 250 kPa. Estimates of the shell viscosity were derived from the experimental measurements for each case and used as inputs for the numerical simulation, yielding κ_s = 3.3 ± 0.4×10^{-9}, 6.0 ± 0.3×10^{-9} and 2.15 ± 0.2×10^{-8} kg/s, respectively. Other simulation parameters were R_0 = 1.5, 2.3 and 3.0 μm and χ = 0.1, 0.2 and 1.55 N/m, respectively.

Figure 3.6 shows three examples of numerically simulated and experimentally measured radius versus time curves for individual ELIP with equilibrium radii of 1.5, 2.3, and 3.0 μm. The excitation peak pressure amplitude for all cases was 250 kPa. Simulations were carried out using the experimentally derived shell viscosity (κ_s) for each individual ELIP (i.e. the average of the estimates derived from both pulses). The shell elasticity (χ) was adjusted considering approximately one order of magnitude (with the upper limit corresponding to the value previously determined for ELIP in the linear regime, χ = 0.1 – 1.55 N/m (Raymond et al. 2014)) to produce an acceptable fit to the experimental data. The numerical simulations show good agreement with the experimentally measured transient impulse response dynamics for each case.

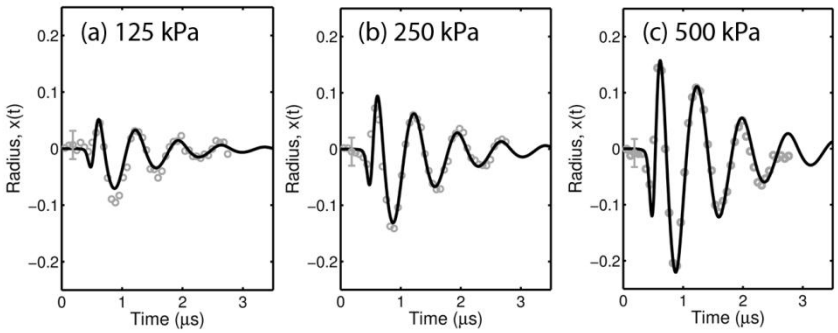

Figure 3.7. Example of experimental and simulated radius-time curves for a single ELIP (R_0 = 2.5 μm, χ = 0.25 N/m) excited by (a) 125 kPa, (b) 250 kPa and (c) 500 kPa peak pressure amplitude pulses (0° pulse). Vertical bars represent the relative error of the radius tracking algorithm, which was determined by the difference between the maximum and minimum radius measured from a recording of the same ELIP without ultrasound exposure.

Figure 3.7 shows an example of simulated and experimentally measured radius versus time curves for a single ELIP exposed to three different peak pressure amplitude pulses: 125, 250 and 500 kPa. As expected, the shell viscosity values obtained from each independent excitation are similar. The estimates of κ_s for each pressure are 5.7, 5.6, and 5.6 × 10^{-9} kg/s, respectively.

3.4 DISCUSSION

The goal of this study was to improve the understanding of the transient oscillation dynamics and shell properties of ELIP. We estimated the damping and shell viscosity from the unforced response of individual ELIP excited by a broadband acoustic impulse excitation measured using ultra-high-speed imaging. The results derived from estimates for individual ELIP were in good agreement with our

previously obtained values based on bulk acoustic attenuation measurements. Overall, the shell viscosity estimates for ELIP in this study are consistent with values reported for commercially available lipid-shelled UCAs. Furthermore, we found that the Marmottant model accurately describes the transient dynamics of an individual ELIP when compared with radius versus time measurements obtained from ultra-high-speed recordings. Thus the viscoelastic shell of ELIP behaves similarly to other lipid-shelled agents.

3.4.1 Contributions to damping effects

The total damping coefficient is the summation of the shell damping (δ_{sh}) and three other damping terms: the radiation damping (δ_{rad}), the thermal damping (δ_{th}), and the viscous damping due to the surrounding liquid (δ_{vis}). Theoretical expressions for predicting the damping factors of a spherically oscillating gas bubble are well-established (Ainslie and Leighton 2011), and the latter three terms can be readily calculated based on the known equilibrium size and eigenfrequency of the microbubble. Figure 3.8 shows the damping coefficients versus radius for an air bubble under the experimental conditions used in this study. Viscous effects (δ_{vis} or δ_{sh}) dominate for bubbles in the size range considered in this study (< 4 μm radius). However, the effect of thermal damping is also considered in this case for air-filled microbubbles at resonance.

Thermal damping is not accounted for explicitly in the Rayleigh-Plesset formulation and is often neglected in linearized models of UCAs as well (Faez et al. 2013). However, thermal damping can be significant for resonant bubbles larger than about 1 μm and is dominant for resonant bubbles larger than ~10 μm (de Jong et al. 2002). Fig. 3.8 shows that for a 1 μm radius bubble, δ_{th} is approximately equal to δ_{rad} and only amounts to 7% of the viscous term δ_{vis}. For a bubble of about 4 μm radius, δ_{th} is approximately equal to the viscous damping coefficient. In this study, we estimated the thermal damping and polytropic exponent based on the resting radius of the microbubble using the expressions given by Hoff et al (2000). It should be noted that the values of δ_{th} shown in Fig. 3.8 were calculated for an unencapsulated air bubble at resonance and include the effects of surface tension on the equilibrium gas pressure. However, δ_{th} may be less significant for an encapsulated bubble due to a lower equilibrium gas pressure resulting from the reduced initial surface tension for a bubble with a stabilizing shell (for example, $\sigma_0 = 0$ for a pre-buckled bubble as was assumed in this study) (Church 1995). Therefore we may have a slight underestimation of the shell damping effect.

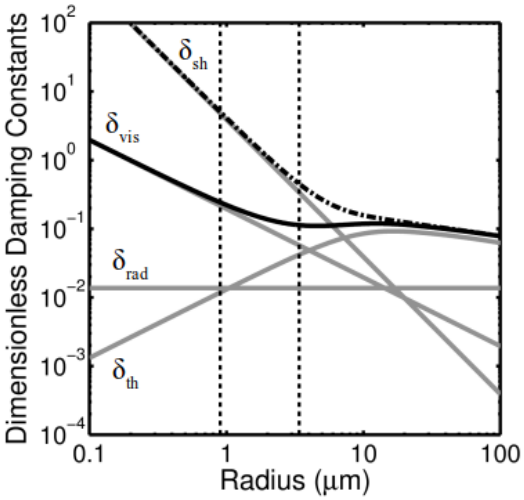

Figure 3.8. The variation of dimensionless damping coefficients (δ_{rad}, δ_{vis}, δ_{th}, δ_{sh}) versus microbubble size at resonance. The total damping coefficients for a free bubble (solid line) and an encapsulated bubble with a shell viscosity of $\kappa_s = 2\times10^{-8}$ kg/s (dash-dot line) are also shown. The vertical dotted lines represent the size range of ELIP considered in this study.

3.4.2 Shell viscosity

Overall, our estimates of the shell viscosity of individual ELIP based on the optical method developed in this study are consistent with our previous measurements obtained using a broadband attenuation spectroscopy technique (Kopechek et al. 2011; Raymond et al. 2014). For low dilatation rates ($< 0.5\times10^{-6}$ s^{-1}), the average value of the shell viscosity in this study ($\kappa_s = (2.1 \pm 0.1)\times10^{-8}$ kg/s, n = 23) is in agreement with our previously reported bulk acoustic measurements in the linear regime ($\kappa_s = (2.0 \pm 0.14)\times10^{-8}$ kg/s (Raymond et al. 2014)). Moreover, the shell viscosity estimates derived from damping measurements on 106 individual ELIP in this study indicate an apparent increase of the shell viscosity with increasing radius, and a decrease with increasing dilatation rate, indicative of shear-thinning behavior. This observation is consistent with previous measurements on commercially available lipid-shelled microbubbles such as SonoVue®(van der Meer et al. 2007) and Definity®(Tu et al. 2011), but is not explained by existing shell models where the viscosity is assumed to be constant over all radii. However, there have recently been attempts to account for this behavior using ad-hoc rheological models (Doinikov and Bouakaz 2011; Li et al. 2013).

The shell viscosity estimates based on the optical approach also showed considerable variations among ELIP of the same size range (see Fig. 3.5). Variations in

shell properties and acoustic response have also been reported in previous studies on lipid-shelled microbubbles (Goertz et al. 2007; Emmer et al. 2009; Luan et al. 2012). Kwan and Borden (2012) and Kooiman et al. (2014) present convincing microscopic images of heterogeneous lipid domains and ascribe this phenomenon to phase separation of the different lipid species on the bubble surface. Similar variations in the local lipid concentration on the shell have been found to affect the nonlinear behavior of DSPC microbubbles at high frequencies (Helfield et al. 2012), although no clear relation between the nonlinear response and shell microstructure was evident. Hosny et al. (2013) quantified the spatial distribution of viscosity in the microbubble shell using a fluorescence lifetime imaging technique and also found a large variation in viscosity that was correlated to differences in the ultrasound response of microbubbles of similar size. Based on the chemical composition and preparation method of ELIP, we expect similar inhomogeneities in local lipid concentration, as well as variation between individual ELIP particles within a population. Moreover, lipid diffusion and the phase transition influenced by the surrounding temperature can be other key factors affecting the heterogeneity of the ELIP shell (Borden and Longo 2004; Buchanan et al. 2008).

Nanostructural surface morphology (Borden 2009), which could not be resolved using the optical techniques in this study (e.g. Fig. 3.2), may nevertheless play a large role in the dynamic behavior of ELIP. For lipid-encapsulated bubbles the shell is usually assumed to be a monolayer due to thermodynamic considerations (Kwan and Borden 2012). However, the shell thickness has not been directly measured for microscopic encapsulated gas bubbles and estimates based on the dynamic response of the microbubble only give information about the interfacial rheological properties of the microbubble (i.e. zero-thickness interface model) (Paul et al. 2014). Therefore, the large variation in viscosity estimates could be due to the number of lipid layers surrounding the encapsulated microbubbles (Hosny et al. 2013). The resolution of the fluorescence images presented in Fig. 3.2 is limited by the focal spot size, which is about 220 nm in the lateral dimension. Thus, we are unable to conclude whether the shell is a lipid monolayer or if it is multilamellar. Multilamellar vesicles, in which the lipid monolayer immediately adjacent to the gas bubble is surrounded by one or more bilayers, have been observed in transmission electron microscopy images of ELIP (Kopechek et al. 2011). The spread of the shell viscosity estimates for ELIP of similar size may indicate the presence of multilamellar vesicles, where the apparent viscosity depends on the number of lamallae.

Another factor affecting the interpretation of the variation in the shell viscosity estimates is the uncertainty, which can be approximated as the random error associated with separate measurements on the same ELIP. We calculated the random error by considering the relative difference between the values obtained from

separate analysis of the two phase-inverted excitation pulses (0° and 180°), i.e. the absolute difference between the two shell viscosity estimates normalized by the average of the two estimates. The median random error was 40% which is approximately the same as the standard deviation shown in figure 3.5a and 3.5b.

3.4.3 Impulse response measurements and analysis

Evaluation of the damping coefficient based on the impulse response is a new and efficient approach applied to characterization of lipid-shelled ELIP in this study. A broadband pulse was applied to acquire the radius versus time impulse response of an individual ELIP, requiring only a single exposure of a few microseconds using an ultra-high-speed camera. Using the Brandaris 128, we were able to record the unforced, exponentially decaying amplitude response from two acoustic impulse excitations, a pulse inversion pair, during each high speed recording (128 frames). This method provides an efficient approach which enabled statistical measurements on a large number of individual ELIP. Additionally, data analysis was straightforward and the simulated transient response of the lipid-encapsulated microbubble accurately tracked the measured radius versus time curves (Figs. 3.6 & 3.7).

We also assessed the validity of this technique by comparing the steady-state response measured using an 8-cycle narrow-band burst excitation with numerical simulations. An example is shown in figure 3.9 in which simulations using two different shell viscosity values (derived from the optical method described here or the bulk acoustic method reported in Raymond et al. (2014) respectively) are compared with experimental measurements. Excellent agreement was found between the simulated and measured radius versus time curves when the effect of the shell was taken into account using the viscosity estimate obtained in this study. For the example shown in Fig. 3.9(a), the shell viscosity estimate (κ_s = 3.0 × 10^{-9} kg/s) was obtained during a previous impulse response exposure of the same individual ELIP. Alternatively, using the population-averaged shell viscosity obtained in Raymond *et al.(2014)* (κ_s = 2.0 × 10^{-8} kg/s) results in an under-prediction of the amplitude of the response to narrow-band forcing (Fig. 3.9(b)). Use of the estimated value obtained for a specific ELIP in this study allows one to obtain much more precise agreement between the experimental theoretical data using the Marmottant model.

3.4.4 Implications for contrast-enhanced imaging

The size range of ELIP is known to be polydisperse, with particle sizes ranging from tens of nanometers to several microns (Raymond et al. 2014; Paul et al. 2012; Kopechek et al. 2011). Differences in the characteristics of nanoscale versus microscale ELIP vesicles may play a role in the scattering properties of individual ELIP. This study found that smaller ELIP are characterized by a substantially lower

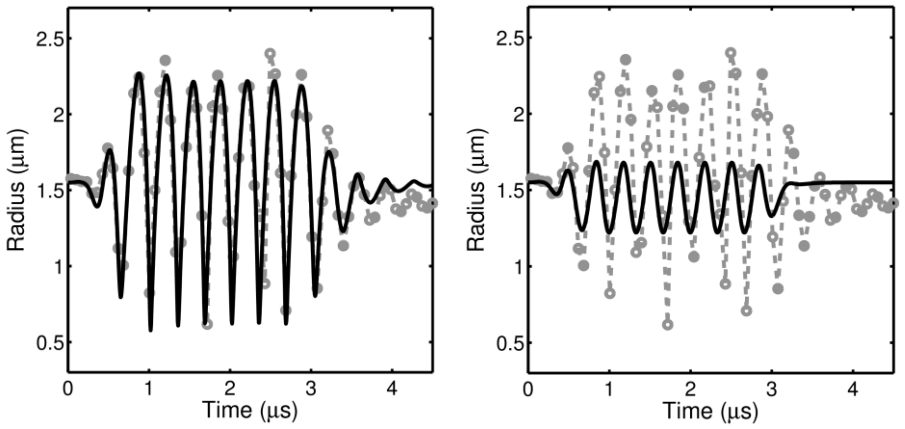

(a) (b)

Figure 3.9. Experimentally measured radius-time curve for a bubble in response to narrow-band forcing (f = 3 MHz, dashed lines). Theoretical radius versus time curves for two different values of the damping coefficient are shown. The solid line represents the simulated damping using (a) the method described in this paper (κ_s = 3.0 × 10^{-9} kg/s) and (b) the shell damping estimated from bulk acoustic measurements (κ_s = 2 × 10^{-8} kg/s). The shell elasticity parameter was taken to be χ = 1.55 N/m as reported in (Raymond et al. 2014).

shell viscosity, which may contribute to increased nonlinear scattering, especially at higher frequencies. Such nonlinear behavior of the smaller populations of ELIP could be exploited for diagnostic ultrasound applications which utilize higher frequencies, such as intravascular ultrasound. For example, the nonlinear acoustic signatures of ELIP could be utilized for improved imaging of pathology in the vasa vasorum, the proliferative small vessels that play a role in atheroma progression in the cardiovascular system.

Goertz et al.(2007) demonstrated that sub-populations of the lipid-shelled clinical UCA Definity® exhibited different frequency-dependent scattering properties as a function of size. These authors hypothesized that differences in the encapsulation microstructure for small and large bubbles may be a key factor influencing the nonlinear scattering at high frequencies. A subsequent study by Helfield et al.(2014b) demonstrated that smaller sub-populations of lipid-shelled microbubbles were not only resonant at higher frequencies, but were also characterized by a substantially lower shell viscosity, suggesting a possible frequency dependence of the lipid shell properties. It is still not clear whether this effect is due solely to the size or if frequency-dependent considerations need to be taken into account in the dynamical models. Doinikov et al. (2009) point out that existing shell models may not capture the observed radius- or frequency-dependence of the shell material properties, and that full description of the rheological properties of the shell may require the use of more

complex models in order to describe the shear-thinning behavior. A more detailed exploration of alternative rheological models is beyond the scope of this paper.

3.4.5 Limitations

Inherent limitations of the optical system resolution result in a bias of the size range of ELIP selected for analysis in this study. The optical resolution of the ultra-high-speed imaging system was 0.4 μm (Chin et al. 2003) and the smallest individual ELIP that was measured in this study was several times larger than the optical resolution limit. The size range of ELIP considered here focused on measurable particles larger than 0.9 microns in radius only and smaller ELIP were not considered for investigation.

The proximity of the microbubble to the OptiCell™ membrane may also affect the measured response. Previous studies have found that the presence of a membrane near an oscillating microbubble can affect the resonance frequency and oscillation amplitude in response to acoustic forcing (Garbin et al. 2007; Overvelde et al. 2011; Helfield et al. 2014). Functionalized UCAs such as ELIP are being developed for targeted imaging and drug-delivery applications, and therefore similar effects are expected to play a role *in vivo*. The acoustic response of adherent targeted bubbles may be influenced by the ligand distribution and bubble-wall interaction (Kooiman et al. 2014) – therefore, future work to investigate the damping for adherent targeted agents using this approach is recommended.

3.5 CONCLUSIONS

In this study a model based on time domain analysis was developed to estimate the shell viscosity for individual ELIP using optically measured radius versus time curves. The decay time constant was measured from the unforced response of the ELIP following excitation by a short acoustic pulse. At low dilatation rates, the shell viscosity is in quantitative agreement with our previously determined values for ELIP. The viscoelastic shell of ELIP was found to behave similarly to other lipid-shelled agents. We demonstrated that qualitative agreement between the measured and simulated radius versus time curves under transient and steady-state acoustic forcing is highly dependent on the shell viscosity. The methods described here can provide accurate estimates of the shell viscosity and damping for individual UCA microbubbles. In contrast to acoustic measurements of a microbubble population with a relatively wide size distribution, this method provides some insight on the variation of properties among single particles within a population. This method also enables efficient measurements on a large number or individual UCA microbubbles because it is based on the response to a single acoustic impulse excitation.

4

Segmented high speed imaging of vibrating microbubbles during long ultrasound pulses

Abstract — Detailed information about the response of microbubbles to long ultrasound pulses (> 100 cycles) is hampered by the limited time span ultra-fast framing cameras (> 10 MHz) cover. We therefore developed a new imaging mode for the Brandaris 128 camera (Chin et al. 2003), facilitating high speed imaging during small time windows (segments), equally distributed over a relatively large time span.

Appeared as a proceedings paper for the IEEE International Ultrasonics Symposium 2012, Dresden, by T. J. A. Kokhuis*, Y. Luan*, F. Mastik, R. H. S. H. Beurskens, M. Versluis and N. de Jong.

4.1 INTRODUCTION

For decades, microbubbles are used clinically as contrast agents in contrast enhanced ultrasound imaging (CEUS). Typically, microbubbles are 1-10 µm in size and consist of a gas core stabilized by lipid, protein or polymer shell. Because of their size, microbubbles cannot extravasate and are contained within the blood circulation after injection. During ultrasound insonification, the microbubbles exhibit volumetric oscillations, which is the main reason for their high echogenicity. This high echogenicity improves the contrast between the blood and the surrounding tissue and is used in cardiology for myocardial perfusion studies or for left-ventricle opacification.

More recently, the possibility of using microbubbles for a variety of new therapeutic applications is investigated. The presence of vibrating microbubbles in the proximity of thrombus has been shown to facilitate thrombolysis (Kondo et al. 1999), a mechanism also referred to as sonothrombolysis. Vibrating microbubbles were observed to enhance the uptake of drugs and genes by inducing a transient porosity of the cell membrane, a mechanism called sonoporation. Furthermore, microbubbles have been shown to mediate reversible opening of the blood-brain barrier (BBB), allowing therapeutic agents to be delivered to the brain (Unger et al. 2004) and to enhance the engraftment of mesenchymal stem cells after acute myocardial infarction (Ghanem et al. 2009).

Although these potential future applications of microbubbles are widely recognized, there is generally not much consensus about the optimal ultrasound parameters. In several studies, long ultrasound cycles up to several thousands of cycles were reported to give the best therapeutic effect for microbubble-mediated stem cell engraftment (Ghanem et al. 2009), thrombolysis (Leeman et al. 2012), gene delivery (Meijering et al. 2007) and reversible opening of the BBB (Hynynen et al. 2001). To understand the therapeutic value of long pulses, an in-depth investigation of the bubble dynamics in response to long pulses is needed. High speed optical imaging has proven to be a powerful tool for revealing the interaction between ultrasound and microbubbles. However, the time span covered by high speed cameras (> 10 MHz) is limited and typically below 15 µs. We therefore developed a new imaging mode for the Brandaris 128 camera. In contrast to previous imaging modes developed for the Brandaris 128 camera, this new mode allows very fast acquisition of successive segments, with inter-segment times as low as multiples of the rotational period of the mirror. By distributing the segments over the time window of ultrasound application, this mode enables the study of microbubble dynamics in response to long ultrasound pulses.

4.2 MATERIALS AND METHODS

4.2.1 Experimental design fast segmented mode

The 128 CCD sensors of the Brandaris128 camera were grouped into separate segments. The number of segments can be varied between 1-128. In this study, we

grouped the CCD sensor arc into 4 segments of 32 sensors each. All CCDs were illuminated during each mirror period. Before each illumination, all the CCDs were flushed, erasing all the information on the photoactive region of the CCDs. The grouping into segments was based on the moment of the charge transfer; a process transferring the image to a buffer channel and terminating the exposure time of the specific CCD. This process was fully controlled by programmable CCD controller cards (C^3) providing independent control of each segment. In this way, only the information on the CCDs within a specific segment could be transferred to the buffer channel. Images already stored in the buffer channels of the CCDs were not affected by the flushing process. The time interval in between subsequent segments was not limited by the readout of the CCD buffer channels (~ 80 ms) and could be set at multiples of the rotational period of the mirror. Start of the acquisition was triggered at a predefined frame rate, corresponding to the preferred inter-segment time. Fig. 4.1A shows the configuration of the Brandaris used in this study. The timing diagram of the triggering is shown in Fig. 4.1B.

4.2.2 Xenon flash source

The pulse duration of the Xenon flash source (MVS-7010, Perkin–Elmer Optoelectronics) used with the Brandaris camera, measured at 50% of the peak value, is 105 μs. This time is too short to illuminate all the segments. Moreover, the repetition rate is limited to 20 Hz. We therefore adapted the electrical circuit of the flash source by introducing a pulse-forming network, consisting of several capacitors and inductors. The adaptation resulted in a pulse duration of 710 μs. Fig. 4.1C shows the pulse duration created by the flash source before (green) and after (black) the adaptation. The extended flash source facilitated illumination of all the segments with a single flash. Please note that in Fig. 4.1C both intensities are normalized. The maximum intensity of a flash after modification was observed to be about 7 times higher compared to the maximum intensity of a flash created by the default flash source.

4.2.3 Preparation of microbubbles

Microbubbles with a perfluorobutane (C_4F_{10}) gas core were made by sonication (Klibanov et al. 2004). The mean diameter of the microbubble distribution was 3.5 μm. The coating was composed of DSPC (59.4 mol %), PEG-40 stearate (35.7 mol%) and DSPE-PEG(2000) (4.9mol %).

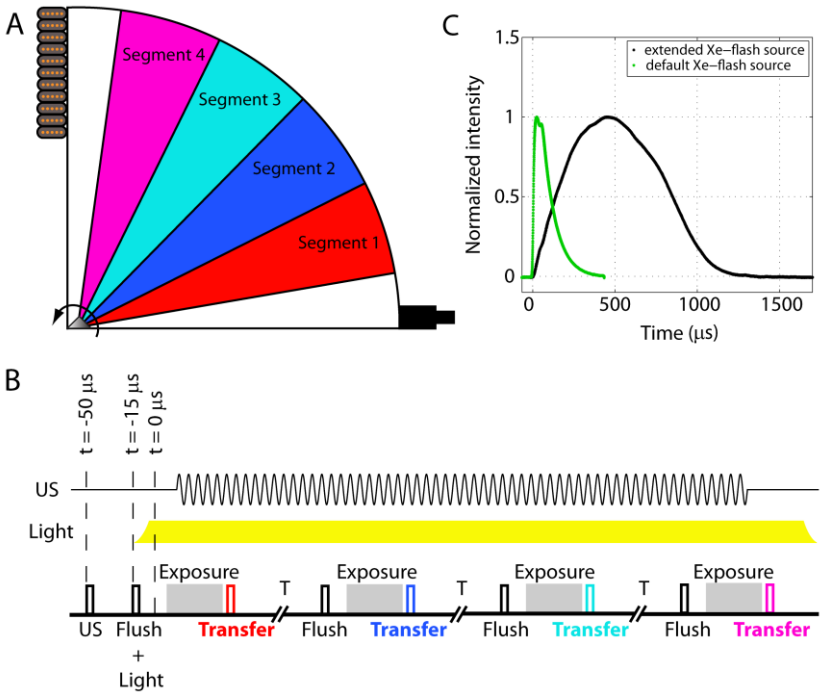

Figure 4.1. (a) Schematic overview of the grouping of the 128 CCD sensors of the Brandaris camera into 4 segments. (b) Timing diagram of triggering. (c) Pulse duration of the Xenon flash source before (green) and after modification (black).

4.3 RESULTS

4.3.1 Proof of principle

To confirm that the transfer of photoelectrons to the transport channels of the CCDs could be controlled independently for the different segments and that the process of flushing the CCDs in between successive segments was successful, a test measurement was performed. The Brandaris was operated in the fast segmented mode in combination with the short light source (see green curve Fig. 4.1C), this to prevent the light source of illuminating more than one segment at a time. The inter-segment time was 180 µs. By delaying the onset of this short single flash with multiples of the inter-segment time, only the corresponding segment that was triggered to transfer the photoelectrons into the transport channel after that specific illumination, before the next flush, was successfully exposed. The other 3 segments not. The result is shown in Fig. 4.2. Plotted is the brightness (i.e. mean pixel intensity) of the 128 CCDs for 4 different situations. Panel A shows the result of an experiment in which a light beam was swept across the CCDs, just before CCD#1 – CCD #32 (i.e.

segment 1) were triggered to transfer the photoelectron into their transport channel. Only the first 32 segments were successfully exposed after readout. Although all CCDs were illuminated by the light beam, because the other 3 segments were not triggered for a charge transfer at this specific time point, the information on these 96 CCDs was lost again after the next flush. However, by delaying the onset of the light flash with multiples of the inter-segment time, the segment which exhibited a successful exposure after readout was also changed. In panel B, the onset of the light was delayed by the inter-segment time, resulting in a successful exposure of segment 2 (CCD #33 – CCD #64). Similarly, in panel C, the onset of the light was delayed by twice the inter-segment time, resulting in a successful exposure of segment 3 (CCD # 65- CCD # 96). Finally, in panel D the onset of the light was delayed by three times the inter-segment time, resulting in a successful exposure of segment 4 (CCD # 97- CCD # 128). The increase (decrease) in intensity observed in the panel A and D is due to the ramp-up and ramp-down of the (short) light source.

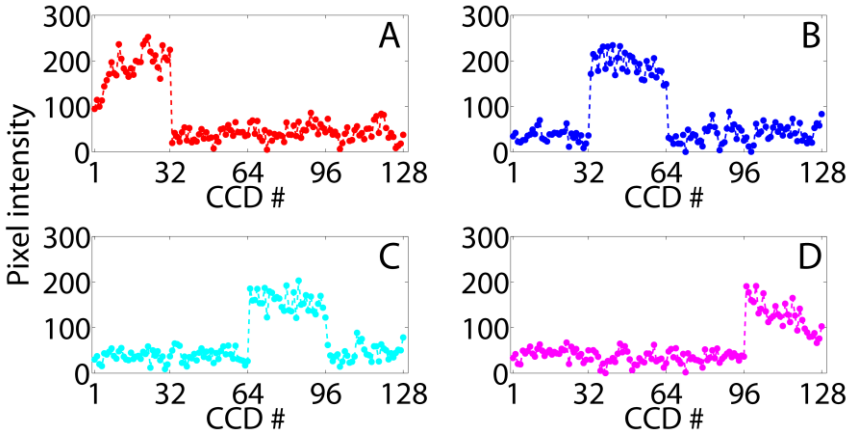

Figure 4.2. In the fast segmented mode, different segments (shown here for 4 segments of 32 CCDs each) can be controlled independently. The Brandaris was operated in the fast segmented mode in combination with the short light source. The inter-segment time was 180 μs. Plotted is the brightness of the 128 CCD sensors for 4 different experiments in which the time point of the onset of the light was altered. Dependent on relation between the onset of the short light source and the time point of charge transfer set for the different segments, only a specific segment will have a successful exposure. Panel A, B, C and D show a successful exposure of segment 1,2,3 and 4 respectively.

4.3.2 Microbubble dynamics during long ultrasound pulses

4.3.2.a Insonification with long pulses at non-destructive MI (0.1)

To capture the dynamics of microbubbles during long ultrasound pulses at non-destructive mechanical index (MI), microbubbles were exposed to a single ultrasound burst and imaged with the fast segmented mode. Fig. 4.3A shows the radius-time curve of a microbubble (R_0 = 3.1 µm) during insonification with 547 cycles at 1 MHz and P_{-} = 100 kPa. The four segments are equally distributed over the time span of ultrasound application, each of them capturing the dynamics of the microbubble for 4.25 µs. The time gap between successive segments (indicated by the vertical red bars) was 180 µs. The transient parts of the oscillation are captured by the first and last segment. The corresponding power spectra of the segments are shown in Fig 4.3B. The bubble exhibited stable oscillations during the entire ultrasound burst. The microbubble radius after insonification appeared to be a little bit smaller, i.e. 2.96 µm.

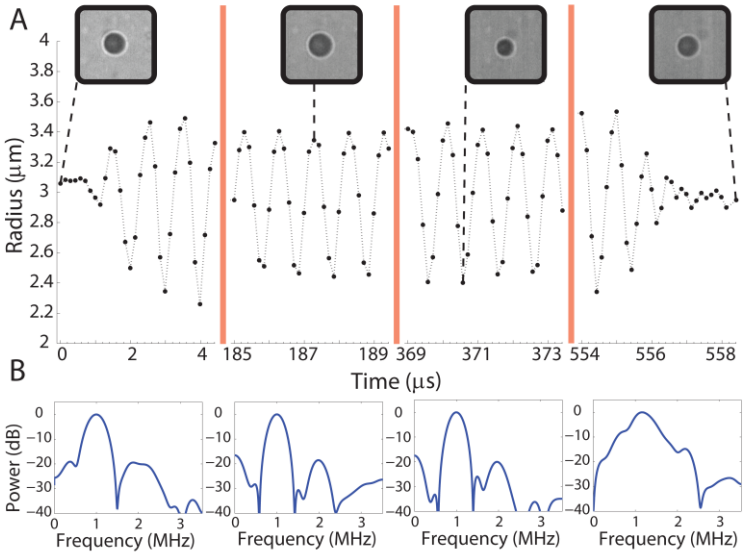

Figure 4.3. (a) Radial excursion of a microbubble during insonification with 547 cycles at 1 MHz and P_{-} = 100 kPa. The time gap in between successive segments was 180 µs (indicated by the vertical red bars). (b) Corresponding power spectra.

4.3.2.b Insonification with long pulses at destructive MI (0.4)

Insonification at high MI (P_{-} = 400 kPa) resulted in violent bubble oscillations and consequent bubble destruction. Interestingly, the smaller bubbles that were generated

(which were either pinched-off from the primary bubble or acoustically-driven deflated primary bubbles) were observed to cavitate until the end of the ultrasound burst. An example is shown in Fig. 4.4. The top row shows the inertia driven violent collapse of a 6.3 μm sized microbubble. The generated smaller bubble continued to vibrate until the end of the ultrasound burst. The corresponding time (with respect to the onset of the ultrasound) is given above each frame.

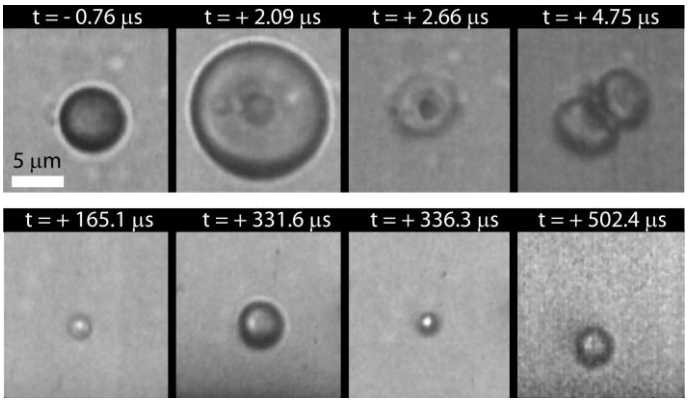

Figure. 4.4. Violent collapse of a 6.3 μm sized microbubble (top row) and the subsequent stable oscillation of the generated smaller bubble (bottom row). The time with respect to the onset of the ultrasound (t = 0 μs) is indicated for each frame. The bubble was insonified with a burst of 500 cycles at 1 MHz and P_ = 400 kPa.

4.4 DISCUSSION

In several studies on therapeutic applications of microbubbles, long ultrasound pulses (up to 10,000 cycles) were proven to be beneficial over shorter pulses. Moreover, not seldomly these long ultrasound pulses are used in combination with high acoustic pressures up to several megapascal. Because detailed information about the response of microbubbles to long ultrasound bursts is lacking, the exact mechanism of these microbubble-mediated therapies remains elusive. Moreover, an important question is whether the therapeutical effects of long ultrasound pulses at destructive mechanical index (MI > 0.4), should be ascribed to the cavitation of the microbubbles or the effect of the ultrasound itself.

We therefore developed a new high speed imaging method for the Brandaris 128 camera which facilitates high speed segmented imaging of vibrating microbubbles within small time windows distributed over a large time span. In a pilot study, microbubbles were insonified with long ultrasound pulses (500 – 600 cycles) at non-destructive MI (≤ 0.1) and destructive (MI > 0.4). At non-destructive MI, microbubbles

exhibited stable oscillations for over 500 μs. The development of surface modes was sometimes observed (Dollet et al. 2008), preferentially for resonant bubbles (Versluis et al, 2010). At MI 0.4, destruction of the bubbles was observed; often resulting in the generation of smaller bubbles. Interestingly, in contrast to the original bubble, these smaller bubbles were observed to oscillate until the end of the ultrasound pulse (> 500 μs), presumably because they are driven at a frequency further away from their eigenfrequency compared to the original bubble. The presence of such oscillating smaller bubbles was already hypothesized by Leeman and co-workers, who found a significant increase in the thrombolytic activity of microbubbles for long ultrasound pulses (> 1000 cycles, 1.5 MPa) over shorter pulses. No increase was observed in case of ultrasound application in the absence of microbubbles (Leeman et al. 2012). Our preliminary data confirms the presence of stable oscillating bubbles during application of long ultrasound pulses at destructive MI. However, the role of these bubbles in the therapeutic efficacy of long ultrasound pulses needs further investigation.

With our modified flash source, we are currently able to image microbubble dynamics during ultrasound pulses lasting up to ~ 750 μs. Efforts are being made to increase this time by additional changes to the electrical circuit of the flash source and by triggering multiple modified flash sources. This would allow high speed segmented imaging of microbubbles in response to ultrasound pulses up to a few milliseconds in length.

5

Nonlinear dynamics of single freely-floating microbubbles by combined optical and ultrafast acoustical characterization

Abstract — The acoustic nonlinear responses of ultrasound contrast agent microbubbles are of great interest for both diagnostic (e.g. contrast-enhanced imaging) and therapeutic (e.g., drug delivery) applications. Previously, optical and acoustical methods were developed to characterize single bubbles floating against a rigid wall. Here we combine simultaneous optical sizing and sensitive acoustical characterization to study quantitatively the nonlinear dynamics of single freely-floating bubbles. A coaxial-flow device was used to isolate individual microbubbles and to direct the bubble flow to the confocal region of the ultrasound transducers and a high-resolution microscope objective. The results showed very stable bubble vibrational response over long burst excitations (1 MHz, 140 μs) under all applied pressures (25 kPa, 50 kPa and 100 kPa). The relative oscillation amplitude at fundamental frequency (ε_f) and at second/third harmonics (ε_{2f}, ε_{3f}), and the ratio of radial excursion in expansion over that in compression (E/C) were derived from the received scattered signal. The nonlinearity (ε_{2f}, ε_{3f}) and asymmetry (E/C) of bubble vibrations were found to increase with increasing oscillation amplitude, and reach the maximum for bubbles at resonance. Moreover, with the same fundamental response (ε_f), the second harmonic response (ε_{2f}) of bubbles smaller than the resonance size is ~150% stronger than bubbles bigger than the resonance size. The data showed agreement with numerical simulations based on the shell-buckling model by Marmottant et al. (2005). The newly developed system can continuously measure bubble populations, thus provides a simple and efficient approach for *in vitro* characterization of contrast agent microbubbles.

In preparation for submission; by Y. Luan, G. Renaud, J.L. Raymond, T. Segers, R.H.S.H. Beurskens, F. Mastik, T.J.A. Kokhuis, G.P.R. Lajoinie, A.F.W. van der Steen, M. Versluis and N. de Jong. The authors thank Michiel Mantan and Geert Springeling from Erasmus MC, Rotterdam, the Netherlands, for their valuable effort in producing the setup.

5.1 INTRODUCTION

Lipid-coated microbubbles are widely used for contrast-enhanced ultrasound imaging in cardiology and radiology (Lindner 2004). They have also been investigated extensively for therapeutic applications, e.g. for drug-delivery and for thrombolysis (Stride and Saffari 2003; Medel et al. 2009). The microbubbles are composed of a stabilizing lipid shell and a gas-core and they expand and compress in response to pressure variations in the surrounding fluid imposed by ultrasound. A detailed knowledge of the dynamic response of lipid-coated microbubbles in response to ultrasound insonation can help to improve the efficacy of diagnostic and therapeutic applications of these agents. The nonlinear higher harmonic signals scattered by microbubbles are exploited by various contrast-enhanced ultrasound imaging (CEUS) techniques, e.g. harmonic imaging (Schrope and Newhouse 1993) and pulse inversion imaging (Simpson et al. 1999). The stability of the bubble response, which was reported to change with the dissolution of the microbubble during prolonged excitations of 1 ms or longer (Viti et al. 2012; Thomas et al. 2013), is a key parameter which affects the viability of an agent for clinical use. Finally, the bubble oscillation amplitude and the acoustic streaming generated are major determinants of the shedding of lipids and liposomes from the bubble surface, as it strongly influences the subsequent transport of the detached materials to the surrounding medium (Gelderblom 2012; Luan et al. 2014). Moreover, all the above characteristics can benefit imaging and/or drug delivery strategies and aid in the design of novel pulsing schemes and the design of new contrast agents.

Both simulations and experiments have shown that the bubble response depends not only on the ultrasound setting, bubble size and on the surrounding fluid viscosity, but also on the lipid shell viscoelastic properties. Whereas the bubble size determines the resonance behavior of the microbubble, the shell viscoelastic properties also change the resonance frequency and damping characteristics. Moreover, the lipid coating adds to the intrinsic (complex) nonlinear features of the bubble oscillation dynamics (Emmer et al. 2009). Previous studies using acoustic measurements and ultra-high-speed optical observations have demonstrated a myriad of nonlinear behaviors specific to lipid-coated microbubbles, including harmonic distortion due to buckling and rupture of the lipid shell (Marmottant et al. 2005), subharmonic emission (Faez et al. 2011), thresholding effects (Emmer et al. 2007), and compression-only behavior (de Jong et al. 2007). These effects are closely related to both the microbubble size and the lipid shell properties. Therefore all characterization efforts should involve an accurate sizing method of single and isolated bubbles (Sijl et al. 2011).

Most previous optical and acoustical characterization methods require manipulation of single microbubbles in a capillary or a flow channel (Maresca et al. 2010; Sijl et al. 2011). In this configuration, the flow channel itself may have an influence on the bubble vibrations. For optical approaches, the instantaneous microbubble vibrations can be captured by a high-speed framing camera running at several tens of million frames per second (Dayton et al. 2002; Bouakaz et al. 2005). However, even at MHz frame rates the sampling frequency can be a limitation in the accuracy of the obtained radius-time curves. Moreover, only a limited number of frames are available and the recording time is therefore restricted by the high frame rate unless complex timing schemes are used (Kokhuis et al. 2012). A few other optical approaches allow the measurement of isolated single microbubbles without constraint on the bubble vibration or motion, e.g., by using laser light scattering (Guan and Matula 2004) or by using optical tweezers to position the bubble away from a neighboring wall (Garbin et al. 2006). However, other limitations of the image resolution exist and the optical measurement system might be difficult and relatively expensive to build.

Acoustical methods offer superior temporal resolution but require a high sensitivity to detect echo signals scattered from an individual bubbles as well an accurate calibration of the system (Sijl et al. 2008). Recently, a sensitive acoustical characterization setup was developed to characterize single microbubbles circulating freely in a highly-diluted suspension (Renaud et al. 2012). This technique can perform continuous monitoring of single microbubbles for a time duration that is limited only by the size of the effective focal region and the velocity of the microbubbles in the measurement area, normally in the milliseconds range. Therefore it can be utilized to measure the dynamic response of microbubbles exposed to prolonged ultrasound. Also, the requirement for an absolute calibration is less stringent as the relative amplitude modulation is directly proportional to the scattered signal. However, the absolute size of individual microbubbles cannot be determined directly using this technique alone, due to the fact that the exact location of the bubble with respect to the focal position is unknown (Renaud et al. 2014).

This work now combines sensitive acoustical characterization with optical sizing to study quantitatively the nonlinear dynamics of freely-floating bubbles under prolonged ultrasound exposure. We first performed a statistical study to characterize the acoustic response, i.e. the stability and the nonlinear dynamic response of single freely-floating lipid-coated microbubbles under long burst excitations (140 μs). Three different acoustic pressures were applied and the nonlinear responses were characterized in the acoustical characterization setup. Next, a co-flow device was used to isolate individual microbubbles to form a bubble train and to direct the flow to the confocal region of the ultrasound transducer and a high-resolution microscope

objective. An optical image of the bubble was captured at the very same moment as the bubble echo was received and the obtained data was processed and compared to numerical simulations of the bubble dynamics and its nonlinear behavior.

5.2 MATERIALS AND METHODS

5.2.1 Microbubble preparation

Biotinylated lipid-coated microbubbles with a C_4F_{10} gas core (F2 Chemicals Ltd, Preston, UK) were made by sonication as described by Klibanov *et al.* (2004). The stock microbubble concentration was verified by a Multisizer III (Beckman Coulter Inc., Fullerton, CA, USA) as ~ 10^9 / ml with a volume-weighted mean size of ~3.5 μm diameter. Two experiments were performed. For the acoustic measurement only, a 5 μl stock solution was diluted directly into 250 mL of water in the measurement tank at room temperature. A magnetic stirrer was used to ensure that microbubbles were circulating freely (Fig. 5.1a). For simultaneous optical and acoustical measurement, the stock solution was diluted (1:50) with phosphate buffered saline (PBS) solution (Invitrogen, Bleiswijk, the Netherlands) and loaded into a 1 mL glass syringe (Hamilton, Reno, NV, USA) which was used to inject the microbubble suspension into the co-flow device at a rate of 5 μl/min by a syringe pump (NE-1000, New Era Pump Systems, NY, USA).

5.2.2 Experimental setup

A pair of high-frequency (HF) 30 MHz transducers (V375-SU, f = 19 mm, Olympus NDT, Waltham, MA, USA) operating in pulse-echo mode are aligned confocally at 90° and probe the bubble scattering cross-section in backscatter as described previously (Roy et al. 1990; Renaud et al. 2012). A low-frequency (LF) 1 MHz focused field transducer (V314, f = 24 mm, Olympus NDT, Waltham, MA, USA) also aligned confocally and positioned at 135° relative to the HF field, was used to drive the bubble oscillations (Fig. 5.1a). The acoustic pressures transmitted by the high frequency (80 kPa) and low frequency (25, 50, or 100 kPa) transducers were measured before the experiment using a calibrated needle hydrophone (Precision Acoustics, Ltd., Dorchester, Dorset, UK). For each recording, a HF probe burst (160 μs duration) and a LF modulation burst (140 μs duration) were precisely timed to arrive simultaneously in the focus, with the duration of the probing wave being slightly longer than that of the driving wave. A schematic exemplary received burst is illustrated in Figure 5.1c. Bursts were separated by an interval of 40 μs, resulting in a pulse repetition frequency of 5 kHz. A recording was triggered by the received echo at an amplitude above 10% of the vertical range, after which a total of 10 bursts were recorded in 2 ms by the waveform digitizer (PX14400, Signatec, CA, USA).

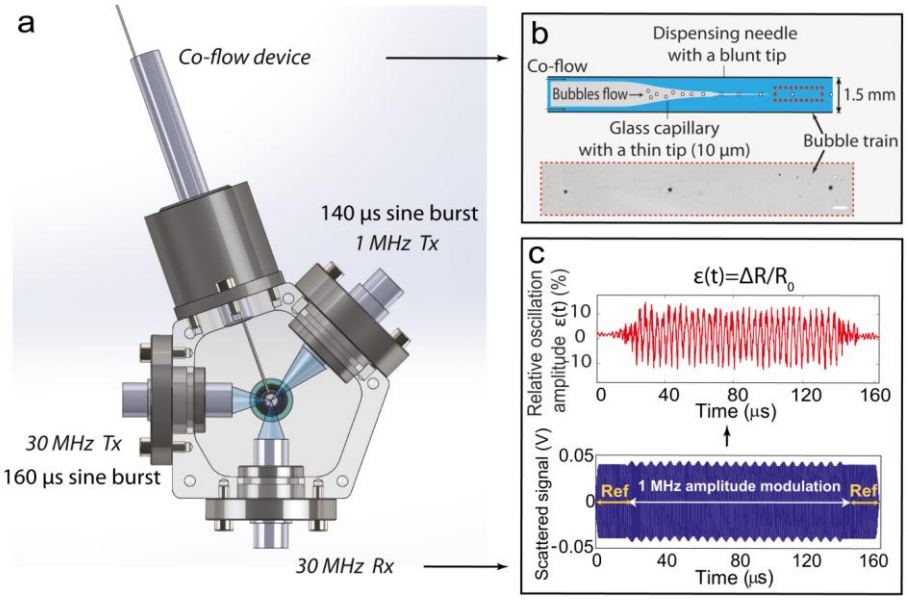

Figure 5.1. (a) A top-view schematic plot of the acoustical characterization setup composed of two transmitting (T_x) transducers and one receiving (R_x) transducer. A co-flow device is configured in the setup; (b) A schematic plot of the co-flow device for the generation of a bubble train with a spacing of ~300 µm between the bubbles; (c) An example of the scattered signal received from a dual-frequency burst containing 160 µs of the 30 MHz probe wave and 140 µs of the 1 MHz drive wave (blue curve) and the relative oscillation amplitude derived from the scattered signal (red curve). The size bar represents 20 µm.

In order to isolate microbubbles and to accurately control the speed of individual bubbles in the region of interest, a co-flow device (developed in-house) was coupled to the acoustical characterization setup (Fig. 5.1a). The co-flow device consists of a central bubble suspension flow, which was focused by a glass capillary with a thin tip (10 µm diameter), and located co-axially within the center of a dispensing needle with a blunt tip (1.5 mm diameter). The bubble flow (~2.5 mm/s) and the co-axial flow (~0.1 m/s) were controlled by separate syringe pumps to control the approximate spacing between individual bubbles. At the exit of the glass capillary, the bubbly flow was accelerated by the co-axial flow so that microbubbles were separated from each other with a spacing of ~300 µm to form a bubble train (Segers and Versluis 2014) (Fig. 5.1b). The co-flow device was mounted in a gimbal which can be manipulated freely in three dimensions to align the bubble train with the optical and acoustical focus.

Figure 5.2a shows the configuration of the acoustical characterization setup combined with optical high-speed imaging. An upright microscope equipped with a 40× water-immersion objective (numerical aperture (NA) = 0.8; Olympus, Zoeterwoude, The Netherlands) was used to resolve single microbubbles. A CMOS-based high-speed camera (Photron APX-RS; Photron Ltd, West Wycombe, UK) running at 6000 frames per second (fps) with a shutter time of 50 µs was used to capture bright-field images of the bubbles. The camera was operated in pre/post trigger mode, to capture a series of images (60 video frames in total within 10 ms) recorded both before and after the trigger signal had arrived (5 ms each), see Fig. 5.2b. Before the experiment, the optical field of view was co-aligned with the acoustical focal area using a thin needle (300 µm diameter) connected to the objective holder, annex microscope revolver. The total length of the needle was the same as the body length of the 40× objective plus its working distance (3.3 mm). The needle was moved by manipulating the x-y stage until a maximum echo of the 30 MHz probe signal was found. In the combined acoustical and optical measurement, the applied acoustic pressure of the LF modulation wave was 50 kPa.

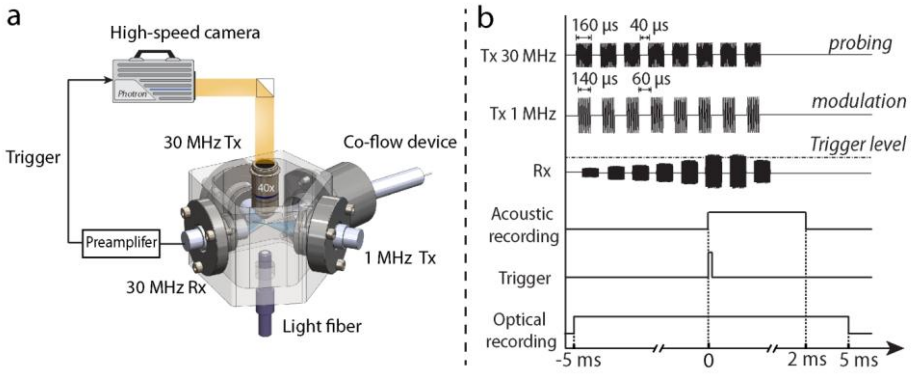

Figure 5.2. (a) A schematic overview of the complete system. (b) The timing diagram of the experiment.

5.2.3 Data analysis

Figure 5.3a shows a typical example of the received acoustic signal in a single recording. The amplitude of the scattered signal varies due to bulk flow and the exact position of the bubble within the focal region (Renaud et al. 2014). For each recording, all bursts for which the mean scattered signal was above 25% of the digitizer vertical range were selected for analysis. For each selected burst, the root mean square noise level was measured during the 10 µs pre-driving and 10 µs post-driving. The received

echo signal was first band-pass filtered around the probing frequency (bandwidth of 20-40 MHz). Then the envelope of the signal was calculated to give the relative bubble oscillation amplitude, ε (Fig. 5.3b) (Renaud et al. 2012). In order to estimate the stability of the bubble response (i.e., to assess possible change in the bubble response that may be induced by lipid shedding and/or fast bubble deflation) during the long driving pulse, this signal was further segmented by windowing in the time domain in order to obtain 12 consecutive segments during each 120 ms bursts (each segment consisting of 10-cycles) (Fig. 5.3c). The frequency spectrum of each segment was then calculated by applying a Fast Fourier Transform (FFT) (Renaud et al. 2014). The following parameters were obtained from the frequency spectrum: the relative oscillation amplitude at fundamental frequency (ε_f) and at the second/third harmonic frequency (ε_{2f}, ε_{3f}), and the ratio of radial excursion in expansion over that in compression (E/C) in the time domain response. The rate of the variation of ε_f ($\Delta\varepsilon_f/10\mu s$), ε_{2f} ($\Delta\varepsilon_{2f}/10$ μs) and ε_{3f} ($\Delta\varepsilon_{3f}/10$ μs) were estimated by calculating the slope of each data set over all segments, respectively. Here we define the symmetrical vibrational response as $0.9 < E/C < 1.1$, while a compression-dominant response is defined as $E/C < 0.9$.

Figure 5.4a shows an image frame captured at the time of the trigger signal. During each optical recording, the microbubble was observed to move across the field of view (190 μm × 380 μm) and was in focus as it passed through the optical focal plane (optical depth of field is approximately 8 μm). The radius (R_{meas}) of each microbubble was estimated from a selected in-focus image frame using an edge-tracking minimum cost algorithm (van der Meer et al. 2007). The systematic error of the optical size measurement of a bubble was estimated using a calibrated dot patterns (Edmund optics, Barrington, NJ, USA). The same algorithm was used to measure the size of 9 calibrated dots varying from 1 μm to 5 μm in radius. Moreover, the random error was estimated by sizing the same dots on 10 different images. Combining the random and the systematic error, we quantified the uncertainty of the optical size measurement to be 100 nm, or 3% of the bubble radius, on average.

To check if the system was accurately aligned, we plotted the location of 12 single microbubbles measured once after the alignment when the optical recording was triggered. For an aligned system, the bubble location at the trigger frame should be in close proximity to each other within a small region. Figure 5.4b is a superimposition of the location of all 12 microbubbles (red dots) at the trigger frame. The result indicate that all bubbles were distributed within a region of 150 μm × 150 μm (around the projected area of the acoustic focal volume) at the trigger frame. This is a convincing proof that a microbubble captured optically was the very same microbubble which was also measured acoustically.

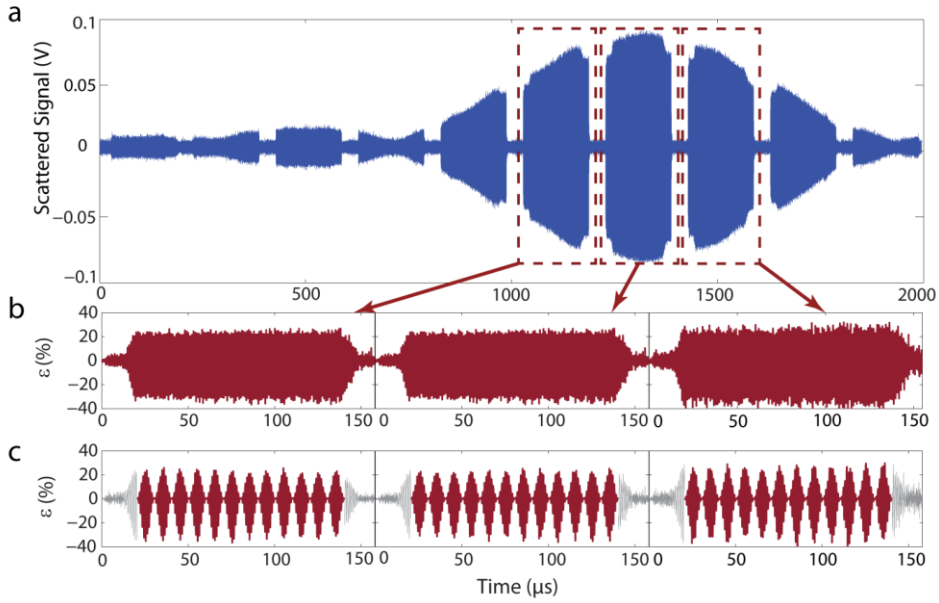

Figure 5.3. A typical example of an acoustic recording and the data analysis. (a) The received scattered signal. (b) The radial responses derived from three selected bursts with the highest amplitude. (c) 12 consecutive 10-cycle segments derived from each selected burst, resulting in 36 segments in total.

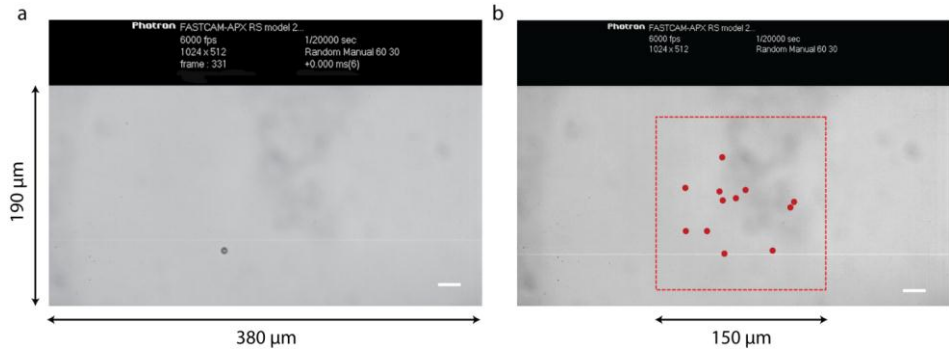

Figure 5.4. (a) A video frame of a microbubble passing through the focal plane in the optical field of view. (b) The location of 12 microbubbles by superimposing 12 frames recorded when the trigger signal was sent to the camera. The dashed rectangle indicates a region of 150×150 μm. The size bar represents 20 μm.

5.2.4 Simulation

The bubble dynamics model proposed by Marmottant et al. (2005) was used to simulate the response of lipid-coated microbubbles to a 1 MHz long burst excitation. The Marmottant model has been shown to accurately simulate highly nonlinear behavior such as "compression-only" behavior, second harmonic and subharmonic emissions and has shown good agreement with single-bubble radius-time curves recorded using ultra-high-speed imaging techniques. An effective shell surface tension σ was defined for three regimes depending on the microbubble radius: buckled, elastic and ruptured.

$$\sigma(R)=\begin{cases} 0 & (R \le R_b) \\ \chi\left(\frac{R^2}{R_b^2}-1\right) & (R_b < R < R_r) \\ \sigma_w & (R \ge R_r) \end{cases} \tag{5.1}$$

When the bubble is smaller than a pre-defined buckling radius (R_b), the shell buckles and the surface tension vanishes. When the bubble radius exceeds a certain ruptured radius (R_r), the coating breaks up and the surface tension becomes equal to the surface tension of water $\sigma_w = 7.2\times10^{-2}$ N/m. For a radius between R_b and R_r, the coating is considered as an elastic material. Here we chose the elastic state as the initial state of the bubble, the initial surface tension was taken as $\sigma(R_0) = 0.02$ N/m, and the elastic modulus was taken as $\chi = 2.5$ N/m (Overvelde et al. 2010). R_b can then be derived from $\sigma(R_0)$ by:

$$R_b = R_0/\sqrt{\frac{\sigma(R_0)}{\chi}+1} \tag{5.2}$$

The effective surface tension is included in a Rayleigh-Plesset-type equation:

$$\rho\left(R\ddot{R}+\frac{3}{2}\dot{R}^2\right) = \left(P_0+\frac{2\sigma(R_0)}{R_0}\right)\left(\frac{R_0}{R}\right)^{3\kappa}\left(1-\frac{3\kappa}{c}\dot{R}\right) - P_0 - \frac{2\sigma(R)}{R} - \frac{4\mu\dot{R}}{R} - \frac{4\kappa_s\dot{R}}{R^2} - P_A(t) \tag{5.3}$$

Where R_0 and R are the initial and time dependent radius of the microbubble, $\rho = 10^3$ kg/m^3 is the density of water, $\mu = 10^{-3}$ Pa·s is the viscosity of the water, $c = 1.5\times10^3$ m/s is the speed of sound in water, and $\kappa = 1.07$ is the polytropic exponent of the C_4F_{10} gas. P_0 and $P_A(t)$ are the ambient pressure and driving acoustic pressure respectively. The shell viscosity $\kappa_s(R_0)$ was considered to be dependent on the initial bubble radius (van der Meer et al. 2007) following the equation:

$$\kappa_s(R_0) = 10^{-9.0+0.28R_0}\ \text{kg/s} \tag{5.4}$$

Simulations were carried out for initial bubble radii ranging from 1 μm to 6 μm with a step of 0.1 μm. The driving pulse $P_A(t)$ was a 140-cycle sine-burst at a frequency of 1 MHz with a peak pressure amplitude of 50 kPa. The relative oscillation

amplitude at the fundamental frequency (ε_f) and at the second harmonic frequency (ε_{2f}) were determined from the fast Fourier transform (FFT) of the normalized radial excursion ($R(t)/R_0$).

5.3 RESULTS

5.3.1 Stability of the bubbles

A total of 732 microbubbles were measured acoustically only and Table 5.1 summarizes the measured statistics. At 25 kPa and 50 kPa, the variation of the radial strain at the fundamental ($\Delta\varepsilon_f$) and at the second harmonic frequencies ($\Delta\varepsilon_{2f}$) per segment (10 μs) for nearly all measured bubbles were within 0.2% and 0.1%, respectively. At 100 kPa, the absolute majority of microbubbles (~90%) were still within this range. These results indicate a very stable bubble response over prolonged ultrasound exposures. Therefore all derived parameters (ε_f, ε_{2f}, ε_{3f}, E/C) were averaged over all segments within each recording for the investigation of nonlinear and asymmetric bubble response.

Table 5.1. The percentage of microbubbles showing a stable response at all applied pressures and a prominent nonlinear and asymmetric response from a low acoustic pressure (≤50 kPa).

% / KPa	Stability		Nonlinearity		
	$\Delta\varepsilon_f$<0.2% /10 μs	$\Delta\varepsilon_{2f}$<0.1% /10 μs	$\varepsilon_{2f}/\varepsilon_f$>−14 dB	$\varepsilon_{3f}/\varepsilon_f$>−20 dB	E/C <0.9
25	100	100	0	0	48
50	100	99	29	21	58
100	91	87	92	75	98

5.3.2 Nonlinear bubble response

The degree of nonlinearity of the bubble oscillations is indicated by ε_{2f} and ε_{3f}, normalized to ε_f. As indicated in Table 5.1, at the lowest excitation amplitude (25 kPa), none of the microbubbles showed a prominent nonlinear response (defined as either $\varepsilon_{2f} / \varepsilon_f$ > -14 dB or $\varepsilon_{3f} / \varepsilon_f$ > -20 dB). However, the proportion of microbubbles showing a prominent nonlinear response increases dramatically with increasing pressure, e.g., from 0% of bubbles indicating prominent second harmonic ($\varepsilon_{2f} / \varepsilon_f$ > -14 dB) at 25 kPa to 92% at 100 kPa. Asymmetry of the oscillations appeared already at a very low pressure, i.e. compression-only behavior for 48% of bubbles at a pressure of 25 kPa

and nearly all microbubbles (98%) showed compression-dominant behavior at a pressure of 100 kPa.

5.3.3 Radius-dependent response

The simultaneous optical measurement of the bubble radius enabled a study of the bubble responses as a function of the initial bubble size. A total of 72 microbubbles ranging from 1.5 μm to 4.6 μm were measured. By plotting ε_f and ε_{2f} as a function of the measured bubble radius (R_{meas}), the resonance curves were derived for the measured bubble population at a pressure of 50 kPa (Fig. 5.5). The blue dots indicate experimentally measured data for individual bubbles, which are in good agreement with the simulation represented by the red dashed curve. The maximum response ($\varepsilon_f \approx 35\%$, $\varepsilon_{2f} \approx 11\%$) can be found for microbubbles of a size of ~3.4 μm in radius, which is within the range of resonant sizes at 1 MHz as reported in earlier studies (Overvelde et al. 2010).

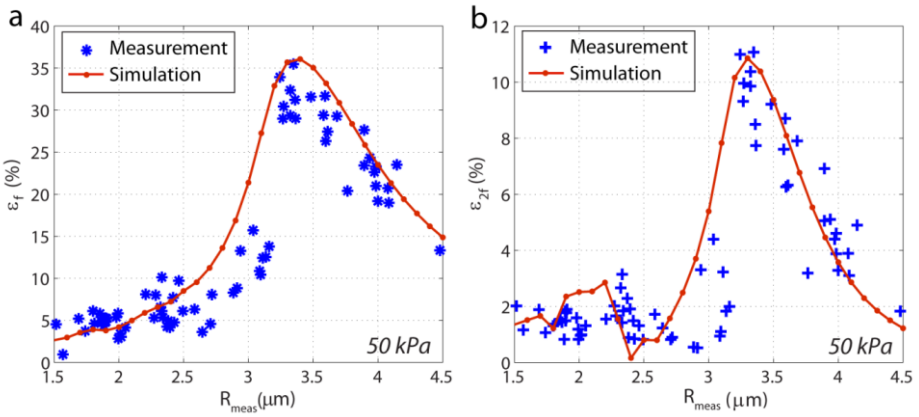

Figure 5.5. The measured and simulated radial strain at fundamental frequency (ε_f, a) and at second harmonic frequency (ε_{2f}, b) as a function of the measured microbubble size (R_{meas}) at the applied pressure of 50 kPa.

5.3.4 The "loop" phenomenon

Figure 5.6 shows the plot of experimentally measured relative oscillation amplitude at second harmonic frequency (ε_{2f}) as a function of that at fundamental frequency (ε_f). First, we observed an increase of the nonlinearity (ε_{2f}) with increasing pressures, e.g., the maximum value of ε_{2f} increases from ~3.8% at 25 kPa to ~12% at 50 kPa (Fig. 5.6a). Second, at a critical pressure, the nonlinearity (ε_{2f}) shows a hysteresis effect with relative oscillation amplitude at the driving frequency (ε_f). Figure 5.6a shows a "loop" shape for data which is most noticeable at 50 kPa and 100

kPa. The combined optical and acoustical measurement at 50 kPa shown in figure 5.6b indicates that the "loop" stems from different microbubble sizes in the population. For bubbles with increasing radius from about 2.4 μm, both ε_f and ε_{2f} increase and arrive at a maximum at resonance (~3.4 μm at 50 kPa). Above the resonance radius, both ε_f and ε_{2f} decreases. Moreover, we found a good agreement between the experiment and the simulation. Dots in figure 5.6c indicate bubbles of 1 μm to 6 μm in radius increasing with a size step of 0.1 μm following the arrows at an acoustic pressure of 50 kPa. Using the relative amplitude at the fundamental as the reference, we find that bubbles smaller than resonance size (3.4 μm) have a higher relative amplitude at the second harmonic (ε_{2f}) than bubbles larger than the resonance size. For example, a bubble of 3 μm and a bubble of 4.1 μm have similar ε_f (21%). However, the smaller bubble has 90% higher ε_{2f} than the bigger bubble.

5.3.5 Radius-dependent asymmetric vibrations

Figure 5.7a illustrates the correlation between the relative oscillation amplitude at the fundamental and the ratio of radial expansion to compression (E/C). Compression-dominant response was observed at all applied pressures, and it is enhanced with increasing ε_f. At 25 and 50 kPa, the expansion over compression ratio correlates inversely and nearly monotonically with ε_f, with compression-dominant behavior ($E/C < 0.9$) becoming more predominant for larger relative amplitude. For relative oscillation amplitude larger than ~15%, the behavior is overwhelmingly compression-dominated. At a pressure of 100 kPa, all of the bubbles oscillated with a prevalence for compression over expansion. As indicated by figure 5.7b, plotting E/C as a function of the measured bubble size indicates that 59% of measured bubbles showed symmetrical oscillations at 50 kPa ($0.9 < E/C < 1.1$). However, for bubbles in the range of resonance size (3-4 μm), we observed the maximum compression-dominant oscillations ($0.5 < E/C < 0.8$). The experimental data showed a good agreement with the simulation results.

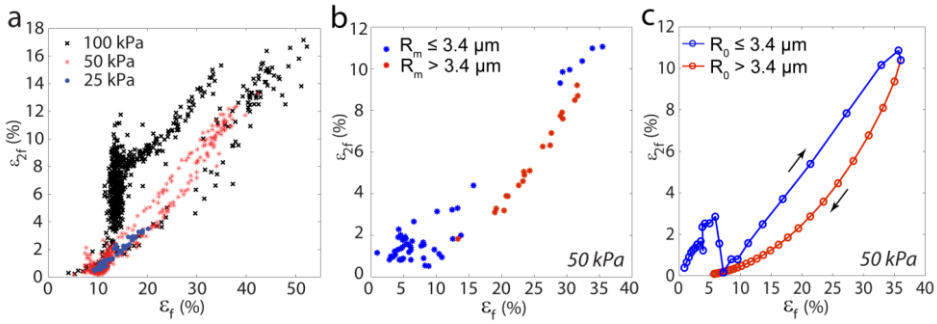

Figure 5.6. "Loop" phenomenon revealed by plotting the relative oscillation amplitude at the second harmonic frequency (ε_{2f}) as a function of that at the fundamental frequency (ε_f). (a) The acoustical measurement of 732 microbubbles at all applied pressures. (b) The combined acoustical and optical measurement of 72 bubbles at 50 kPa. (c) The simulation with Marmottant model at 50 kPa.

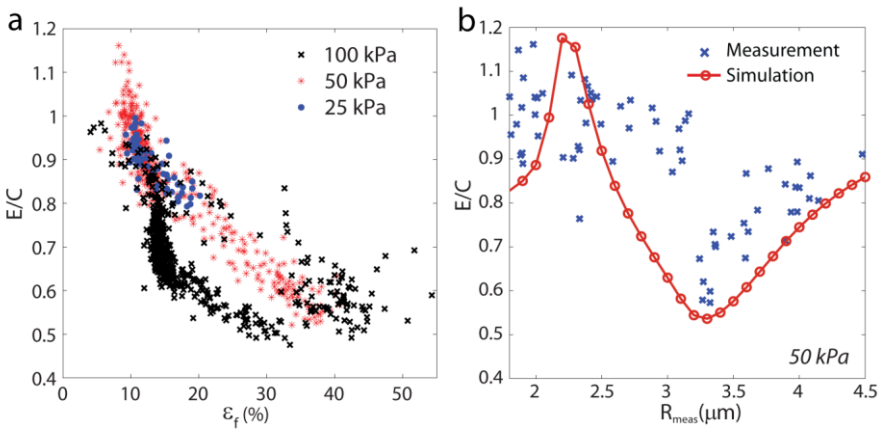

Figure 5.7. (a) Ratio of radial expansion to compression (E/C) versus the relative oscillation amplitude at the fundamental (ε_f) at all applied pressures. (b) The simulated and measured E/C as a function of the measured microbubble size (R_{meas}) at 50 kPa.

5.4 DISCUSSION

5.4.1 The bubble train

In the original sensitive acoustical measurement setup, contrast agent microbubbles were diluted directly into the water bath. Stirring the bath provides good mixing and isolation of single microbubbles, which flow into the focal region at random positions and are measured by chance when the scattered echo signal is large enough to generate a trigger signal. This technique is simple and the data acquisition

procedure can be automated to a large degree in order to provide hundreds of measurements on single bubbles per hour. However, we found it was necessary to modify this approach for the combined acoustic and optical system because the optical focal depth (8 μm) is much smaller than the acoustical focal size (150 μm). We found that producing a bubble train which is aligned with the optical focal plane can largely increase the chance of optically capturing the bubbles and this approach is critical to realize simultaneous optical sizing and acoustic measurement of single microbubbles. By manipulating the ratio between the velocity of the bubble flow and co-axial flow, we were able to isolate single bubbles with a space interval which allows a single microbubble at a time to pass through the acoustic focal volume. Additionally, utilizing the high speed camera with a shutter time of 50 μs is essential to resolve the bubble motion with a velocity of ~0.1 m/s.

5.4.2 Stable and nonlinear radial dynamics

We found a very stable radial response of freely-floating microbubbles over long bursts of ultrasound excitations (140 cycles, 1 MHz) with an applied pressure up to 100 kPa. It was reported earlier by Viti et al. (2012) and Thomas et al. (2013) that radial dynamics of bubbles can change by deflation over consecutive bursts of ultrasound excitations for minutes at low pressures. Their hypothesis was that the bubble deflation resulted from diffusive gas loss or lipid material shedding. The time scale of the present study, however, was 3 to 4 orders smaller (~1 ms), and the variations of the responses were only minor within this time range. This may suggest that no transient events (e.g., fragmentation, dissolution or lipid shedding) took place at this short time scale (1-2 ms) under typical ultrasound imaging pressures (≤100 kPa).

We observed prominent nonlinear and asymmetric bubble response of freely-floating microbubbles at 50 kPa. Plotting the relative oscillation amplitude at the fundamental frequency, ε_f, as a function of the bubble size reveals a strong nonlinear behavior and skewing of the curve both in experiment and in simulation (Fig. 5.5a). The asymmetry of the bubble vibrations (i.e., compression-dominant behavior) increases with the amplitude of oscillations, and reaches the maximum for bubbles at resonance (Fig. 5.7). The data acquired was in agreement with previously reported studies on bubbles floating against a hard surface (van der Meer et al. 2007). It was shown that the nonlinear and asymmetric bubble response can be ascribed to the variation of the shell viscoelastic state (i.e., initial surface tension and shell elasticity) during bubble vibrations (Overvelde et al. 2010; Sijl et al. 2011). Figure 5.8 shows the simulated radius dependent response at 1 kPa, 10 kPa, and 50 kPa. At a driving pressure of 1 kPa, the bubble vibrates in the elastic regime. The radius-dependent response curve is symmetrical and the bubble resonant size is ~6.7 μm. An increase of

the acoustic pressure induces skewing of the resonance curves and decrease of the resonance size. At 10 kPa, the radius of maximum response is at a bubble size of ~4.7 μm, 30% lower than the resonance size at 1 kPa. Here the bubble oscillates more towards a "buckled" regime (Eq. 5.1), leading to skewing of the resonance curve (Overvelde et al. 2010). At 50 kPa, the bubble vibrates further more in the ruptured regime thus the effective elasticity is closer to zero. This makes the bubble behave more like a free gas bubble which has a more symmetrical resonance curve than at lower driving pressures. It should be noted that the shell buckling during bubble vibration can result in compression-dominant behavior. An earlier study by Sijl et al. (2011) found a maximum negative offset of the bubble radial dynamics (i.e., compression-only behavior) at the resonance frequency through a weakly nonlinear analysis by Marmottant model. This is in agreement with the observation in this study (Fig. 5.7).

The loop phenomena captured in this study (Fig. 5.6) showed up to ~150% higher second harmonic response comparing bubbles smaller than the resonance size to bubbles larger than the resonance size having the same fundamental response. As indicated by figure 5.8, this can be ascribed to the less skewed radius-dependent curve at the second harmonic frequency than at the fundamental. As an example, the two blue dots in the figure indicate bubbles above and below resonance with the same fundamental response. However, the corresponding second harmonic response is ~90% higher for the bubble smaller than the resonance size. Moreover, we noticed a 'gap' in the loop between the two bubbles with ε_f of 15% and 30% in figure 5.6b. However, the size distribution of all 72 investigated bubbles (not shown here) indicates that there is no lack of recordings with bubbles of the corresponding radius (~ 3.1 ± 0.1 μm). As indicated by figure 5.5 and figure 5.6c, this gap can be due to the skewing of the resonance curve and also the sparse dots in the simulated data correspondingly.

5.4.3 Benefits of the system for efficient statistical characterization of microbubbles

A successful recording requires both an accurate optical recording of a single isolated microbubble in focus and an acoustic recording with a signal to noise ratio above a pre-set value (4 in this study). The efficiency of the measurement is determined by multiple factors, i.e., the velocity of the bubble flow, the spacing of the bubble train, the amplitude of the received signal (should be above a threshold level) and the alignment of the system. An accurately aligned system is able to perform continuous measurements for hours with the bubble detection rate varying from ~2 s to ~80 s for each recording. This means that a statistical characterization study of 500 microbubbles can be done in an hour if the system is running continuously. Of course

other factors should be taken into account, e.g., changing of the bubble concentration in the bubble flow over time, interference of a bubble population in the water tank due to continuous injection of the bubble flow, etc.

Besides the investigations on nonlinear bubble dynamics, this system is also a powerful tool to study the bubble translation driven by primary radiation force. This would benefit *in vitro* characterizations of contrast agents (Vos et al. 2007) and/or for investigations of drug delivery using microbubbles. Optical recordings in this study clearly revealed bubble motion along the axial direction of the 1 MHz pressure wave. We measured the velocity of 3 microbubbles near a size of 3.2 μm in radius, which was 0.1 m/s on average, a value very similar to bubble translation velocities predicted by simulations (Vos et al. 2007). Further investigations will follow up in the future.

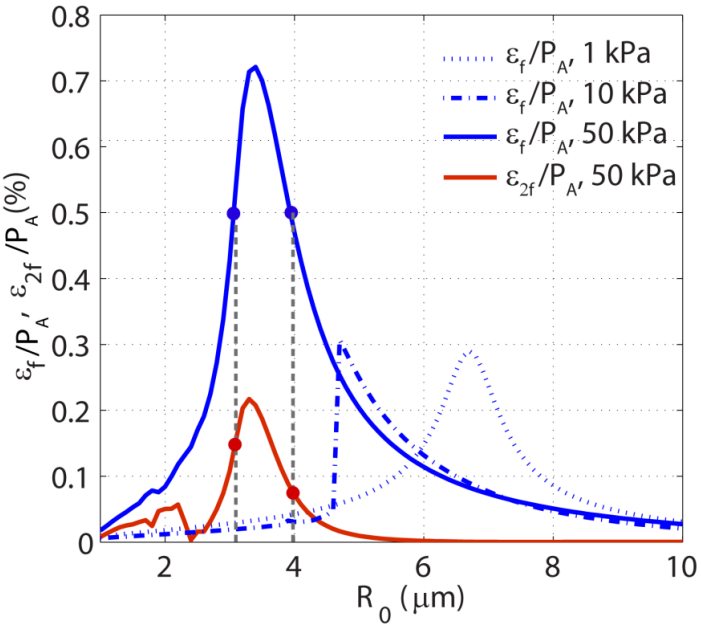

Figure 5.8. The simulated radius dependent response for relative amplitude of oscillation at fundamental frequency and at second harmonic frequency divided by the acoustic pressure amplitude P_A (ε_f/P_A, blue curves; ε_{2f}/P_A, red curve) at 1 kPa, 25 kPa and 50 kPa. The blue dots and red dots indicate the fundamental and second harmonic response of two microbubbles above and below the resonance size respectively.

5.5 CONCLUSIONS

In this paper, we have described a new technique which for the first time acquired radius-time response of individual freely-floating microbubbles through combined

optical sizing and highly-sensitive acoustical characterization. The results showed very stable bubble vibrational response over long burst excitations (1 MHz, 140 μs) under all applied pressures (25 kPa, 50 kPa and 100 kPa). The nonlinearity (ε_{2f}, ε_{3f}) and asymmetry (i.e., compression-dominant behavior) of bubble vibrations were found to increase with increasing oscillation amplitude, and reach the maximum for bubbles at resonance. At the same fundamental response, the second harmonic response of bubbles smaller than the resonance size is up to 150% stronger than bubbles bigger than the resonance size. This can be explained by a less skewed radius-dependent response at the second harmonics than the fundamental. The acquired data can be precisely described by simulated results using Marmottant model, and was in good agreement with previously reported studies on bubbles floating against a hard surface. The new system shows its great potential for *in vitro* characterization of contrast agent microbubble populations.

6

Lipid shedding from single oscillating microbubbles

Abstract — Lipid-coated microbubbles are used clinically as contrast agents for ultrasound imaging, and they are being developed for a variety of therapeutic applications. The lipid encapsulation and shedding of the lipids by acoustic driving of the microbubble has a crucial role on microbubble stability and on ultrasound-triggered drug delivery, however little is known about the dynamics of lipid shedding under ultrasound excitation. Here we present a study to optically characterize the lipid shedding behavior of individual microbubbles on a time scale of nanoseconds to microseconds. A single ultrasound burst of 20 to 1000 cycles, with a frequency of 1 MHz and an acoustic pressure varying from 50 to 425 kPa was applied. In the first step, high-speed fluorescence imaging was performed at 150,000 frames per second (fps) to capture the instantaneous dynamics of lipid shedding. Lipid detachment was observed within the first few cycles of ultrasound. Subsequently, the detached lipids were transported by the surrounding flow field, either parallel to the focal plane (*in-plane shedding*), or in a trajectory perpendicular to the focal plane (*out-of-plane shedding*). In a second step, the onset of lipid shedding was studied as a function of the acoustic driving parameters, e.g. pressure, number of cycles, bubble size and the oscillation amplitude. The latter was recorded with an ultrafast framing camera running at 10 million fps. A threshold for lipid shedding under ultrasound excitation was found for a relative bubble oscillation amplitude higher than 30%. Lipid shedding was found to be reproducible, showing that the shedding event can be controlled.

Appeared in *Ultrasound in Medicine & Biology*, by Y. Luan, G.P.R. Lajoinie, E.C. Gelderblom, I. Skachkov, A.F.W van der Steen, H.J. Vos, M. Versluis, N. de Jong, Vol. 40, Issue 8, pp.1834-46, August 2014. The authors would like to thank Heleen Dewitte and Dr. Ine Lentacker (Ghent University, Ghent, Belgium) for providing microbubble samples and for valuable discussions. The authors also thank Gert-Wim Bruggert (University of Twente) for technical support.

6.1 INTRODUCTION

Lipid-shelled microbubbles are used clinically as contrast agents for ultrasound imaging, and they are currently developed for a variety of therapeutic applications, such as gene and drug delivery (Lentacker et al. 2007; Vandenbroucke et al. 2008; Lentacker et al. 2010), thrombolysis (Tiukinhoy-Laing et al. 2007; Medel et al. 2009), and metabolic gas transport (Choi et al. 2010). A typical lipid-coated microbubble has a gaseous core that is encapsulated by a thin phospholipid shell. The shell was reported to play a key role in clinical applications of ultrasound-mediated diagnosis and therapies (Stride and Saffari 2003; Ferrara et al. 2007). First and foremost, the lipid shell can maintain the stability of the microbubble by imparting low surface tension, high mechanical stability and low gas permeability (Pu et al. 2006). Aided by the use of a low-solubility gas, such as perfluorobutane (C_4F_{10}), the dissolution of the coated microbubble in the blood stream takes a few minutes, which is several orders of magnitude larger than for an uncoated air-filled microbubble (< 0.01 s) (Kabalnov et al. 1998; Kabalnov et al. 1998). For applications such as ultrasound contrast imaging, a stable microbubble with optimal scattering characteristics is critical for achieving prolonged image contrast (Sarkar et al. 2009). Secondly, microbubbles can be preloaded with drug molecules or drug carrying vesicles either within or attached to the lipid shell. Under ultrasound excitation, the shedding of the lipids can be used to deliver the molecules or attached vesicles (Vandenbroucke et al. 2008; Lentacker et al. 2010). In such applications, control of the release from the microbubble surface into the target area is essential.

Recently there has been wide interest in gaining knowledge regarding lipid shedding behavior under exposure to ultrasound by several authors (Borden et al. 2005; O'Brien et al. 2011; Cox and Thomas 2013). Lipid shedding and the accompanying microbubble dissolution were observed by Borden et al. (2005) for microbubbles exposed to a series of one-cycle pulses with the peak negative pressure ranging from 400 kPa to 800 kPa. They proposed that the surface area reduction due to gas diffusion from the microbubble could lead to the expulsion of excessive shell materials. Later on, Thomas et al. (2012) investigated the dissolution of single microbubbles as a function of the bubble radial oscillation based on ultra-high speed imaging. The amount of microbubble dissolution was claimed to be associated with the amount of expelled lipid materials. Furthermore, O'Brien et al. (2011) ascribed the shedding of lipids to the over-saturation of lipid particles on the microbubble surface. From their theoretical model they predicted that an instantaneous reduction (i.e., upon ultrasonic compression) of the surface area of 41% is required to trigger lipid shedding from phospholipid-coated microbubbles. Moreover, a recent experimental study by (Cox and Thomas 2010; Cox and Thomas 2013) suggested that the lipid shell

collapse might be accompanied by the generation of sub-micron bubble fragments, leading to a fast shrinkage of the microbubble. All of these studies were limited by the following reasons. First, either the time resolution (hundreds of milliseconds in Borden et al. (2005)) or the recording time (ten microseconds in Thomas et al. (2012)) of the imaging systems was not sufficient to resolve the details of lipid shedding dynamics. Secondly, microbubble dissolution was used as a measure for shedding. The dissolution was an indirect measure from an increased surface tension through the decreased concentration of lipids on the bubble shell. Therefore it is not necessarily applicable to directly study the physical mechanisms underlying lipid shedding behavior. Moreover, there was no consensus from the previous work on the exact loss mechanisms of the shell material under ultrasound excitation. This is especially true for those mechanisms that are directly coupled to the microbubble oscillation dynamics.

The objective of this work was to optically characterize, on time scales ranging from hundreds of nanoseconds to a millisecond, the lipid shedding behavior of individual microbubbles exposed to a single burst of ultrasound. First, high-speed fluorescence imaging at 150,000 frames per second (fps) was used. Both the acoustic pressures and the pulse length were varied in a parametric study. Secondly, lipid shedding was investigated as a function of microbubble oscillation amplitude by combining a comparatively low frame rate fluorescence recording (at 1000 fps) with an ultra-high speed camera running at 10,000,000 fps in bright field mode. This enabled us to relate the occurrence of a shedding event to the microbubble oscillation amplitude, with the potential to test the model proposed by O'Brien et al. (2011).

6.2 MATERIALS AND METHODS

6.2.1 Microbubble formulation

Microbubbles were prepared by mixing 1,2-dipalmitoyl-sn-glycero-3-phosphocholine (DPPC) (Lipoid, Ludwigshafen, Germany) and 1,2-distearoyl-sn-glycero-3-phosphoethanolamine-N-[PDP(polyethylene glycol)-2000] (DSPE-PEG-SPDP) for functionalized bubbles or 1,2-distearoyl-sn-glycero-3-phosphoethanolamine-N-methoxy(polyethylene glycol)-2000 (DSPEPEG) (both Avanti polar lipids, Alabaster, AL) for non-functionalized bubbles in a molar ratio of 65:35 in chloroform. For fluorescent labeling of the microbubble membrane, the lipophilic dye 1,1'-dioctadecyl-3,3,3'3'-tetramethylindocarbocyanine perchlorate (DiI) (Sigma-aldrich, Bornem, Belgium) was added to the lipid mixture. After chloroform evaporation, the lipid film was dissolved in a 1:2:7 glycerine-propyleneglycol-H2O mixture to obtain a clear solution with a final lipid concentration of 4×10^{-4} mmol/mL. This lipid solution was aliquotted in 2.5 mL chromatography vials of which the

headspace was filled with perfluorobutane gas (C_4F_{10}, F2 chemicals, Preston, UK). Finally, DiI-labeled microbubbles were obtained by high speed shaking of the chromatography vial in a Capmix™ device (3 M-ESPE, Diegem, Belgium) for 15s.

6.2.2 Experimental setup

6.2.2.a Experiment A – Shedding dynamics

Figure 6.1a shows the experimental setup. It contains a sample holder, fluorescence excitation setup and an optical recording system.

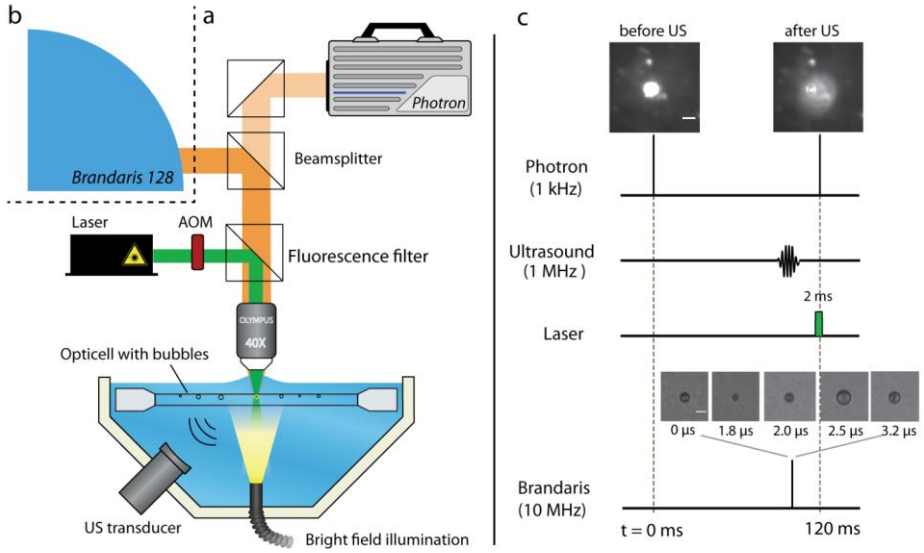

Figure 6.1. (a-b) A schematic view of the experimental setup for experiment A and B respectively and (c) The timing diagram of experiment B.

For the sample holder setup, the Opticell™ unit (NUNC, Thermo Fisher Scientific, Wiesbaden, Germany) containing the microbubbles diluted with PBS solution (Invitrogen, Bleiswijk, The Netherlands) was placed in a water bath (T≈22°C) connected to a 3D micropositioning stage. A focused, single-element transducer (C302; Panametrics, Waltham, USA) with a center frequency of 1 MHz was fixed on the side of the water tank. For each microbubble which was floating against the Opticell chamber, a single burst with a pulse length of 50, 100 or 500 cycles at an acoustic pressure varying from 85 to 425 kPa was applied. See Table 6.1.A for an overview of the acoustic settings used. Acoustic pressures were calibrated in a separate setup with

a needle hydrophone (0.2 mm PVDF, Precision Acoustics, Dorchester, UK) prior to the experiment. For each acoustic setting, a minimum of 5 individual microbubbles were examined, and 80 microbubbles in total were investigated in this set of experiments.

For the optical recording system, an upright fluorescent microscope equipped with a 40× water immersion objective (the numerical aperture (NA) = 0.8; Olympus, Zoeterwoude, The Netherlands) was focused on the microbubble sample. A 5-Watt continuous wave (CW) laser (λ = 532 nm; Cohlibri; Lightline, Osnaburg, Germany) was employed for fluorescence excitation of the fluorescent label DiI. The laser light was gated using an acousto-optic modulator (AOM) (AOTF.nC-VIS; AA Optoelectronic, Orsay, France) to generate a single pulse with a duration of 2 ms. For positioning the microbubble during the experiment, a simultaneous bright field illumination was used (KL1500LCD, Schott, Mainz, Germany). High-speed fluorescence recordings were acquired with a CMOS-based high-speed camera (SA-1.1; Photron Ltd, West Wycombe, UK), operating at 150,000 fps.

6.2.2.b Experiment B – Bubble dynamics and release

The ultra-fast framing Brandaris 128 camera (Chin et al. 2003; Gelderblom et al. 2012) was combined with the Photron camera to study the occurrence of shedding versus the amplitude of microbubble oscillations (Figure 6.1b). To enable this combination, the optical beam from the objective was split into two pathways by an 80%/20% beam-splitter. One light path (80%) was captured by the Brandaris camera operated at a frame rate of 10,000,000 fps and recording 128 frames. The other light path (20%) was projected into the Photron high-speed camera running at 1000 fps.

Seventy microbubbles were investigated in this set of experiments. The ultrasound burst consists of 20, 50, 100 and 1000 cycles at 170 kPa and 100 cycles at 50, 85, 170 and 255 kPa (Table 6.1.B). The Brandaris camera was synchronized with the arrival of the acoustic wave to record the microbubble oscillations. To track the release of fluorescent materials, the Photron camera was programmed to capture a fluorescent image of the microbubble before and after the ultrasound excitation respectively, with an exposure time of 1 ms. Details of the timing diagram of a single recording are shown in figure 6.1c.

Table 6.1. The acoustic setting for experiment A and experiment B. The excitation frequency was 1 MHz in all experiments.

kPa / cycles	A					B			
	85	**170**	**255**	**340**	**425**	**50**	**85**	**170**	**255**
20								x	
50	x	x	x	x	x			x	
100	x	x	x	x	x	x	x	x	x
500	x	x	x	x	x				
1000								x	

6.3 RESULTS

6.3.1 Data analysis

In figure 6.2, a cartoon of the lipid shedding events is presented. Three types of lipid motion were observed. The first type is the movements of lipid shell materials across the microbubble surface, but without observable lipid shedding. It appears as the generation of fluorescently-labeled lipid clusters (budding), or the rotational and vortical motion (rearrangement) of these lipid clusters while maintaining attachment to the shell. The second category is when lipid shell materials are detached from the bubble surface, and are transported either within (or parallel with) the focal plane (*in-plane shedding*). The third type is when the detached particles are transported perpendicular to the focal plane, which leads to the spread of an out-of-focus fluorescent halo (*out-of-plane shedding*), captured from the top view.

In experiment A, *in-plane shedding* and *out-of-plane shedding* (see the detailed illustration in later sections) were quantified in two different ways. In the case of *in-plane shedding*, the maximum distance between the detached vesicles and the microbubble surface is defined as the transport distance d_T. For each shedding event, the transport distance of the vesicles was measured in each frame for the entire duration of ultrasound exposure using a semi-automated tracking routine programmed in MATLAB® (Mathworks Inc., Natick, MA, USA). The maximum value was chosen as d_T. For *out-of-plane shedding*, only the optical projection of the detached lipids moving perpendicular to the focal plane could be recorded, resulting in an out-of-focus halo with a uniform intensity distribution surrounding the microbubble (Connor 1986). According to Olsen and Adrian (2000), the diameter of the image d_i of

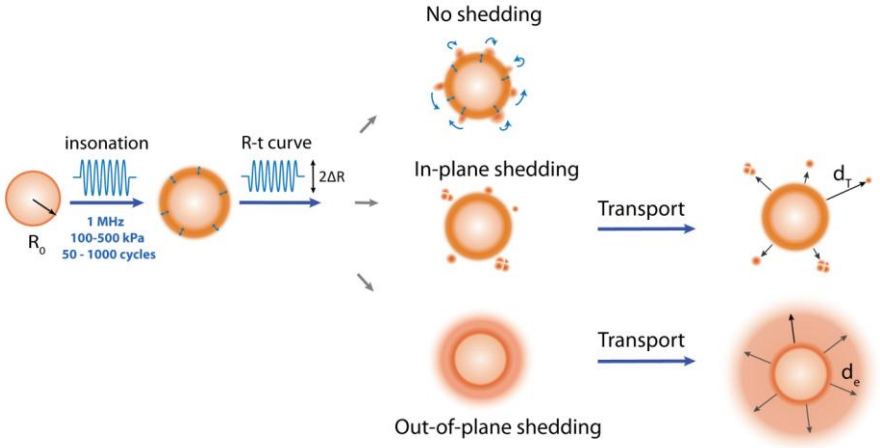

Figure 6.2. Schematic view of the motion of lipid shell under insonation.

the fluorescent vesicle located at a distance z from the focal plane can be evaluated from:

$$d_i(z) = (M^2 d_p^{\,2} + 5.95(M+1)^2 \lambda^2 f^{\#2} + \frac{M^2 z^2 D_a^{\,2}}{(s_0+z)^2})^{1/2} \tag{6.1}$$

where M = 40 is the magnification, $d_p \approx 2\times10^{-7}$ m is the vesicle diameter, λ = 532 nm is the wavelength of the fluorescent light emitted by the vesicle, $f^{\#} = 2\times NA = 1.6$ is the focal number, $D_a = 5\times10^{-3}$ m is the lens aperture diameter, and $s_0 = 3.3\times10^{-3}$ m is the working distance of the lens. Correspondingly, d_i is the image size of a virtual object (the observed halo with a diameter of d_h) in the focal plane that obeys the relation:

$$d_i(z=0) = (M^2 d_h^{\,2} + 5.95(M+1)^2 \lambda^2 f^{\#2})^{1/2} \tag{6.2}$$

Since $s_o >> z$, the combination of Eq. (1) and (2) leads to:

$$z = \sqrt{\frac{s_0^{\,2}(d_h^{\,2} - d_p^{\,2})}{D_a^{\,2}}} \tag{6.3}$$

Thus for a given d_h, the estimated transport distance of the shed vesicles ($d_e = z\text{-}R_0$, where R_0 is the initial microbubble radius) could be derived. From each frame of the recording, d_h was measured by first stretching the image intensity histogram to obtain maximum contrast. Fifty evenly distributed lines in polar coordinates (where the

center of the microbubble was defined as the origin) then gave the radial intensity profiles of the bubble, as was previously described by (Gelderblom (2012). The average intensity profile over all lines was taken in order to determine the -9 dB threshold for sizing the fluorescence halo.

In experiment B, the raw data obtained by the two cameras (Photron and Brandaris) were analyzed separately. First, from the Photron camera, d_e was obtained by analyzing the subtracted image of the recording made before the ultrasound exposure from the one obtained afterwards. The same algorithm as described above was applied. Secondly, from the Brandaris recording of the microbubble oscillations, the radius time (R-t) curve was obtained using a custom-designed image analysis software based on edge-tracking minimum cost algorithm (van der Meer et al. 2007). R_0 was obtained by averaging the measured R during 0.5 μs before the arrival of ultrasound. The maximum amplitude of oscillation (ΔR) was evaluated in the sustained oscillation regime: the transient effects were graphically suppressed by multiplying a Hanning window to the signal.

6.3.2 Experiment A – Shedding dynamics

6.3.2.a Budding & Rearrangement

Under ultrasound excitation, we observed movement of the lipids incorporated within the microbubble shell without any noticeable occurrence of shedding. Most common were the forming of lipid clusters (budding) and random movement of lipid clusters around the shell (rearrangement). Budding and rearrangement could be seen on the same microbubble and was not observed to be related to lipid shedding behavior.

Budding is the generation of one or multiple micron-sized fluorescent buds around the microbubble shell. These fluorescent buds can remain attached or they can be subsequently detached from the microbubble surface during insonification. Figure 6.3 shows a typical example, in which the fluorescent buds start to form 20 μs after start of the ultrasound exposure at θ = 58° of the bubble circumference in the focal plane (the center of the microbubble is defined as the origin, with θ = 0° at the three o'clock position). Budding behavior of lipid-coated microbubbles was considered to play a key role in the stability of the microbubble (Borden et al. 2005; Kwan and Borden 2012). It was explained as the accumulation of collapsed lipid strands and globular aggregates due to bending, folding, or buckling of the bubble shell. The rapid aggregation of microscopic folds can locally relieve the stress sustained within the lipid monolayer (Kwan and Borden 2012).

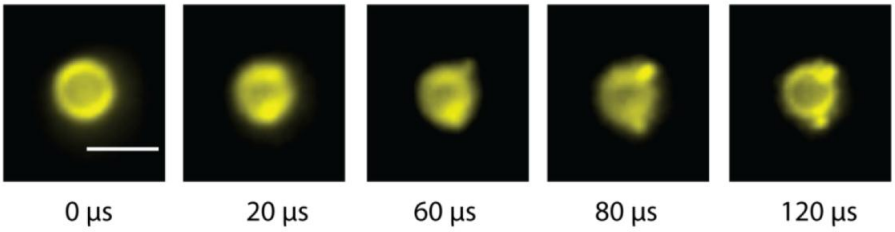

Figure 6.3. Budding behavior of a microbubble (255 kPa, 100 cycles). The image at 0 µs indicates the moment before ultrasound was turned on. The scale bar represents 5 µm.

The fluorescent buds generated on the microbubble shell showed displacement and rotational motion on the 2-D projected surface of the microbubble. Figure 6.4 depicts a typical rearrangement behavior during a long ultrasound exposure (500 µs). A bud is formed at 153° of the circumference, which is subsequently transported to 130°. This rearrangement of lipid buds has not been reported before in literature. Remarkably, the velocity of the rotational lipid motion is between 0.01 to 0.1 m/s, which is in the same order of magnitude as the velocity field of the acoustic microstreaming around an oscillating microbubble (Elder 1959; Marmottant et al. 2006; Ooi et al. 2007; Collis et al. 2010). There are two possible explanations for this phenomenon: first, small vortical flow structures may be generated close to the microbubble shell (Wang et al. 2013), this can be related to a seemingly random motion of lipid vesicles relative to the microbubble surface. Second, a microbubble can exhibit circular orbiting motions under ultrasound excitation (Ooi et al. 2007). This orbiting motion may lead to the rotational motion of the attached vesicles relative to the observer.

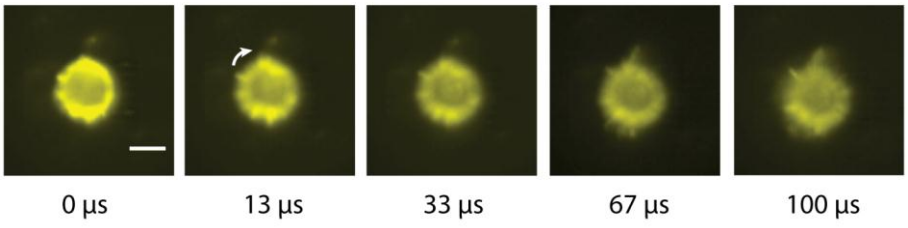

Figure 6.4. Rearrangement of phospholipids over the microbubble shell (255 kPa, 500 cycles). The arrow indicates the rotational motion of a lipid cluster. The scale bar represents 5 µm.

6.3.2.b Lipid shedding

In-plane shedding

In-plane shedding is the detachment of fluorescent vesicles from one or several spots which are distributed non-uniformly on the microbubble surface. Mostly no blurring of the fluorescent vesicles can be observed during the transport, suggesting that they are traveling in (or parallel to) the focal plane. The phenomenon is in correspondence with 'vesicle shedding' formulated previously by Baoukina et al. (2008) and Kwan and Borden (2012), in which lipid clusters were first formed due to the collapse of the lipid monolayer by the process of buckling or 'vesiculation'. Then these semi-vesicles of hundreds of nanometers eventually detached from the bubble shell and form liposomes or micelles. We assume that the same physical process applies to the in-plane shedding event. Figure 6.5 shows a typical example of in-plane shedding. After 140 μs of ultrasound exposure, budding occurs accompanied by the rearrangement of the fluorescent clusters. The detachment of a lipid cluster takes place at 267 μs, followed by the transport of the cluster further away through the drag force in the flow field during ultrasound exposure.

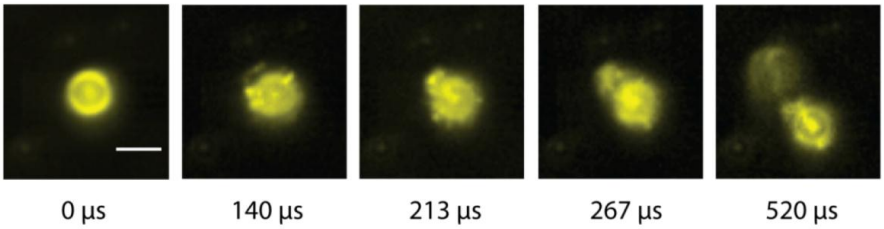

Figure 6.5. In-plane shedding from a microbubble (170 kPa, 500 cycles). The scale bar represents 5 μm.

Out-of-plane shedding

Out-of-plane shedding is the detachment and transport of lipid shell materials from the microbubble surface perpendicular to the focal plane. Observing from the top, as an out of focus effect, a blurred spot (halo) forms surrounding the microbubble, and spreads as the shell material is moving further away. A typical example is shown in figure 6.6 (focal plane A), where a halo appears after 13 μs of insonification. The halo continues to spread symmetrically until ultrasound was turned off. The larger the halo, the further the shed vesicles are transported (Olsen and Adrian 2000).

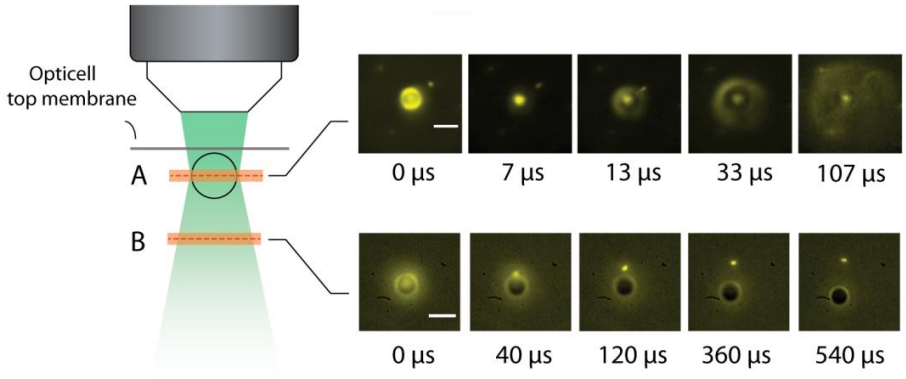

Figure 6.6. Observations of out-of-plane shedding at two focal planes: Focal plane A - at the center of the microbubble (340 kPa, 100 cycles); Focal plane B - around 10 µm below the center of the microbubble (170 kPa, 500 cycles). The trajectory of transport is indicated by the blue dashed arrow. The scale bar represents 10 µm.

To ascertain that we are looking strictly at out-of-plane motion of the shed vesicles, we put the plane of focus to approximately 10 µm below the center of the microbubble, as indicated in figure 6.6 (focal plane B). The first image indicates the initial state of the microbubble before ultrasound exposure. As expected, a halo is visible around the microbubble due to out of focus imaging of the microbubble. Note that it appears similar as the last image in figure 6.6 (focal plane A), in which a 'cloud' forms around the microbubble after the shedding event. Following shedding the optical halo shrinks, and the shed particle turns into tiny fluorescent vesicles that are imaged in focus (at 540 µs). This indicates that the detached lipid shell materials are transported perpendicular and away from the supporting Opticell™ membrane.

6.3.2.c Counts of shedding events

All the shedding events are counted for all acoustic settings in Table 6.1.A, and are plotted in 15 separate graphs in figure 6.7. Each bar indicates the percentage of microbubbles showing either *in-plane shedding* (blue) or *out-of-plane shedding* (red) at the applied acoustic pressure (85, 170, 255, 340, 425 kPa) and for the applied burst length (50, 100, 500 cycles).

We found that the acoustic parameters are crucial for the occurrence of shedding events. For example, with a pulse of 50 cycles, a pressure of 170 kPa is required to trigger the shedding. The occurrence of shedding increases with increasing pressure: at a pressure of 85 kPa with 100 cycles, only 17% of microbubbles show shedding behavior while this increases to 100% for a pressure of 340 kPa. In general, *in-plane shedding* can be observed at lower pressure amplitudes compared to *out-of-plane*

shedding: nearly all *in-plane shedding* events occur within a pressure range of 85 to 255 kPa, while for *out-of-plane shedding*, pressures must be as high as 425 kPa to accomplish 100% shedding for all pulse lengths. The present data shows only a minor trend of increased occurrence of *out-of-plane shedding* with increasing pulse length (e.g., it rises from 6 % with 50 cycles to 20% with 500 cycles at 170 kPa), see figure 6.7.

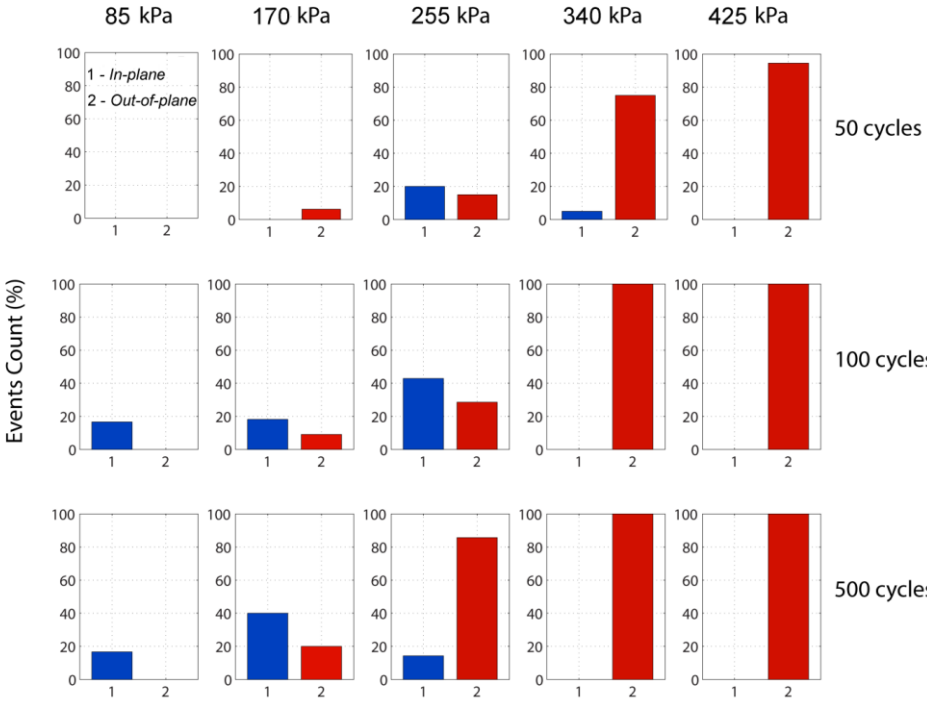

Figure 6.7. Counts of In-plane shedding (blue) and out-of-plane shedding (red) as a function of the acoustic settings.

6.3.2.d Transport

The transport of detached lipid vesicles into the surrounding medium plays a crucial role in characterizing a lipid shedding event. On the one hand, we could only optically define the occurrence of a lipid detachment when the transport process starts. On the other hand, it is the dynamics of the transport (i.e., the direction, the velocity and the typical length scale) that distinguishes *in-plane shedding* from *out-of-plane shedding*.

Figure 6.8 shows the transport distance (d_T) and estimated transport distance (d_e) for 3 individual microbubbles exhibiting *in-plane shedding* and *out-of-plane shedding,* respectively. For *in-plane shedding*, the start of transport is observed, namely after 50 cycles of the ultrasound pulse. The transport ceases almost immediately after the ultrasound has stopped, as shown by bubble 1 in figure 6.8a (170 kPa, 500 cycles). However, in the case of *out-of-plane shedding*, the transport initiates within the first few frames of the recording. Then it continues for a period of time after the ultrasound has been turned off (i.e., ~100 μs for bubble 2 in figure 6.8b (255 kPa, 50 cycles)).

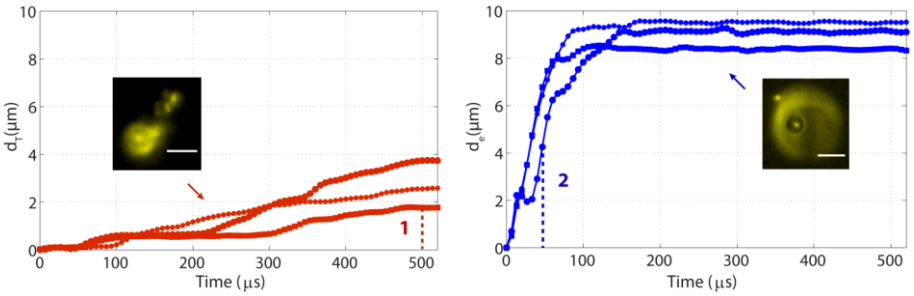

Figure 6.8. Plot of the transport distance (d_T) and the estimated transport distance (d_e) as a function of time for 3 individual microbubbles exhibiting (a) in-plane shedding and (b) out-of-plane shedding, respectively. Ultrasound was turned on in the first frame. Dashed lines indicate the time when ultrasound was turned off. Scale bars represent 5 μm.

In figure 6.9, the final estimated transport distance (d_e) for all microbubble showing *out-of-plane shedding* is plotted as a function of the bubble size and the acoustic pressure. The markers represent the data for each microbubble. We found that the microbubble size plays an important role: bubbles with an initial radius ranging from 2.5 μm to 3 μm show a maximum d_e for all acoustic pressures. This radius is within the range of previously determined resonant sizes at 1 MHz (van der Meer et al. 2007; Luan et al. 2012). Furthermore, increasing the pressure increases the maximum transport distance of the lipid shell materials. Finally, the size of microbubbles having the maximum transport distance shows a trend of decrease with increasing acoustical pressure, i.e., from 2.94 μm at 85 kPa to 2.66 μm at 340 kPa. This is in agreement with previous studies which reported that the frequency of maximum response decreases with increasing acoustic pressure due to a 'shell-softening' behavior (van der Meer et al. 2007; Overvelde et al. 2010; Faez et al. 2011). All these results suggest that microbubble oscillation amplitude is the major determinant of the transport distance. Data in this experiment does not show a clear influence of the pulse length on the distance of transport, possibly due to the limited number of experiments (the pulse length is therefore not plotted here but is studied in more

detail below). It should be noted that data recorded at 425 kPa are not included here for the following reasons: a) the microbubbles move out of the field of view due to primary and/or secondary radiation forces; b) the intensity of the halo was too low to reliably track its edge.

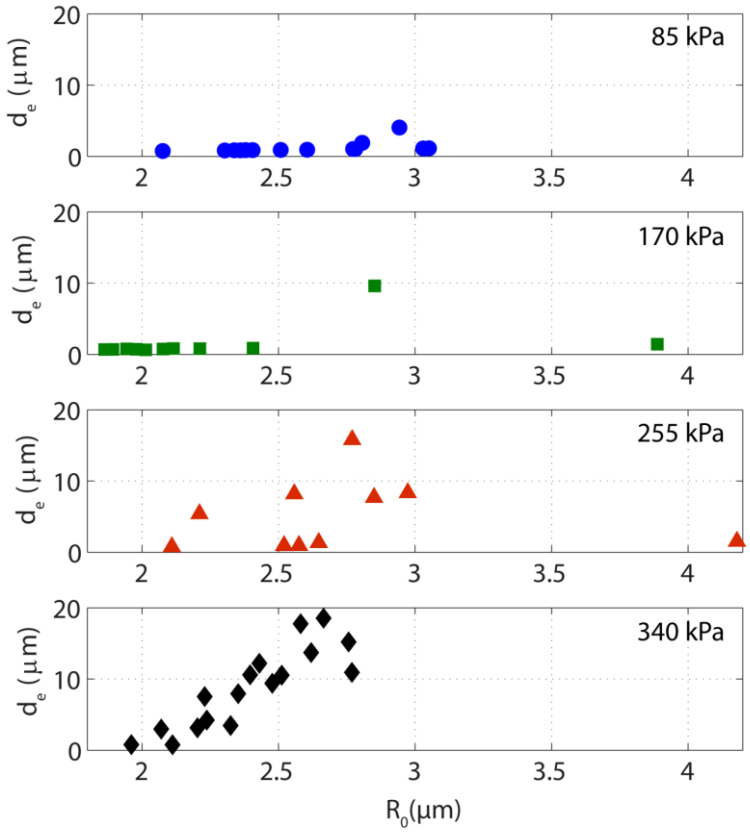

Figure 6.9. The final value of de of each microbubble plotted as a function of the microbubble radius (R_0) and the acoustic pressure.

6.3.3 Experiment B – Shedding occurrence

We now study in more detail the shedding as a function of the amplitude of the microbubble vibration. Figure 6.10 shows d_e as a function of the relative amplitude of oscillations ($\Delta R/R_0$) for 47 individual microbubbles. As displayed by the figure, below $\Delta R/R_0$ of 0.3, the value of d_e remains below 2.0 µm, while no apparent lipid shedding

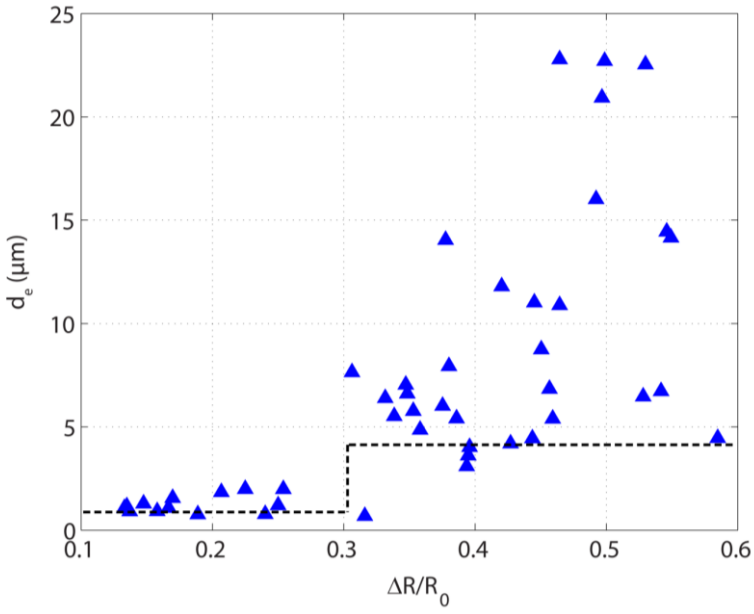

Figure 6.10. Plot of the d_e as a function of the relative amplitude of oscillation ($\Delta R/R_0$) for microbubbles insonified at 50 to 255 kPa, with the pulse length of 100 cycles. The black dashed line indicates a clear threshold at $\Delta R/R_0 \approx 0.3$.

can be resolved. However, when $\Delta R/R_0$ arrives at 0.3, d_e has an abrupt increase to around 7.6 μm, and this value rises to 22.7 μm at $\Delta R/R_0$ of 0.5. The mean square error (MSE) estimator was applied to assess the change point of the present data set (Qiu 2005):

$$\mathrm{MSE(m)} = \sum_{i=1}^{m}(X_i - \bar{X}_1)^2 + \sum_{i=m+1}^{47}(X_i - \bar{X}_2)^2 \quad (6.4)$$

where $X_1, X_2, \ldots X_{47}$ represents the 47 data points (d_e) sorted by the ascending $\Delta R/R_0$; $\bar{X}_1 = \frac{\sum_{i=1}^{m} X_i}{m}$ and $\bar{X}_2 = \frac{\sum_{i=m+1}^{47} X_i}{47-m}$.

The data point after the first minimum value of MSE(m) at m = 13 corresponds to $\Delta R/R_0 = 0.3$ and thus it represents the threshold of the occurrence of the *out-of-plane shedding*.

Figure 6.11 displays the influence of pulse length and relative radial oscillation amplitude on the transport distance for 41 microbubbles. The different colors represent data acquired at different pulse lengths. Several trends can be observed from this data. First, in agreement with figure 6.10, no transport is visible for a relative radial excursion $\Delta R/R0 < 0.3$, and de shows an increase with $\Delta R/R0$. Second,

at a given ΔR/R0, de is larger for longer pulse duration. This graph thus shows that both pulse duration and radial excursion determine the transport.

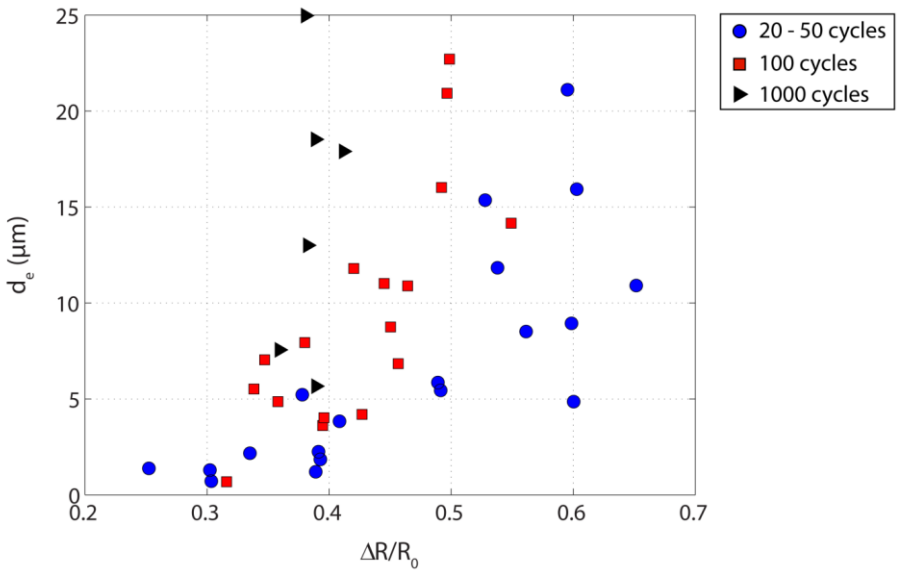

Figure 6.11. Plot of de as a function of $\Delta R/R_0$ for microbubbles insonified at 170 kPa, with the pulse length varying from 20 to 1000 cycles.

6.4 DISCUSSION

6.4.1 Occurrence of lipid shedding

In this study a lipophilic dye DiI was incorporated to trace the dynamics of the microbubble lipid shell. DiI has been proven as a reliable probe for lipid motion (Borden et al. 2005; Gullapalli et al. 2008). It has a low critical micelle concentration in the aqueous phase and is weakly fluorescent in water, but once incorporated into a lipid membrane it is highly fluorescent and photostable. The DiI molecules can diffuse laterally once applied, resulting in a staining of the entire lipid membrane. The diffusion coefficient of DiI is similar to that of the phospholipids, indicating that the DiI dynamics reflect the lipid dynamics.

Each shedding event that we observed actually consists of two separate physical processes: the detachment of shell materials from the microbubble shell, and the subsequent transport of the shed particles by the convective medium. We noticed two types of the lipid shedding events, *in-plane shedding* and *out-of-plane shedding.* In case of *in plane shedding*, the phospholipid particles were moving in the focal plane. For

out-of-plane shedding the vesicles were moving perpendicularly to the focal plane causing an unfocused image, or halo. We derived a threshold for *out-of-plane shedding*, which is around 30% of the relative radius excursion of the microbubble. The few cases of *in-plane shedding* were not considered here. The rare observations of *in-plane shedding* in experiment B can be due to the settings: only two frames of fluorescent recordings were acquired using the Photron camera (before and after ultrasound excitation, respectively, see figure 6.1c), due to the limited amount of illumination light available by combining two high-speed cameras. By subtracting these two images, without the ability to monitor the lipid motion, it is difficult to define the occurrence of *in-plane shedding* since single vesicles cannot be differentiated from the background signal.

The dynamics and the threshold of lipid shedding help us in better understanding the process of lipid shedding. Based on the observation of the time scale of a shedding event (several to tens of microseconds), and their strong dependence on the oscillation amplitude, we assume here that lipid shedding can be due to the surface area reduction of the lipid shedding events, which is in agreement with previous studies (Borden et al. 2005; Thomas et al. 2012). For a microbubble undergoing spherical oscillations, 30% of relative radial excursion is equivalent to ~50% of the surface reduction of the microbubble. This threshold value is in agreement with the previous work of (O'Brien et al. 2011), where a surface reduction of 41% was predicted for the collapse of a over-densely populated lipid monolayer. This assumption however may not be exclusive, and other physical processes can be involved, e.g., fragmentation of microbubbles and pinch off of the fragments together with the lipid shell materials (Cox and Thomas 2013). This possible shedding mechanism is not the focus of this study, but will be investigated in detail in the future study.

6.4.2 Convective transport

An oscillating gas bubble can generate a steady streaming flow consisting of vortical flow structures surrounding the bubble (Ooi et al. 2007). This cavitation microstreaming was interpreted as a nonlinear response of the flow caused by viscous attenuation effects within the thin oscillatory boundary layers surrounding the bubble wall (Marmottant et al. 2006). Various streaming patterns were reported in literature on vibrating millimeter-sized bubbles attached to the wall (Elder 1959; Collis et al. 2010).

Here, we capture vortical flow structures displayed by the transport trajectories of shed vesicles from micrometer-sized bubbles. Figure 6.12 shows one example, in which the detached lipid vesicles show translational motion towards and away from the microbubble shell during 500 μs of ultrasound excitation. The vesicles quickly

move out of focus when leaving the microbubble, while staying in focus during the back trip. This is in accordance with the symmetrical vortices reported previously (see, e.g. Elder (1959); Marmottant and Hilgenfeldt (2003) and figure 6.12 – lower panel). In addition, the transport velocity in this example is about 0.08 m/s, which is one order of magnitude larger than previously reported data for larger gas bubbles oscillating at lower radial amplitudes (Marmottant et al. 2006).

We hypothesize that the initiated streaming flow field (i.e., streaming patterns and flow velocity) is responsible for the distinct *in-plane shedding* and *out-of-plane shedding*. Higher pressures can lead to asymmetrical oscillations of microbubbles, thus generating different boundary conditions and flow dynamics compared to the stable, more symmetrical, oscillations driven at lower pressures (Collis et al. 2010). Several phenomena support this hypothesis. First, we observe a faster occurrence of lipid shedding (onset of transport) for *out-of-plane shedding* than *in-plane shedding*. At 85 to 170 kPa, 66% of *in-plane shedding* events were detected after at least 70 pulses of insonation; On the contrary, all *out-of-plane shedding* events at 425 kPa were captured within only 30 ultrasound pulses. This may indicate a high flow velocity for a rapid start of transport in *out-of-plane shedding* through the process of larger radial excursion. Second, we observed the prolonged transport of *out-of-plane shedding* after the ultrasound was turned off (Figure 6.8), but not for *in-plane shedding*. The reason could be the higher flow velocity which represents a higher flow inertia of the *out-of-plane shedding*. Third, the different transport trajectories for the two types of shedding indicate different streaming patterns. It was reported that the streaming pattern and flow velocity is strongly dependent on the mode of oscillations of the microbubble (Ooi et al. 2007), which can build up upon certain pressure threshold within a few cycles of insonation for bubbles at resonance (Versluis et al. 2010; Versluis 2013).

We assume that the shape deformation and/or corresponding microbubble fragmentation occurring in the orthogonal plane is related with the *out-of-plane shedding* behavior. However, this assumption cannot be validated by the present setup. The reason is that, on the one hand, the dynamics of lipid shedding and the amplitude and phase of the microbubble oscillations could not be captured simultaneously. On the other hand, even for a microbubble appearing spherically oscillating in a top view, it could actually perform shape deformations in a direction perpendicular to the wall, as observed from the side (Vos et al. 2008). A ‘side-view’ setup (Vos et al. 2011), in which the optical plane is perpendicular to the present focal plane, must be applied to validate this assumption.

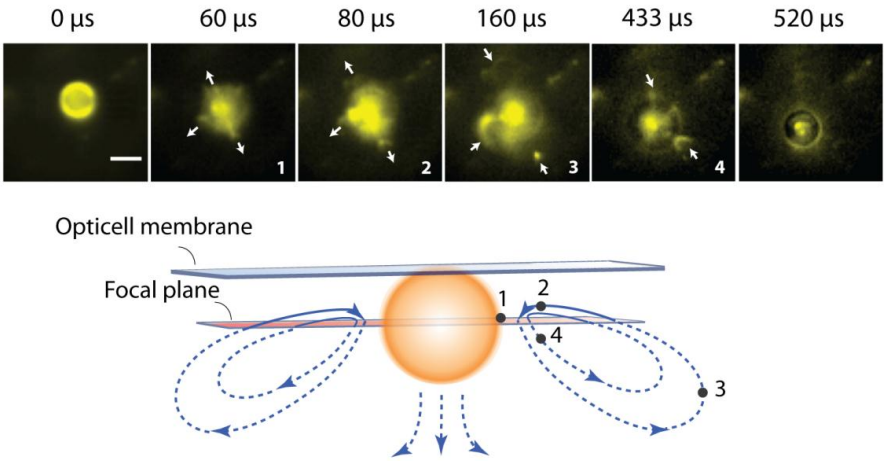

Figure 6.12. Streaming vortices traced by lipid vesicles shed from a microbubble (255 kPa, 500 cycles). The schematic plot indicates the vortical flow structure correspondingly. The scale bar represents 5 µm.

6.4.3 Experimental uncertainties

Photobleaching of the fluorescent dye and a low SNR of the fluorescent images are two major factors that could potentially influence the measurement result. However, the method to trace the shed materials was not sensitive to photobleaching because of an intensity normalization step in each frame. Moreover, the laser intensity was adjusted to a level that minimizes photobleaching while maintaining sufficient fluorescent signal during the experiment.

A calculation of the Stokes number (S_t) based on the experimental conditions indicates that the shed lipid vesicles can closely follow the streaming lines generated by an oscillating microbubble. The Stokes number is a dimensionless number corresponding to the motion of particles suspended in a fluid medium. It is defined as the ratio of the response time of a particle (τ_p) to the characteristic time scale of the flow field (τ_f):

$$S_t = \frac{\tau_p}{\tau_f} \tag{6.5}$$

where

$$\tau_p = \frac{2\rho_p R_p^{\,2}}{9\mu} \tag{6.6}$$

ρ_p ($\sim 10^3$ kg/m3) is the density of the lipid particles or vesicles, R_p is the particle radius ($\sim 1\times10^{-7}$ m), and μ is the dynamic viscosity of the surrounding water (10^{-3} Pa s). τf is taken as the smallest time scale of the flow field, which is on the scale of the ultrasound field ($\sim 1\times10^{-6}$ s). Combining (4) and (5) gives $S_t \approx 0.002$ (<< 1), implying the fidelity of the detached lipid vesicles in following the fluid streamlines.

The size of a microbubble is a crucial factor for the lipid shedding behavior. For microbubbles investigated in experiment A, 80% of the bubbles were smaller than 2.8 μm, which are considered to be smaller than the resonant size for a frequency of 1 MHz (van der Meer et al. 2007). This suggests that we may underestimate the occurrence of lipid shedding in figure 6.7. This issue was worked around in experiment B by taking the relative radial excursion as the variable.

The present top-view study is based on observations of a 2-D projection of shedding events which take place in 3 dimensions. To evaluate the trajectory of shed lipids for out-of-plane shedding, we use its out-of-focus halo image. This approach is insufficient to resolve full details of the shedding dynamics. Additionally, we mapped the distance of transport with the size of the halo, based on a model presented earlier by Adrian and Yao (1985) and Olsen and Adrian (2000). It is an approximation obtained by modeling both the Airy function and the geometric image as Gaussian functions. Several assumptions have been made here. The first is that the entire field of view is illuminated with equal laser intensity. Second, the detached lipid vesicle is a point source with a size smaller than the wavelength of the laser light. Third, the fluorescence light is emitted isotropically in all directions. Fourth, the direction of transport is strictly perpendicular to the focal plane. Although these are reasonable assumptions based on current experimental settings, an accurate derivation can only be made when multiple factors are precisely measured (e.g., the particle size; the angle between the trajectory and the wall). Our future investigation will focus on the side-view study, which will provide a direct approach to resolve the dynamics of out-of-plane shedding in detail and the measurement of their transport distance from the images, since the vesicles that travel away from the wall will be in the optical plane.

6.4.4 Applications

To accomplish efficient shedding events among the largest amount of microbubbles in a population, sufficient acoustic pressure should be applied with a frequency near the main resonance frequency of the microbubbles. The influence of pulse length on the occurrence of shedding showed only a minor trend in the present data (on the contrary to the transport distance). Under *in vivo* conditions, microbubble oscillations could be less within small blood vessels and high blood viscosity, thus a higher applied pressure may be required compared to *in vitro* conditions (Zheng et al. 2007). Therefore, for applications of ultrasound-mediated drug delivery, the

ultrasound frequency should be tuned to the resonant frequency of the majority of microbubbles in a population, to achieve an efficient drug delivery at comparatively low acoustic pressures. However, for applications where the stability of microbubbles is essential, such as diagnostic ultrasound imaging, the applied pressure should be chosen as a trade-off between the good image quality and a high stability of microbubbles.

We optically captured the cavitation microstreaming surrounding microbubbles of the size range for clinical use for the first time, traced by shed lipid shell materials. This is a key step towards a deeper understanding of the streaming field in connection with lipid shedding events, for potential applications of controllable drug delivery. First, the streaming flow can transport the shed lipid vesicles up to tens of micrometers away, depending on both the applied pressure and the pulse length. For 77% of the shedding events in this study, the detached shell materials are driven away from the wall (*out-of-plane* shedding). This implies that for small blood vessels, e.g., capillaries (5 – 10 μm) and arterioles (20 - 30 μm), the drug delivery may be efficient; however, longer pulse length and higher acoustic pressure could be necessary for larger vessels. Secondly, the rate of transport is around 0.1 m/s. This value is comparable to the human blood flow velocity in veins and arteries (~ 0.01 - 1 m/s mean flow velocity), especially near the vessel wall where the blood flow is lower than the mean flow velocity. This suggests that the lipid particles loaded with therapeutic agents can overcome the blood flow within short time duration (hundreds of micro-seconds to milliseconds) after being released, and reach the target site. Finally, it has been proposed that the shear stress generated by cavitation microstreaming can produce several biological effects such as gene degradation, hemolysis of erythrocytes and sonoporation (Gormley and Wu 1998; Ohl et al. 2006; Collis et al. 2010). Probing the shear rates near the cell membrane with fluorescent tracer vesicles can further clarify the mechanisms of gene and drug transfection.

6.5 CONCLUSIONS

Based on high speed fluorescence imaging, lipid shedding events were resolved. Two distinct release phenomena have been observed, being a transport of vesicles along the wall of the bubble container (*in-plane shedding*), and a transport perpendicular to the wall (*out-of-plane shedding*). A threshold on relative radial excursion $\Delta R/R_0$ of 0.3 is necessary for *out-of-plane shedding*, and this type of shedding is initiated already within a few tens of cycles of the acoustic exposure. It is concluded that the transport of detached shell materials by the surrounding streaming flow field strongly depends on the radial excursion of the microbubble and the pulse length.

7

Liposomes release from a vibrating microbubble on nanoseconds timescale

Abstract — When ultrasound contrast agents microbubbles (MBs) are preloaded with liposomes, they can be applied as a potential drug delivery vehicle. The fate of the liposomes under ultrasound excitations is of prime interest for investigations, since it is an essential step in the application of drug delivery. Previous studies on regular lipid-shelled MBs have shown lipid shedding phenomena, accompanied by MB shrinkage under ultrasound excitations. Here we present a multi-modal study to optically characterize shedding behavior of liposome-loaded MBs (lps-MBs) based on high-speed fluorescence imaging. First, the dynamics of shedding were resolved by the Brandaris camera operating at up to 2 million frames per second (Mfps). Shedding of shell material was observed after few cycles of the excitation pulse. Second, a parametric study using a Photron camera running at 75 kfps indicates a significant influence of MB resonance on the shedding behavior. Third, the shedding behavior was investigated as a function of the MB oscillatory dynamics, facilitated by combination of the two fast cameras. We found a threshold of the relative amplitude of oscillations (35%) for the onset of lipids shedding. Overall, the shedding behavior from lps-MBs could well be controlled by the excitation pulse.

Appeared as a proceedings paper for the IEEE International Ultrasonics Symposiumn 2013, Prague, Czech Republic, by Y. Luan, G.P.R. Lajoinie, E.C. Gelderblom, I. Skachkov, H. Dewitte, I. Lentacker, H.J. Vos, A.F.W van der Steen, M. Versluis and N. de Jong.

7.1 INTRODUCTION

In recent years, ultrasound contrast agent microbubbles (MBs) have become a promising tool for ultrasound-triggered drug delivery (Klibanov et al. 2002; Ferrara et al. 2007; Lentacker et al. 2009). A typical lipid-coated MB is comprised of a gaseous core that is encapsulated by a thin phospholipid shell which stabilizes the MB (Pu et al. 2006). While the gaseous core can serve as a cavitation nucleus, the lipid shell can be utilized for bearing therapeutic agents by, e.g., incorporating the drug within or directly linked to the MB shell (Lentacker et al. 2010; Liang et al. 2010). More recently, liposome-loaded MBs (lps-MBs) have been developed that are even more considered as potential drug delivery vehicles. Liposomes contain a lipid bilayer shell and an aqueous core, ensuring a high drug payload and a low toxicity to the surrounding tissue. When the liposomes are conjugated to the MBs surface through covalent thiol-maleimide linkages (Geers et al. 2011), the complex can largely enhance the intracellular drug uptake upon the application of ultrasound (Lentacker et al. 2010).

In the application of lps-MBs for ultrasound-triggered drug delivery, the fate of the liposomes is of prime interest, since it plays a key role in elucidating the drug delivery process in detail. Although lipid shedding phenomena have been observed previously for lipid-coated MBs under insonations (Borden et al. 2005), little is known about the shedding of drug-carrying vesicles from the MB surface.

The objective of this work is to optically resolve the shedding behavior from individual lps-MBs exposed to a single burst of ultrasound. The first results are presented here.

7.2 MATERIALS AND METHODS

7.2.1 Method

The shedding of the liposomes occurs at a time scale of nanoseconds to microseconds which needs fast cameras to resolve. In this study we used a fluorescence lipid probe to label liposomes attached to the MB shell, combined with a continuous wave (CW) laser for the excitation of the fluorophore. First, fluorescence imaging by an ultrafast framing camera operating at a frame rate of 0.75-2 Mfps was applied to capture the starting moment of the shedding behavior. Yet, the limited amount of frames (128) prevented imaging the transportation distance of the shed liposomes during long pulses (50 – 500 cycles). Therefore, a second study on individual lps-MBs was performed parametrically with a camera running at 75 kfps to measure the liposome transportation speed and distance. Third, the prevalence of lipid shedding related to MB oscillation amplitude was investigated by combining these two fast cameras.

7.2.2 Experimental setup

As shown in figure 7.1a, the experimental setup combines a sample holding system with an acoustic excitation setup and an optical imaging system. An Opticell unit (NUNC, Thermo Fisher Scientific, Wiesbaden, Germany) containing the MBs diluted with PBS solution (Invitrogen, UK) was placed in a water bath (T≈22°C) connected to a 3D micro-positioning stage. A focused, single-element transducer (C302, Panametrics, USA) transmitted ultrasound pulses with a center frequency of 1 MHz. An upright fluorescent microscope equipped with a 40×water-immersed objective (NA=0.9; Olympus, The Netherlands) was focused at the MB sample. A CW laser (5 W@532 nm; Cohlibri; Lightline, Germany) was employed for fluorescence excitation of the fluorescent label DiI. An optical light guide (SCHOTT AG, Mainz, Germany) was mounted at the bottom of the tank to illuminate the region-of-interest in the unit. The light guide was connected to either a Xenon flash light source (A-260 Vision Light Tech, Uden, NL) or halogen light source (KL1500LCD, Schott, Germany), depending on the frame rate of the recordings.

For the recordings to resolve the timescale of the shedding (experiment 1), the Brandaris-128 camera was operated in fluorescence mode (Gelderblom et al. 2012). For each MB, a single burst with a pulse length of 100 cycles, 200 kPa was applied. For the parametric study of the transportation distance (experiment 2), a CMOS-based high-speed camera (SA-1.1, Photron Ltd, UK) operated at 75 kfps was connected to the optical system. A single pulse of 50, 100 or 500 cycles at an acoustic pressure varying from 100 to 500 kPa in steps of 100 kPa was employed. Up to 5000 frames were recorded per MB to capture the entire event. 60 MBs were investigated in experiment 2.

The third experiment setup involves the combination of the two cameras. The photron camera was used to capture two fluorescence pictures of the MB with millisecond-exposure before and after the ultrasound excitation respectively. From these images the prevalence of shedding, and final transportation distance are obtained. Simultaneously, the Brandaris camera, operated at 10 Mfps in bright-field mode, was synchronized with the arrival of the acoustic wave to record the MB oscillation amplitude. The ultrasound burst consisted of 20, 50, 100 and 1000 cycles at 200 kPa. The timing diagram of a single recording in experiment 3 is shown in figure 7.1b. 46 MBs were studied in this experiment.

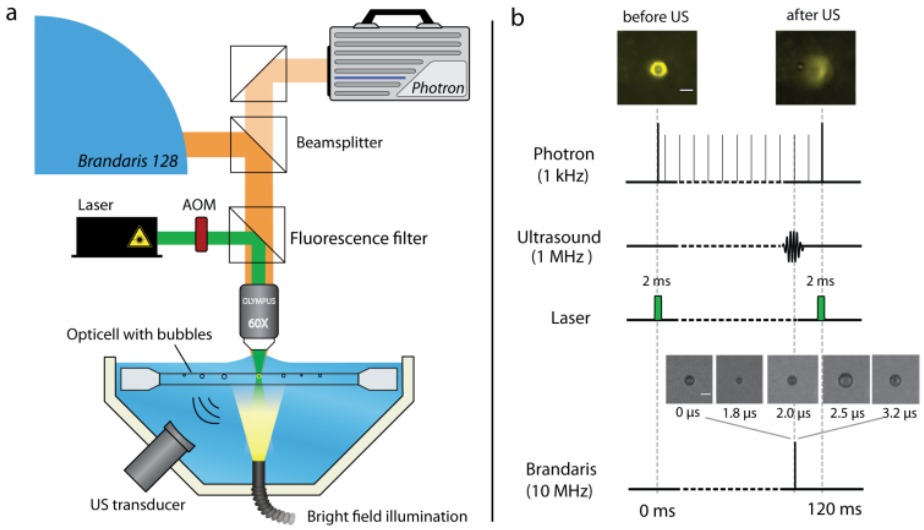

Figure 7.1. (a) Schematic view of the experimental setup for recordings shedding dynamics by 1) only the Brandaris 128 camera, 2) the Photron camera, and 3) the combination of both cameras. (b) the timing diagram of experiment 3).

7.2.3 Liposome-loaded microbubbles

MB lipid solution and liposome dispersion (mixed with fluorescence DiI) were prepared separately as formulated by Geers *et al.* (2011) and Gelderblom (2012). Then MBs were covalently loaded with maleimide-functionalized liposomes by adding 100 µL of the liposome dispersion to 900 µL of the bubble lipid mixture in a 2.5mL chromatography vial. After filling the headspace with perfluorobutane gas, the vial was shaken for 15 s in a CapMix™ device. This resulted in the formation of lps-MBs having DiI labeled liposomes.

7.3 RESULTS

7.3.1 Observations of the shedding behavior

With reference to experiment 1, high-speed fluorescence imaging enabled resolving the moment of shedding on the timescale of an ultrasound pulse. Figure 7.2 shows the shedding behavior captured by the camera operated at around (a) 0.75 Mfps and (b) 1.96 Mfps, respectively. In both cases, within several (<10) microseconds of the ultrasound excitation, fluorescently-labeled shell material was observed to be detached uniformly from the MB surface, accompanied by a further transportation process. After ultrasound was turned off, the transportation also ceased, leaving a

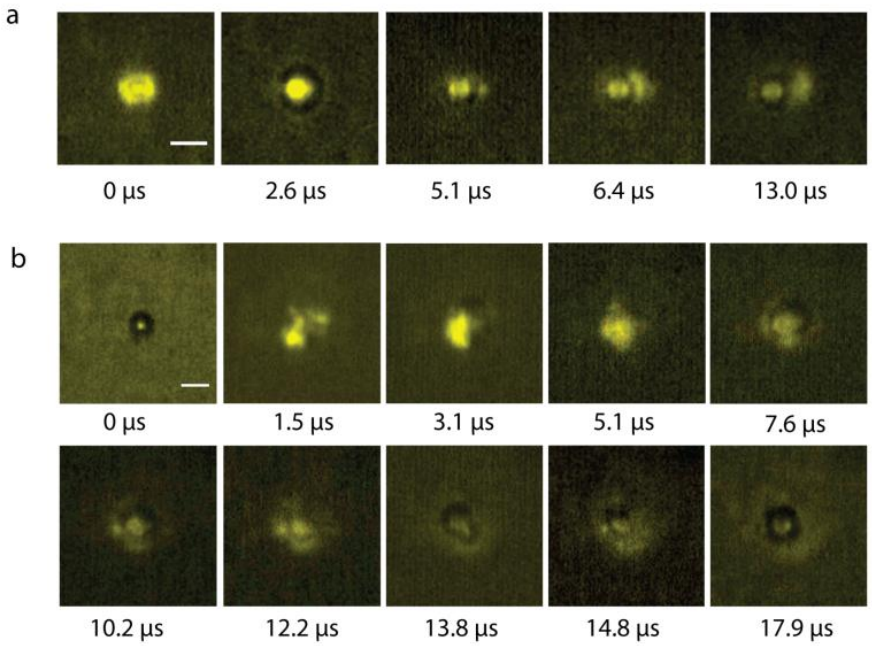

Figure 7.2. Dynamics of the shedding behavior recorded by the Brandaris 128 camera running at (a) 0.75 Mfps and (b) 1.96 Mfps. Scale bars represent 5 µm.

fluorescent cloud surrounding the MB. In Figure 7.2b, after around 6 cycles of MB oscillations, the emergence of the fluorescent spot in the surrounding region was resolved.

7.3.2 Parametric study of the shedding transportation

In experiment 2, the shedding distance was tracked for the entire duration of the pulse. Shedding distance d_S is defined as the distance of the front of the shed material with respect to the initial position of the MB wall. It was derived for each MB frame by frame from the radial intensity profile of the fluorescent image (Gelderblom 2012). Figure 7.3 examples d_S as a function of time for 3 single MBs insonified with different US settings. For all of the three cases, d_S increases during the US exposure, indicating the continuous transportation of the detached shell materials by a flow field around the MB. After the ultrasound was turned off, the transportation proceeded for a period, until an optically resolved final shedding distance d_{SF} was reached.

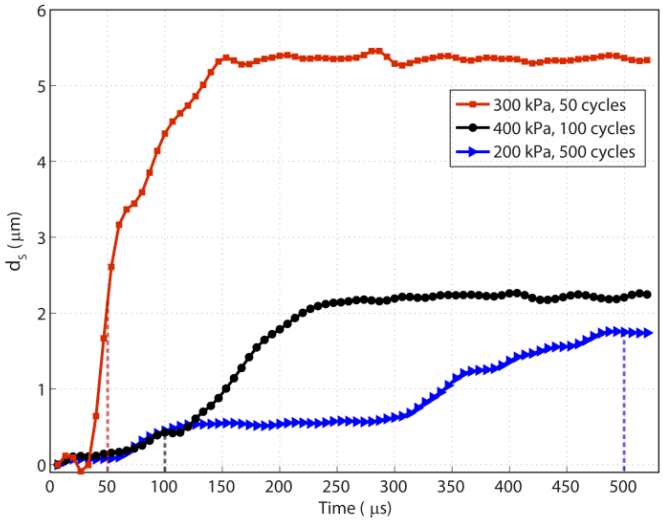

Figure 7.3. Plot of dS as a function of time for 3 insonified MBs. Dashed lines indicate the time when ultrasound was turned off.

The final shedding distance was derived for all MBs and was plotted as a function of the MB size and the acoustic pressure, see figure 7.4. We found that the MB size plays a significant role in the shedding behavior. MBs with an initial radius of 3 µm show largest d_S for any given acoustic pressure. Such radius corresponds to resonant MBs at 1 MHz (van der Meer et al. 2007; Luan et al. 2012). Furthermore, increasing pressure increases the transportation distance. Both results suggest that microbubble oscillation amplitude is the major determinant of the transportation distance. The current data does not show a clear trend between the pulse length and the transportation distance.

7.3.3 Shedding related to MB oscillation amplitude

In experiment 3, the parameter dS was used to define the occurrence of a shedding event. The shedding occurrence and distance was derived by subtracting the fluorescence images recorded before and after US. From the Brandaris recording of the same MB, an R-t curve was obtained, from which the maximum amplitude of oscillation (ΔR) was derived. Figure 7.5 shows the relative shedding distance (dR = dSF/R0) as a function of the relative amplitude of oscillations (ΔR/R0). This graph shows a clear threshold of ΔR/R0 ≈ 0.35 for triggering the shedding behavior of an individual MB.

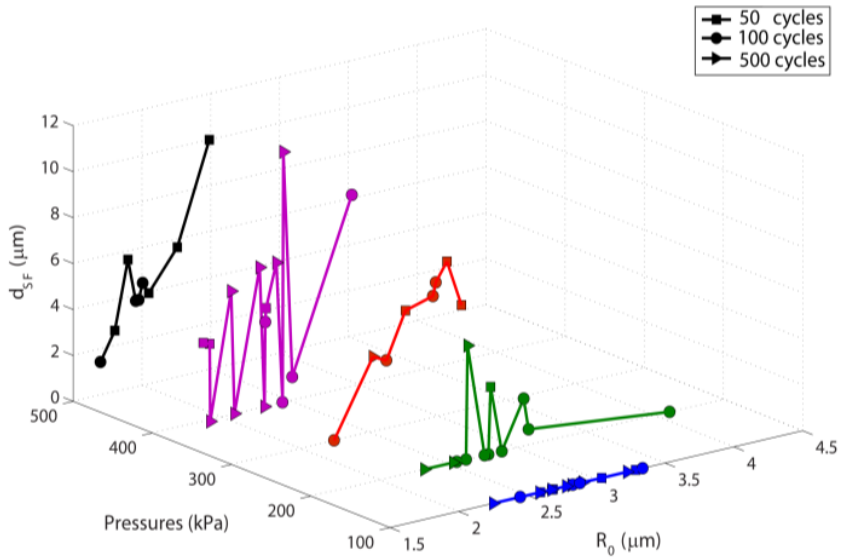

Figure 7.4. The final shedding distance (dS) plotted as a function of MB size and the acoustic pressure.

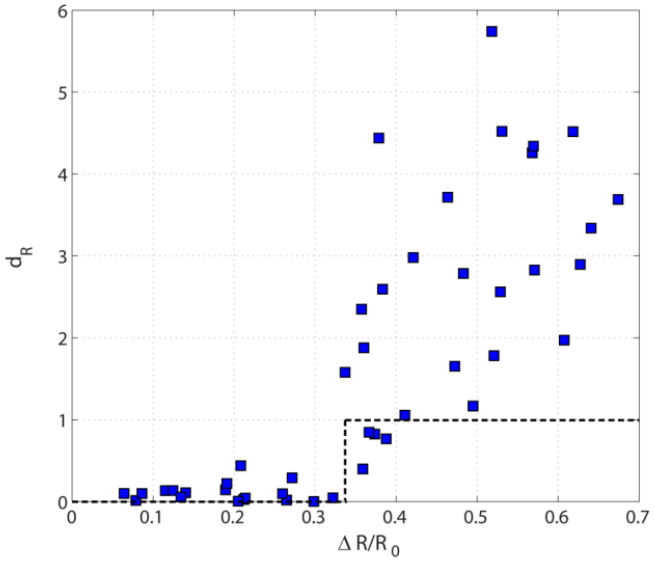

Figure 7.5. Plot of relative shedding distance (d_R) as a function of the relative amplitude of oscillation ($\Delta R/R_0$). The black dashed line indicates a clear threshold at around $\Delta R/R_0 \approx 0.35$.

7.4 DISCUSSION AND CONCLUSION

This study showed that MB oscillation amplitude is of key significance for the shedding dynamics of lps-MBs. When it arrives at ~0.35, a fast shedding (occurs within 10 cycles of MB oscillations) of excessive shell materials can be triggered. Then transportation of the shed particles was strongly influenced the resonance of MBs. To the author's knowledge, this study is the first to track the dynamic lipid shedding process quantitatively by fluorescence imaging at a high frame rate. The results are further discussed below.

7.4.1 Detachment & transportation

Each shedding event we observed in this study actually consists of two independent physical processes: the detachment of shell materials from the MB shell, and subsequent transportation of these shed particles by the surrounding medium.

We detected a shedding occurrence for oscillation amplitudes larger than 35%. Oscillation amplitudes of 35% correspond to a surface reduction of 60% in the compression half-cycle. The presence of a threshold on the shedding occurrence is in agreement with the previous study by O'Brien *et al.* (2011), who proposed a lipid shedding model for lipid-coated MBs under insonation. They argued that the occurrence of lipid shedding was driven by the lipid monolayer collapse due to the oversaturation of phospholipids on the MB shell, taking place on a timescale of a typical ultrasound pulse. A surface reduction of at least 41% was derived from the model as requisite for the film collapse. For a lps-MB, we speculate on a similar shedding process: During the compression phase of the oscillation, a shedding event is triggered instantly when the radius reaches the threshold value ($\Delta R/R_0 \approx 0.35$ as obtained here). The difference between the actually found threshold value and the value given in O'Brien et al. (2011) can be attributed to a slightly different MB system (lipids, or lipids + liposomes). During the subsequent transportation, vortical flow structures displayed by the detached liposomes were captured in this study (results not shown here). These flow structures and the flow velocity are on the same order of magnitude as previously reported micro-scale steady streaming generated around an oscillating bubble (Elder 1959; Marmottant et al. 2003; Ooi et al. 2007). A further calculation of the Stokes number (S_t) for the liposomes based on the experimental conditions gives $S_t \approx 0.01$ ($<< 1$), implying that the shed particles can closely follow the streaming field generated by an oscillating MB.

7.4.2 Experimental uncertainties

When using fluorescent dyes to track the liposomes, photobleaching and a low SNR in the frames could influence the measurement result. Yet, the method to obtain the

front of the shed material was insensitive to photo bleaching because of an intensity normalization step in each frame. Moreover, the laser intensity was adjusted to a level that minimizes photobleaching while maintaining sufficient fluorescent signal. To check noise influences on the shedding distance, ten shedding distance graphs such as exampled in Fig. 7.3 were analyzed. The relative maximum error of shedding distance (d_{S_error}) was determined by:

$$d_{S\_error} = (d_{S\_max} - d_{S\_min}) / d_{S\_av} \times 100\% \quad (7.1)$$

where d_{S_max} and d_{S_min} are maximum and minimum values of measured d_S for each MB, while d_{S_av} is the averaged d_S. These values are measured in the time interval after insonification. The value of d_{S_error} for all ten MBs was averaged, giving a final averaged d_{S_error} of 6%. The found range of d_S in the experiments was 0 to 12 μm maximum, on which an error of 6% is not significant. This shows that the analysis algorithm to obtain the shedding distance produces stable results.

7.4.3 Controlled drug delivery

This study proved in vitro the feasibility of the controllable release of drug-carrying liposomes from lps-MBs by manipulating US settings. The main determinant of shedding and transportation was found the radial excursion amplitude, which is strongly related to MB resonance behavior. To achieve an efficient drug delivery at the lowest acoustic pressure, the US frequency should be tuned to the resonant frequency of the majority of MBs in a population. In the current experimental settings, a pressure of 200 kPa at 1 MHz was sufficient to overcome the shedding threshold. This corresponds to a mechanical index (MI) of 0.2, which is well below regulatory safety limits for medical ultrasound. Such pressure amplitudes are easily generated with current diagnostic ultrasound machines, showing the large potential for drug delivery with regular US machines.

An optically resolved transportation distance of order 10 μm may seem small on a length scale of the human body. Yet, a MBs targeting technique (Klibanov 2007) would possibly enable a highly localized drug release. Furthermore, the transportation rate of shed particles is on the scale of ~ 0.1 m/s. This value is comparable to the human blood flow velocity in veins and arteries (~ 0.01 - 1 m/s mean flow velocity), especially nearby the vessel wall where the blood flow generally is lower than the mean flow velocity. This suggests that the liposome particles can overcome the blood flow within a short time duration (hundreds of micro-seconds to milliseconds) after being shed, and reach the region of interest in the vicinity.

It is worth noting that shedding events captured in this study were 2D projected dynamics that took place in a 3D space. The observation of the events is thus limited by the focus plane. For an overall investigation of the events, a ‘side-view’ observation

would be necessary (Vos et al. 2008). Further studies will be performed to fully elucidate the shedding behavior from a complete 3D view.

8

Investigations on the liposomes release relative to the microbubble dissolution

Abstract — The liposome-loaded microbubbles are a highly successful design for ultrasound-mediated drug delivery. Although *in vitro* studies have shown greatly improved cell permeability and subsequent drug uptake using this drug delivery vehicle, little is known about the process underlying liposome release and the physical mechanisms such as shell destruction and microbubble dissolution. Earlier, we observed lipid shedding from the microbbuble surface using high-speed fluorescence imaging (Gelderblom 2012). For this purpose, the ultra-high speed camera Brandaris (10 Mfps) and a Photron camera (1000 fps) was combined to investigate the occurrence of shedding as a function of microbubble oscillation dynamics (Luan et al. 2014). Here we apply the same technique for liposome-loaded microbubbles. The data was supplemented with the observation of the bubble dissolution for hundreds of milliseconds after the shedding event. No significant difference in the threshold for shedding was found between lipids and liposomes, however, a fast dissolution which may be related to bubble fragmentation of up to 30% of the initial bubble size occurred. It was observed that gradually bubble dissolute over hundreds of milliseconds until a final stabilization was reached. The close correlation between lipid/liposome shedding and microbubble destruction provides clinical support in the acoustic parameter space for combined imaging and drug delivery with ultrasound.

By Y. Luan, G.P.R. Lajoinie, E.C. Gelderblom, I. Skachkov, H. Dewitte, I. Lentacker, A.F.W. van der Steen, H.J. Vos, M. Versluis and N. de Jong.

8.1 INTRODUCTION

Microbubble-mediated drug delivery is investigated for the enhancement of drug delivery efficiency and for improved controllability at the target site. The stabilizing microbubble shell, imparting a low surface tension and resisting gas permeation (Borden et al. 2002), plays a major role in carrying drug molecules. For example, incorporated drug molecules can be within the microbubble shell or within drug-loaded vesicles attached to the shell (Lentacker et al. 2009; Klibanov et al. 2010). One highly successful design of drug delivery vehicles is a liposome-loaded microbubble, which was developed by conjugating liposomes to the microbubble surface through biotin-avidin or covalent thiol-maleimide linkages (Kheirolomoom et al. 2007; Schroeder et al. 2007; Geers et al. 2011). It can carry both hydrophilic and hydrophobic drugs, and has a higher drug payload compared to lipid-shelled microbubbles. The strategy of applying this liposome-loaded microbubble in ultrasound-mediated drug delivery is to focus ultrasound field in the target region, insonifying the bubbles, to locally release the attached liposomes. Previous studies on Doxorubicin (DOX) - liposome loaded microbubbles and lipoplex-loaded microubbles (containing pDNA or siRNA) showed strongly improved DOX cytotoxicity (Lentacker et al. 2010) and pDNA and siRNA delivery to cells *in vitro* (Lentacker et al. 2007; Vandenbroucke et al. 2008). Although the therapeutic effect has been proved, little is known about the process underlying liposome release (e.g., the dynamics, the timescale) and the physical mechanisms such as shell destruction and subsequent microbubble dissolution.

Lipid shedding behavior from lipid-coated microbubbles was studied before (Gelderblom 2012; Luan et al. 2014). High-speed fluorescence imaging was performed to optically resolve the shedding behavior. We found a fast detachment of the lipid shell material (within a few microseconds) and a subsequent transport of the detached shell material by acoustic streaming. The shedding was observed at two different time scales, namely *in plane shedding* (1 μs timescale) and *out-of-plane shedding* (100 μs timescale). By using Brandaris 128 camera (10 Mega frames per second (Mfps)) and a camera Photron (1000 fps), we found a threshold in the relative oscillation amplitude of around 0.3 for initiation of lipid shedding (Luan et al. 2014). For liposome-loaded microbubbles, a comparative study to lipid-shelled bubbles is crucial to understand the process of liposome release, and in a further step, to quantify the release. It was reported that microbubble dissolution is closely related with the loss of lipid shell material (Borden et al. 2005; Thomas et al. 2012; Viti et al. 2012). The static bubble dissolution after the destruction of the lipid shell was considered as an indirect measure from an increased surface tension through the decreased concentration of lipids on the bubble shell (Chomas et al. 2001; Borden et

al. 2005). Therefore, to measure the dissolution of a microbubble directly after the shedding event as a relevant parameter is highly desirable.

Here we study the shedding of liposomes from single microbubbles relative to the oscillation dynamics, as well as the dissolution of the very same microbubbles. The key questions to investigate are the process of liposome release (i.e., how and when do liposomes detach, where do they go, what do they take with them), and on the other hand the fate of the microbubble during and after the shedding (i.e., if bubble destruction occur correspondingly). We used a fluorescence lipid probe to label the liposomes, combined with a continuous wave (CW) laser as the excitation illumination for the fluorescence microscopy. Similar to the previous study for characterizing lipid shedding from lipid-shelled microbubbles (Luan et al. 2014), the Brandaris camera was operated at 10 Mfps to resolve the microbubble oscillation dynamics during ultrasound exposure. Before and after the insonification, one fluorescent image was recorded each to determine the occurrence of lipid shedding. The difference is that here the Photron camera was running continuously at 1000 fps to monitor the subsequent bubble dissolution in bright-field mode for hundreds of milliseconds.

8.2 MATERIAL AND METHODS

8.2.1 Microbubble formulation

Microbubbles were prepared by mixing 1,2-dipalmitoyl-sn-glycero-3-phosphocholine (DPPC) (Lipoid, Ludwigshafen, Germany) and either 1,2-distearoyl-sn-glycero-3-phosphoethanolamine-N-[PDP(polyethylene glycol)-2000] (DSPE-PEG-SPDP) for functionalized bubbles or 1,2-distearoyl-sn-glycero-3-phosphoethanolamine-N-[methoxy(polyethylene glycol)-2000 (DSPEPEG)(both Avanti polar lipids, Alabaster, AL) for non-functionalized bubbles in a molar ratio of 65:35 in chloroform. For fluorescent labeling of the microbubbles membrane, the lipophilic dye DiI (Sigma-aldrich, Bornem, Belgium) was added to the lipid mixture. After chloroform evaporation, the lipid film was dissolved in a 1:2:7 glycerine-propyleneglycol-H_2O mixture to obtain a clear solution with a final lipid concentration of 4×10^{-4} mmol/mL. This lipid solution was aliquotted in 2.5 mL chromatography vials of which the headspace was filled with perfluorobutane gas (F2 chemicals, Preston, UK). Finally, bubbles were obtained by high-speed shaking of the chromatography vial in a Capmix™ device (3 M-ESPE, Diegem, Belgium) for 15 s.

Maleimide-functionalized liposomes were prepared by mixing DPPC, 1,2-distearoyl-snglycero-3-phosphoethanolamine-N-[maleimide(polyethylene glycol)-2000] (ammonium salt) (DSPE-PEG maleimide) (Laysan Bio Inc, Arab, AL), cholesterol and fluorescent dye DiI (1,1'-dioctadecyl-3,3,3'3'-tetramethylindocarbocyanine perchlorate), all dissolved in chloroform in a round-bottom flask at a 49:15:35:1 molar

ratio and a final lipid concentration of 16 mg/mL lipids. The chloroform was evaporated and the remaining lipid film was hydrated with distilled water. The liposomes were sized by extrusion through a 200 nm polycarbonate filter using a mini-extruder at 60°C (Avanti Polar Lipids, Alabaster, AL).

Microbubbles were covalently loaded with maleimide-functionalized liposomes by adding 100 µL of the liposome dispersion to 900 µL of the bubble lipid mixture in a 2.5 mL chromatography vial. After filling the headspace with perfluorobutane gas, the vial was shaken for 15 s in a CapMix™ device. This results in the formation of microbubbles with DiI-labeled liposomes attached on the shell.

8.2.2 Experimental setup

The Opticell™ unit (NUNC, Thermo Fisher Scientific, Wiesbaden, Germany) containing the microbubbles diluted with PBS solution (Invitrogen, Bleiswijk, the Netherlands) was placed in a water bath (T = 22°C) connected to a 3D micropositioning stage. A focused, single-element transducer (C302; Panametrics, Waltham, USA) with a center frequency of 1 MHz was fixed on the side of the water tank. 43 microbubbles were investigated in total. For each microbubble, a single burst with a pulse length of 100 cycles at an acoustic pressure of 85 kPa, 128 kPa, 170 kPa or 255 kPa was applied. Acoustic pressures were calibrated in a separate setup with a needle hydrophone (0.2 mm PVDF, Precision Acoustics, Dorchester, UK) prior to the experiment. Two fast framing cameras were combined in the optical system (Fig. 8.1a). 80% of the light path transmitted through the objective was projected by a beam-splitter into the Brandaris 128 camera (Chin et al. 2003; Gelderblom et al. 2012) operated at a frame rate of 10 Mfps, to record the microbubble oscillation dynamics. The other 20% of the light path was captured by the Photron camera running at 1000 fps. The laser was turned on for a duration of 2 ms before and after the ultrasound excitation respectively to track the location of fluorescence materials. In addition, bright field images were captured subsequently for a duration of 350 ms to monitor the microbubble dissolution. The timing diagram of a single recording is shown in figure 8.1b.

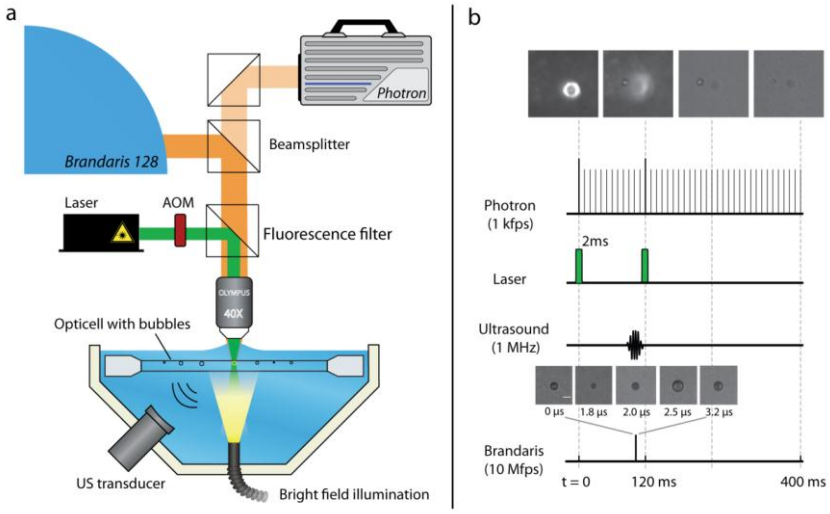

Figure 8.1. (a) A schematic view of the experimental setup and (b) the timing diagram of the experient.

8.2.3 Data analysis

8.2.3.a Derived parameters

In our last paper, we have described an *out-of-plane shedding* (Luan et al. 2014), in which the detached particles are transported perpendicular to the focal plane, leading to the spread of an out-of-focus fluorescent halo observed from the top view. Here we use the same method to estimate the shedding distance (d_e) from the top view observation. The size of the fluorescent halo (with a diameter of d_h) was derived by subtracting the image made before the ultrasound exposure from the one obtained afterwards. The transfer function is written as (Olsen et al. 2000; Luan et al. 2014):

$$d_e = \sqrt{\frac{s_0^{\,2}(d_h^{\,2} - d_p^{\,2})}{D_a^{\,2}}} - R_0 \tag{8.1}$$

where R_0 is the initial radius of the microbubble, $d_p \approx 2\times10^{-7}$ m is the vesicle diameter, $D_a = 5\times10^{-3}$ m is the lens aperture diameter, and $s_0 = 3.3\times10^{-3}$ m is the working distance of the lens.

Figure 8.2 shows a typical example of a single recording and parameters derived from particular frames. The second parameter was the relative amplitude of oscillations ($\Delta R/R_0$) calculated from the radius-time (R-t) curves obtained from the Brandaris recording. A custom-designed image analysis software based on edge-tracking minimum cost algorithm was used to obtain the radius time (R-t) curve (van

der Meer et al. 2007). Then the relative amplitude of oscillation ($\Delta R/R_0$) was evaluated by averaging the maximum and the minimum amplitude of oscillations. The last two parameters describe the dissolution of the microbubble during and after the insonification. The instantaneous dissolution ($\Delta R_i/R_0 = (R_0-R_i)/R_0$) was measured from the bright-field recording, and R_i is the bubble radius at first frame after the ultrasound excitation. Moreover, the relative size reduction of the static dissolution ($\Delta R_s/R_0 = (R_0-R_s)/R_0$) was derived by tracking the bubble radius in each frame for around 350 ms after the insonification, and R_s is the radius when the bubbles was stabilized at around 300 ms. The same edge-tracking minimum cost algorithm was applied as before.

The threshold of the occurrence of shedding was estimated by using the mean square error (MSE) estimator to assess the change point of a data set (Qiu 2005; Luan et al. 2014):

$$\mathrm{MSE(m)} = \sum_{i=1}^{m}(X_i - \bar{X}_1)^2 + \sum_{i=m+1}^{n}(X_i - \bar{X}_2)^2 \qquad (8.2)$$

where $X_1, X_2, \ldots X_n$ represents the data points (d_e) sorted by the ascending $\Delta R/R_0$; $\bar{X}_1 = \frac{\sum_{i=1}^{m} X_i}{m}$ and $\bar{X}_2 = \frac{\sum_{i=m+1}^{n} X_i}{n-m}$. The data point after the first minimum value of *MSE (m)* represents the threshold change location.

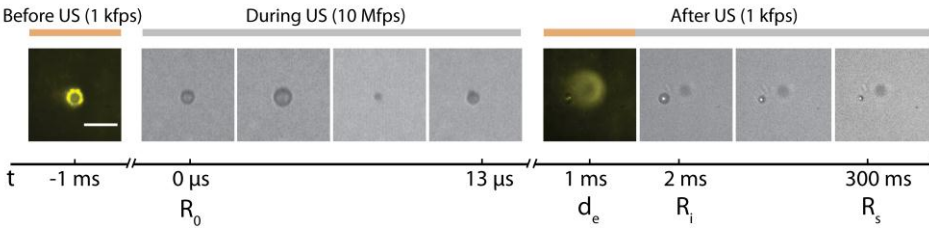

Figure 8.2. An example of a typical recording. The ultrasound was turned on at 0 µs. The derived parameters are initial bubble radius (R_0), the estimated shedding distance (d_e), the bubble radius measured immediately after insonification (R_i), and the final stabilizing radius (R_s). The size bar represents 10 µm.

8.2.3.b Simulation

To understand the static dissolution process in response to the shedding of lipid shell material, we performed simulations on the static diffusion of uncoated microbubbles with an air core and a C_4F_{10} gas core, respectively, based on the model described by Epstein and Plesset (1950), Chomas et al. (2001). The rate of radius change for a free gas bubble can be written as:

$$\frac{d\varepsilon}{d\tau} = -\frac{(1-f)+\frac{\delta}{\varepsilon}}{1+\frac{2\delta}{3\varepsilon}} + \left[\frac{\tau}{\varepsilon} + 2\sqrt{\frac{c_s}{2\pi\rho}}\right] \tag{8.3}$$

where ε and τ are non-dimensional radius and non-dimensional time, respectively. They can be expressed by the bubble radius (R) and time (t) through the following equation:

$$\varepsilon = \frac{R}{R_0}; \tau = \sqrt{\left(\frac{2\kappa c_s}{\rho R_0^2}\right)} t \tag{8.4}$$

with R_0 the initial bubble radius; κ the coefficient of diffusivity, ρ the density of the gas bubble and c_s the saturation gas concentration; The other two parameters δ and f can be described by:

$$\delta = \frac{2M\sigma}{\bar{R}TR_0\rho(\infty)}; f = \frac{C_i}{C_s} \tag{8.5}$$

where M is the molecular weight of the gas; $\bar{R}$ = 8.31 N·m/(k·mol) is the universal gas constant; T = 295 K is the temperature; σ = 0.072 N/m is the surface tension of water; $\rho(\infty)$ is the density of a gas bubble with gas-liquid interface of zero curvature; c_i and c_s are the initial gas concentration and the saturation gas concentration in the surrounding medium. Therefore f varies from 0 (degassed water, as was assumed in this study) to 1 (complete saturation). The constants used for simulation of an air bubble and a C_4F_{10} bubble are listed in Table 8.1.

Table 8.1. Constants used in the modeling of dissolution of unencapsulated bubble (Chomas et al. 2001).

Gas	$M\times10^{-3}$ (kg/mol)	$\rho/\rho(\infty)$ (kg/m^3)	$\kappa\times10^{-10}$ (m^2/s)	$c_s\times10^{-3}$ (kg/m^3)
Air	**28**	**1.2**	**20**	**8.15**
C_4F_{10}	**238**	**11.2**	**6.86**	**1.44**

8.3 RESULTS

8.3.1 The occurrence of shedding

The shedding of lipid shell materials occurred transiently and can hardly be resolved unless they are transported away from the microbubble surface due to the acoustic streaming (Luan et al. 2014). Therefore the transport of shed lipid shell materials was utilized to define the occurrence of the shedding. Figure 8.3 illustrates the transport distance (d_e) as a function of the relative amplitude of the microbubble vibrations ($\Delta R/R_0$). A 100-cycle burst varying from 50 to 255 kPa was applied. By

using the mean square error (MSE) estimator, a threshold change location at m = 23 among the 43 data points sorted by the ascending $\Delta R/R_0$ was derived. This corresponds to the relative oscillation amplitude $\Delta R/R_0$ of 0.38. Figure 8.2 shows that below this threshold value, d_e stays below approximately 2.0 µm, and no apparent shedding or very minor shedding was captured. However, above the threshold value, d_e has an abrupt increase to around 5.3 µm, and it rises to a maximum of 23.9 µm at a $\Delta R/R_0$ of around 0.5.

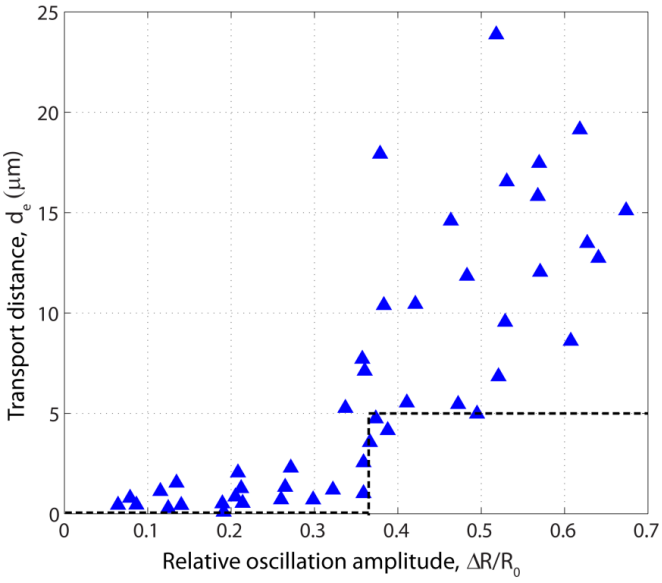

Figure 7.3. Plot of the d_e as a function of the relative amplitude of oscillations ($\Delta R/R_0$) for microbubbles insonified at 85 kPa to 255 kPa, with a pulse length of 100 cycles.

8.3.2 Dissolution & shedding

8.3.2.a Instantaneous dissolution

For each microbubble, we divide the dissolution process into two stages. The first stage is an instantaneous dissolution which was the bubble dissolution took place during and/or within very short time (1 ms) after ultrasound exposure. The relative size reduction ($\Delta R_i/R_0$) was derived to quantify this process. In figure 8.4, $\Delta R_i/R_0$ was plotted as a function of the relative amplitude of oscillations ($\Delta R/R_0$). The MSE estimator indicates a threshold value in $\Delta R/R_0$ of 0.34, very close to the observed threshold value of the shedding. A step function is shown in this plot: below the

threshold, very minor short shrinkage ($\Delta R_i/R_0 < 0.07$) can be observed; however, there is an abrupt increase of $\Delta R_i/R_0$ to 0.25 above this threshold value.

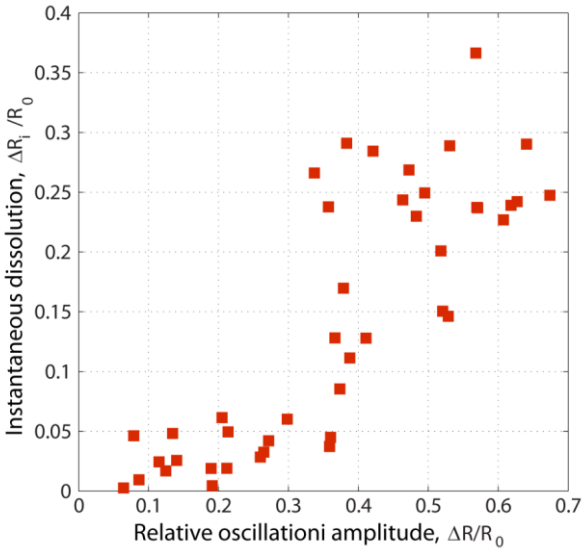

Figure 8.4. Plot of the relative rapid shrinkage as a function of the relative amplitude of oscillations ($\Delta R_i/R_0$) for microbubbles insonified at 85 to 255 kPa, with a pulse length of 100 cycles.

8.3.2.b Static dissolution

The second dissolution stage is a longer process that lasts for a duration of several hundreds of milliseconds. Figure 8.5 illustrates the radius-time (R-t) curves of 4 individual liposome-loaded microbubbles as an example. Microbubbles showed either no deflation (a, d) or a gradual size reduction (b, c). We found that with a similar initial radius (e.g., bubbles of 2.5 - 2.9 μm, close to the resonance size), higher pressures (e.g., 255 kPa in case b and 170 kPa in case c) are more probable to induce dissolution of the bubble than lower pressures (e.g., 85 kPa in case a). However, the initial bubble size seems also play a role: under the same acoustic setting, the bubble much larger than the resonance size (d) does not show any deflation, which is in contrast with the microbubble near resonance (c) (van der Meer et al. 2007).

The rate of static deflation (v_s) was quantified by the slope of the linear fit of the initial 100 ms of the R-t curve, and was plotted as a function of the relative amplitude of oscillations (Fig. 8.6a). Here a threshold value of 0.34 was derived by the MSE estimator. The dissolution rate increases dramatically above this threshold, up to 7.2 μm/s at maximum. For microbubbles showed a final stabilization at a certain size (Fig.

8.6b), the relative size reduction ($\Delta R_s/R_0$, where ΔR_s is the absolute difference between the initial radius and the radius measured 350 ms after the ultrasound application) was also investigated as a function of $\Delta R/R_0$ (Fig. 8.6b). Similar to figure 8.3, a step change can be found: $\Delta R_s/R_0$ is either very smaller (smaller than 0.7 for $\Delta R/R_0 \leq 0.34$) or large (larger than 0.5 for 75% of microbubbles at $\Delta R/R_0 > 0.34$).

We also noticed a strong correlation between the occurrence of dissolution and the occurrence of lipid shedding for all investigated microbubbles. We defined three parameters for each bubble based on the threshold of the events, the occurrence of shedding (0 or 1), the occurrence of instantaneous dissolution (0 or 1), and the occurrence of static dissolution (0 or 1) based on observations. The correlation between the occurrence of shedding and that of the instantaneous and the static dissolution was investigated. The result was that the correlation of instantaneous shrinkage and the shedding was 0.90, while the correlation between static dissolution and shedding was 1.00. An example is given in figure 8.5, where a bubble has no shedding behavior (a) is corresponding to a constant radius after ultrasound exposure, while the shed bubble has a gradual size reduction after insonification (c).

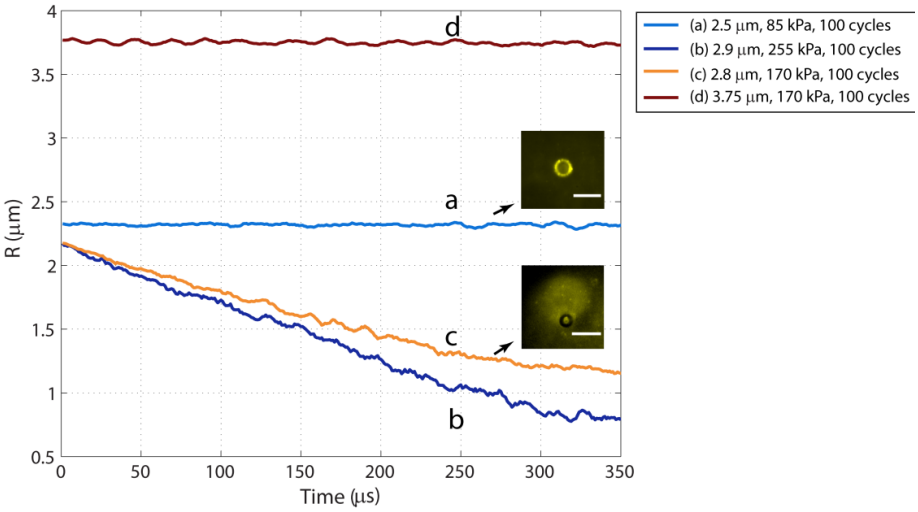

Figure 8.5. Radius as a function of time for 4 different microbubbles exposed to an ultrasound burst. Size bars represent 10 μm.

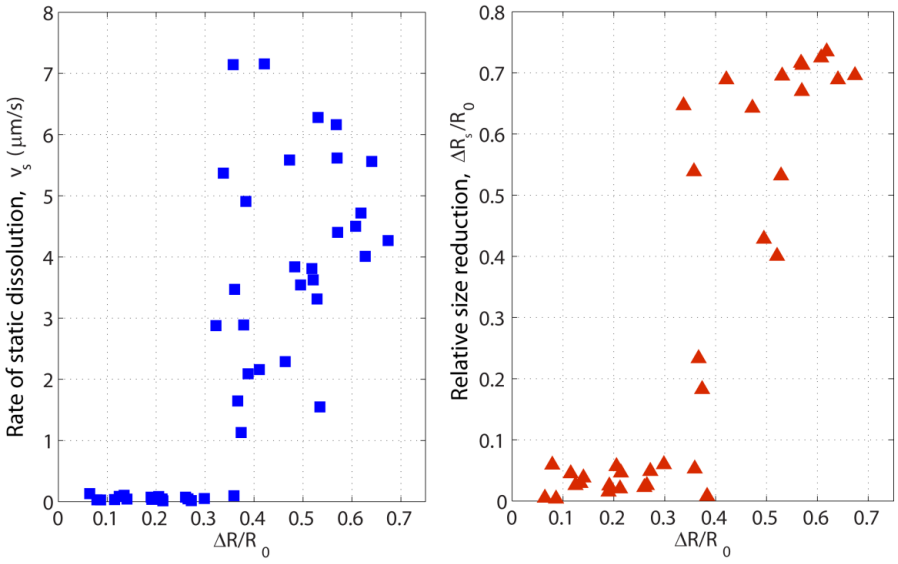

Figure 8.6. Rate of (a) static dissolution and (b) the relative size reduction of microbubbles as a function of relative amplitude of bubble oscillations ($\Delta R/R_0$). The ultrasound settings were 85 to 255 kPa in pressure, and the pulse length was 100 cycles.

We also compared the measured static dissolution rate with that was derived from the simulation for an unencapsulated air bubble and an unencapsulated C_4F_{10} bubble of the same size. Figure 8.7 illustrates the measured static dissolution of two exemplary single bubbles which are around 2.2 μm in radius after the instantaneous dissolution. Bubble 1 stabilizes at around 1.5 μm after 200 ms, while bubble 2 has a final radius of around 1 μm after 250 ms. For both bubbles the rate of static dissolution is much faster than the simulated static diffusion rate of a C_4F_{10} bubble (black curve), but is comparable to that of an air microbubble (red curve). For example, it takes around 120 milliseconds for bubble 1 to shrink to 1.5 μm. However, a same size reduction takes ~170 times longer (12 s) for an unencapsulated C_4F_{10} bubble of the same initial radius, while it takes the same time scale (70 ms) for the shrinkage of an unencapsulated air bubble. We investigated all 24 bubbles which showed a final stabilization: the rate of static dissolution is several tens to hundreds of times faster than that of a C_4F_{10} bubble but similar with (only 1-2 times slower) that of a free air bubble. The results suggest that a gas exchange may occur between the C_4F_{10} gas core and the surrounding medium, so an air bubble was remained after the shedding event and dissolved quickly. This phenomenon was described earlier for

individual sulfur hexafluoride (SF_6) microbubbles coated with a soluble surfactant placed into an air-saturated medium (Kwan and Borden 2010).

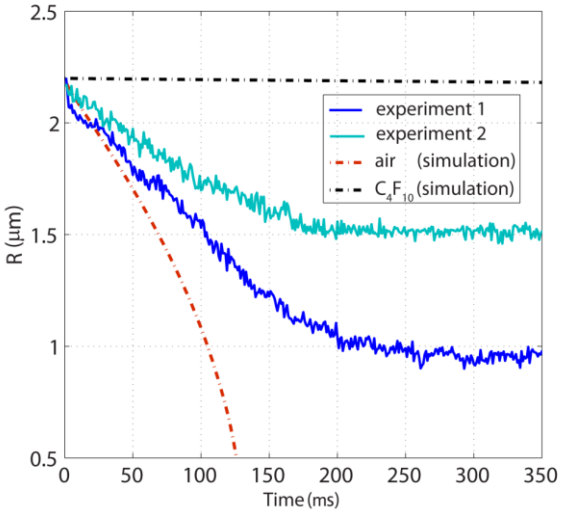

Figure 8.7. The measured static dissolution of two microbubbles after shedding and the simulated dissolution of an unshelled air bubble (red dashed curve) and an unshelled C_4F_{10} bubble (black dashed curve). Bubble 1 (dark blue curve) and bubble 2 (light blue curve) were applied with 150 kPa and 255 kPa in pressure and 100 cycles in pulse length, respectively.

8.4 DISCUSSION

8.4.1 Liposome detachment

Previously, lipid shedding from lipid-shelled microbubbles triggered by ultrasound excitations was monitored by high-speed fluorescence imaging (Gelderblom 2012; Luan et al. 2014). The process of lipid shedding was formulated as the expulsion of lipid shell material during bubble vibration. In this study, liposome particles that were attached to the lipid shell were fluorescently-labeled, and showed similar shedding behavior as compared to lipid-shelled microbubbles. First, the threshold of shedding for both varieties was comparable (~30% - 35%). Second, there is prominent bubble shrinkage after shedding, and the rate of dissolution is comparable to the static diffusion of a free air bubble. This suggests that there can be a prominent destruction of the lipid shell accompanied by the liposomes release.

Another issue to investigate is the content of the released material, i.e., if liposomes themselves can be disrupted and release the content encapsulated in the aqueous core under the prolonged pulse applied. It has been reported before that the liposome content leakage was found at acoustic pressures as high as 7 MPa with a short pulse (5

cycles) (Klibanov et al. 2010). Here we performed a pilot *in vitro* study by labeling the liposome aqueous core with doxorubicin (Dox-liposomes). The initial concentration of doxorubicin within the core of the liposome was high, such that fluorescent molecules quenched leading to a low image intensity. Upon rupture of the liposomes, free doxorubicin was released into the surrounding medium and the fluorescence intensity was enhanced. Three fluorescent images were recorded and compared. The first image was taken from the original sample, which was prepared by injecting a diluted Dox-liposomes solution (46.9 μg doxorubicin in 500 μL original solution) into the Opticell chamber. The second image was taken after the ultrasound treatment. The third sample was a control by adding 1% Triton X-100 to the original sample to dissolve all liposomes thereby release the doxorubicin. Figure 8.8 shows the histograms of the three images. The sample added with Triton shows a great enhancement (two times higher) of the image intensity compared to the original sample. However, insonation does not show an apparent increase of pixel intensity, indicating that either a minor amount of doxorubicin was ruptured or no content release had occurred.

Therefore we conclude here that in case of a liposome-loaded microbubble, phospholipids on the microbubble shell together with the attached liposome particles or liposome clusters could be piled out during the compression phase of the microbubble vibration, in a similar process as lipid shedding from encapsulated bubbles when ultrasound was applied. A schematic view of the release process is depicted in figure 8.9.

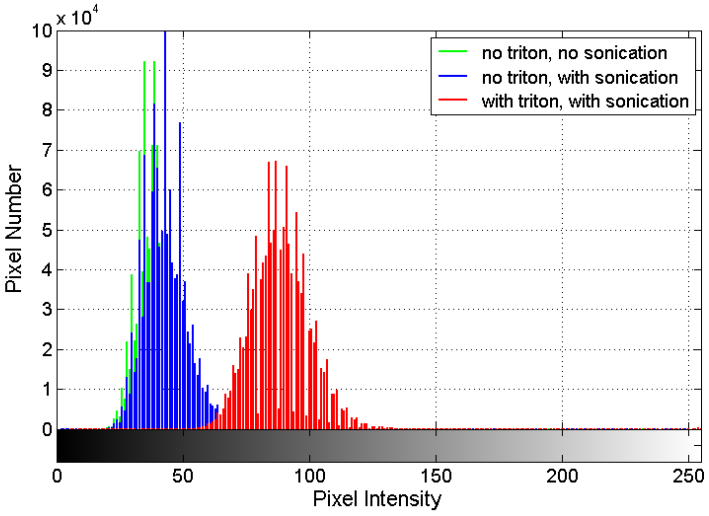

Figure 8.8. Image histogram of Doxorubicin loaded liposomes for the original sample, the insonified sample, and the sample added with triton.

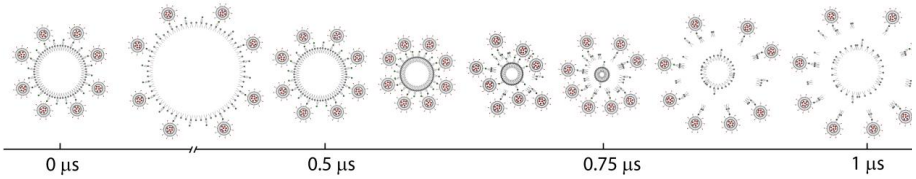

Figure 8.9. A schematic view of the speculated process of liposome release during one ultrasound cycle. The liposomes are expelled with lipid shell from the microbubble surface during the compression phase of bubble oscillations.

8.4.2 Fragmentation and shedding

We observed an instantaneous dissolution of ~25% of the intial bubble size on average at the relative oscillation amplitude above ~40%. The significant size decrease of microbubbles on the time scale of milliseconds after the ultrasound exposure indicates the occurrence of either fragmentation or acoustically driven diffusion of the bubble (Chomas et al. 2001). Considering the high correlation (0.9) between shedding and the instantaneous dissolution, we speculate that bubble fragmentation may be involved during the shedding of the shell material. Ultra-high-speed imaging by Brandaris camera covered only the first 10-12 cycles of bubble oscillations, which was therefore not sufficient to resolve fragmentation over a prolonged ultrasound excitation. However, by combining the fluorescence recordings and bright-field images after the shedding event, we were able to find several cases where fragmented bubbles distributed in a same way compared to that of the fluorescent vesicles/particles. Figure 8.10 shows 3 particular examples. In figure 8.10a, fragmentation initiated in the first few cycles of oscillations. After the insonation, a daughter bubble appears in the same focal plane next to the original bubble, and from the fluorescent recording we observe the distribution of a large amount of fluorescent shell material at the same location. This indicates that the daughter bubble may carry shell material with it, and it can maintain a stable size for even a longer time duration than the original bubble. Figure 8.10b shows an example of a dark 'imprint' on the left of the original microbubble, which was fragmented during the ultrasound exposure. The fluorescent image shows a fluorescent halo corresponding to the location of the imprint. We speculate here that during the insonation a daughter microbubble may be generated and been transported away from the focal plane by the local flow field. In figure 8.10c, a surface mode oscillation of the microbubble was captured, which was reported as a sign of bubble fragmentation (Versluis et al. 2010). Multiple bubble fragments and/or vesicles were distributed surrounding the microbubble, and as was expected, the distribution

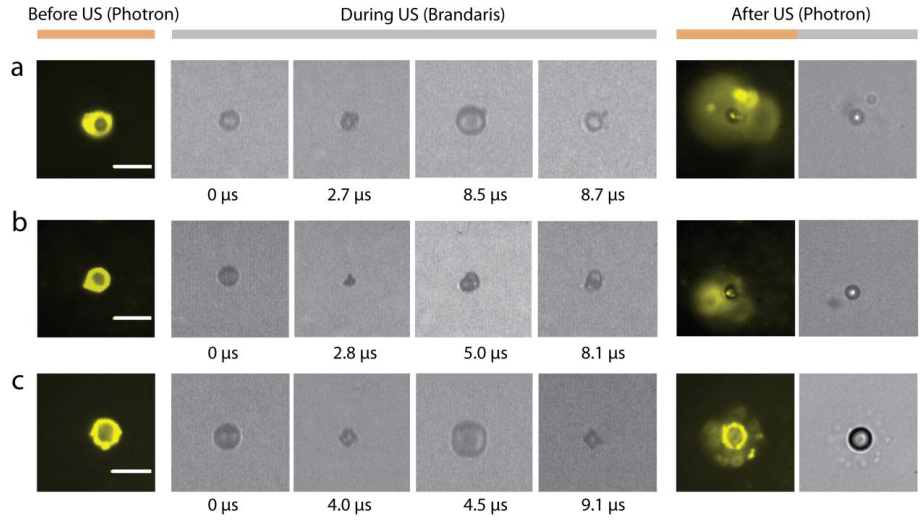

Figure 8.10. Three examples of different distribution patterns of shed shell materials. The Brandaris recordings during the ultrasound excitations indicate microbubble oscillation dynamics and/or fragmentations. The ultrasound settings for each case are: (a) 128 kPa, 100 cycles; (b) 170 kPa, 100 cycles and (c) 128 kPa, 100 cycles. Scale bars represent 10 µm.

pattern of daughter bubbles and/or vesicles showed to be similar with that of the shed materials displayed by the fluorescent recording.

For all investigated bubbles, we clarified four categories of phenomena which may be related to the fragmentation of bubbles during lipid shedding. The observation was obtained from the bubble oscillation dynamics during the ultrasound exposure (by the Brandaris camera), the fluorescent recording after insonification (by Photron camera), and the bright field image taken right after the insonification (also by Photron camera). The first category is shedding of shell material, without observable bubble fragments in the neighborhood afterwards. For this category, normally a halo appears surrounding the bubble in the fluorescent image, suggesting the occurrence of out-of-plane shedding reported in our previous work (Luan et al. 2014). Here either no fragmentation occurred, or the fragments were transported away perpendicularly. As illustrated in figure 8.11, 30% of the investigated bubbles belong to this category. Both the second and the third category have observable shedding events, and the bubble was fragmented during the first 10 cycles of ultrasound exposure. For the second category, one or multiple black imprints appear after the shedding event (Fig. 8.10b), suggesting that out-of-plane shedding of fluorescent shell materials together with daughter bubble fragments may occur. However, for the third category, daughter bubble fragments and/or lipid vesicles were captured in the same focal plane (Fig.

8.10c). This may be corresponding to the in-plane shedding observed for lipid-shelled microbubbles (Gelderblom 2012; Luan et al. 2014). It should be noted that the occurrence of the second category (31%) is much larger than the third category (6%) - As was found previously; out-of-plane shedding dominates the shedding behavior. The rest of bubbles (34%) do not show a shedding behavior and fall in category 4.

The pinch off of daughter bubble fragments together with lipid shell materials and the subsequent transport out of the focal plane by the surrounding streaming field will be demonstrated by the side-view observations in Chapter 7.

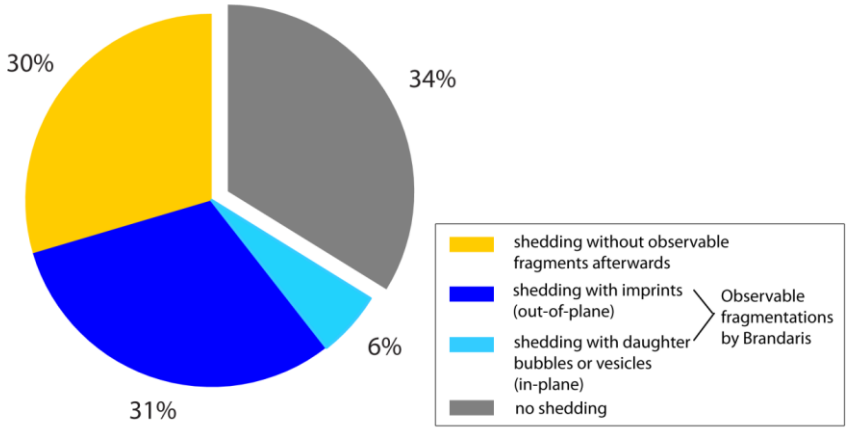

Figure 8.11. The percentage of different observed phenomena captured by the bright field recording (shedding or no observable shedding) combined with fluorescence recording (fragmentation or no observable fragmentation).

8.4.3 Shedding and static dissolution

Subsequent to the instantaneous dissolution, we captured a longer static dissolution occurring on the order of hundreds of milliseconds. The correlation between the occurrence of lipid shedding and that of the static dissolution was 1.00. Additionally, the threshold (~35% of relative oscillation amplitude) of lipid shedding and that of the static dissolution was the same. These phenomena indicate that the static dissolution can be due to the loss of the lipids from the shell together with attached liposomes. This speculation is in agreement with previous studies that destruction of the lipid shell can lead to bubble shrinkage, and the bubble surface reduction is closely related with the amplitude of oscillations (Dayton et al. 1999; Borden et al. 2005; Thomas et al. 2012).

The rate of dissolution varied from individual bubbles (on the order of 1-10 μm/s), all of which were on the similar scale (only slightly slower) with the rate of natural

dissolution of an unencapsulated air microbubble predicted by simulation (Dayton et al. 1999). A majority of bubbles showed a linear diffusion profile, which was observed previously for single SF_6 microbubbles after gas exchange in an air-saturated medium (Kwan et al. 2010). Here we hypothesize that the bubbles may experience a fast gas exchange (with air in the PBS buffer used for dilution) during the expansion and compression phases under ultrasound exposure. Additionally, a final stabilization at around 0.5-1.5 μm after a size reduction of up to 70% in radius was found for nearly all microbubbles. The stabilization was explained by previous studies as the presence of condensed lipid molecules where the shell became "jammed" and increasingly rigid at smaller diameters. Therefore the density (amount) of lipid molecules again proves to be a key factor to decrease the surface tension, to resist gas permeation into the surrounding medium and thus stabilize the bubble (Chomas et al. 2001; Borden et al. 2002; O'Brien et al. 2011).

However, here we cannot validate the hypothesis on either the bubble dissolution due to the shell destruction or the stabilization due to the remained shell materials. Since we cannot quantitatively measure the mass of the shed (or remaining) lipid shell materials. The reasons include the following factors which can greatly influence the intensity profile of the fluorescent image: 1) the transportation trajectory of the shell materials which is perpendicular to the focal plane; 2) the focusing of the image; 3) the quenching of the highly-dense fluorophore (DiI molecules) on the bubble shell; 4) photobleaching of the fluorophore by the laser illumination. If the rate of long bubble dissolution is proportional to the loss of shell materials, as was claimed by previous studies (Borden et al. 2005; Thomas et al. 2012), then the release of liposomes can indeed be quantified based on the mapping displayed by figure 8.6b. Above the shedding threshold, the relative bubble size reduction is comparable, and the amount of liposome release would be only dependent on the initial bubble size.

8.4.4 Clinical implication

This *in vitro* study provides direct implications for combined therapeutic and imaging applications of liposome-loaded microbubbles. Above the threshold of the bubble oscillations, liposomes can be released together with lipid shell material. Therefore, using mono dispersed bubble populations close to resonance would be most preferable strategy to achieve efficient drug delivery. However, upon the destruction of the lipid shell after prolonged excitation, bubbles would rapidly shrink (within hundreds of milliseconds) with a size reduction of up to 70%. This means that either different acoustic parameters, e.g., a higher frequency, should be applied after insonification, or initially bubbles of different sizes should be applied since only bubbles much smaller or much larger than the resonant size in a population would contribute to the contrast-agents detection signals (Guidi et al. 2010).

8.5 CONCLUSIONS

In this study we investigated the process of liposome release from single microbubbles and related physical phenomena, e.g., the bubbles vibrational dynamics, the subsequent bubble dissolution. Comparing to lipid-shelled microbubbles, the loading of liposomes did not affect the shedding behavior: a very similar threshold of oscillation amplitude (~35%) can initiate the shedding of liposomes with lipids and possibly with daughter bubble fragments. In the meantime, a fast dissolution of up to 30% occurred which may be related with bubble fragmentations. It was followed by a gradual bubble dissolution for hundreds of milliseconds until a final stabilization was reached. The same threshold values for dissolution with shedding and the close correlations between them suggest that the amount of liposomes release may be estimated directly from the subsequent dissolution rate.

9

The mechanism for lipid shedding from microbubbles near a boundary lies in their non-spherical oscillations

Abstract — There has been growing interests nowadays in gaining knowledge regarding the mechanical release of shell materials from lipid-coated microbubbles for the application of drug delivery. Previous studies on the microbubble shedding behavior based on top view observations have revealed qualitatively the dynamics of lipid shedding and the subsequent transport of the detached lipids by the acoustic streaming. These studies however assumed a spherical bubble behavior which has been shown not to hold at relatively high pressures ($\geq$ 100 kPa). An in-depth understanding of lipid shedding was inhibited by the limited vision.In this study, the side view ultra-high-speed and high speed fluorescence imaging technique was applied to reveal the details of non-spherical bubble oscillations relative to the detachment and transport of the phospholipids initially coating the microbubble. Three regimes of shedding dynamics (mechanisms) were illustrated: lipid oversaturation, pinch off of daughter bubble fragments, and jetting. First, a model developed on the base of the Rayleigh Plesset equation is established that demonstrates how the lipids locally oversaturate in the region of the bubble in contact with a rigid supporting membrane. The theoretical quantification agrees well with the experimental observations. Second, we experimentally observed the generation of bubble fragments leading to immediate bubble shrinkage, which cannot be a quantification parameter for the shedding as previously proposed. Third, the bubble jetting deposited the material on the supporting membrane. From a clinical perspective, this regime can facilitate the transport of therapeutic agents towards the targeted cells instead of into the blood stream, opening promising possibilities for pushing further the current limitations of drug delivery with microbubbles.

In preparation for submission; by G.P.R. Lajoinie, Y. Luan, E.C. Gelderblom, B. Dollet, I. Lentacker, H. Dewitte, N. de Jong, M.Versluis. The authors acknowledge Philippe Marmottant for sharing his knowledge and expertise on the streaming surrounding a microbubble floating against a membrane that allowed for understanding and calculating the transportation of the detached shell material.

9.1 INTRODUCTION

Microbubbles have been utilized as ultrasound contrast agents for a few decades now (Stride and Saffari 2003). The application of microbubbles for therapy, however, is still at an early stage of development (Unger et al. 2002). The formulations for microbubble-based contrast agents have been constantly improved to allow longer circulation times through the vascular system, making visible even the smallest of vessels. The air core was replaced by a less diffusible gas core (usually a perfluorocarbon gas), which was encapsulated by a coating material (e.g., phospholipids, surfactants or polymer) to stabilize the bubble (Cosgrove 2006). In parallel, targeted contrast agents were developed by embedding in the coating a specific ligand that adhere to the disease-specific markers expressed by the cell membranes (e.g., aminoacids) (Klibanov 2007). The progress in ultrasound contrast opens new possibilities for therapeutic applications such as thrombolysis, gene therapy and drug delivery (Lindner and Kaul 2001; Cohen et al. 2003; Lentacker et al. 2007; Medel et al. 2009). A promising approach in order to apply microbubbles to drug delivery consists in incorporating genes or drug molecules into the microbubble shell (Vandenbroucke et al. 2008; Geers et al. 2010). At high acoustic pressures (> 200 kPa), microbubbles can respond to the ultrasound exposure by releasing the drugs loaded on the microbubble surface either directly via mechanical effects, or indirectly, via thermal effects (e.g., for temperature-sensitive liposomes) into the target tissue (Hauck et al. 2006; Klibanov et al. 2010).

For the success of future drug delivery applications with microbubbles, it is essential to understand the process of the drug release in response to the ultrasound exposure. There has been growing interests in gaining knowledge regarding the mechanical release of shell materials from lipid-coated microbubbles (Borden et al. 2005; Gelderblom 2012; Luan et al. 2014). Lipid shedding and the accompanying microbubble dissolution were observed by Borden et al. (2005) for microbubbles exposed to a series of single-cycle pulses with the peak negative pressure ranging from 400 to 800 kPa. They proposed that the surface area reduction caused by gas diffusion from the microbubble leads to the expulsion of excessive shell materials. Later, Kwan et al. (2012) have specifically investigated the process of lipid monolayer collapse. They concluded that this is a cyclic nucleation and aggregation of folding events, which can be a major stabilizing mechanism for lipid-coated microbubbles. In another study performed by Gelderblom et al. (2012), lipid shell materials were labeled with a fluorescent probe, and a continuous wave laser was applied so that sufficient optical contrast could be achieved to resolve the small particles (several to hundreds of nanometers). The dynamics of lipid shedding and the subsequent transport of the detached lipid shell materials were monitored using high-speed

fluorescence imaging at a frame rate of 100,000 frames per second (fps). Using this technique, Luan et al. (2014) further investigated lipid shedding in relation with the microbubble oscillation dynamics recorded using ultra-high-speed imaging at 10 million fps. This study also allowed for the extraction of the activation thresholds for lipid shedding, while the transport process was quantified indirectly by measuring the size of the fluorescent halo emitted by the shell material.

In all these works, the microbubble shedding behavior was experimentally observed using top view microscopy. Any subsequent analysis or modeling assumes a spherical bubble behavior which has been shown not to hold at the high pressures (≥ 100 kPa) (Vos et al. 2008) required to obtain shedding from a microbubble (Luan et al. 2014). Moreover, the presence of a neighboring boundary, a situation that applies both to in-vitro and in-vivo clinical conditions, strongly influences the appearance of diverse non-spherical behaviors as well as the microstreaming patterns generated in the surrounding medium (Elder 1959; Ooi et al. 2007). The shedding mechanism therefore remains a delicate issue that did not meet with any generally accepted description or modeling, although it is crucial to be utilized for diagnosis and therapy.

In the present paper, we study the shedding from oscillating microbubbles from a completely new perspective. The side view ultra-high-speed and high-speed fluorescence imaging was combined to reveal the details of the non-spherical bubble oscillations that lead to the detachment and transport of the phospholipids initially coating the microbubble. The pressures above the threshold for shedding and below the threshold for inertial cavitation (from 166 to 414 kPa) were applied. A model developed on the base of the Rayleigh Plesset equation is established that demonstrates how the lipids locally oversaturate in the region of the bubble in contact with the Opticell membrane, where they subsequently detach. We explain for the first time, theoretically and experimentally, the mechanisms behind the shedding phenomenon. The implications of different shedding dynamics (mechanisms) for the application of drug delivery were discussed.

9.2 MATERIALS AND METHODS

9.2.1 Bubble preparation

Biotinylated microbubbles (Klibanov et al. 2004) were prepared by sonication. The coating was composed of 1,2-distearoyl-sn-glycero-3-phosphocholine (59.4 mol %; Sigma-Aldrich, Zwijndrecht, the Netherlands), polyoxyethylene-40 stearate (357 mol%; Sigma-Aldrich),1,2-distearoyl-sn-glycero-3-phosphothanolamine-N-methoxy(polythyleneglycol)-2000 (DSPE-PEG) (4.1% mol; Avanti polar lipids, Alabaster, AL, USA) and DSPE-PEG(2000)-biotin (0.8 mol%; Avanti Polar Lipids). For fluorescence labeling of the microbubble membrane, the lipophilic dye 1,1′-

dioctadecyl-3,3,3′3′-tetramethylindocarbocyanine perchlorate (DiI) (Molecular Probes, Eugene, OR, USA) was dissolved in ethanol and added to the solution before sonication.

9.2.2 Sample preparation

For the sample holder, the topside of an OptiCell (Thermo Fisher Scientific, Waltham, MA, USA), a 75-µm thick polystyrene membrane, was served as a target surface. 24 hours before the experiment, the membrane was coated with NeutrAvidin (Life Technologies Europe, Bleiswijk, The Netherlands) by adding 1 mL of 1 µg/mL solution of NeutrAvidin in phosphate-buffered saline (PBS) (Life Technologies Europe). The OptiCell membrane was incubated overnight at room temperature in a humidity chamber. Right before the experiment, the surface was rinsed with PBS to remove all the unbound protein and incubated for 1 h with 1% bovine serum albumin (BSA) (Sigma-Aldrich) to prevent unspecific binding. Afterwards, the surface was cut into rectangular pieces of 5 mm x 20 mm. Before using each piece, it was rinsed again with PBS, then mounted with the coated side down in a tank filled with PBS. Biotinylated microbubbles were injected into the tank and allowed to interact with the coated surface by flotation for 5 minutes. In the end, the surface was carefully rinsed with PBS to remove all unbounded microbubbles.

9.2.3 Experimental setup

The experimental setup is shown in figure 9.1a. The bound microbubbles were immersed in a water bath ($T \approx 22°C$) at a 45° angle relative to the vertical axis and could be independently positioned with a 3-D micropositioning stage. A focused, single-element transducer (C302, Panametrics, Waltham, MA, USA) with a center frequency of 1 MHz was fixed on one side of the water tank and was used to insonify the microbubbles. In such configuration, the effect of buoyancy is kept similar to previously performed experiments. Moreover the buoyancy, significant on millisecond timescales is negligible on the microsecond timescale of the oscillations. For each recording, a single microbubble attached to the Opticell membrane was exposed to a single ultrasound burst with a pulse length of 100 cycles with an acoustic pressure of 166, 249, 332 or 414 kPa. The acoustic pressures were measured before the experiment in a separate setup with a calibrated needle hydrophone (0.2 mm, Precision Acoustics, Dorchester, UK). A total of 106 single microbubbles were investigated in this experiment. The bubbles selected one by one before each US exposure are chosen around the expected resonant size. Moreover, a relevant number of bubbles out of resonance are insonified to cover the range of available bubble sizes.

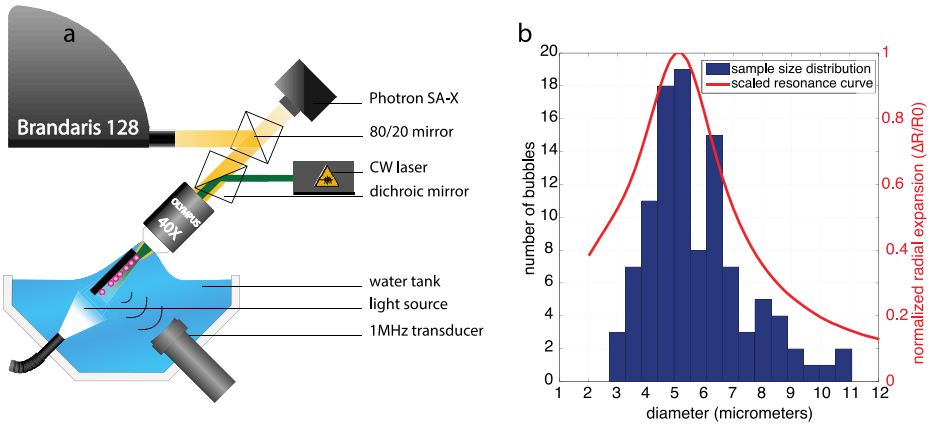

Figure 9.1. Experimental setup. (a). Side view setup used to insonify and study the fluorescently-labeled microbubbles. The microscope and the sample are rotated at 45° angle, leading to a side view observation. The high speed observations are recorded simultaneously by the Photron SA-X and the Brandaris 128 cameras. (b) Size distribution of the investigated individual bubbles and normalized simulated (5kPa) resonance curve of the bubbles.

The optical recordings were realized using a fluorescence microscope equipped with a 40× water-immersion objective (LUMPFL etc numerical aperture [NA] = 0.8; Olympus, Zoeterwoude, The Netherlands). The microscope was fixed at a 45° angle relative to the vertical direction in order to observe the targeted microbubbles from the side. A continuous wave laser (5W , λ = 532 nm; Cohlibri, Lightline, Osnabrück, Germany) was focused onto the sample through the same microscope to excite the fluorescence labeling. The laser light was gated using an acousto-optic modulator (AOTF.nC-VIS, AA Optoelectronic, Orsay, France) to generate a single pulse with a duration of 500 µs. Simultaneously, a bright-field illumination was used (KL2500LED, Schott, Mainz, Germany) superimposed with the fluorescence recording. High-speed recordings were acquired with a CMOS-based high-speed camera (SA-X, Photron, West Wycombe, UK), operating at 5,000 frames per second (fps). Ultra-high-speed imaging was performed with the Brandaris 128 camera (Chin et al. 2003; Gelderblom et al. 2012) at a frame rate 3 order of magnitude faster at 5 million fps. In order to compare the rapid non-spherical oscillations of the microbubble with the shedding of the fluorescent material captured immediately after the ultrasound exposure both recording were combined. The combination was enabled through the splitting of the optical beam in two pathways by an 80%/20% beam splitter. 80% of light was directed into the Brandaris camera, while the 20% light path was directed toward the Photron camera. Figure 9.1b shows the size distribution of the bubbles studied. The resonance curve shown in the same figure is computed using the model described in the following section for a pressure of 5 kPa and shows that most of the bubbles

studied were in the resonance size range (3-4 μm) (van der Meer et al. 2007). To confirm the validity of the current settings, before the experiment, a test study was performed for 12 targeted microbubbles by rotating the membrane to a top-view configuration. Then identical shedding phenomena was captured compared with the previous experiment – lipid shedding and subsequent transport was appeared as the spread of a fluorescence halo around the microbubble.

9.2.4 Modeling

9.2.4.a 2D modeling of non-spherical microbubble oscillations

The ultra-high speed imaging of the microbubble oscillations shows that the displacement of the Opticell membrane during the ultrasound exposure is not significant as compared to the change in the microbubble radius that is typically of several micrometers. The maximal expected displacement of the membrane can be estimated using the no-slip boundary condition. For the studied range of pressures this displacement is:

$$d = \frac{p}{2\pi f Z} \approx 40nm \tag{9.1}$$

which is negligible as compared to the observed bubble oscillations that are typically in the order of the micrometer. Here Z is the acoustic impedance of water and p the acoustic pressure. Thus the membrane can be considered as fixed as a presumption of the numerical model described in the following. To predict the microbubble dynamics attached to a wall as observed from the side view, we build up a 2D model based on a spherical coordinate system. The center of the contact area of the bubble attached to the membrane is taken as the origin. We consider in first approximation the velocity potential as radial in this coordinate system (the justification of the approximation can be found in the discussions), which allows for rewriting the Rayleigh-Plesset equation in 2 dimensions:

$$\rho\left(\ddot{R}(\theta,t)R(\theta,t) + \frac{3}{2}\dot{R}(\theta,t)^2\right) = P_i - P_e \tag{9.2}$$

with

$$\mathrm{P_i} = -4\alpha\frac{\mathrm{v\dot{R}(\theta,t)}}{\mathrm{R(\theta,t)}} - \Delta\mathrm{P} + \mathrm{P_0}\left(\frac{\mathrm{V}}{\mathrm{V_0}}\right)^{\gamma} \tag{9.3}$$

and

$$\mathrm{P_e} = \mathrm{P_0} + \mathrm{P_A} \tag{9.4}$$

Each bubble is discretized and is divided into angular sectors. $R = R(\theta, t)$ is the length of the segment that links the surface of the bubble with the origin of the referential at the angle θ and corresponds to the length of the angular sector (see Fig

9.12); ρ is the density of water, and P_i and P_e are the pressures respectively inside and outside the bubble. ν is the viscosity of water to which a coefficient α≈8 is applied in order to account for the realistic total damping of the bubble, including the thermal damping in accordance with previous studies (de Jong et al. 1992; Hoff et al. 2000; Lajoinie et al. 2014); P_0 is the ambient pressure, P_A is the applied ultrasound pressure, V_0 is the initial bubble volume and V is the time-dependent bubble volume. γ is the polytropic exponent of the gas. ΔP is the local pressure drop across the interface. The Young-Laplace equation is used to generalize this pressure drop due to the surface tension (Batchelor 1968):

$$\Delta P = \sigma_w \left(\frac{1}{R_c} + \frac{1}{r_{loc}}\right) \tag{9.5}$$

where , σ_w is the surface tension of water, R_c is the radius of curvature in the axisymmetric direction and r_{loc} is the local curvature on the bubble surface in the observation plane and is calculated from the equation of a circle passing by the point of interest as well as its two closest neighbors. This curvature is determined from the average radius of the bubble and practically calculated from the bubble volume so that:

$$R_c = \left(\frac{3V}{4\pi}\right)^{1/3} \tag{9.6}$$

In general, each of the divided angular sectors of the microbubble obeys the previous relation and all of them are coupled through the volume of gas that in turn determines the internal gas pressure. The set of differential equations – one equation per angular sector – is then solved using the ODE45 solver of Matlab. The pressure inside the bubble is calculated at each timestep from the volume and the volume is calculated by summation of the individual sectors volumes. The bubbles display a pinning behavior that is attributed to the targeting and this contact line boundary condition was implemented in the model. Experimentally the length of this contact line appears to be a fourth to a third of the bubble radius and can get smaller (≈ 1/5) for bubble of 2 μm or less in radius. Practically, the length of the contact area induces minor changes on the bubble oscillations (i.e., size of the neck), but does not change any of the conclusions presented here.

9.2.5 Microbubble resonance behavior

For the side view experiment, we found diversified bubble behaviors at the applied pressures that are above the threshold required for the lipid shedding (166, 249, 332 and 414 kPa). In general, microbubbles display a highly non-spherical behavior, including bubble fragmentation, pinch-off of submicron bubbles, and jetting. The relative radial expansion of the individual microbubbles irradiated by an ultrasound

burst at various pressures is shown in figure 9.2a. It displays an important spreading of data points and a large deviation from the characteristic predictable responses. The data was fitted with the damped bubble oscillation equation (Leighton 1994):

$$\frac{Rpos}{R_0} = \frac{1}{\rho(R_0)^2} \frac{1}{\left(\left(\left(\frac{a}{R_0}\right)^2 - (2\pi f)^2\right)^2 + (2\pi\delta f)^2\right)^{1/2}} \tag{9.7}$$

The total damping coefficient δ and the eigenfrequency of the system $\omega_0 = \frac{a}{R_0}$ were left as free parameters for the fit. ρ is the density of water; R_0 is the initial bubble radius, f is the applied frequency and a is a fitting parameter. Figure 9.2a clearly shows the trend of the bubble to oscillate with higher amplitude at higher pressures. Here the relative amplitude of the bubble expansion was chosen as the relevant parameter as under high pressures, bubbles are highly compressed and can therefore not be accurately measured during the compression phase (Viti et al. 2012).

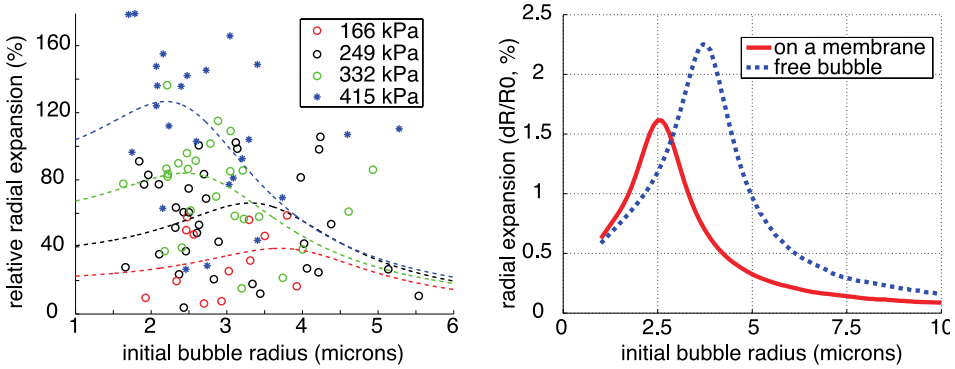

Figure 9.2. (a) Spread responses of 106 individual microbubbles studied. The responses are fitted for each excitation pressure with the response curve of a microbubble with the attenuation and the eigen frequency as free parameters. (b) Response curves of bubbles vibrating in free field and bubbles vibrating on a membrane for a pressure of 5kPa simulated by the model developed in the study.

Figure 9.2b shows the resonance curves of a free microbubble (ranging from 1.2 µm to 10 µm in radius) and that of a bubble floating against a membrane. The simulation was performed by the 2D model (equation 1) presented in the last section for an applied pressure of 5 kPa – linear regime. This shift of the resonance peak is in agreement with previously reported observations and is the first known influence of the proximity of the membrane on the oscillation dynamics of microbubbles (Garbin et al. 2007; Overvelde et al. 2010). This provides additional confirmation of the simulation performed based on the new model.

9.3 RESULTS

9.3.1 Non-spherical oscillations

9.3.1.a Large oscillations

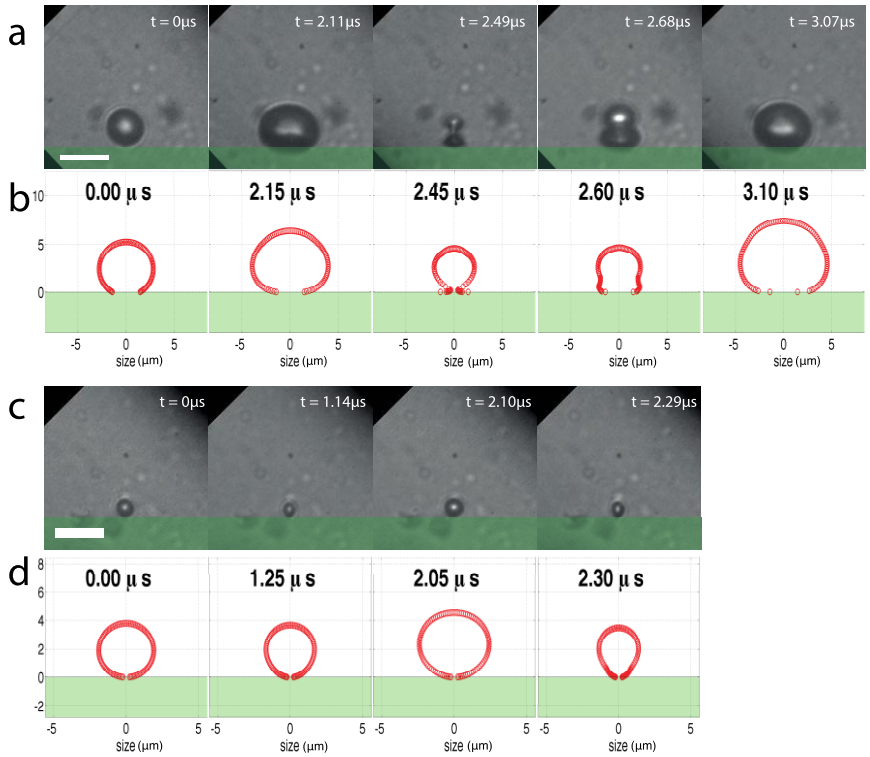

Figure 9.3. Non-spherical bubble dynamics. a.c. respectively 3.8 and 1.9 µm radii microbubbles insonified with a 1 MHz 100 cycles 166 kPa ultrasound burst. The green rectangle represents the Opticell membrane and the scale bar represents 10 µm (b,d) Corresponding numerical simulations with the same sizes and pressures that show a good agreement with the experiments.

Figure 9.3a,b demonstrates the highly non-spherical bubble oscillations. The bubble appears to collapse first on the sides, which is then followed by the collapse of the upper part. It is clear from the optical recordings that the part of the bubble in contact with the Opticell membrane collapses further than the upper part ($\theta \approx \pi/2$). This behavior is incompatible with a spherical assumption for the bubble oscillations as suggested by the top-view observations. Depending on the bubble size, this collapse will result in the appearance of a neck (Fig. 9.3a,b) for bigger bubbles with a larger pinning area or a spear on the bottom of the bubble for smaller microbubbles (Fig. 9.3c,d). This phenomenon was previously observed by Vos et al. (2008) for a non-

targeted bubble floating against an OptiCell wall. The simulation of a non-targeted (or non-pinned) bubble based on our model always result in the formation of a spear as shown in Figure 9.5.cd. The simulation results performed under the same physical conditions as the experiment (Fig. 9.3.b,d) show a very good agreement with the experiment. It should be noted that the modeling of the vibrations as described above results in a phase difference in the motion between each calculation point on the bubble surface. The initial radius increases with increasing θ leading to an increasing phase difference. Therefore the phase difference is mostly a consequence of the initial conditions.

9.3.1.b Surface modes oscillations

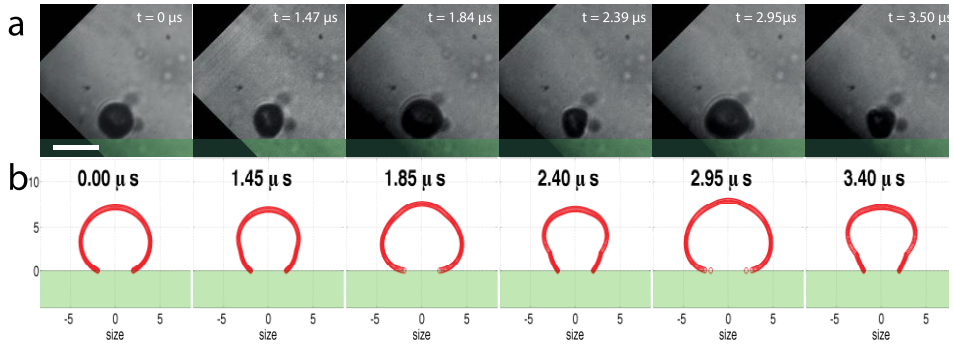

Figure 9.4. Shape oscillations in a microbubble. a. a 3.8 µm radius microbubble insonified with a burst of 1 MHz, 100 cycles at 166 kPa displaying shape oscillations. The scale bar represents 10 µm. (b) Corresponding simulation where the variable surface tension term introduced by the presence of a phospholipid shell was included.

In a few cases (less than 5%), small vibration amplitudes were observed and the energy was instead dissipated through surface oscillations as shown in figure 9.4a. (Dollet et al. 2008; Versluis et al. 2010; Vos et al. 2011). Similar to the examples illustrated by figure 9.3, the shape vibration can be accurately predicted by the model. For this simulation, the model used in the previous section was modified to include the influence of the shell that is otherwise not taken into considerations due to the high pressures applied (Overvelde et al. 2010), here we incorporated a surface tension term into the model as described by Marmottant et al. (2005). The addition of an extra shell viscosity term on the other hand did not show a strong influence. The reason is that we found almost no shedding of fluorescent materials from the microbubble for all cases. This behavior is of lower interest for the drug delivery applications and therefore is not the focus of our investigations here.

9.3.2 The shedding

High-speed fluorescence recording reveals the shedding behavior of microbubbles. For a majority of cases, the shedding of the coating material along the axis of symmetry of the bubble was observed (Fig. 9.7d). This shedding is often coupled to the expulsion of smaller bubbles (Fig. 9.6a and Fig. 9.8a) taking away a significant amount of fluorescent material that we later qualify as pinch-off. Another clearly different type of shedding behavior involves the jetting of a microbubble. This shedding behavior results in the deposition of the fluorescent material on the membrane supporting the bubble. In the following sections, we will present our proposed shedding mechanisms based on the experimental observations and the simulation.

9.3.2.a Lipids oversaturation

The most commonly considered mechanism for detachment of the shell material from the surface of a microbubble involves the oversaturation of the lipid layer during the compression phase as it is the most straightforward and intuitive. It is however mostly explained in terms of spherical oscillations (Borden et al. 2005; O'Brien et al. 2011; Kwan et al. 2012), which may not apply for a bubble floating against a surface at pressures of above 100 kPa (Vos et al. 2011).

In the free field, the fully symmetrical collapse of a bubble is prevented by a rapid increase of pressure and temperature in the gas core. Both the side-view observations and the 2D modeling for a bubble near a boundary show a phase difference along the surface of the bubble causing the lower part of the bubble to retract first. The reduction of the radius at small θ angle does not lead to a significant increase of pressure within the gas core, as the volume of the bubble remains significant due to the phase lag of the higher part of the bubble. One can then expect that, above a given pressure, nothing prevents the lower part of the bubble from fully collapsing represented by the appearance of a spear at the bottom of the microbubble (Fig. 9.3c,d. and 9.5b,d). This can lead to a local oversaturation of phospholipids close to the membrane where they will ultimately detach and be transported away by the local flow field.

Figure 9.5 shows simulated lipid shell collapse for a pinned (targeted) (a,b) microbubble and a non-pinned bubble (c,d). The overall shape of the bubble observed in experiment is well reproduced. The shell material concentration represented by the red markers is increased over time beyond local stability in the collapsing region at the bottom of the bubble. The detachment of the coating material is expected to occur just before reaching these extreme concentrations, at this location. In contrast, the

shape oscillations as was illustrated by figure 9.4 do not present these high concentration areas and therefore do not shed any fluorescent material.

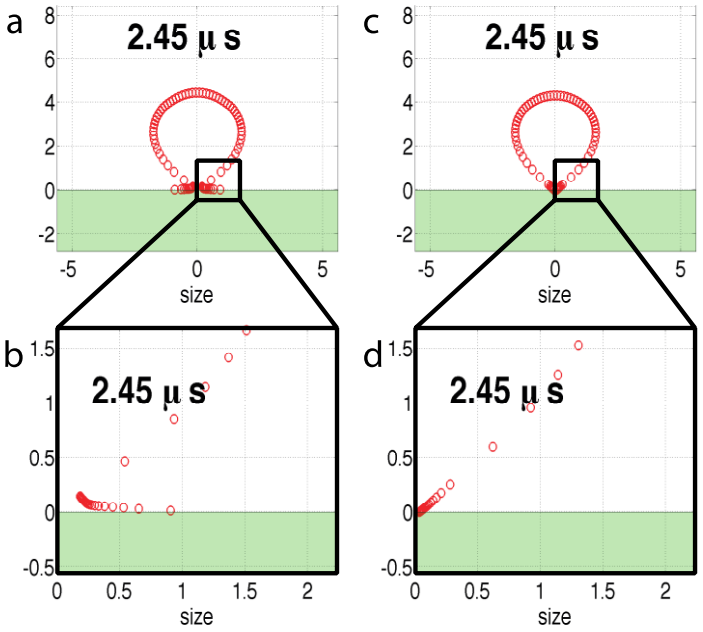

Figure 9.5. Shedding by oversaturation of phospholipids. (a,b) Collapse of a pinned bubble floating against an Opticell. (c,d) Collapse of an unpinned bubble against a membrane. In both cases the concentration of phospholipids in the proximity of the membrane is very high as compared to the rest of the bubble, initiating their detachment from the interface.

9.3.2.b Pinch-off

The shedding behavior as presented in the previous paragraph is often accompanied by the pinch-off of one or two submicron daughter bubbles from the top of the original microbubble. These events appeared hardly predictable and reproducible. The secondary daughter bubbles nonetheless appear to carry some shell material with them away from the membrane (Chomas et al. 2001). Figure 9.6a shows the detachment of two pinched-off bubbles in two consecutive ultrasound cycles and figure 9.6d. shows the collapse of the same bubble where a gas ligament is formed before the appearance of a sub-micron bubble. The formation of the gas ligament just before the pinch-off events suggests that the pinch-off actually originates from the break-up of this unstable ligament. Thus the apparently high concentration of shell material around those daughter bubbles can be explained in two ways: first the ligament is being formed during the collapse of the bubble, when the phospholipid

concentration on the microbubble surface is the highest, thus creating a dense coating on the daughter bubble. Secondly, it is possible that the daughter bubble collects the fluorescent material that detaches from the bottom of the bubble where the spear forms and is transported along the same path.

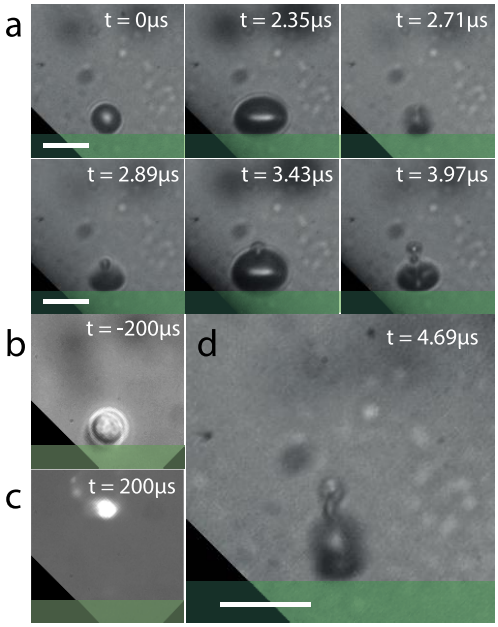

Figure 9.6. Pinch-off (a) example of pinch off of a submicron bubble from the top of the oscillating bubble in two successive ultrasound cycles. (b,c) Location of the fluorescent material before and after ultrasound exposure recorded with the photron camera. (d) Image of the collapse of the bubble taken with a 200 ns shutter time showing the gas ligament that will form a secondary bubble.

A direct implication of this pinch-off is the immediate size reduction of the microbubbles that is measured just after the ultrasound burst as was suggested by other studies (Thomas et al. 2012; Cox and Thomas 2013) and our earlier investigations (Chapter 8) We observed up to 30% of instantaneous shrinkage of microbubbles during the ultrasound exposure. Moreover, the pinch-off of submicron bubbles deteriorates the reproducibility of the lipid shedding behavior both by interfering with the detached phospholipids (e.g., the amount and the location) over the duration of the ultrasound exposure and by modifying the properties of the microbubble (e.g., the size and the shell properties).

9.3.2.c Jetting

Figure 9.7a,b,c. depict another lipid shedding mechanism. It shows the formation of a jet from the top of the microbubble towards the membrane, as was also reported earlier by top-view observations (Benjamin and Ellis 1966; Ohl et al. 2006). During the jetting, the fluorescent coating is transported from the top part of the bubble through the gas core and deposited on the supporting membrane. This is yet another type of shedding originating from a completely different physical mechanism as compared to the two phenomena presented in previous sections. Here the phospholipids saturation may not play a significant role.

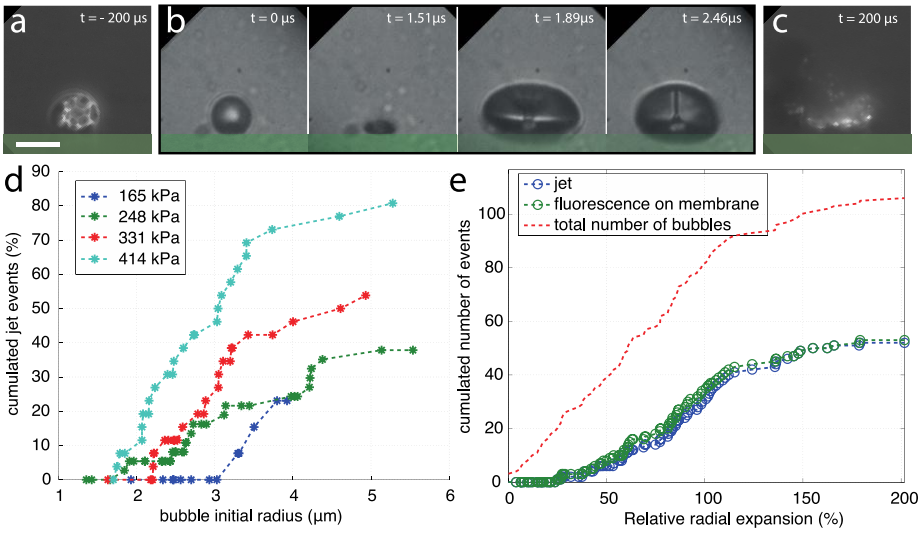

Figure 9.7. Bubble jetting. (a,c) Fluorescence images taken before and after the ultrasound exposure that show the release of the fluorescent material on the membrane. (b) Snapshots of the ultra-high-speed recording of the formation of the jet in the bubble toward the membrane. (d) Proportion of cumulated jetting event as a function of the bubble size for the four different pressures used and showing the reduction in the threshold and the increase in the number of jetting events as a function of the initial bubble size. (e) Cumulated jetting events count and deposition on the membrane as function of the oscillation amplitude. The total number of bubbles observed is plotted with the dashed red line.

Figure 9.7d. demonstrates the influence of the excitation pressure on the occurrence of jetting: a higher pressure reduces the threshold of bubble initial radius (i.e., bubbles smaller than the resonance size also exhibit jetting) and increases the total number of jets so that 85% of the observed bubbles display a jetting behavior at a pressure of 415 kPa. Simultaneously the jetting appears to depend more on the bubble size than the amplitude of oscillation as suggested by figure 9.7d. Larger

bubbles present more jetting occurrences than smaller bubbles under a given pressure. Resonant bubbles (approx. 2.5 μm in radius) that display the maximal relative radial oscillations do not significantly increase the count of jetting events. However, as indicated by figure 9.7e, the correspondence between the jetting events and the deposition of fluorescent material on the membrane is clear. A correlation of the observed jetting events with the observed material deposition on the membrane for the 106 individual bubbles studied gives 81% of correspondence.

9.3.3 Transport of the shell material by streaming

It was proposed before that the microstreaming surrounding the microbubble during the ultrasound exposure is an important transport mechanism following the shedding events. The velocities observed were typically on the order of 0.1 m/s.

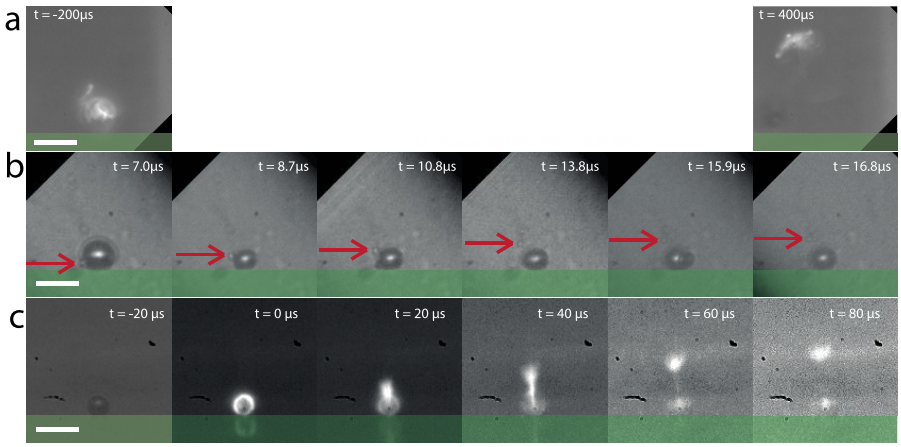

Figure 9.8. Experimental evidence of streaming. (a). Location of the fluorescence shell materials before and after the ultrasound exposure. (b) Snapshots of the transport of an attached small bubble away from the surface of the big bubble. (c) Release of the fluorescent material from an oscillating microbubble showing a clear transport toward the opposite of the membrane.

The experimental evidence of this streaming process captured from the side view is presented in figure 9.8b,c. measured at two different timescales. Figure 9.8b shows the transport trajectory of a tiny particle in the fluid that is first transported along the microbubble surface, then away from the big microbubble. The whole process occurs within a few microseconds. Figure 9.8c shows a typical example of fluorescent material transport on tens of microseconds timescale. The fluorescent material was detached from the bubble and moves upward.

Marmottant et al. (2003; 2006) raised this streaming analysis for 100 μm sized bubbles resonating at lower frequencies. They observed a significant streaming field due to the non-spherical oscillation of the microbubble. The description was simplified into two decoupled oscillatory motions: the volumetric oscillations of the bubble and the oscillatory translation of the bubble. They calculated the streaming due to the phase difference between those two oscillatory motions. They observed experimentally a phase difference of 13 degrees between those two oscillations and used the singularity method in Stokes flow to calculate the streaming pattern and velocity. The analysis was applied to our system as we demonstrated experimentally a similar microbubble behavior. The volumetric and translational oscillations were derived from the computation of our model and the result is plotted in figure 9.9b. The model predicts a very similar phase difference between 13 and 14 deg at resonance (the black dashed line) depending on the pressure. The highest phase difference at R_0 = 1.5 μm is below the resonant radius (2.3 um) and corresponds to the peak in the expansion to compression ratio, which indicates a very non-linear bubble behavior (Fig. 9.9a). In comparison, a free bubble displays no phase difference and the peak of the expansion to compression ratio is shifted to larger bubbles in coherence with the shift in the resonant radius.

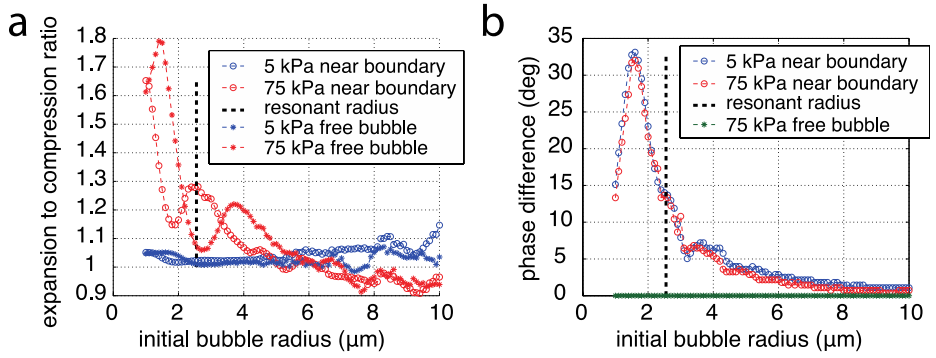

Figure 9.9. (a) Expansion to compression ratio for a free bubble(*) and a bubble on a membrane(o) at two pressures: 5 kPa (blue) and 75 kPa (red).(b) Phase difference between the volumetric oscillation and the translation of the center of the bubble as a function of the initial bubble radius in a simplified description of the oscillations of the bubble.

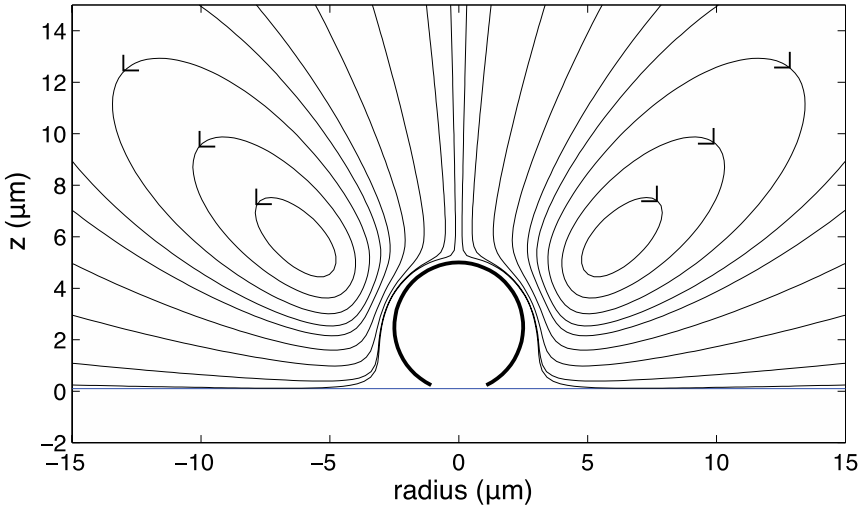

Figure 9.10. Streamlines around a 2.5 μm radius bubble sitting on a membrane.

The velocity field resulted from this approach (Marmottant et al. 2003) is then given by a combination of 3 Stokes singularities, a stokeslet (stk), a dipole (dip) and a hexapole (hexp). The velocity profile of the streaming obtained for a 2.5 μm bubble exposed to a burst of 100 cycles at 1 MHz is shown in figure 9.10. It explains the trajectory of the fluorescent material: the detached phospholipids will move along the surface of the microbubble and be transported straight up as illustrated by figure 9.8c.

We define ε_z and ε_R as the relative volumetric oscillations and relative translation amplitudes as defined in Marmottant et al. (2003), and plot these two calculated parameters (normalized by the pressure) as a function of the microbubble size (Fig. 9.11.a,b). The amplitude of the streaming velocity (normalized by the pressure squared) is plotted in figure 9.11c.

The velocity of a point located on the z axis (see Fig. 9.12) writes:

$$u = \beta\,(\mathrm{stk} + \mathrm{dip} + \mathrm{hexp}) \tag{9.8}$$

where

$$\mathrm{stk} = \frac{2}{\bar{z}-\bar{d}} - \frac{1}{\bar{z}+\bar{d}} - \frac{(\bar{z}-\bar{d})^2}{(\bar{z}+\bar{d})^3} - \frac{8\,\bar{d}\,\bar{z}}{(\bar{z}+\bar{d})^3} \tag{9.9}$$

$$\mathrm{dip} = -\left(\frac{1}{(\bar{z}-\bar{d})^3} - \frac{7}{(\bar{z}+\bar{d})^3} + \frac{6\,\bar{d}}{(\bar{z}+\bar{d})^4}\right) \tag{9.10}$$

$$\mathrm{hexp} = -\frac{1}{2}\left(\frac{1}{(\bar{z}-\bar{d})^6} - \frac{1}{(\bar{z}+\bar{d})^6}\right) \tag{9.11}$$

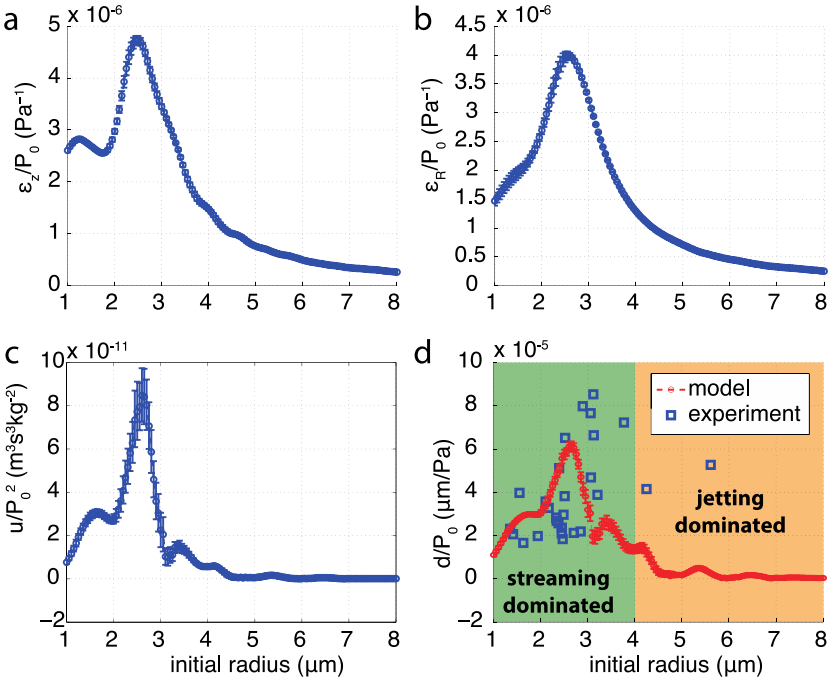

Figure 9.11. (a,b) Coefficient of vertical and volumetric oscillations of the bubble scaled by the applied pressure. (c) Calculated amplitude of the streaming velocity scaled by the pressure squared, and (d) displacement after 50 ultrasound cycles calculated from the velocity field. The error bars represent the deviation that is introduced by the variation of pressure in this simplified description.

and

$$\beta = \varepsilon_z \varepsilon_R \sin\left(\varphi . \frac{\pi}{180}\right) . R_0 . \omega \tag{9.12}$$

z is as described in figure 9.12, d is the initial distance of the center of the bubble to the wall – slightly smaller than the ambient bubble radius due to pinning – and the overbar is used to notify a non-dimensional space variable as a result of the division by the initial bubble radius R_0. The prefactor gives the typical velocity of the streaming and is proportional to the phase difference between the two oscillatory motions. The participations of the Stokes functions as described above are non-dimensional. The displacement along the vertical axis given by:

$$z(t) = \int_0^t u\big(z(t)\big)dt \tag{9.13}$$

is plotted in figure 9.11d. together with the experimental data. The integration is carried out over the duration of the ultrasound burst, in this case 100 μs. The displacement calculated here is valid for bubbles in permanent regime and at a fixed

location. Quite often the bubble breaks-up, jets or moves rapidly on the membrane thus disturbing the streaming field. This displacement can therefore not be seen as the expected value for a given bubble but as the range of the population of bubbles. It is also not surprising to find the maximum displacement for larger bubbles than expected by the calculation considering phenomena such as the pinch-off that rapidly make the microbubble shrink. Considering the large variation in the observed bubble responses, the calculation agrees reasonably well with the experiments. It should be noted here that from the computation, if the streaming velocity scales with the pressure squared, the displacement scales with the pressure, and therefore the transport distance in an ideal case is expected to be proportional to the applied pressure as shown in figure 9.11d. Also from figure 9.11d. it can be seen that this behavior is difficult to retrieve experimentally probably due to the number of physical phenomena presented in this study that interfere with the streaming around the microbubble.

9.4 DISCUSSION

9.4.1 About the 2D model

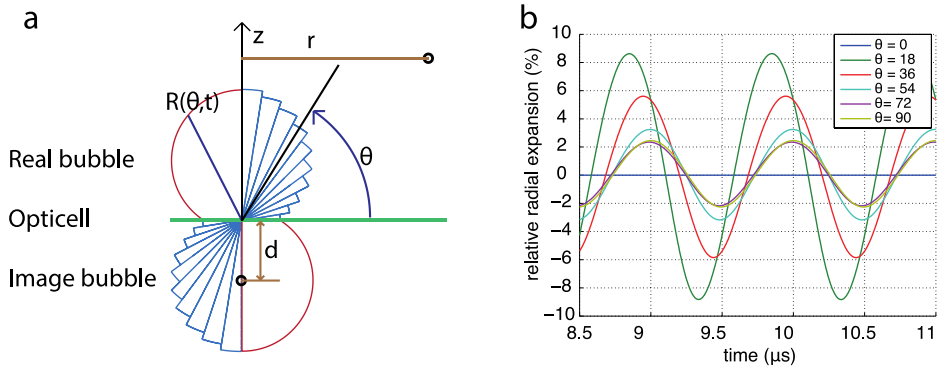

Figure 9.12. (a) Model decomposition schematics and precision of the coordinate systems. (b) Simulated radius time curves of the interface of a bubble near a membrane for different θ angles showing the variable phase difference on the surface of the microbubble.

From the side view observation, we captured highly non-spherical microbubble oscillation dynamics, which can be correctly predicted by the axisymmetrical numerical model developed in this study. However, there are several practical issues to be discussed here. First, the reflection of the acoustic wave on the Opticell membrane is neglected (≈ 1%). The addition of this reflected pressure should be considered in the case of a more rigid wall and would result in larger oscillation amplitude of the microbubbles. Second, the model used in most of the study (with the

exception of section “surface modes oscillations”) does not account for the shell influence. Such a choice is motivated by the known negligible impact of a phospholipid shell at high pressures as applied in this study (Overvelde et al. 2010). Two errors can be associated with this model. The first and minor one is the assumption that the effects of the surface tension, in accordance with the rest of the model, are radial in our coordinate system. This can modify slightly the contribution of the surface tension for lower angles and partially explain the differences observed in the position of neck in the collapsing bubble in the experiment (Fig 9.3a) and in the simulation. The second and more significant error associated with this decomposition can be a consequence of the orientation of the velocity field that is considered radial in the spherical reference frame chosen. Vos et al. (2011) derived an equation for the admissible velocity potential of such a bubble sitting on a membrane by considering the spherical harmonics of order 2 as approximation for the bubble wall motion.

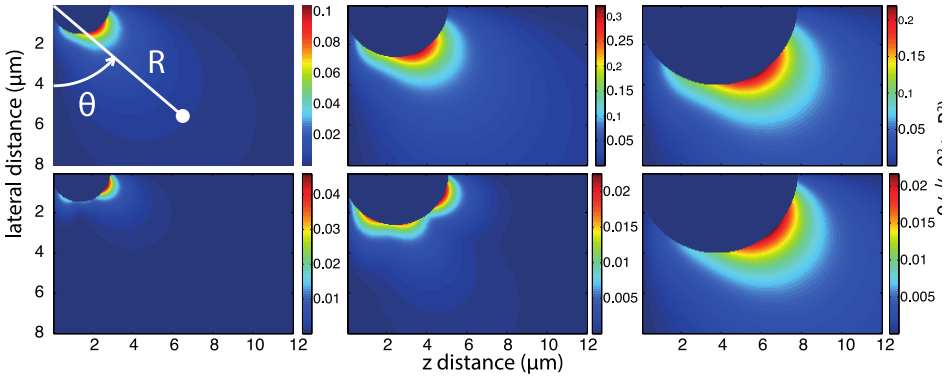

Figure 9.13. Ratio of the tangential velocity over the total velocity around an oscillating microbubble sitting on a membrane computed for bubble sizes R= 1.5 μm, 2.5 μm and 3.5 μm. The half space including half of the bubble is displayed. The membrane is on the left side.

The velocity potential was computed from the equation using Matlab and was numerically differentiated to obtain the velocity field. From this velocity field, the ratio of the tangential velocity to the total velocity is computed and the result is plotted in figure 9.13 for three bubble sizes. The tangential velocity is maximal when the velocity of the interface is maximal and can reach 30% of the total speed. Thus the radial velocity is at least $\sqrt{1-0.3^2} \approx 95\%$ of the total velocity and the range of the error is less than a bubble radius. Considering the velocity as radial in our spherical referential therefore proves to be a valid approximation.

9.4.2 Influence of targeting

Different from our preliminary study in which microbubbles floating against a wall were investigated, targeted microbubbles were used in this study. We captured a pinning behavior (at the bottom of the bubble surface which is in contact with the membrane) of the microbubble. This pinning behavior was represented in the axisymmetric model by pinning numerically the point of the bubble that is closest to the membrane. A good agreement between the simulation and the experimental observation was captured. As was expected, this did not introduce any visible change in the simulated resonance curve nor vibration amplitudes. Also, this pinning behavior of a targeted bubble does not change the shedding dynamics (mechanism) compared to a bubble floating against a wall as observed previously in the top-view study (Luan et al. 2014).Noted that from the *in vivo* perspective, using targeted microbubbles is preferable for applications of drug delivery since they can specifically bind to diseased endothelial cells on the blood vessel wall (Kiessling et al. 2012).

9.4.3 Applications

In this study we captured three distinct lipid shedding dynamics (mechanisms), which have different implications in terms of drug release applications. The pinch off brings the issue of the efficiency and reproducibility of the transport. First, the secondary bubbles can trap the shed materials and travel away from the wall. This will prevent an efficient drug delivery since the diameter of veins (0.5 - 2 mm) or arteries (0.5 - 8.5 mm) are normally larger than the transport distance (~20 μm). Second, the spreading of the measured data (e.g., Fig. 9.11d) can be partly attributed to the pinch-off behavior. This may lead to a low controllability of the drug delivery approach. It should be noted that the experimental observations show that the pinch-off also plays a major role in the fast bubble dissolution during the ultrasound exposure.It is a completely different physical process from the shedding caused by oversaturation of the phospholipids on the bubble surface. Therefore to estimate the amount of expelled shell material indirectly by measuring the bubble dissolution is not a suggested approach.

In comparison, another shedding dynamics, jetting, can have a clear interest in terms of the drug delivery application. Targeted microbubbles are specially preferable in this cases, since they can selectively bind to endothelial cells expressing disease-specific markers (e.g., aminoacids). The dynamics of jetting will directly deposit large amounts of drug-carrying lipids on the cell membranes within the targeted region. This can prevent the transport of drug molecules into the blood stream, largely improving the efficiency and safety for drug delivery purpose, especially in larger veins and arteries.

9.5 CONCLUSIONS

Based on high-speed fluorescence imaging from the side view in this study and previous top view studies, for the first time, we acquired an in-depth understanding of the lipid shedding behavior. We captured highly non-spherical bubble vibrations, leading to lipids shedding with two very distinct shedding dynamics: lipids oversaturation perturbated by the pinch-off of daughter bubbles and microjetting toward the membrane. Theoretical explanations have been brought to light through a newly built axisymmetric model. We also found similar oscillation/shedding dynamics between targeted and non-target bubbles in the presence of a neighboring wall. Additionally, the streaming field surrounding the microbubble was calculated and showed good agreement with the experimental data. The practical benefit of using targeted microbubbles was discussed and the jetting of bubbles under higher pressures was proved to be the most preferable as an efficient drug delivery approach.

10

SPIO labeling of endothelial cells using ultrasound and targeted microbubbles at low mechanical index

Abstract — *In vivo* cell tracking is an emerging field and a promising technique for tracking therapeutic cells as well as tumor and endothelial cells for cardiovascular diseases and cancer. The aim of this study was to find optimal ultrasound parameters for ultrasound contrast agent-mediated superparamagnetic iron oxide (SPIO)-labeling of endothelial cells at low mechanical index (MI) for future applications of MRI tracking. The optimal ultrasound parameters were 40 kPa at 1 MHz, 10,000 cycles, 20 Hz pulse repetition frequency, applied for 30 seconds just before SPIO addition. This gave a ~12 times increase of SPIO uptake in endothelial cells *in vitro* compared to the control with 85% cell viability. This technique shows great potential for safe labeling of endothelial cells with SPIO for MRI tracking.

In preparation for submission; by I. Skachkov, Y. Luan, S. van Tiel, A.F.W. van der Steen, N. de Jong, M. Bernsen*, K. Kooiman*. Parts of this work appeared in proceedings of IEEE Ultrasonics Symposium International 2012, Dresden, Germany. * Both authors contributed equally to this study.

10.1 INTRODUCTION

In vivo cell tracking is a very promising technique to visualize cells of interest inside the body. On one hand, it allows tracking of motile therapeutic cells like immune cells, stem cells, and endothelial progenitor cells to sites of inflammation, cancer, or ischemia (Gazeau and Wilhelm 2010; Hong et al. 2010; Edmundson et al. 2013). On the other hand, it can be used to track tumor cells (Hong et al. 2010), tumor vasculature (Gimi et al. 2006), or endothelial cells in tissue engineered valves (Ramaswamy et al. 2012) and vascular grafts (Fayol et al. 2013).

After labeling the cells of interest with an image tag, they can be tracked by an imaging modality, for example MRI, PET, SPECT, or ultrasound. Each modality has its advantages and disadvantages. Ultrasound based cell tracking is relatively safe and inexpensive but not applicable for whole body imaging. PET and SPECT are very sensitive techniques, and radioactive tracers can be accurately located when combined with x-ray CT, but cannot be used often because of ionizing radiation. MRI has most of the advantages of all the above modalities, since it is precise, harmless, and thus is better suited for longitudinal studies (Hong et al. 2010; Fu et al. 2011; Taylor et al. 2012; Youn and Hong 2012).

For tagging cells to increase the MRI contrast and to visualize the labeled cells, mainly two groups of MRI contrast agents can be used: 1) Gadolinium-based agents, and 2) iron-based agents. Whereas gadolinium-based contrast agents are highly toxic, superparamagnetic iron oxide particles (SPIO) nanoparticles of 80-150 nm in size (Gamarra et al. 2005) are relatively safe compounds (Frank et al. 2004; Reddy et al. 2012). However, most of the SPIO-cell labeling techniques currently used *in vitro* are not applicable *in vivo* because of their high toxicity or broad systemic effect (Rodriguez-Porcel et al. 2012). There has therefore been growing interest in safe site-specific cell labeling techniques. One such powerful tool is the ultrasound contrast agent microbubble which has a low diffusible gas core (e.g., C_4F_{10}) that is encapsulated by a coating material (e.g., phospholipids). Under the excitation of ultrasound, the microbubble undergoes cavitation which is sequential compression and expansion due to pressure variations in the surrounding medium. The cavitation of microbubbles has been shown to increase cell membrane permeability and capillary permeability, allowing the delivery of therapeutic materials into cells and interstitial tissue (Ferrara et al. 2007; Kooiman et al. 2014; Lentacker et al. 2014). Up till now there is no consensus on the mechanism of the enhanced uptake. One of the theories is a phenomenon called sonoporation, when reversible or non-reversible cell membrane pores are generated upon microbubble oscillations or violent collapse. Recently, it was reported that the efficacy of cellular uptake of therapeutic agents can be improved by up to ~5 times when using targeted microbubbles (tMB), which has a

ligand added in the lipid coating to adhere to the disease-specific cell membrane biomarkers (Klibanov 2009; Phillips et al. 2012; Xie et al. 2012).

Successful SPIO tumor cell labeling using ultrasound and non-targeted microbubbles (non-tMB) has been reported *in vitro* (Yang et al. 2011). However, microbubbles are blood pool agents and will therefore not come into contact with tumor cells *in vivo*. Endothelial cells which form the inner lining of vessel are therefore the main target cell of microbubbles (Correas et al. 1997; Greis 2009). The *in vivo* study by Gao et al. (2009) demonstrated arterial wall uptake of SPIO particles using microbubbles and ultrasound, but under only one acoustic setting (3.5 MPa acoustic pressure, 8.5 MHz frequency, Mechanical Index (MI) of 1.2), which induced considerable artery wall damage. To the best of our knowledge, no studies have been performed to characterize in-depth the parameters (e.g., the acoustic settings, the addition time and incubation time of SPIO) that strongly influence the efficacy and safety of SPIO-labeling of endothelial cells using tMB at low MI (< 1).

The aim of our *in vitro* study was to find optimal parameters for non-invasive microbubble-mediated SPIO-labeling of endothelial cells for the future application of MRI tracking of tumor vasculature and tissue engineered vasculature structures. We used lipid-shelled microbubbles targeted against CD31 (PECAM1), a biomarker constitutively expressed on endothelial cell membranes (Newman and Newman 2003). Iron specific Prussian Blue staining in combination with Calcein AM based cell viability assays were applied to define the most efficient and safe condition for SPIO-labeling of endothelial cells *in vitro*. Concerning the acoustic setting, a fixed ultrasound driving frequency of 1 MHz was used, and the pulse length and a series of low acoustical pressures (< 200 kPa) were measured.

10.2 MATERIALS AND METHODS

10.2.1 Endothelial cells

Human umbilical vein endothelial cells (HUVEC) (Lonza, Verviers, Belgium) were cultured in EGM-2 (Lonza) medium in T75 flasks (BD, Breda, the Netherlands) in a humidified incubator at 37°C with 5% CO_2. Cells were detached with 0.25% Trypsin in EDTA (Lonza) and replated on one side of acoustically transparent OptiCell™ (NUNC, Wiesbaden, Germany) chambers. Then, HUVECs were cultured as described for two days until 70% confluence.

10.2.2 Targeted microbubbles

Biotinylated lipid-coated microbubbles consisting of a coating of DSPC (59.4 mol %; P 6517; Sigma-Aldrich, Zwijndrecht, the Netherlands), PEG-40 stearate (35.7 mol %; P 3440; Sigma-Aldrich), DSPE-PEG(2000) (4.1 mol %; 880125 P; Avanti Polar

Lipids, Alabaster, AL, USA), and DSPE- PEG(2000)-biotin (0.8 mol %; 880129 C; Avanti Polar Lipids) with perfluorobutane (C_4F_{10}) gas core were made by sonication as described by (Klibanov et al. 2004). Biotinylated anti-human CD31-antibody (R&D Systems, Europe, Abingdon, United Kingdom) was conjugated to the microbubbles via avidin-biotin bridging as described by (Lindner and Kaul 2001; Skachkov et al. 2014).

10.2.3 Cell treatment

The concentration of tMB was evaluated by Coulter Counter (Beckman Coulter, Mijdrecht, the Netherlands) measurements. Ten million tMB were added to an OptiCell™ chamber with cells plated on the bottom, which was turned upside down to let microbubbles adhere to the cells by flotation. The cell to bubble ratio was 1:3. Then the chamber was incubated at 37°C for 5 min before the experiment. SPIO nanoparticles (Endorem™, Gerber S.A., Paris, France) were added at four time-points: 5 min before, immediately before (0 min), 5 min after, and 15 min after insonification as illustrated in figure 10.1A, at a final concentration of 22.4 μg Fe/ml. Each OptiCell™ chamber was divided into six acoustically non-overlapping areas (2.5 cm x 3 cm each; see Fig. 10.1B), which covered the beam area (6.5 mm for -6dB beam width) at the focus of the 1.0 MHz transducer (V303; Panametrics-NDT, Olympus NDT, Waltham, MA, USA), as verified in advance with a calibrated 0.2 mm PVDF needle hydrophone (Precision Acoustics Ltd, Dorchester, UK). Then the OptiCell chamber with the configuration shown in figure 10.1C was placed into a 37 °C water bath and connected to a 2D micropositioner (Fig. 10.1D). The 1 MHz focused transducer was configured at 45° angle below the sample and the acoustic focus was aligned with the center of each subsection.

During the experiment, the position of the OptiCell chamber was manipulated so that the center of each subsection was insonified in sequence at a predefined pressure (10 to 160 kPa Fig. 10.1 C). A prolonged burst of 10,000 cycles with a pulse repetition rate of 20 Hz was applied. The first subsection without the application of ultrasound application was used as the control. The effect of different total insonification time was determined (1 s, 10 s and 30 s) at 40 kPa, 80 kPa, and 160 kPa. To investigate the effect of the incubation time with SPIO, the OptiCells were incubated at 37°C for 5 min, 1 h and 3 h after insonification, with adding SPIO 5 min prior to insonification. All experiments were repeated three times. Results were derived by averaging all three datasets and the standard deviation is indicated by the error bars.

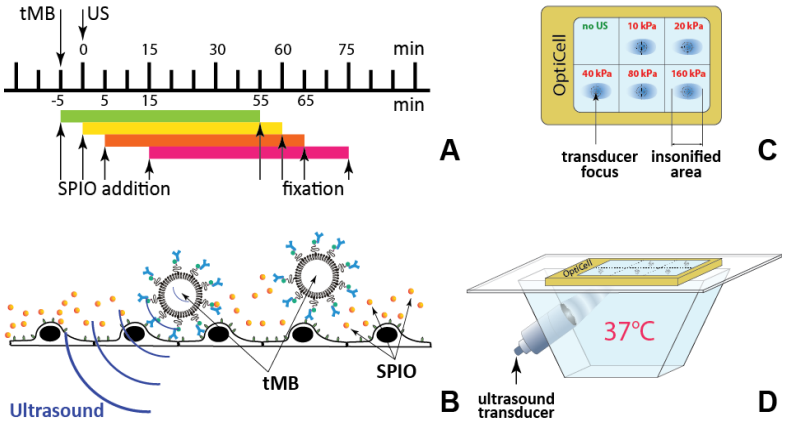

Figure 10.1. (A) Timing diagram of the experiment. The time of insonification (0 min) was used as the reference time. Targeted microbubbles (tMB) were added 5 min before the ultrasound was applied; SPIO was added 5 min before, 0 min, 5 min, and 15 min after insonification. Fixation of cells was done 60 min after SPIO addition. (B) Schematic representation of tMB adhered to HUVECs. (C) Scheme of insonification of the OptiCell™ chamber subsections (1 MHz, 10.000 cycles, 20 Hz PRF). (D) The experimental setup.

10.2.4 SPIO labeling

After the treatment described above (see also Fig. 10.1A), cells were rinsed three times with PBS (Invitrogen, Groningen, the Netherlands) and fixed with 4% formaldehyde (Sigma-Aldrich, Zwijndrecht, the Netherlands) for 10 minutes. After fixation the cells were washed three times with PBS, which was followed by incubation with Prussian Blue solution for 30 min (aqueous solution of 10% hydrochloric acid (Sigma-Aldrich) and 5% potassium ferrocyanide (Sigma-Aldrich)) to assessing the SPIO-labeling (Clark 1973). Next, the cells were washed three times with PBS and the nuclei were stained with 0.1% nuclear fast red solution (Sigma-Aldrich). Then, the OptiCells were dried for 48 hours and microscopically examined using a microscope (Olympus, Zoeterwoude, the Netherlands) equipped with x20 Plan (NA 0.4) objective (Olympus) and a color camera (Axiocam MRc, Carl Zeiss, Germany). SPIO uptake was assessed by manually counting Prussian Blue positive cells among ~500 cells (acquired in 5 fields of view) located within a circle of 6 mm diameter around the center point of each insonified area.

10.2.5 Cell viability assay

For each SPIO uptake measurement, cell viability was determined by Calcein AM assay in parallel. Cells were treated with SPIO, tMB and ultrasound as described before. Thirty minutes after SPIO addition, Calcein AM was added to the OptiCell

chamber (C3100MP; Invitrogen; 0.25 μM from a 1 mM stock prepared in DMSO (Sigma-Aldrich)) and incubated for 30 minutes. Then propidium iodide (PI; 25 μg/ml P4864, Sigma-Aldrich) and Hoechst 33342 (Invitrogen; 5 μg/ml) were added to the cells and microscopic examination was performed with a fluorescent microscope (Olympus) equipped with the same setup as applied for SPIO labeling measurements, only that a x5 LMPlanFl (NA 0.13) objective (Olympus) was used here. For each condition five different fields of view were acquired within the 6 mm circle around the center of the insonified area. Different filter sets (U-MWU2, 330-385/420 nm; and U-MWIB2, 460-490/510 nm, Olympus; U-MWG2, 510-550/570 nm, Olympus) were applied for detecting all cells (stained with Hoechst), viable cells (stained with Calcein AM), and dead cells (stained with propidium iodide) respectively. All images were automatically analyzed with Find Maxima function in ImageJ (Rasband, W.S., ImageJ, U. S. National Institutes of Health, Bethesda, Maryland, USA, http://imagej.nih.gov/ij/, 1997-2014.).

10.3 RESULTS

10.3.1 Cell treatment

During the ultrasound burst, we observed the displacement of targeted microbubbles. This was most pronounced for the 30 seconds insonification period, as shown in figure 10.2. During insonification, tMB moved, clustered and fused (Fig. 10.2B-D). After 30 sec of insonification, all microbubbles were gone (Fig. 10.2E).

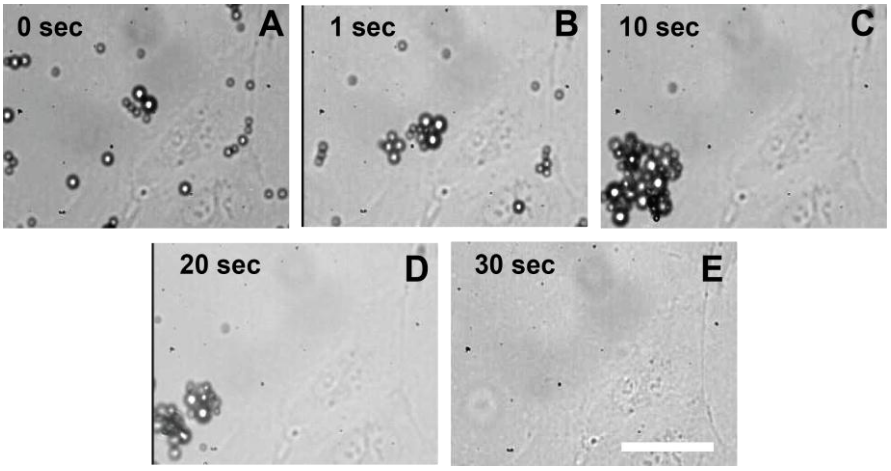

Figure 10.2. tMB displacement during insonication (1 MHz, 80 kPa, 10,000 cycles, PRF 20 Hz, 30 s treatment). Scale bar = 10 μm.

10.3.2 SPIO labeling

To detect SPIO uptake by HUVEC, Prussian Blue staining was performed after fixating the cells. In the absence of ultrasound, only a small fraction of cells incorporated SPIO naturally (Fig. 10.3A and B), and iron particles were detected as a small aggregates distributed in the cytoplasm (Fig.10.3B). Ultrasound and microbubble treated cells, however, demonstrated much higher SPIO uptake as shown in figure 10.3C and D. Iron particles were detected as large or small aggregates in the cytoplasm (Fig. 10.3D).

10.3.3 Insonification duration and acoustic pressure

Figure 10.4 shows the efficacy of SPIO uptake by HUVEC cells and the corresponding cell viability as a function of the acoustic pressure and the total sonication duration (1, 10, or 30 seconds). A very limited amount of SPIO uptake (< 2%) was observed without applying ultrasound. The total ultrasound exposure time was a key factor for SPIO uptake efficacy. For example, the amount of SPIO positive cells did not exceed 4% for 1 second and 6% for 10 seconds of sonication. However, the amount of SPIO positive cells increased to more than 10% with 30 seconds of insonification. Additionally, the pressure also influenced SPIO uptake significantly. With 30 seconds of insonification, the proportion of SPIO positive cells increased dramatically with the pressure (e.g., from ~10% at 40 kPa to ~16% at 160 kPa). At the same time, cell viability (Fig. 10.4B) decreased with both the increasing acoustical pressure and the insonification time, for example at 80 kPa, the cell viability decreased from ~70% for 10 s of insonation to ~60% for 30 s of insonation. For 30 seconds of exposure time, the cell viability dropped by nearly two-fold from 40 kPa to 160 kPa. In general, the cell viability remained high for the pressure up to 40 kPa. Specifically, insonification for 30 seconds demonstrated the best SPIO uptake and was selected for further experiments. We did not investigate a longer insonification time because after 30 seconds all tMB were destroyed (see Fig. 10.4C).

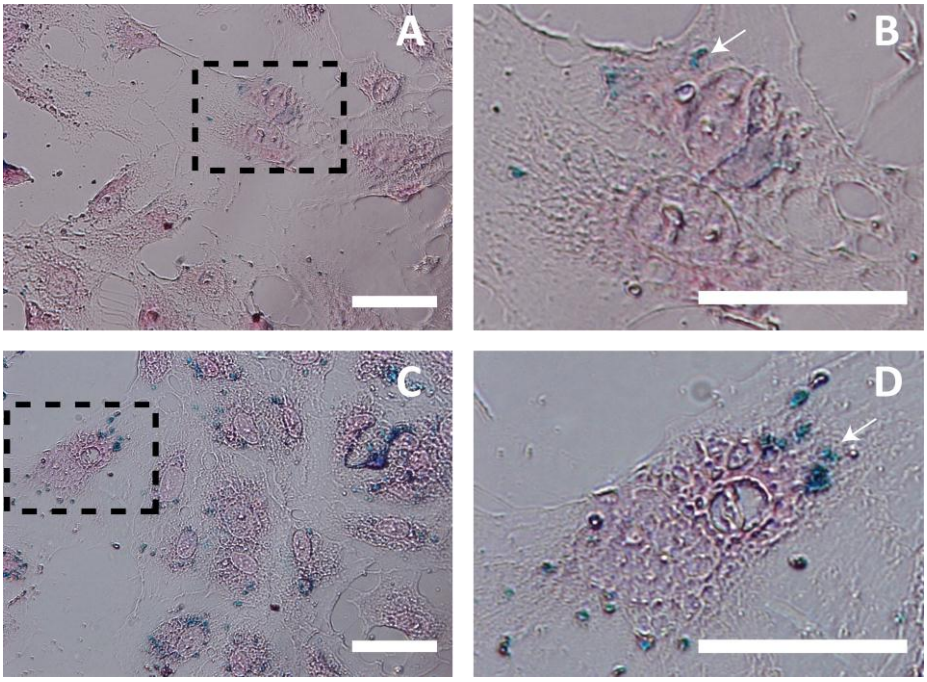

Figure 10.3. Prussian Blue staining for SPIO uptake for control (A and B) and ultrasound and tMB treated HUVEC (C and D; 80 kPa, 1 hour of incubation, SPIO was added 5 min prior insonification). B and D are zoomed in from A and C as illustrated by the dashed rectangles. In B and D, one example of a SPIO aggregate is labeled with an arrow. Scale bar = 20 µm.

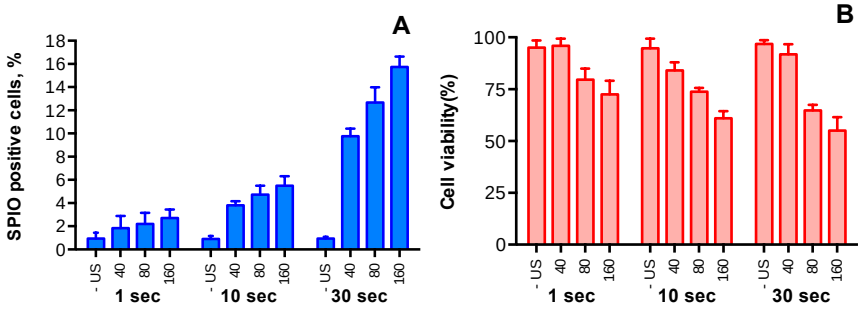

Figure 10.4. The effect of the duration of ultrasound insonification time on intracellular SPIO uptake efficiency and cell viability.

10.3.4 SPIO incubation time

The influence of the SPIO incubation time (5 min, 1 h or 3 h) after the treatment with ultrasound and tMB on SPIO uptake and cell viability is illustrated in figure 10.5. In general, SPIO uptake increased prominently with the incubation time, for example for 180 kPa SPIO uptake increased from below ~4% to ~22%. The largest ratio between control and treated uptake was at 1 h of incubation for all pressures. Cell viability (Fig. 10.5B) remained high (> 75%) at 40 kPa for all incubation times. It decreased with the pressure (80-160 kPa) for 1 h and 3 h of the incubation time. A longer incubation time did not lower cell viability, as cell viability was slightly higher after three hours of incubation than after one hour of incubation. Based on the results from this experiment, 1 h of incubation with SPIO was selected for further investigations.

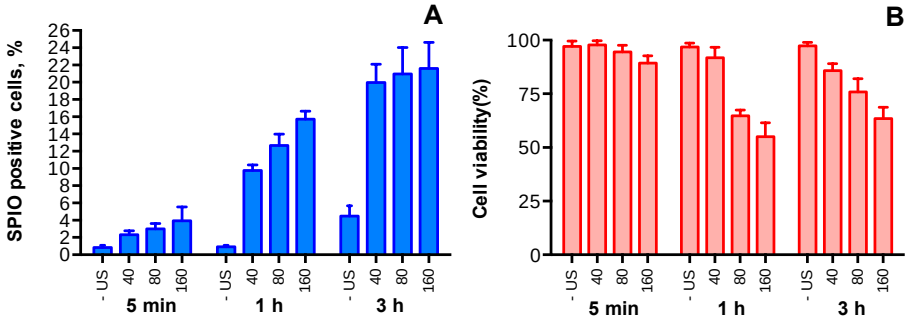

Figure 10.5. The effect of SPIO incubation time on intracellular SPIO uptake efficiency and cell viability.

10.3.5 SPIO addition time

In figure 10.6, the percentage of SPIO positive cells and cell viability are plotted for four different moments of SPIO addition relative to the moment of insonification at different acoustic pressures. Similar to previous measurements, no ultrasound application gave less than 2 % of SPIO positive cells. For both additions of SPIO 5 minutes prior (-5 min) as well as just before (0 min) the ultrasound application, we obtained a relatively large percentage of SPIO positive cells (~>10%) for acoustic pressures of above 20 kPa. Moreover, the percentage of SPIO positive cells increased with higher pressures up to ~12-15 % for SPIO addition before the insonification. In contrast, SPIO addition at 5 and 10 minutes after ultrasound application resulted in much lower SPIO uptake (< 8%). Similarly, the cell viability remained above 50% for all settings.

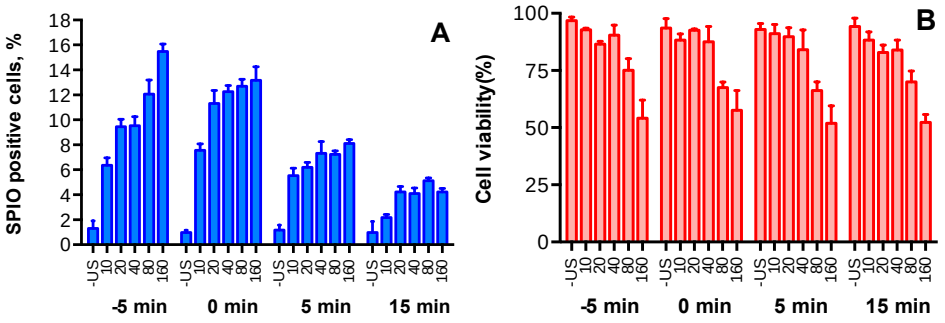

Figure 10.6. The effect of SPIO addition time on intracellular SPIO uptake efficiency and cell viability.

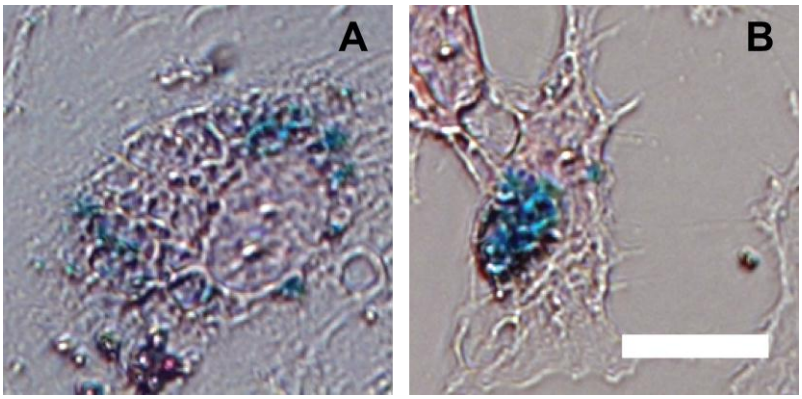

Figure 10.7. Different intracellular SPIO distribution patterns. A. small SPIO aggregates distributed in the cytoplasm (-5 min SPIO addition 10 kPa); B. a large SPIO aggregate in the nuclear area (15 min SPIO addition 160 kPa). SPIO were stained by Prussian Blue and nuclei of cells by Nuclear Fast Red. Scale bar represents 10 μm.

Figure 10.7 illustrates individual examples of SPIO distribution within the cell, indicated by Prussian Blue staining. The intensity of the stain indicates the concentration of the SPIO particles within the area qualitatively. The staining patterns can be either small (sub-micron) with a high SPIO concentration (A) or comparatively large (several microns) with a low SPIO concentration in the cytoplasm (B).

10.4 DISCUSSION

10.4.1 Microbubble oscillation dynamics

Our study shows that ultrasound-activated tMB can greatly enhance SPIO uptake by endothelial cells *in vitro* at low MI (<0.2). The acoustic settings (the driving

pressure and insonification time) showed a significant effect on the efficacy of SPIO labeling.

Oscillating microbubbles are known to induce three drug uptake routes, namely pore formation, stimulated endocytosis, and opening of cell-cell contacts (Kooiman et al. 2014). The three different drug uptake routes may require different microbubble oscillation dynamics. Although the exact link between the type of microbubble behavior and drug uptake is not known, several studies reported that endocytosis was stimulated at longer (3,250-10,000 cycles) acoustic cycles (Meijering et al. 2009; Jin et al. 2013). SPIO are 80-150 nm (Gamarra et al. 2005) nanoparticles which may require uptake by endocytosis as this has been shown to be the main uptake mechanism for therapeutics larger than ~9 nm in radius (Armstrong et al. 2004; Meijering et al. 2009). This is the reason why we chose to study 10,000 acoustic cycles. In our study we used 1 MHz as the ultrasound frequency as this is the most common used frequency for microbubble-mediated drug delivery studies, and is also around the resonance frequency of microbubbles (Kooiman et al. 2014).

We found an increasing trend of both SPIO positive cells and cell death with the acoustic pressure increase. Note that we studied acoustic pressures up to 160 peak negative pressure, a regime in the amplitude of radial oscillations increases with pressure (Vos et al. 2008; Overvelde et al. 2011). Previous studies by Vos et al. (2011) has reported that highly non-spherical bubble vibrations can be induced at the pressure as low as 100 kPa for bubbles at resonance. At this stage the acoustic streaming generated by vibrating microbubbles and the produced shear stresses can be one of the mechanisms for enhanced permeability of the cell membrane (Mukherjee et al. 2000; Prentice et al. 2005; Ohl et al. 2006; Ooi et al. 2007). As was expected, the total duration of insonification also showed an effect on the SPIO uptake. It was reported that at a low mechanical index (MI < 0.1), a bubble can repeatedly oscillate for the full duration of the prolonged pulse; while with higher MI, the bubbles are destroyed before the ultrasound is turned off (Mannaris and Averkiou 2012). We indeed observed microbubbles still being present up to 30 seconds at 80 kPa peak negative pressure (MI = 0.08) (Fig. 10.2). The improved uptake with prolonged insonification may be related with the persistent effect produced by microstreaming generated by bubble vibrations as formulated earlier. Moreover, we noticed displacement of tMB with subsequent bubble clustering and merging driven by secondary radiation force over the prolonged burst, as illustrated by figure 10.2. Previously, tMB detachment due to the attractive secondary Bjerknes force between two tMB was reported (Garbin et al. 2009; Kokhuis et al. 2013). The displacement of detached MBs and the aggregation of bubbles formed bigger bubbles clusters, which have a lower resonance frequency than individual bubbles (Dayton et al. 1999). At a low driving frequency (e.g., 1 MHz as applied in this study), bubble clusters with a

higher response close to resonance, could have contributed to the enhanced SPIO uptake.

10.4.2 Microbubble selection

It was previously shown (Yang et al. 2011) that using SPIO incorporated in the microbubble shell in combination with ultrasound could be ~3 folds increase of SPIO labeling *in vitro* without compromising cell viability. Polymer shell microbubbles that behave differently exposed to ultrasound than lipid shell microbubbles were applied. Polymer microbubbles have a stiff shell, which can respond to ultrasound exposure under a high MI (> 1) by cracking and releasing the encapsulated gas (Kooiman et al. 2014). Lipid shelled microbubbles, on the other hand, oscillate at low acoustic pressures and can also fuse. They can therefore have a more prolonged interaction with cells than polymer microbubbles. This could explain why we found an ~12 folds increase in SPIO labeling comparing to the control group. Moreover, the study by Yang et al was done using tumor cells, which are never directly exposed to the blood flow. In this respect, endothelial cells seem to be a better candidate for studying SPIO labeling for tracking tumor neovascularization by MRI.

It was previously shown that lipid shell microbubbles together with intravenous SPIO injection could be used for SPIO extravasation in blood brain barrier (Liu et al. 2011) and in aortic arch (Gao et al. 2009). However these studies do not cover cell labeling, they demonstrate possibility of using co-administration approach for labeling underling tissues.

10.4.3 The mechanism of SPIO uptake

The natural uptake of SPIO (by HUVECs) was previously reported by (van Tiel et al. 2010), although the percentage of labeled cells is not sufficient for cell tracking. In our study, HUVECs showed ~1% natural uptake after one hour of incubation, and this values increased to ~5% after three hours. The treatment with ultrasound and tMB leads to dramatic increase of (~10-fold) SPIO uptake after 1 hour incubation. We also observed that the SPIO labeling efficacy was influenced by the SPIO addition time in respect to the treatment with tMB and ultrasound. We observed the highest efficacy when SPIO were added with the tMB (0 min) for acoustic pressures up to 80 kPa. When SPIO were added 5 or 15 minutes after treatment, SPIO uptake was lower, but still significantly (more then 5 folds) higher than natural uptake. This may suggest different uptake mechanisms than sonoporation, since resealing of pores created by ultrasound activated microbubbles have been reported on a relatively short time scale of up to a minute (Fan et al. 2012; Hu et al. 2013). One of the theories is the stimulated endocytosis, when the macromolecules actively uptake by the cells via cell membrane invagination. Our results also suggest that both uptake by pore formation and

stimulated endocytosis occurred when SPIO were added 5 minutes before or just before (0 min) treatment. This was supported by an earlier study by Meijering et al. (2009). They reported uptake by both pore formation and endocytosis using similar acoustic settings. However, they addressed the influence of therapeutic size on the uptake route for dextran particles larger than ~9 nm in hydrostatic radius, the primary uptake route was endocytosis instead of pore formation. However, pore sizes between 1 nm (Yang et al. 2008) and > 100 μm^2 (Hu et al., 2013) have been observed, with pores < 100 μm^2 could still reseal, according to a recent study (Hu et al. 2013). SPIO are 80-150 nm (Gamarra et al. 2005) nanoparticles which could accordingly enter cells via resealable pores. The reason why Meijering et al (2009) observed dextran particles larger than ~9 nm mainly to be taken up by endocytosis, could be different type of microbubble used (SonoVue versus tMB in our study) and/or the type of cells studied (bovine aortic endothelial cells versus HUVEC in our study). Moreover, induced pores > 100 μm^2 do not tend to reseal (Hu et al. 2013) which may lead to cell death. This could explain why higher acoustic pressures (e.g., ≥ 80 kPa) correspond to increased cell death.

The amount of SPIO positive cells was almost two times higher when SPIO were added 5 compared to 15 minutes after insonification. This suggests a relatively short temporal window when the drug can be actively taken up, especially when compared to the study by Yudina et al. who reported a temporal window of 24 hours (Yudina et al. 2011). The difference could be due to the type of microbubble (SonoVue versus targeted homemade microbubble in our study), type of cells (C6 rat glioma cells versus HUVEC in our study) and/or the therapeutic compound studied (small 1.4 kDa molecule TOTO-3 dye versus the 120-180 nm SPIO in our study).

In our study, we defined a cell as SPIO positive when we detected 1 or multiple SPIO within the cell. We also observe different labeling patterns, namely differences in the intensity and the distribution of SPIO particles within the cell. Some cells took up small spots (submicron) of SPIO as dense granules (~2 nm in diameter), while others had large SPIO aggregates in the cytoplasm. This may also suggest uptake by pore formation and endocytosis as SPIO homogeneously distributed in the cytoplasm may suggest pore formation whilst small aggregates could indicate endocytic uptake. It was reported that the aggregates size increased with incubation time due to endosome fusion (Dice and Chiang 1989).

10.4.4 Clinical implications

It was shown before that single cell tracking is possible by MRI using iron oxide as the label (Shapiro et al. 2006). The micron-sized paramagnetic iron oxide (MPIO) particles used in that study are ten times bigger (1.6 μm) than SPIO. As it was revealed before (van Tiel et al. 2010) that the iron content of cells labeled with SPIO is less

(~10 folds) than with MPIO, more cells may have to be labeled by SPIO to be detectable by MRI *in vivo*.

From the *in vivo* perspective, using tMB instead of non-tMB is preferable for endothelial cell labeling and drug delivery since tMB can be specifically targeted to diseased endothelial cells (Kiessling et al. 2012). In addition, when ultrasound is applied to bound tMB, the vibrations of the ultrasound-activated tMB will have a direct effect on the cell membrane. This may be the reason why tMB have been shown to be ~5 times more effective in stimulating cellular uptake of therapeutics *in vitro* as well as *in vivo* (Phillips et al. 2012; Xie et al. 2012). CD31 used as target in this study was chosen as model ligand because it is constitutively expressed on endothelial cell membranes. It can therefore be used to label endothelial cells with SPIO in tissue-engineered valves or vascular grafts *in vitro*. However, CD31 cannot be used *in vivo* as it is expressed throughout the entire vasculature tree (DeLisser et al. 1994). For targeting MB to tumor vasculature, $\alpha_v\beta_3$ or vascular endothelial growth factor receptor 2 (VEGFR2) can be used (Kiessling et al. 2012).

SPIO uptake by ultrasound-activated tMB *in vivo* is expected as we recently reported that tMB bound to $\alpha_v\beta_3$ can stimulate endothelial cell drug uptake *in vivo* (Skachkov et al. 2014). tMB targeted to VEGFR2 are of interest because BR55, a tMB against VEGFR2, has recently successfully been used in a phase 0 clinical trial for prostate cancer (Wijkstra et al. 2012; ClinicalTrials.gov Identifier: NCT01253213). Our future studies will focus on *in vivo* SPIO labeling as well as *in vivo* MRI tracking of the labeled endothelial cells.

Tracking of endothelial cells is important for cancer and cardiovascular diseases. There are several ways of SPIO cell labeling *in vitro* (Frank et al. 2004; Bernsen et al. 2010). Most of these techniques require different transfection agents, which cannot be used *in vivo* due to the associated high toxicity and systemic effects. We therefore studied a technique, based on ultrasound-activated ultrasound contrast agents that will be *in vivo* compatible. Our results show the potential of using this technique for safe and efficient *in vitro* SPIO endothelial cell labeling for MRI tracking. For future applications, one hour of SPIO incubation after ultrasound exposure (shown to be efficient in this study) can be reached by drip infusion. Even though SPIO blood half-life time is less than 8 min, SPIO can be safely administered by drip infusion for over 30 min (Reimer and Tombach 1998). The labeling efficiency in more than 10% should be also enough for MRI tracking.

10.5 CONCLUSION

Our study shows that ultrasound-activated tMB are a promising technique to non-invasively enhance SPIO uptake by endothelial cells. From the current *in vitro* study,

we derived optimal ultrasound parameters for SPIO delivery to HUVECs, that is, 40 kPa at 1 MHz, 10,000 cycles, 20 Hz pulse repetition frequency, applied for 30 seconds just before SPIO addition. This setting gives an up to 12 times increase of SPIO uptake compared to the control with 85% cell viability. The SPIO uptake was dependent on multiple factors, including the ultrasound settings, the time of SPIO addition, and the incubation time of SPIO with cells after the ultrasound treatment. Our data also suggests that SPIO uptake took place by pore formation and stimulated endocytosis.

11

Targeted microbubble mediated sonoporation of endothelial cells *in vivo*

Abstract — Ultrasound contrast agents as drug delivery systems are an emerging field. Recently, we reported that targeted microbubbles are able to sonoporate endothelial cells *in vitro*. In this study we investigated whether targeted microbubbles can also induce sonoporation of endothelial cells *in vivo*, thereby making it possible to combine molecular imaging and drug delivery. Live chicken embryos were chosen as *in vivo* model. $\alpha_v\beta_3$-targeted microbubbles attached to the vessel wall of the chicken embryo were insonified at 1 MHz at 150 kPa (1× 10.000 cycles) and at 200 kPa (1× 1.000 cycles) peak negative acoustic pressure. Sonoporation was studied by intravital microscopy using the model drug propidium iodide (PI). Endothelial cell PI uptake was observed in 48% at 150 kPa (n = 140) and in 33% at 200 kPa (n = 140). Efficiency of PI uptake depended on the local targeted microbubble concentration and increased up to 80% for clusters of 10-16 targeted microbubbles. Ultrasound or targeted microbubbles alone did not induce PI uptake. This intravital microscopy study reveals that sonoporation can be visualized and induced *in vivo* using targeted microbubbles.

Accepted for publication in the IEEE Transactions of Ultrasonics, Ferroelectrics, and Frequency Control, 2014; by I. Skachkov, Y. Luan, A.F.W. van der Steen, N. de Jong, K. Kooiman. The authors would like to thank Robert Beurskens, Frits Mastik and Michiel Manten (Erasmus MC, Rotterdam) for their technical assistance. The authors thank the Optical Imaging Centre of Erasmus MC for use of their confocal facilities.

11.1 INTRODUCTION

Ultrasound contrast agents (UCA) are widely used for increasing the ultrasound scattering of the blood pool. In cardiology, the contrast for example improves endocardial border delineation and allows quantification of myocardial perfusion (Wei 2012). In radiology, it, amongst others, can be used for detecting tumor perfusion (Madsen and Rasmussen 2011; Alzaraa et al. 2013). UCA are gas encapsulated microbubbles, which oscillate in response to ultrasound (Stride 2009). Currently, microbubbles with specific ligands attached to their coating, known as targeted microbubbles, are under investigation as contrast agents for ultrasound molecular imaging of cardiovascular disease and cancer (Lindner 2010; Kiessling et al. 2012).

Microbubbles are also a promising concept as ultrasound-triggered local drug delivery system. In general, an oscillating microbubble can increase the permeability of adjacent cell membranes and facilitate cellular drug uptake. This is known as sonoporation and can be crucial for cellular uptake of cell-impermeable drugs. Sonoporation has mostly been studied using non-targeted microbubbles. The mechanism still remains unknown (Hernot and Klibanov 2008; Bohmer et al. 2009; Sutton et al. 2013). Sonoporation has only been reported in cells adjacent to oscillating microbubbles (van Wamel et al. 2006; Fan et al. 2010), which can be a challenge *in vivo* because microbubbles circulate in the vasculature (Correas et al. 1997; Greis 2009). Recently, we reported that targeted microbubbles, which adhered to the cell, can induce sonoporation *in vitro* (Kooiman et al. 2011). At the same time, it has been reported that cells grown under flow are less susceptible to sonoporation (Park et al. 2011). Therefore reliable models for studying the mechanism and efficacy of sonoporation are a perquisite. Currently, intravital *in vivo* models exist for studying microbubble rheology and adherence of targeted microbubbles like rat or mouse cremaster muscle and dorsal skin-fold chamber, and hamster cheek pouch (Villanueva et al. 2007; Schneider et al. 2012; Xie et al. 2012), which potentially can be used for studying sonoporation. However, these models are complicated and also fall under strict animal experiment legislation regulations. This is not the case for chicken embryos, for which the chorioallantoic membrane (CAM) has been used by several groups for studying different types of drug delivery systems, including microbubbles (Stieger et al. 2007; Vargas et al. 2007). In this study we investigated if we could use the chorioallantoic membrane (CAM) model to in real time study targeted microbubble sonoporation *in vivo*. The microbubbles were targeted to $\alpha_v\beta_3$-integrin, since this integrin is constitutively expressed by chicken embryo endothelial cells (Jilani et al. 2003). Using intravital microscopy, we studied the uptake of the model drug propidium iodide by ultrasound-activation of adherent targeted microbubbles.

11.2 MATERIALS AND METHODS

11.2.1 Targeted microbubbles

Biotinylated lipid-coated microbubbles with a C_4F_{10} gas core were made by sonication as described by Klibanov et al (2004). The coating was composed of DSPC (59.4 mol %; P 6517; Sigma-Aldrich, Zwijndrecht, the Netherlands); PEG-40 stearate (35.7 mol %; P 3440; Sigma-Aldrich); DSPE-PEG(2000) (4.1 mol %; 880125 P; Avanti Polar Lipids, Alabaster, AL, USA) and DSPE-PEG(2000)-biotin (0.8 mol %; 880129 C; Avanti Polar Lipids). The purity of all lipids was > 99%. The fluorescent lipid dye DiI (Invitrogen, Bleiswijk, the Netherlands) was added to the lipid solution before sonication. Biotinylated anti-mouse $\alpha_v\beta_3$-antibody (R&D Systems, Europe, Abingdon, United Kingdom) was conjugated to the biotinylated microbubbles via avidin-biotin bridging by subsequent incubation of microbubbles with streptavidin and biotin (30 min each step) on ice as described by Lindner et al (Lindner et al. 2001) with the exception that less streptavidin and biotinylated antibody were added to 1×10^9 microbubbles, namely 20 µg and 5 µg respectively. By Coulter Counter (Multisizer 3, Beckman Coulter, Mijdrecht, the Netherlands) measurements we determined that the MB mean diameter was 2.5 µm.

11.2.2 Intravital microscopy CAM model

Fertilized White Leghorn chicken eggs (*Gallus gallus domesticus*) were purchased from Drost BV (Loosdrecht, the Netherlands). After 6 days of incubation in a humidified incubator at 37°C (stage HH27 according Hamburger-Hamilton criteria (Hamburger et al. 1992)), the embryo was taken out of the eggshell. Then, 7 µl of targeted microbubbles (1×10^8 targeted microbubbles/ml) were mixed with 2 µl of PI (final concentration 0.2 mg/ml Sigma Aldrich, Zwijndrecht, the Netherlands) and 1 µl of Hoechst 33342 (final concentration 1 mg/ml Invitrogen) at room temperature just before the injection. Five µl of this mixture was injected in one of the vitelline veins using a capillary glass needle and the Visualsonics injection system (VisualSonics Inc., Toronto, ON, Canada). After injection, the embryo was placed back in the incubator for 15 min to allow targeted microbubbles to circulate and adhere to the vessel wall. Then, the yolk was removed (Williams and Ordahl 1996) to increase embryo transparency. The upper part of an OptiCell chamber (NUNC, Wiesbaden, Germany) was cut out and the space was filled with 1% agarose (Sigma Aldrich, Zwijndrecht, the Netherlands). The yolkless embryo was then placed on the agarose, pinned with entomology pins (size 000) and put in the experimental setup, with implemented heating system to keep the embryo at 37 °C, see Fig. 11.1.

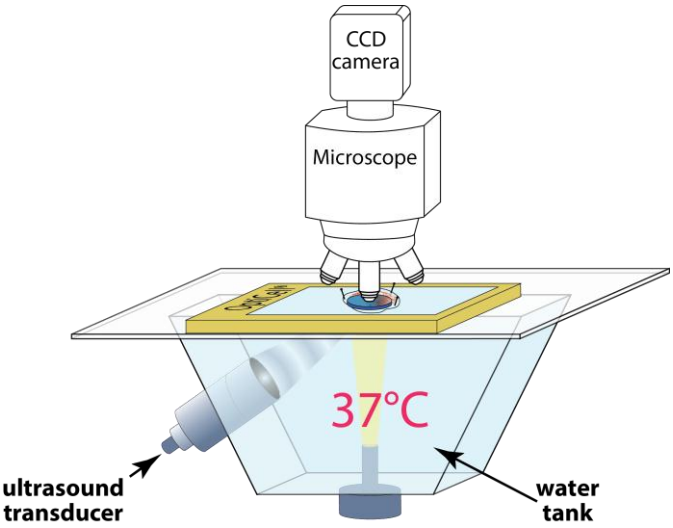

Figure 11.1. Experimental setup (not drawn to scale).

The Olympus microscope was equipped with a high sensitivity CCD camera (LCL-902K, Watec, Orangeburg, NY, USA), a 40× water-immersed objective (LUMPlanFI, NA 0.8, Olympus) and fluorescent filter sets suitable for detection of DiI and PI (U-MWG2 filter, excitation 510-550nm, emission 590nm, Olympus), and Hoechst (U-MWU2 filter, excitation 330-385nm, emission 420nm, Olympus). Targeted microbubbles were insonified with a 1 MHz single element transducer (V302; Panametrics-NDTTM, Olympus NDT, Waltham, MA, USA) using a single burst of a 10.000 cycle sine-wave at 150 kPa peak negative acoustic pressure (P_) or a single burst of a 1.000 cycle sine-wave burst at P_ = 200 kPa. Prior to the study the transducer was calibrated with a 0.2 mm PVDF needle hydrophone (Precision Acoustics Ltd, Dorchester, UK). The -6dB diameter of the insonified area in focus was found to be 7.2 mm. To be sure that insonified areas were not overlapping every microbubble-vessel wall complex was studied in different parts of the CAM and no more than four microbubble-vessel wall complexes were studied per embryo.

Before, during and after insonification, images were recorded with a high-sensitivity CCD video camera (25 frames/second; LCL-902K, Watec). The total field of view (FOV) was 78×58 µm. The cell membrane impermeable dye PI was used as indicator for sonoporation. The nuclear dye Hoechst 33342 was used to find the focal plane of the endothelial cell nuclei before insonification. Sonoporation was studied in CAM vessels of more than 50 µm in diameter. The duration of the experiment with one embryo was no longer than two hours.

In all experiments, microbubbles were considered a cluster, when they were no more than 3 μm apart, which was the average single microbubble diameter. Targeted microbubbles laying more than 10 μm (i.e. an average nucleus size) apart from each other were considered as a separate cluster, and therefore excluded from the experiment, as we wanted to study single microbubble or single cluster-vessel wall complexes.

11.2.3 Immunofluorescence

Immunofluorescent $\alpha_v\beta_3$-integrin staining of a vitelline vein was done on a 6-day old chicken embryo. Fluorescent Oregon Green 488 streptavidin (1 mg/ml; Invitrogen) was mixed with biotinylated $\alpha_v\beta_3$ antibody (0.5 mg/ml; R&D Systems; see 2A) or corresponding biotinylated IgG1 κ antibody (BD Biosciences, Breda, the Netherlands) in 1:1 volume ratio and incubated for 30 min at room temperature under agitation (30 RPM on an orbital rotator PTR-35, Grant-bio, Shepreth, UK). A glass capillary needle was placed in a vitelline vein as described before and the vessel was cut ~0,5 cm upstream and downstream to the injection site. Then, the vessel was perfused with 5 μl of the fluorescent streptavidin antibody mixture and the needle was taken out. Perfusion with antibody only or streptavidin only was used as control. After 5 min, the vein was flushed with 5 μl of PBS by inserting the capillary needle downstream into the lumen. Then ~1 cm^2 CAM tissue piece was cut and fixated with 4% formaldehyde for 5 min. After fixation, the sample was washed three times with PBS and embedded in Mowiol (Merck, Darmstadt, Germany). Confocal fluorescent microscopy was performed with an inverted microscope (LSM510META; Carl Zeiss, Germany), 10× lens (Plan-Neofluar, NA 0.3), excitation of 488 nm, and emission of 530-600 nm.

11.3 RESULTS

Fig. 11.2 shows $\alpha_v\beta_3$-integrin immunofluorescent staining in chorioallantoic membrane veins of 6 day-old chicken embryos. $\alpha_v\beta_3$-integrin staining was observed throughout the vessel (Fig. 11.2A) indicating the targeted microbubbles could bind at different locations within the vasculature. The fluorescent signal was present only in the vein (see Fig. 11.2B), because only the vein was perfused with the fluorescent streptavidin - $\alpha_v\beta_3$-integrin antibody complex. The fluorescent streptavidin - control antibody conjugate perfusion did not show significant fluorescence (Fig. 11.2C). When the vein was perfused with fluorescent streptavidin alone or with antibody alone, we did not observe any fluorescent staining.

Sonoporation was only studied in embryos that had stable and continuous blood flow. In total we studied 280 targeted microbubble-vessel wall complexes that were

randomly selected (n = 80 embryos) at least ~100 µm away from branches avoiding oscillatory blood flow. Only microbubble-vessel wall complexes at the top of the vessel could be studied as the red blood cells obscured other vessel wall locations.

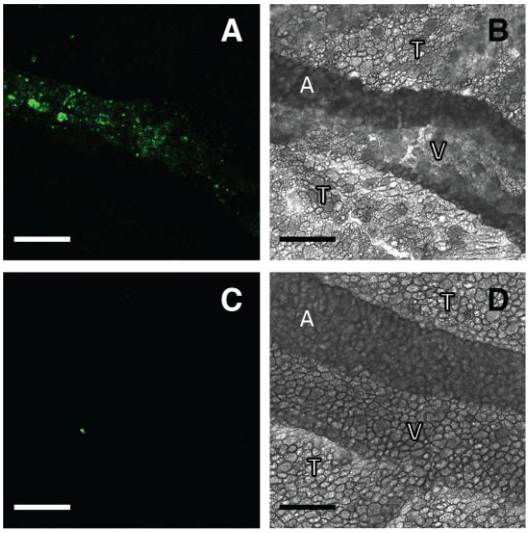

Figure 11.2. $\alpha_v\beta_3$-integrin expression in 6 day-old chicken embryos veins. Immunofluorescent (A, C) and corresponding bright field (B, D) image of veins (V), arteries (A) and surrounding tissue (T) of CAM vein perfused with fluorescent streptavidin $\alpha_v\beta_3$-integrin (A, B) and control antibody (C, D) conjugates. Scale bar 100 µm.

We observed that different numbers of targeted microbubbles adhered to the vessel wall, ranging from 1 to 16. An example of six targeted microbubbles attached to the vessel wall is shown in Fig. 11.3. In Fig 11.3A the bright field image shows the six attached targeted microbubbles before insonification. Fluorescent staining with Hoechst 33342 highlighted all cell nuclei of the vessel wall surrounding the targeted microbubbles, as shown in Fig. 11.3B. Fig. 11.3C shows the same six targeted microbubbles in fluorescence before ultrasound application. It also shows that the endothelial cells did not contain PI before ultrasound application. No microbubbles were observed in the FOV after ultrasound application (200 kPa, 1.000 cycles). After insonification, PI uptake was detected in the nuclei of two endothelial cells as displayed in Fig. 11.3D. Only the cells to which the six targeted microbubbles adhered demonstrated PI uptake, indicating these cells got sonoporated.

In total, endothelial cell PI uptake was observed in 48% at 150 kPa (10.000 cycles; n = 140) and in 33% at 200 kPa (1.000 cycles; n = 140). In all cases, we did not observe any microbubbles in the FOV after the ultrasound application. The uptake of PI as a function of the number of adherent targeted microbubbles is shown in

Fig. 11.4. When 1 or 2 targeted microbubbles adhered, we observed no uptake for 150 kPa and 5% of PI uptake for 200 kPa. The sonoporation efficiency increased when more targeted microbubbles adhered. For both P_, PI uptake increased up to 80% when 10-16 targeted microbubbles adhered. In addition, a higher local concentration of targeted microbubbles increased the probability of sonoporation of more than one cell as also shown in Fig. 11.4. Sonoporation of different number of cells is indicated by the colors in the staked columns: blue for one single sonoporated cell, red for two cells, green for three cells and purple for four sonoporated cells. When 1-5 targeted bubbles adhered, we only observed single cell sonoporation at both P_. At 150 kPa, clusters of 6-10 targeted microbubbles sonoporated one cell (15.4%), two cells (30.8%), three cells (38.5%), and four cells (15.4%). For clusters of 10-16 targeted microbubbles this was 26.7%, 40%, 33.3%, and 0% respectively. At 200 kPa, clusters of 6-10 targeted microbubbles induced sonoporation of one cell (27.3%), two cells (54.5%), and three cells (18.2%). For 10-16 adherent targeted microbubbles, this was 18.8%, 50%, and 31.2% respectively.

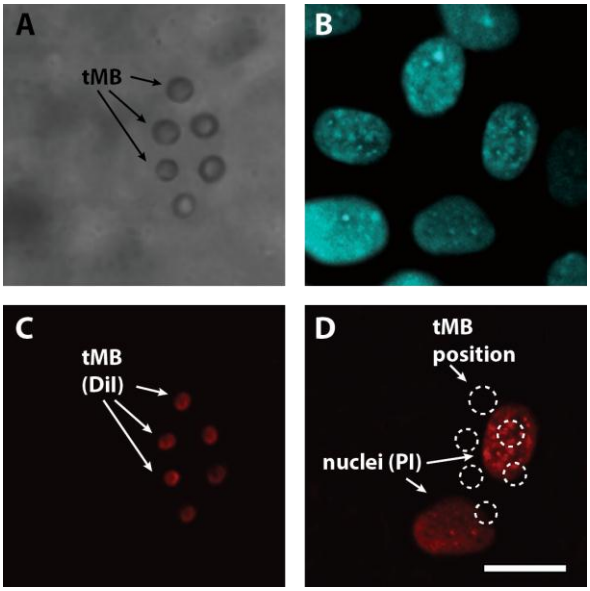

Figure 11.3. PI uptake by endothelial cells in live chicken embryo (35x35 µm cropped images). (A) Bright field image of targeted microbubbles adhering to the vessel wall; (B) Nuclei of endothelial cells stained with Hoechst 33342; (C) Fluorescence image before ultrasound application; (D) Fluorescence image 3 min after ultrasound application. Image C and D were made with the same light filter settings. Applied ultrasound: 1 MHz, 200 kPa, 1.000 cycles. Scale bar 10 µm.

Extravasation of red blood cells or vessel rupture was not noticed at these low acoustic pressures. There was no significant difference in mean heart rate before (80 ± 15 beats per minute) and after the experiment (82 ± 18 beat per minute), suggesting no vasculature damage. Ultrasound or targeted microbubbles alone did not induce PI uptake.

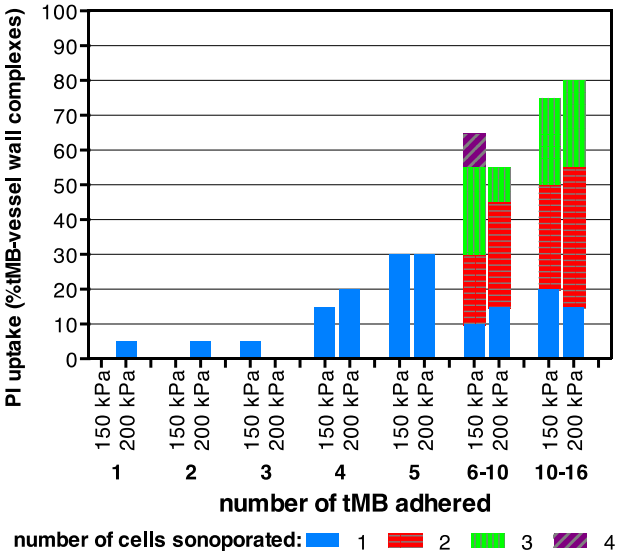

Figure 11.4. Efficiency of PI uptake as function of the number of adhered targeted microbubbles (tMB) (n=280 separate FOV). For every condition 20 single cell microbubble complexes were observed for 1, 2, 3, 4, 5, 6-10, and 10-16 adhered targeted microbubbles. Colors in stack columns indicates: blue - one cell, red - two cells, green - three cells, and purple - four cells sonoporated after sonication of one microbubble-vessel wall complex.

11.4 DISCUSSION

To the best of our knowledge, this is the first study that shows that targeted microbubbles can induce sonoporation *in vivo*. In addition, we showed the suitability of the CAM model to study sonoporation in real time using intravital microscopy.

In this study we used two DNA binding dyes: Hoechst 33342 and PI. Hoechst is a cell membrane permeable non-intercalating dye, which binds to the minor groove of DNA and stains nuclei of live cells (Sriram et al. 1992). PI binds to DNA and RNA by intercalating between the bases (Wilson et al. 1985). In addition, PI is impermeable for live cells and can only permeate live cells when the cell membrane is compromised. Because these two dyes have different DNA binding sites, it is unlikely that we underestimated sonoporation due to simultaneous use of these dyes.

In our study we applied low acoustical pressure ultrasound to targeted microbubble-vessel wall complexes. We observed similar sonoporation efficiencies at 150 kPa (1×10.000 cycles) and 200 kPa (1×1.000 cycles), suggesting both are equally well suited for inducing sonoporation *in vivo* in the CAM model. As Mannaris et al. (2012) showed a gradual decrease in the scattered ultrasound by lipid-coated microbubbles at 200 kPa and 1 MHz, this may suggest our microbubbles were not responding anymore beyond 1.000 cycles and thus could explain why we found similar results.

We found that sonoporation efficiency increased when more targeted microbubbles adhered to the vessel wall. A higher local microbubble concentration also increased the chance of sonoporating more than one cell. This could be explained by more microbubbles having a larger interaction area with the cells, thus probably inducing more pores. Another reason could be that the multiple microbubbles oscillated as one cluster. A microbubble cluster may have a different resonance frequency which could have been closer to the transducer excitation frequency of 1 MHz (Kotopoulis and Postema 2010). This could have resulted into larger microbubble oscillations as microbubbles at resonance have a maximum amplitude of oscillation (Stride 2009).

Recently, other groups have identified drug-loaded targeted microbubbles to be up to 5.5 times more effective than non-targeted microbubbles (Phillips et al. 2012; Xie et al. 2012; Chang et al. 2013; Fan et al. 2013; Tlaxca et al. 2013). As we found the local targeted microbubbles concentration to be an important factor for efficiency of targeted microbubble sonoporation, getting enough microbubbles to adhere at the site of treatment is important. Studies are ongoing to improve adherence of targeted microbubbles which include dual targeting (Ferrante et al. 2009; Maul et al. 2010), varying ligand linker length (Ham et al. 2009), deflating microbubbles (Rychak et al. 2006), or changing microbubble shell composition (Kooiman et al. 2012), whilst models reveal an optimal microbubble radius of 1-2 μm (Maul et al. 2010). Furthermore, targeted microbubbles can be pushed towards the vessel wall to increase binding under flow conditions by acoustic radiation force (Rychak et al. 2007; Gessner et al. 2012) or a magnetic field (Owen et al. 2012).

In our current study, we observed all microbubbles to be gone from the field of view after ultrasound application. This may be due to microbubble deflation, but for microbubble clusters could also have been due to microbubble detachment as it was previously reported that neighboring microbubbles attract one another. This attractive force detaches one of the microbubbles when it exceeds the binding force (Kokhuis et al. 2013).

The dose of targeted ultrasound contrast agent used in our study was 5 μl of 1×10^8 microbubbles/ml. Assuming the total HH27 chicken embryo blood volume is 170 μl

(Kind 1975), the final targeted microbubbles concentration in the embryo blood was 2.8×10^6 microbubbles/ml. This concentration is similar to the recommended concentration in blood of the ultrasound contrast target-ready MicroMarker® by VisualSonics® for molecular imaging studies in mice.

In our study we did not notice red blood cell extravasation, which can be a side effect or desired bio-effect of ultrasound-activated microbubble therapy. (Stieger et al. (2007) observed real time dextran (150 kDa; 8.5 nm) extravasation and using electron microscopy identified intracellular and intercellular gaps and extravasation of blood in the CAM model. They used higher acoustic pressures than we did, namely 500 kPa and higher. The authors attributed this to jetting of microbubbles, which is one of the proposed microbubble behaviors needed to stimulate drug uptake. As the mechanism of stimulated drug uptake by ultrasound-activated microbubbles is still unknown (Sutton et al. 2013), the CAM model seems a promising model to in real time study microbubble-cell interactions to unravel the mechanism. Depending on therapeutic goals, this will allow control over the type of stimulated drug uptake so vessel damage can be avoided when desired.

We previously reported that sonoporation by targeted microbubbles *in vitro* depended upon the amplitude of oscillation as we found a threshold above which the microbubbles had to oscillate to induce sonoporation. To visualize the oscillations of the microbubbles, we used the Brandaris 128 high-speed camera in that study (Kooiman et al. 2011). In another study we reported about the feasibility of using the yolkless CAM model to characterize microbubble oscillations *in vivo* with the Brandaris 128 (Faez et al. 2012). Our future research will focus on combining *in vivo* targeted microbubble behavior and real time sonoporation using the CAM model.

The main limitation of our study is using chicken embryos as *in vivo* model as the embryonic vessels may not resemble the clinical situation. For example, they have has less tight endothelial cell junctions (Ribatti et al. 2001), making these neovessels more permeable and hence maybe more easily affected by ultrasound-activated microbubbles. However, neovessels are also associated with tumors and atherosclerotic plaques (Michel et al. 2011; Lampugnani 2012; Bottos and Bardelli 2013), which may make the CAM model a relevant *in vivo* model for studying ultrasound and microbubble-mediated therapy to treat these diseases.

In conclusion, this is the first study that shows that targeted microbubbles are able to induce sonoporation *in vivo* using the low acoustic pressure of 150kPa and 200 kPa at 1 MHz. This method can be used to combine molecular ultrasound imaging with drug delivery for the detection and treatment of cardiovascular diseases and cancer.

12
Discussion and conclusions

When the oak is felled the whole forest echoes with it fall,
but a hundred acorns are sown in silence by an unnoticed breeze.

— *Thomas Carlyle*

In this thesis, new systems and methods have been developed and optimized for in-depth understanding of the microbubble acoustic response to achieve future application of controlled drug delivery. Both conventional lipid-coated microbubbles and novel drug-carrying vehicles (i.e., liposome-loaded microbubbles, echogenic liposomes) were studied. Three major topics were investigated experimentally. First is the optical and acoustical characterization of single microbubbles (e.g., stability, nonlinearity, bubble size, shell properties) (**Chapter 2-5**). Second is the monitoring of lipid shell materials shedding relative to bubble vibrational dynamics from both the top-view and the side-view (**Chapter 6-9**). The last section focuses on the application of contrast-enhanced ultrasound-mediated delivery of materials (e.g., SPIO particles) *in vitro* (endothelial cells) and *in vivo* (chicken embryo) (**Chapter 10, 11**). The acoustic response of individual bubbles varies due to the surrounding physical environment (e.g., temperature and the viscosity of surrounding medium), ultrasound settings (i.e., exciting frequency, pressure, pulse length) and, last but not the least, the intrinsic bubble properties (i.e., the bubble size, shell viscoelastic properties).The series of studies presented in this thesis not only emphasizes the variability of individual microbubble behavior, but also aims to extract common characteristics from bubble populations that were investigated. The main outcomes will be discussed and summarized based on our understanding, and implications for clinical applications will be formulated in the following sections.

12.1 NEW SYSTEMS AND METHODS

Development of novel systems and methods enabled in-depth investigations on single microbubble acoustic response (e.g., vibrational dynamics, fragmentations, dissolution and lipid shedding) in this thesis. In **Chapter 3**, a broadband impulse response technique was used to optically characterize single echogenic liposome (ELIP) agents. Compared to the spectroscopy approach applied in **Chapter 2**, only a single exposure was required and the analysis procedure was largely simplified. In **Chapter 4**, we developed a high-speed segmented imaging scheme of Brandaris 128 camera. Microbubble vibrations under a prolong ultrasound burst were monitored within small time windows distributed over a much longer excitation duration (0.5 - 0.6 ms). In **Chapter 5**, we were able to characterize single freely-floating microbubbles exposed to prolonged ultrasound bursts (of up to milliseconds) for the first time. A co-flow device was combined with an ultra-fast acoustic measurement system, which utilizes the highly-sensitive dual-frequency radial modulation technique. This system provides a simple approach for statistical measurements on a larger population of microbubbles as an alternative to the ultra-fast framing camera. A combined setup of Photron camera and Brandaris camera developed in **Chapter 6-9**

enabled an in-depth investigation of lipid shedding behavior relative to the microbubble vibrational dynamics. Particularly, by rotating the microscope system 45° and keeping sufficient light for two high-speed cameras, we obtained side view observations to uncover the non-spherical lipid shedding and transport phenomena.

12.2 PARAMETRIC STUDIES

One of the major topics in this thesis is the characterization of individual microbubble responses (e.g., vibrations, fragmentations, lipid shedding and dissolution) under different experimental settings. To manipulate the bubble response using the optimal setting was the goal. The experimental conditions (parameters investigated) for each chapter are listed in Table 12.1. First and foremost, the acoustic pressure showed to be one of the key factors to determine the microbubble vibrational response and corresponding physical phenomena (e.g., stability, nonlinearity, fragmentations, lipid shedding and sonoporation). For instance, bubble fragmentations and lipid shedding events occur when the applied pressure is above several hundreds of kPa (**Chapter 8 and 9**) and the occurrence of lipid shedding increases with the pressure (**Chapter 6**). Second, the pulse length exhibited less influence than the pressure on lipid shedding, but prominently affects events taking place on a longer time scale (e.g., transport of shell materials by the surrounding streaming flow field). Both the pressure and the pulse length strongly influence cellular uptake of SPIO particles driven by sonoporation and stimulated endocytosis, which can be related with induced bubble dynamics and the acoustic streaming generated by the prolonged ultrasound burst (Vos 2010). Third, the frequency and the bubble size are complementary factors for the bubble resonance behavior. For a population of individual bubbles of various sizes, a fixed frequency of 1 MHz was used in most studies in this thesis (**Chapter 4-11**). We chose this value due to that it is close to the frequency applied in clinical diagnostic imaging, and it was widely used for previous studies both *in vitro* and *in vivo* (Hwang et al. 2005). The lipid shedding behavior was also investigated as a function of the microbubble oscillation amplitude (**Chapter 6-9**), which represents the combined effect of the acoustic pressure, the frequency and the bubble size. A threshold value (~30% of the relative oscillation amplitude) exists for the occurrence of lipid shedding events and/or the accompanied bubble dissolution.It should be noted that although extensive parametric studies has been performed *in vitro*, more factors should be taken into consideration for applications of ultrasound-controlled drug delivery *in vivo*. A major difference would be the flow environment (e.g., viscosity between water in *in vitro* studies and blood in vivo) which can dramatically change the bubble stability, oscillation dynamics, and the

streaming flow field generated in the surroundings (Kabalnov et al. 1998; Faez et al. 2012).

Table 12.1. An overview of the experimental settings (conditions) for all chapters in this thesis (The tick symbol represents that the corresponding parametric study was performed).

Chapter	Acoustic settings			Temperature (°C)	Bubble size	Investigated microbubble samples				High-speed (fluorescence) imaging (fps)	
	Pressure	Pulse length	Frequency			Lipid - coated		Liposome loaded	Echogenic liposomes	Brandaris	Photron
						Non - targeted	Targeted				
2	✓		✓	22	✓	☑		☑		15 M	
3	✓		broadband	37	✓				☑	17 M	
4	✓		1 MHz	22	✓	☑				5 M	
5	✓					☑					6 K
6	✓	✓			✓	☑				10 M	2 images
7	✓	✓			✓			☑		10 M/2 M	2 images
8	✓							☑		10 M	1 K
9	✓				✓		☑			5 M	5 K
10	✓	✓		37			☑				
11		✓					☑				

12.3 LIPID SHEDDING

One of the major investigations performed in this thesis is the characterization of the lipid shell material shedding from the microbubble surface. Two separate physical processes were distinguished: the detachment of shell materials from the microbubble surface, and the subsequent transport of the detached particles by the convective medium surrounding the microbubble. The shedding event occurs on a time scale which is 2-3 orders of magnitude faster than the transport. Therefore, we define the occurrence of shedding by the observations of the transport. We found a threshold in microbubble oscillation amplitude (~30%) to initiate the shedding event. Two shedding dynamics were differentiated according to the trajectory of transport, in-plane shedding and out-of-plane shedding. In-plane shedding is the transport of lipid clusters (and/or liposomes) within or parallel to the focal plane. In contrast, the dominant out-of-plane shedding was not as intuitive. Observed from the top view, it appeared as the spreading of a fluorescent halo around the microbubble. However, the side view observations showed a non-spherical transport trajectory out of the focal plane. Three shedding mechanisms were captured: lipid oversaturation, pinch off of fragmented daughter bubbles, and jetting. Specifically, jetting leads to the deposition of large amounts of shell materials directly on the supporting membrane, which is preferable for the application of controlled drug delivery. Both the top view and the side view studies revealed that lipid shedding is accompanied by considerable

microbubble destruction, including fragmentation and gas exchange during bubble vibrations (leading to instantaneous dissolution normally within 1 ms), as well as the subsequent static dissolution (over hundreds of milliseconds) due to the loss of shell materials. Figure 12.1 presents an overview of different lipid shedding regimes.

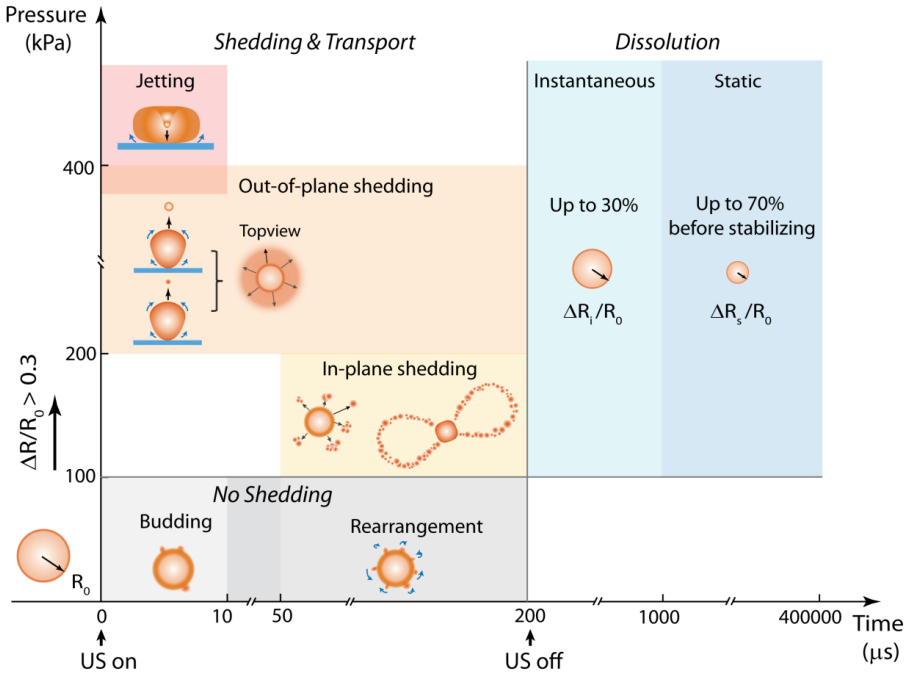

Figure 12.1. A schematic overview of lipid shedding behavior and the microbubble dissolution based on the experimental observations in this thesis. Different colors represent different regimes of events. R_0 – intial bubble radius; $\Delta R/R_0$ – relative amplitude of oscillation; $\Delta R_i/R_0$ – size reduction due to instantaneous dissolution; $\Delta R_s/R_0$ – size reduction due to static dissolution.

12.4 EFFECTS OF LIPOSOME LOADING

We have shown in **Chapter 2** that liposome-loaded microbubbles exhibit higher damping of the oscillation compared with lipid-shelled microbubbles. Assuming the same physical conditions, we derived a larger shell viscosity for liposome-loaded microbubbles. Correspondingly, we observed a higher pressure threshold to initiate bubble oscillations -- the previously described thresholding behavior (Emmer et al. 2007) -- which was ascribed to the more substantial energy losses resulting from the interactions between densely distributed liposomes. Another possible reason can be

the addition of cholesterol in the liposome formulation to maintain the membrane integrity (Geers et al. 2011). However, as was reported in **Chapter 3**, for the echogenic liposomes with a similar formulation of encapsulating liposomes, no apparent difference in shell damping was found compared to lipid-coated bubbles. Therefore the first explanation of the increasing shell viscosity for liposome-loaded microbubbles could be valid in our opinion.

Considering the release of shell materials, liposome-loaded microbubbles did not shown prominent differences compared to lipid-coated bubbles, as was illustrated by **Chapter 6-8**. We derived a comparable threshold of relative oscillation amplitude (~30-35% for both lipid-shelled bubbles and liposomes-loaded bubbles). Additionally, similar shedding dynamics was observed for both categories, and the rate of long term dissolution (hundreds of milliseconds) after the ultrasound excitation for the two groups were comparable. Therefore we hypothesized that for liposome-loaded microbubbles, the liposome particles were detached together with portions of the phospholipid shell, leading to shell materials loss. It seems that the increased damping of microbubble vibrations imparted by loading liposomes onto the microbubble surface, as was reported earlier, does not lead to an apparent difference in the shedding behavior. However, it should be noted that the high-speed fluorescence imaging approach was not able to provide quantitative measurements for lipid shedding. The current setup is therefore limited to detecting qualitative differences (e.g., the threshold of shedding events, the amount of lipid shedding) between the two groups.

12.5 CLINICAL RELEVANCE AND FUTURE PROSPECTS

12.5.1 Single bubble characterization techniques

In order to optimize ultrasound contrast agent microbubbles for diagnostic and therapeutic applications, it is of high necessity to develop single bubble characterization techniques which can perform fast, continuous and simple measurements on large quantities of microbubbles. Studies in this thesis made various attempts. A wide-band detection scheme with ultra-high speed camera Brandaris (**Chapter 3**) enabled bubble characterization with a single exposure. In another scheme, the exposure was segmented in order to resolve the bubble acoustic response over long bust excitations (**Chapter 4**). Lastly, the sensitive bubble characterization technique combined with simultaneous optical sizing (**Chapter 5**) for the first time realized statistical studies on single freely-floating microbubbles. This system is also a potential tool for characterizing single bubbles by primary radiation force. With further improvements in triggering scheme and alignment procedure, it

might be commercially realizable in the near future as an assistive "black box" to obtain pre-knowledge of new agents for researchers and clinicians.

12.5.2 Targeted microbubbles

Comparing to microbubbles floating against a nearby membrane, microbubble targeting did not introduce any visible change in the shedding dynamics and vibrational amplitude (**Chapter 9**). Previous knowledge on non-targeted microbubbles floating against a wall can be utilized to predict the behavior of targeted bubbles. From the *in vivo* perspective, using targeted microbubbles instead of non-targeted microbubbles is preferable for diagnostic imaging and localized drug delivery since targeted bubbles are close to the endothelium and can be specifically targeted to diseased cells (**Chapter 10**).

12.5.3 Combined diagnostic and therapeutic applications

Among three regimes of lipid shedding dynamics, the lipid oversaturation and the pinch off of daughter bubble fragments are the most commonly observed phenomena. The transport distance is several tens of microns, which can be used for drug deliveries in capillaries (5-10 μm) and arterioles (20-30 μm). However, for drug delivery in larger veins or arteries (0.5-8 mm), jetting is the most preferable regime since the detached agents can be delivered directly to the cell membrane where targeted microbubbles are attached to.

For applications combining ultrasound imaging and drug delivery, the stability of microbubbles is crucial. At low pressures (≤100 kPa), stable bubble response was found within the first few milliseconds (**Chapter 5**). This can be utilized to design the imaging pulse sequence. For drug delivery applications, sufficient acoustic pressure (> 200 kPa) should be applied with a frequency near the main resonance frequency of the microbubble population (**Chapter 6**). After releasing the agents, bubbles shrink quickly within hundreds of milliseconds (**Chapter 8**). Only bubbles much larger or much smaller than the resonance size will persist. Therefore applying different pulse schemes (e.g., adjusting applied frequency) before and after the shedding event is necessary.

With the various progresses in understanding the acoustic behavior of contrast agents *in vitro* and *in vivo* outlined in this thesis, we made a crucial step closer to clinical realization of contrast-mediated ultrasound-controlled drug delivery. However, more knowledge on bubble-cell interactions and bubble acoustic response for *in vivo* conditions is needed to make this a reality. Our interpretation of the micro-world is based on direct observations. As we already learned in lipid shedding studies, a side view observation gave us completely new perspectives comparing to the top

view. I believe that the development of new techniques and attempts at looking from new angles will improve our knowledge and understanding of this micro-world.

Bibliography

Adrian, R J and C S Yao, Pulsed laser technique application to liquid and gaseous flows and the scattering power of seed materials. *Appl Opt*, 24(1): 44-52, 1985.

Agneni, A and L Balis-Crema, Damping measurements from truncated signals via Hilbert transform. *Mechanical Systems and Signal Processing*, 3(1): 1-13, 1989.

Ainslie, M A and T G Leighton, Review of scattering and extinction cross-sections, damping factors, and resonance frequencies of a spherical gas bubble. *J Acoust Soc Am*, 130(5): 3184-3208, 2011.

Alkan-Onyuksel, H, S M Demos, G M Lanza, M J Vonesh, M E Klegerman, B J Kane, J Kuszak, and D D McPherson, Development of inherently echogenic liposomes as an ultrasonic contrast agent. *J. Pharm. Sci.*, 85(5): 486-490, 1996.

Alzaraa, A, G Gravante, W Y Chung, D Al-Leswas, B Morgan, A Dennison, and D Lloyd, Contrast-enhanced ultrasound in the preoperative, intraoperative and postoperative assessment of liver lesions. *Hepatol Res*, 43(8): 809-819, 2013.

Armstrong, J K, R B Wenby, H J Meiselman, and T C Fisher, The hydrodynamic radii of macromolecules and their effect on red blood cell aggregation. *Biophys J*, 87(6): 4259-4270, 2004.

Baoukina, S, L Monticelli, H J Risselada, S J Marrink, and D P Tieleman, The molecular mechanism of lipid monolayer collapse. *Proc. Natl. Acad. Sci. U. S. A.*, 105(31): 10803-10808, 2008.

Batchelor G. K., An introduction to fluid dynamics. F.R.S., London (Cambridge University Press), 1967. Pp. xvii, 615; Plates 24; Numerous Figures. *Quarterly Journal of the Royal Meteorological Society*, 94(401): 435-435, 1968.

Benjamin, T B and A T Ellis, The Collapse of Cavitation Bubbles and the Pressures thereby Produced against Solid Boundaries. *Philosophical Transactions of the Royal Society of London. Series A, Mathematical and Physical Sciences*, 260(1110): 221-240, 1966.

Bernsen, M R, A D Moelker, P A Wielopolski, S T van Tiel, and G P Krestin, Labelling of mammalian cells for visualisation by MRI. *European radiology*, 20(2): 255-274, 2010.

Biedermann, B C, B Coll, D Adam, and S B Feinstein, Arterial microvessels: an early or late sign of atherosclerosis? *J. Am. Coll. Cardiol.*, 52(11): 968; author reply 968-969, 2008.

Bohmer, M R, A L Klibanov, K Tiemann, C S Hall, H Gruell, and O C Steinbach, Ultrasound triggered image-guided drug delivery. *Eur J Radiol*, 70(2): 242-253, 2009.

Borden, M A, Nanostructural features on stable microbubbles. *Soft Matter*, 5(4): 716-720, 2009.

Borden, M A, D E Kruse, C F Caskey, S K Zhao, P A Dayton, and K W Ferrara, Influence of lipid shell physicochemical properties on ultrasound-induced microbubble

destruction. *Ieee Transactions on Ultrasonics Ferroelectrics and Frequency Control*, 52(11): 1992-2002, 2005.

Borden, M A and M L Longo, Dissolution behavior of lipid monolayer-coated, air-filled microbubbles: Effect of lipid hydrophobic chain length. *Langmuir*, 18(24): 9225-9233, 2002.

Borden, M A and M L Longo, Oxygen Permeability of Fully Condensed Lipid Monolayers. *The Journal of Physical Chemistry B*, 108(19): 6009-6016, 2004.

Borden, M A, G V Martinez, J Ricker, N Tsvetkova, M Longo, R J Gillies, P A Dayton, and K W Ferrara, Lateral phase separation in lipid-coated microbubbles. *Langmuir*, 22(9): 4291-4297, 2006.

Bottos, A and A Bardelli, Oncogenes and angiogenesis: a way to personalize anti-angiogenic therapy? *Cell Mol Life Sci*, 70(21): 4131-4140, 2013.

Bouakaz, A, M Versluis, and N de Jong, High-speed optical observations of contrast agent destruction. *Ultrasound Med. Biol.*, 31(3): 391-399, 2005.

Buchanan, K D, S Huang, H Kim, R C MacDonald, and D D McPherson, Echogenic liposome compositions for increased retention of ultrasound reflectivity at physiologic temperature. *J. Pharm. Sci.*, 97(6): 2242-2249, 2008.

Castle, J, M Butts, A Healey, K Kent, M Marino, and S B Feinstein, Ultrasound-mediated targeted drug delivery: recent success and remaining challenges. *Am J Physiol Heart Circ Physiol*, 304(3): H350-357, 2013.

Chang, C and R L Powell, Effect of particle size distributions on the rheology of concentrated bimodal suspensions. *Journal of Rheology (1978-present)*, 38(1): 85-98, 1994.

Chang, S, J Guo, J Sun, S Zhu, Y Yan, Y Zhu, M Li, Z Wang, and R X Xu, Targeted microbubbles for ultrasound mediated gene transfection and apoptosis induction in ovarian cancer cells. *Ultrason Sonochem*, 20(1): 171-179, 2013.

Chapman, R B and M S Plesset, Thermal Effects in the Free Oscillation of Gas Bubbles. *Journal of Fluids Engineering*, 93(3): 373-376, 1971.

Chatterjee, D and K Sarkar, A Newtonian rheological model for the interface of microbubble contrast agents. *Ultrasound Med Biol*, 29(12): 1749-1757, 2003.

Chen, X, J Wang, M Versluis, N de Jong, and F S Villanueva, Ultra-fast bright field and fluorescence imaging of the dynamics of micrometer-sized objects. *Rev Sci Instrum*, 84(6): 063701, 2013.

Chetty, K, E Stride, C A Sennoga, J V Hajnal, and R J Eckersley, High-speed optical observations and simulation results of SonoVue microbubbles at low-pressure insonation. *IEEE Trans Ultrason Ferroelectr Freq Control*, 55(6): 1333-1342, 2008.

Chin, C T, C Lancee, J Borsboom, F Mastik, M E Frijlink, N de Jong, M Versluis, and D Lohse, Brandaris 128: A digital 25 million frames per second camera with 128 highly sensitive frames. *Rev. Sci. Instrum.*, 74(12): 5026-5034, 2003.

Choi, J J, J A Feshitan, B Baseri, S Wang, Y S Tung, M A Borden, and E E Konofagou, Microbubble-size dependence of focused ultrasound-induced blood-brain barrier opening in mice *in vivo*. *IEEE Trans. Biomed. Eng.*, 57(1): 145-154, 2010.

Chomas, J E, P Dayton, J Allen, K Morgan, and K W Ferrara, Mechanisms of contrast agent destruction. *IEEE Trans Ultrason Ferroelectr Freq Control*, 48(1): 232-248, 2001.

Chomas, J E, P Dayton, D May, and K Ferrara, Threshold of fragmentation for ultrasonic contrast agents. *J Biomed Opt*, 6(2): 141-150, 2001.

Chomas, J E, P A Dayton, D May, J Allen, A Klibanov, and K Ferrara, Optical observation of contrast agent destruction. *Applied Physics Letters*, 77(7): 1056-1058, 2000.

Church, C C, The effects of an elastic solid surface layer on the radial pulsations of gas bubbles. *The Journal of the Acoustical Society of America*, 97(3): 1510-1521, 1995.

Clark, G, *Staining procedures used by the Biological Stain Commission*. 3 ed. 1973: Published for the Biological Stain Commission by Williams & Wilkins.

Cohen, M G, E Tuero, J Bluguermann, R Kevorkian, D H Berrocal, O Carlevaro, E Picabea, M P Hudson, R J Siegel, L Douthat, A B Greenbaum, D Echt, W D Weaver, and L R Grinfeld, Transcutaneous ultrasound-facilitated coronary thrombolysis during acute myocardial infarction. *Am. J. Cardiol.*, 92(4): 454-457, 2003.

Collis, J, R Manasseh, P Liovic, P Tho, A Ooi, K Petkovic-Duran, and Y Zhu, Cavitation microstreaming and stress fields created by microbubbles. *Ultrasonics*, 50(2): 273-279, 2010.

Connor, J A, Digital imaging of free calcium changes and of spatial gradients in growing processes in single, mammalian central nervous system cells. *Proc. Natl. Acad. Sci. U. S. A.*, 83(16): 6179-6183, 1986.

Correas, J M, O Helenon, L Pourcelot, and J F Moreau, Ultrasound contrast agents. Examples of blood pool agents. *Acta Radiol Suppl*, 412: 101-112, 1997.

Cosgrove, D, Ultrasound contrast agents: an overview. *Eur. J. Radiol.*, 60(3): 324-330, 2006.

Cox, D J and J L Thomas, Ultrasound-induced dissolution of lipid-coated and uncoated gas bubbles. *Langmuir*, 26(18): 14774-14781, 2010.

Cox, D J and J L Thomas, Rapid shrinkage of lipid-coated bubbles in pulsed ultrasound. *Ultrasound Med. Biol.*, 39(3): 466-474, 2013.

Crum, L A, The polytropic exponent of gas contained within air bubbles pulsating in a liquid. *The Journal of the Acoustical Society of America*, 73(1): 116-120, 1983.

Dayton, P A, J S Allen, and K W Ferrara, The magnitude of radiation force on ultrasound contrast agents. *J. Acoust. Soc. Am.*, 112(5 Pt 1): 2183-2192, 2002.

Dayton, P A, K E Morgan, A L Klibanov, G H Brandenburger, and K W Ferrara, Optical and acoustical observations of the effects of ultrasound on contrast agents. *IEEE Trans Ultrason Ferroelectr Freq Control*, 46(1): 220-232, 1999.

de Jong, N, A Bouakaz, and P Frinking, Basic Acoustic Properties of Microbubbles. *Echocardiography*, 19(3): 229-240, 2002.

de Jong, N, R Cornet, and C T Lancée, Higher harmonics of vibrating gas-filled microspheres. Part one: simulations. *Ultrasonics*, 32(6): 447-453, 1994.

de Jong, N, M Emmer, C T Chin, A Bouakaz, F Mastik, D Lohse, and M Versluis, "Compression-only" behavior of phospholipid-coated contrast bubbles. *Ultrasound Med. Biol.*, 33(4): 653-656, 2007.

de Jong, N, P J A Frinking, A Bouakaz, M Goorden, T Schourmans, X Jingping, and F Mastik, Optical imaging of contrast agent microbubbles in an ultrasound field with a 100-MHz camera. *Ultrasound Med. Biol.*, 26(3): 487-492, 2000.

de Jong, N, L Hoff, T Skotland, and N Bom, Absorption and scatter of encapsulated gas filled microspheres: theoretical considerations and some measurements. *Ultrasonics*, 30(2): 95-103, 1992.

DeLisser, H M, P J Newman, and S M Albelda, Molecular and functional aspects of PECAM-1/CD31. *Immunology today*, 15(10): 490-495, 1994.

Devin, C, Survey of Thermal, Radiation, and Viscous Damping of Pulsating Air Bubbles in Water. *The Journal of the Acoustical Society of America*, 31(12): 1654-1667, 1959.

Dice, J F and H L Chiang, Lysosomal degradation of microinjected proteins. *Revisiones sobre biologia celular : RBC*, 20: 13-33, 1989.

Doinikov, A A and A Bouakaz, Review of shell models for contrast agent microbubbles. *IEEE Trans Ultrason Ferroelectr Freq Control*, 58(5): 981-993, 2011.

Doinikov, A A, J F Haac, and P A Dayton, Modeling of nonlinear viscous stress in encapsulating shells of lipid-coated contrast agent microbubbles. *Ultrasonics*, 49(2): 269-275, 2009.

Dollet, B, S M van der Meer, V Garbin, N de Jong, D Lohse, and M Versluis, Nonspherical oscillations of ultrasound contrast agent microbubbles. *Ultrasound Med. Biol.*, 34(9): 1465-1473, 2008.

Edmundson, M, N T Thanh, and B Song, Nanoparticles based stem cell tracking in regenerative medicine. *Theranostics*, 3(8): 573-582, 2013.

Elder, S A, Cavitation Microstreaming. *J. Acoust. Soc. Am.*, 31(1): 54-64, 1959.

Emmer, M, A van Wamel, D E Goertz, and N de Jong, The Onset of Microbubble Vibration. *Ultrasound Med. Biol.*, 33(6): 941-949, 2007.

Emmer, M, H J Vos, D E Goertz, A van Wamel, M Versluis, and N de Jong, Pressure-dependent attenuation and scattering of phospholipid-coated microbubbles at low acoustic pressures. *Ultrasound Med. Biol.*, 35(1): 102-111, 2009.

Emmer, M, H J Vos, M Versluis, and N de Jong, Radial modulation of single microbubbles. *IEEE Trans Ultrason Ferroelectr Freq Control*, 56(11): 2370-2379, 2009.

Epstein, P S and M S Plesset, On the Stability of Gas Bubbles in Liquid-Gas Solutions. *The Journal of Chemical Physics*, 18(11): 1505-1509, 1950.

Faez, T, M Emmer, M Docter, J Sijl, M Versluis, and N de Jong, Characterizing the Subharmonic Response of Phospholipid-Coated Microbubbles for Carotid Imaging. *Ultrasound Med. Biol.*, 37(6): 958-970, 2011.

Faez, T, M Emmer, K Kooiman, M Versluis, A van der Steen, and N de Jong, 20 years of ultrasound contrast agent modeling. *IEEE Trans Ultrason Ferroelectr Freq Control*, 60(1): 7-20, 2013.

Faez, T, D Goertz, and N de Jong, Characterization of Definity ultrasound contrast agent at frequency range of 5-15 MHz. *Ultrasound Med. Biol.*, 37(2): 338-342, 2011.

Faez, T, I Skachkov, M Versluis, K Kooiman, and N de Jong, *In Vivo* Characterization of Ultrasound Contrast Agents: Microbubble Spectroscopy in a Chicken Embryo. *Ultrasound Med. Biol.*, 38(9): 1608-1617, 2012.

Fan, C H, C Y Ting, H J Lin, C H Wang, H L Liu, T C Yen, and C K Yeh, SPIO-conjugated, doxorubicin-loaded microbubbles for concurrent MRI and focused-ultrasound enhanced brain-tumor drug delivery. *Biomaterials*, 34(14): 3706-3715, 2013.

Fan, Z, R E Kumon, J Park, and C X Deng, Intracellular delivery and calcium transients generated in sonoporation facilitated by microbubbles. *J Control Release*, 142(1): 31-39, 2010.

Fan, Z, H Liu, M Mayer, and C X Deng, Spatiotemporally controlled single cell sonoporation. *Proceedings of the National Academy of Sciences of the United States of America*, 109(41): 16486-16491, 2012.

Fayol, D, C Le Visage, J Ino, F Gazeau, D Letourneur, and C Wilhelm, Design of biomimetic vascular grafts with magnetic endothelial patterning. *Cell transplantation*, 22(11): 2105-2118, 2013.

Feinstein, S B, Contrast ultrasound imaging of the carotid artery vasa vasorum and atherosclerotic plaque neovascularization. *J. Am. Coll. Cardiol.*, 48(2): 236-243, 2006.

Ferrante, E A, J E Pickard, J Rychak, A Klibanov, and K Ley, Dual targeting improves microbubble contrast agent adhesion to VCAM-1 and P-selectin under flow. *J Control Release*, 140(2): 100-107, 2009.

Ferrara, K, R Pollard, and M Borden, Ultrasound microbubble contrast agents: fundamentals and application to gene and drug delivery. *Annu Rev Biomed Eng*, 9: 415-447, 2007.

Frank, J A, S A Anderson, H Kalsih, E K Jordan, B K Lewis, G T Yocum, and A S Arbab, Methods for magnetically labeling stem and other cells for detection by *in vivo* magnetic resonance imaging. *Cytotherapy*, 6(6): 621-625, 2004.

Frinking, P J, A Bouakaz, N de Jong, F J Ten Cate, and S Keating, Effect of ultrasound on the release of micro-encapsulated drugs. *Ultrasonics*, 36(1-5): 709-712, 1998.

Fu, Y, N Azene, Y Xu, and D L Kraitchman, Tracking stem cells for cardiovascular applications *in vivo*: focus on imaging techniques. *Imaging in medicine*, 3(4): 473-486, 2011.

Gamarra, L F, G E S Brito, W M Pontuschka, E Amaro, A H C Parma, and G F Goya, Biocompatible superparamagnetic iron oxide nanoparticles used for contrast agents: a structural and magnetic study. *Journal of Magnetism and Magnetic Materials*, 289(0): 439-441, 2005.

Gao, W Q, X Li, P C Liu, Z Y Bai, Y F Zhong, H B Han, J F Li, W Liu, Z Z Zheng, Y J Sui, X L Ma, X J Lu, H Xu, and X Z Zeng, Investigation *in vivo* of effect of ultrasound-mediated microbubble destruction on entrance of feridex into the aortal wall. *Zhonghua yi xue za zhi*, 89(39): 2797-2801, 2009.

Garbin, V, D Cojoc, E Ferrari, E Di Fabrizio, M L J Overvelde, S M van der Meer, N de Jong, D Lohse, and M Versluis, Changes in microbubble dynamics near a boundary revealed by combined optical micromanipulation and high-speed imaging. *Applied Physics Letters*, 90(11): -, 2007.

Garbin, V, D Cojoc, E Ferrari, E Di Fabrizio, M L J Overvelde, M Versluis, S M van der Meer, N de Jong, and D Lohse. Time-resolved nanoseconds dynamics of ultrasound contrast agent microbubbles manipulated and controlled by optical tweezers, 6326(Issue): 63261V-63261V-63268, Year.

Garbin, V, B Dollet, M Overvelde, D Cojoc, E Di Fabrizio, L van Wijngaarden, A Prosperetti, N de Jong, D Lohse, and M Versluis, History force on coated microbubbles propelled by ultrasound. *Physics of Fluids (1994-present)*, 21(9): -, 2009.

Gazeau, F and C Wilhelm, Magnetic labeling, imaging and manipulation of endothelial progenitor cells using iron oxide nanoparticles. *Future medicinal chemistry*, 2(3): 397-408, 2010.

Geers, B, I Lentacker, S Cool, J Demeester, S C De Smedt, and N N Sanders, Ultrasound responsive doxorubicin-loaded microbubbles; towards an easy applicable drug delivery platform. *J Control Release*, 148(1): e59-60, 2010.

Geers, B, I Lentacker, N N Sanders, J Demeester, S Meairs, and S C De Smedt, Self-assembled liposome-loaded microbubbles: The missing link for safe and efficient ultrasound triggered drug-delivery. *J Control Release*, 152(2): 249-256, 2011.

Gelderblom, E C, *Ultra-high-speed fluorescence imaging*. 2012: Enschede. p. 144.

Gelderblom, E C, H J Vos, F Mastik, T Faez, Y Luan, T J Kokhuis, A F van der Steen, D Lohse, N de Jong, and M Versluis, Brandaris 128 ultra-high-speed imaging facility: 10 years of operation, updates, and enhanced features. *Rev. Sci. Instrum.*, 83(10): 103706, 2012.

Gessner, R C, J E Streeter, R Kothadia, S Feingold, and P A Dayton, An *in vivo* validation of the application of acoustic radiation force to enhance the diagnostic utility of molecular imaging using 3-d ultrasound. *Ultrasound Med Biol*, 38(4): 651-660, 2012.

Ghanem, A, C Steingen, F Brenig, F Funcke, Z Y Bai, C Hall, C T Chin, G Nickenig, W Bloch, and K Tiemann, Focused ultrasound-induced stimulation of microbubbles augments site-targeted engraftment of mesenchymal stem cells after acute myocardial infarction. *J. Mol. Cell. Cardiol.*, 47(3): 411-418, 2009.

Gimi, B, N Mori, E Ackerstaff, E E Frost, J W Bulte, and Z M Bhujwalla, Noninvasive MRI of endothelial cell response to human breast cancer cells. *Neoplasia*, 8(3): 207-213, 2006.

Goertz, D E, N de Jong, and A F van der Steen, Attenuation and size distribution measurements of Definity and manipulated Definity populations. *Ultrasound Med. Biol.*, 33(9): 1376-1388, 2007.

Gorce, J M, M Arditi, and M Schneider, Influence of bubble size distribution on the echogenicity of ultrasound contrast agents: a study of SonoVue. *Invest. Radiol.*, 35(11): 661-671, 2000.

Gormley, G and J Wu, Observation of acoustic streaming near Albunex[sup [registered sign]] spheres. *The Journal of the Acoustical Society of America*, 104(5): 3115-3118, 1998.

Greis, C, Ultrasound contrast agents as markers of vascularity and microcirculation. *Clin Hemorheol Microcirc*, 43(1-2): 1-9, 2009.

Guan, J and T J Matula, Using light scattering to measure the response of individual ultrasound contrast microbubbles subjected to pulsed ultrasound *in vitro*. *J. Acoust. Soc. Am.*, 116(5): 2832-2842, 2004.

Guidi, F, H J Vos, R Mori, N de Jong, and P Tortoli, Microbubble characterization through acoustically induced deflation. *IEEE Trans Ultrason Ferroelectr Freq Control*, 57(1): 193-202, 2010.

Gullapalli, R R, M C Demirel, and P J Butler, Molecular dynamics simulations of DiI-C18(3) in a DPPC lipid bilayer. *Phys Chem Chem Phys*, 10(24): 3548-3560, 2008.

Ham, A S, A L Klibanov, and M B Lawrence, Action at a distance: lengthening adhesion bonds with poly(ethylene glycol) spacers enhances mechanically stressed affinity for improved vascular targeting of microparticles. *Langmuir*, 25(17): 10038-10044, 2009.

Hauck, M L, S M LaRue, W P Petros, J M Poulson, D Yu, I Spasojevic, A F Pruitt, A Klein, B Case, D E Thrall, D Needham, and M W Dewhirst, Phase I trial of doxorubicin-containing low temperature sensitive liposomes in spontaneous canine tumors. *Clin. Cancer Res.*, 12(13): 4004-4010, 2006.

Helfield, B L, E Cherin, F S Foster, and D E Goertz, Investigating the subharmonic response of individual phospholipid encapsulated microbubbles at high frequencies: a comparative study of five agents. *Ultrasound Med. Biol.*, 38(5): 846-863, 2012.

Helfield, B L, B Y Leung, X Huo, and D E Goertz, Scaling of the viscoelastic shell properties of phospholipid encapsulated microbubbles with ultrasound frequency. *Ultrasonics*, 54(6): 1419-1424, 2014.

Hernot, S and A L Klibanov, Microbubbles in ultrasound-triggered drug and gene delivery. *Adv Drug Deliv Rev*, 60(10): 1153-1166, 2008.

Heyes, J, L Palmer, K Bremner, and I MacLachlan, Cationic lipid saturation influences intracellular delivery of encapsulated nucleic acids. *J. Controlled Release*, 107(2): 276-287, 2005.

Hoff, L, P C Sontum, and J M Hovem, Oscillations of polymeric microbubbles: effect of the encapsulating shell. *J. Acoust. Soc. Am.*, 107(4): 2272-2280, 2000.

Hoffman, R L, Factors affecting the viscosity of unimodal and multimodal colloidal dispersions. *Journal of Rheology (1978-present)*, 36(5): 947-965, 1992.

Hong, H, Y Yang, Y Zhang, and W Cai, Non-invasive cell tracking in cancer and cancer therapy. *Current topics in medicinal chemistry*, 10(12): 1237-1248, 2010.

Hosny, N A, G Mohamedi, P Rademeyer, J Owen, Y Wu, M X Tang, R J Eckersley, E Stride, and M K Kuimova, Mapping microbubble viscosity using fluorescence lifetime imaging of molecular rotors. *Proc Natl Acad Sci U S A*, 110(23): 9225-9230, 2013.

Hu, Y, J M Wan, and A C Yu, Membrane perforation and recovery dynamics in microbubble-mediated sonoporation. *Ultrasound Med. Biol.*, 39(12): 2393-2405, 2013.

Huang, S-L, *Ultrasound-Responsive Liposomes*, in *Liposomes*, V Weissig, Editor. 2010, Humana Press. p. 113-128.

Hynynen, K, N McDannold, N Vykhodtseva, and F A Jolesz, Noninvasive MR imaging-guided focal opening of the blood-brain barrier in rabbits. *Radiology*, 220(3): 640-646, 2001.

Jilani, S M, T J Murphy, S N Thai, A Eichmann, J A Alva, and M L Iruela-Arispe, Selective binding of lectins to embryonic chicken vasculature. *J Histochem Cytochem*, 51(5): 597-604, 2003.

Jin, L F, F Li, H P Wang, F Wei, P Qin, and L F Du, Ultrasound targeted microbubble destruction stimulates cellular endocytosis in facilitation of adeno-associated virus delivery. *International journal of molecular sciences*, 14(5): 9737-9750, 2013.

Kabalnov, A, J Bradley, S Flaim, D Klein, T Pelura, B Peters, S Otto, J Reynolds, E Schutt, and J Weers, Dissolution of multicomponent microbubbles in the bloodstream: 2. Experiment. *Ultrasound Med. Biol.*, 24(5): 751-760, 1998.

Kabalnov, A, D Klein, T Pelura, E Schutt, and J Weers, Dissolution of multicomponent microbubbles in the bloodstream: 1. Theory. *Ultrasound Med. Biol.*, 24(5): 739-749, 1998.

Kheirolomoom, A, P A Dayton, A F Lum, E Little, E E Paoli, H Zheng, and K W Ferrara, Acoustically-active microbubbles conjugated to liposomes: characterization of a proposed drug delivery vehicle. *J Control Release*, 118(3): 275-284, 2007.

Kiessling, F, J Bzyl, S Fokong, M Siepmann, G Schmitz, and M Palmowski, Targeted ultrasound imaging of cancer: an emerging technology on its way to clinics. *Curr. Pharm. Des.*, 18(15): 2184-2199, 2012.

Kind, C, The development of the circulating blood volume of the chick embryo. *Anat Embryol (Berl)*, 147(2): 127-132, 1975.

Klibanov, A L, Microbubble contrast agents: targeted ultrasound imaging and ultrasound-assisted drug-delivery applications. *Invest. Radiol.*, 41(3): 354-362, 2006.

Klibanov, A L, Ultrasound molecular imaging with targeted microbubble contrast agents. *J. Nucl. Cardiol.*, 14(6): 876-884, 2007.

Klibanov, A L, Preparation of targeted microbubbles: ultrasound contrast agents for molecular imaging. *Med. Biol. Eng. Comput.*, 47(8): 875-882, 2009.

Klibanov, A L, M S Hughes, J K Wojdyla, J H Wible, Jr., and G H Brandenburger, Destruction of contrast agent microbubbles in the ultrasound field: the fate of the microbubble shell and the importance of the bubble gas content. *Acad. Radiol.*, 9 Suppl 1: S41-45, 2002.

Klibanov, A L, P T Rasche, M S Hughes, J K Wojdyla, K P Galen, J H Wible, Jr., and G H Brandenburger, Detection of individual microbubbles of ultrasound contrast agents: imaging of free-floating and targeted bubbles. *Invest. Radiol.*, 39(3): 187-195, 2004.

Klibanov, A L, T I Shevchenko, B I Raju, R Seip, and C T Chin, Ultrasound-triggered release of materials entrapped in microbubble-liposome constructs: a tool for targeted drug delivery. *J Control Release*, 148(1): 13-17, 2010.

Kokhuis, T J, V Garbin, K Kooiman, B A Naaijkens, L J Juffermans, O Kamp, A F van der Steen, M Versluis, and N de Jong, Secondary bjerknes forces deform targeted microbubbles. *Ultrasound Med. Biol.*, 39(3): 490-506, 2013.

Kokhuis, T J A, Y Luan, F Mastik, R H S H Beurskens, M Versluis, and N de Jong. Segmented high speed imaging of vibrating microbubbles during long ultrasound pulses. in *Ultrasonics Symposium (IUS), 2012 IEEE International*(Issue): 1343-1346, Year.

Kondo, I, K Mizushige, T Ueda, H Masugata, K Ohmori, and H Matsuo, Histological observations and the process of ultrasound contrast agent enhancement of tissue plasminogen activator thrombolysis with ultrasound exposure. *Jpn. Circ. J.*, 63(6): 478-484, 1999.

Kooiman, K, *Therapeutic Bubbles*. 2011, Erasmus University Rotterdam.

Kooiman, K, M Emmer, T J A Kokhuis, J G Bosch, H M de Gruiter, M E van Royen, W A Van Cappellen, A B Houtsmuller, A F W Van der Steen, and N de Jong. Lipid distribution and viscosity of coated microbubbles. in *Ultrasonics Symposium (IUS), 2010 IEEE*(Issue): 900-903, Year.

Kooiman, K, M Foppen-Harteveld, A F van der Steen, and N de Jong, Sonoporation of endothelial cells by vibrating targeted microbubbles. *Journal of controlled release : official journal of the Controlled Release Society*, 154(1): 35-41, 2011.

Kooiman, K, T J A Kokhuis, I Skachkov, J G Bosch, A W van der Steen, W A van Cappellen, and N de Jong. Surface contact of bound targeted microbubbles. in *Ultrasonics Symposium (IUS), 2012 IEEE International*(Issue): 2161-2163, Year.

Kooiman, K, H J Vos, M Versluis, and N de Jong, Acoustic behavior of microbubbles and implications for drug delivery. *Adv Drug Deliv Rev*, 72C: 28-48, 2014.

Kopechek, J A, K J Haworth, J L Raymond, T Douglas Mast, S R Perrin, M E Klegerman, S Huang, T M Porter, D D McPherson, and C K Holland, Acoustic characterization of echogenic liposomes: frequency-dependent attenuation and backscatter. *J. Acoust. Soc. Am.*, 130(5): 3472-3481, 2011.

Kotopoulis, S and M Postema, Microfoam formation in a capillary. *Ultrasonics*, 50(2): 260-268, 2010.

Kwan, J J and M A Borden, Microbubble dissolution in a multigas environment. *Langmuir*, 26(9): 6542-6548, 2010.

Kwan, J J and M A Borden, Lipid monolayer collapse and microbubble stability. *Adv. Colloid Interface Sci.*, 183-184: 82-99, 2012.

Lajoinie, G, E Gelderblom, C Chlon, M Bohmer, W Steenbergen, N de Jong, S Manohar, and M Versluis, Ultrafast vapourization dynamics of laser-activated polymeric microcapsules. *Nat Commun*, 5: 3671, 2014.

Lampugnani, M G, Endothelial cell-to-cell junctions: adhesion and signaling in physiology and pathology. *Cold Spring Harb Perspect Med*, 2(10), 2012.

Leeman, J E, J S Kim, F T Yu, X Chen, K Kim, J Wang, F S Villanueva, and J J Pacella, Effect of acoustic conditions on microbubble-mediated microvascular sonothrombolysis. *Ultrasound Med. Biol.*, 38(9): 1589-1598, 2012.

Leighton, T G, *The Acoustic Bubble*. 1994: Academic Press.

Lentacker, I, I De Cock, R Deckers, S De Smedt, and C T W Moonen, Understanding ultrasound induced sonporation: Definitions and underlying mechanisms. *Adv Drug Deliv Rev*, 2014.

Lentacker, I, S De Smedt, J Demeester, V Van Marck, M Bracke, and N Sanders, Lipoplex-loaded microbubbles for gene delivery: A Trojan horse controlled by ultrasound. *Hum. Gene Ther.*, 18(10): 1046-1046, 2007.

Lentacker, I, S C De Smedt, and N N Sanders, Drug loaded microbubble design for ultrasound triggered delivery. *Soft Matter*, 5(11): 2161-2170, 2009.

Lentacker, I, B Geers, J Demeester, S C De Smedt, and N N Sanders, Design and evaluation of doxorubicin-containing microbubbles for ultrasound-triggered doxorubicin delivery: cytotoxicity and mechanisms involved. *Mol Ther*, 18(1): 101-108, 2010.

Lentacker, I, N Wang, R E Vandenbroucke, J Demeester, S C De Smedt, and N N Sanders, Ultrasound exposure of lipoplex loaded microbubbles facilitates direct cytoplasmic entry of the lipoplexes. *Mol Pharm*, 6(2): 457-467, 2009.

Li, Q, T J Matula, J Tu, X Guo, and D Zhang, Modeling complicated rheological behaviors in encapsulating shells of lipid-coated microbubbles accounting for nonlinear changes of both shell viscosity and elasticity. *Phys. Med. Biol.*, 58(4): 985-998, 2013.

Liang, H D, J Tang, and M Halliwell, Sonoporation, drug delivery, and gene therapy. *Proc Inst Mech Eng H*, 224(2): 343-361, 2010.

Lindner, J R, Microbubbles in medical imaging: current applications and future directions. *Nat Rev Drug Discov*, 3(6): 527-532, 2004.

Lindner, J R and S Kaul, Delivery of drugs with ultrasound. *Echocardiography*, 18(4): 329-337, 2001.

Liu, H L, P Y Chen, H W Yang, J S Wu, I C Tseng, Y J Ma, C Y Huang, H C Tsai, S M Chen, Y J Lu, C Y Huang, M Y Hua, Y H Ma, T C Yen, and K C Wei, *In vivo* MR quantification of superparamagnetic iron oxide nanoparticle leakage during low-frequency-ultrasound-induced blood-brain barrier opening in swine. *Journal of magnetic resonance imaging : JMRI*, 34(6): 1313-1324, 2011.

Luan, Y, T Faez, E Gelderblom, I Skachkov, B Geers, I Lentacker, T van der Steen, M Versluis, and N de Jong, Acoustical properties of individual liposome-loaded microbubbles. *Ultrasound Med. Biol.*, 38(12): 2174-2185, 2012.

Luan, Y, G Lajoinie, E Gelderblom, I Skachkov, A F van der Steen, H J Vos, M Versluis, and N de Jong, Lipid Shedding from Single Oscillating Microbubbles. *Ultrasound Med. Biol.*, 2014.

Madsen, H H and F Rasmussen, Contrast-enhanced ultrasound in oncology. *Cancer Imaging*, 11 Spec No A: S167-173, 2011.

Mannaris, C and M A Averkiou, Investigation of Microbubble Response to Long Pulses Used in Ultrasound-Enhanced Drug Delivery. *Ultrasound Med. Biol.*, 38(4): 681-691, 2012.

Maresca, D, M Emmer, P L van Neer, H J Vos, M Versluis, M Muller, N de Jong, and A F van der Steen, Acoustic sizing of an ultrasound contrast agent. *Ultrasound Med. Biol.*, 36(10): 1713-1721, 2010.

Marmottant, P and S Hilgenfeldt, Controlled vesicle deformation and lysis by single oscillating bubbles. *Nature*, 423(6936): 153-156, 2003.

Marmottant, P, S van der Meer, M Emmer, M Versluis, N de Jong, S Hilgenfeldt, and D Lohse, A model for large amplitude oscillations of coated bubbles accounting for buckling and rupture. *J. Acoust. Soc. Am.*, 118(6): 3499-3505, 2005.

Marmottant, P, M Versluis, N de Jong, S Hilgenfeldt, and D Lohse, High-speed imaging of an ultrasound-driven bubble in contact with a wall: "Narcissus" effect and resolved acoustic streaming. *Experiments in Fluids*, 41(2): 147-153, 2006.

Maul, T M, D D Dudgeon, M T Beste, D A Hammer, J S Lazo, F S Villanueva, and W R Wagner, Optimization of ultrasound contrast agents with computational models to improve selection of ligands and binding strength. *Biotechnol Bioeng*, 107(5): 854-864, 2010.

Medel, R, R W Crowley, M S McKisic, A S Dumont, and N F Kassell, Sonothrombolysis: an emerging modality for the management of stroke. *Neurosurgery*, 65(5): 979-993; discussion 993, 2009.

Medwin, H, Counting bubbles acoustically: a review. *Ultrasonics*, 15(1): 7-13, 1977.

Meijering, B D, R H Henning, W H Van Gilst, I Gavrilovic, A Van Wamel, and L E Deelman, Optimization of ultrasound and microbubbles targeted gene delivery to cultured primary endothelial cells. *J. Drug Target.*, 15(10): 664-671, 2007.

Meijering, B D, L J Juffermans, A van Wamel, R H Henning, I S Zuhorn, M Emmer, A M Versteilen, W J Paulus, W H van Gilst, K Kooiman, N de Jong, R J Musters, L E Deelman, and O Kamp, Ultrasound and microbubble-targeted delivery of macromolecules is regulated by induction of endocytosis and pore formation. *Circulation research*, 104(5): 679-687, 2009.

Michel, J B, R Virmani, E Arbustini, and G Pasterkamp, Intraplaque haemorrhages as the trigger of plaque vulnerability. *Eur Heart J*, 32(16): 1977-1985, 1985a, 1985b, 1985c, 2011.

Morgan, K E, J S Allen, P A Dayton, J E Chomas, A L Klibaov, and K W Ferrara, Experimental and theoretical evaluation of microbubble behavior: effect of transmitted phase and bubble size. *IEEE Trans Ultrason Ferroelectr Freq Control*, 47(6): 1494-1509, 2000.

Mukherjee, D, J Wong, B Griffin, S G Ellis, T Porter, S Sen, and J D Thomas, Ten-fold augmentation of endothelial uptake of vascular endothelial growth factor with ultrasound after systemic administration. *J. Am. Coll. Cardiol.*, 35(6): 1678-1686, 2000.

Nanda, N C, History of echocardiographic contrast agents. *Clin. Cardiol.*, 20(10 Suppl 1): I7-11, 1997.

Newman, C M and T Bettinger, Gene therapy progress and prospects: ultrasound for gene transfer. *Gene Ther.*, 14(6): 465-475, 2007.

Newman, C M, A Lawrie, A F Brisken, and D C Cumberland, Ultrasound gene therapy: on the road from concept to reality. *Echocardiography*, 18(4): 339-347, 2001.

Newman, P G and G S Rozycki, The history of ultrasound. *Surg. Clin. North Am.*, 78(2): 179-195, 1998.

Newman, P J and D K Newman, Signal transduction pathways mediated by PECAM-1: new roles for an old molecule in platelet and vascular cell biology. *Arterioscler. Thromb. Vac. Biol.*, 23(6): 953-964, 2003.

O'Brien, J P, N Ovenden, and E Stride, Accounting for the stability of microbubbles to multi-pulse excitation using a lipid-shedding model. *J. Acoust. Soc. Am.*, 130(4): EL180-185, 2011.

Ohl, C D, M Arora, R Ikink, N de Jong, M Versluis, M Delius, and D Lohse, Sonoporation from jetting cavitation bubbles. *Biophys. J.*, 91(11): 4285-4295, 2006.

Olsen, M G and R J Adrian, Out-of-focus effects on particle image visibility and correlation in microscopic particle image velocimetry. *Experiments in Fluids*, 29(1): S166-S174, 2000.

Ooi, A, P Tho, and R Manasseh, Cavitation microstreaming patterns in single and multiple bubble systems. *J. Acoust. Soc. Am.*, 122(5): 3051-3051, 2007.

Overvelde, M, V Garbin, B Dollet, N de Jong, D Lohse, and M Versluis, Dynamics of Coated Microbubbles Adherent to a Wall. *Ultrasound Med. Biol.*, 37(9): 1500-1508, 2011.

Overvelde, M, V Garbin, J Sijl, B Dollet, N de Jong, D Lohse, and M Versluis, Nonlinear Shell Behavior of Phospholipid-Coated Microbubbles. *Ultrasound Med. Biol.*, 36(12): 2080-2092, 2010.

Owen, J, Q Pankhurst, and E Stride, Magnetic targeting and ultrasound mediated drug delivery: benefits, limitations and combination. *Int J Hyperthermia*, 28(4): 362-373, 2012.

Palanchon, P, P Tortoli, A Bouakaz, M Versluis, and N de Jong, Optical observations of acoustical radiation force effects on individual air bubbles. *Ultrasonics, Ferroelectrics and Frequency Control, IEEE Transactions on*, 52(1): 104-110, 2005.

Park, J, Z Fan, and C X Deng, Effects of shear stress cultivation on cell membrane disruption and intracellular calcium concentration in sonoporation of endothelial cells. *J Biomech*, 44(1): 164-169, 2011.

Paul, S, R Nahire, S Mallik, and K Sarkar, Encapsulated microbubbles and echogenic liposomes for contrast ultrasound imaging and targeted drug delivery. *Comput Mech*, 53(3): 413-435, 2014.

Phillips, L C, A L Klibanov, B R Wamhoff, and J A Hossack, Intravascular ultrasound detection and delivery of molecularly targeted microbubbles for gene delivery. *IEEE Trans Ultrason Ferroelectr Freq Control*, 59(7): 1596-1601, 2012.

Pi Hsien, C, K K Shun, W Shih-Jeh, and H B Levene, Second harmonic imaging and harmonic Doppler measurements with Albunex. *Ultrasonics, Ferroelectrics, and Frequency Control, IEEE Transactions on*, 42(6): 1020-1027, 1995.

Porter, T R and F Xie, Therapeutic ultrasound for gene delivery. *Echocardiography*, 18(4): 349-353, 2001.

Prentice, P, A Cuschierp, K Dholakia, M Prausnitz, and P Campbell, Membrane disruption by optically controlled microbubble cavitation. *Nature Physics*, 1(2): 107-110, 2005.

Price, R J, D M Skyba, S Kaul, and T C Skalak, Delivery of colloidal particles and red blood cells to tissue through microvessel ruptures created by targeted microbubble destruction with ultrasound. *Circulation*, 98(13): 1264-1267, 1998.

Prosperetti, A, Thermal effects and damping mechanisms in the forced radial oscillations of gas bubbles in liquids. *The Journal of the Acoustical Society of America*, 61(1): 17-27, 1977.

Pu, G, M A Borden, and M L Longo, Collapse and shedding transitions in binary lipid monolayers coating microbubbles. *Langmuir*, 22(7): 2993-2999, 2006.

Ramaswamy, S, P A Schornack, A G Smelko, S M Boronyak, J Ivanova, J E Mayer, Jr., and M S Sacks, Superparamagnetic iron oxide (SPIO) labeling efficiency and subsequent MRI tracking of native cell populations pertinent to pulmonary heart valve tissue engineering studies. *NMR in biomedicine*, 25(3): 410-417, 2012.

Raymond, J L, K J Haworth, K B Bader, K Radhakrishnan, J K Griffin, S L Huang, D D McPherson, and C K Holland, Broadband attenuation measurements of phospholipid-shelled ultrasound contrast agents. *Ultrasound Med. Biol.*, 40(2): 410-421, 2014.

Reddy, L H, J L Arias, J Nicolas, and P Couvreur, Magnetic nanoparticles: design and characterization, toxicity and biocompatibility, pharmaceutical and biomedical applications. *Chemical reviews*, 112(11): 5818-5878, 2012.

Reimer, P and B Tombach, Hepatic MRI with SPIO: detection and characterization of focal liver lesions. *European radiology*, 8(7): 1198-1204, 1998.

Renaud, G, J Bosch, A van der Steen, and N de Jong, Single microbubbles vibrations measured with an "acoustical camera". *J. Acoust. Soc. Am.*, 134(5): 3975, 2013.

Renaud, G, J G Bosch, A F van der Steen, and N de Jong, Chirp resonance spectroscopy of single lipid-coated microbubbles using an "acoustical camera". *J. Acoust. Soc. Am.*, 132(6): EL470-475, 2012.

Renaud, G, J G Bosch, A F Van Der Steen, and N de Jong, Low-Amplitude Non-linear Volume Vibrations of Single Microbubbles Measured with an "Acoustical Camera". *Ultrasound Med. Biol.*, 2014.

Renaud, G, J G Bosch, A F W van der Steen, and N de Jong, An "acoustical camera" for *in vitro* characterization of contrast agent microbubble vibrations. *Applied Physics Letters*, 100(10), 2012.

Ribatti, D, B Nico, A Vacca, L Roncali, P H Burri, and V Djonov, Chorioallantoic membrane capillary bed: a useful target for studying angiogenesis and anti-angiogenesis *in vivo*. *Anat Rec*, 264(4): 317-324, 2001.

Rodriguez-Porcel, M, M W Kronenberg, T D Henry, J H Traverse, C J Pepine, S G Ellis, J T Willerson, L A Moye, and R D Simari, Cell tracking and the development of cell-based therapies: a view from the Cardiovascular Cell Therapy Research Network. *JACC. Cardiovascular imaging*, 5(5): 559-565, 2012.

Rychak, J J, A L Klibanov, K F Ley, and J A Hossack, Enhanced targeting of ultrasound contrast agents using acoustic radiation force. *Ultrasound Med Biol*, 33(7): 1132-1139, 2007.

Rychak, J J, J R Lindner, K Ley, and A L Klibanov, Deformable gas-filled microbubbles targeted to P-selectin. *J Control Release*, 114(3): 288-299, 2006.

Sarkar, K, A Katiyar, and P Jain, Growth and Dissolution of an Encapsulated Contrast Microbubble: Effects of Encapsulation Permeability. *Ultrasound Med. Biol.*, 35(8): 1385-1396, 2009.

Sarkar, K, W T Shi, D Chatterjee, and F Forsberg, Characterization of ultrasound contrast microbubbles using *in vitro* experiments and viscous and viscoelastic interface models for encapsulation. *The Journal of the Acoustical Society of America*, 118(1): 539-550, 2005.

Sboros, V, E Glynos, S D Pye, C M Moran, M Butler, J Ross, R Short, W N McDicken, and V Koutsos, Nanointerrogation of ultrasonic contrast agent microbubbles using atomic force microscopy. *Ultrasound Med. Biol.*, 32(4): 579-585, 2006.

Schneider, M, A Broillet, I Tardy, S Pochon, P Bussat, T Bettinger, A Helbert, M Costa, and F Tranquart, Use of Intravital Microscopy to Study the Microvascular Behavior of Microbubble-Based Ultrasound Contrast Agents. *Microcirculation*, 19(3): 245-259, 2012.

Schrope, B A and V L Newhouse, Second harmonic ultrasonic blood perfusion measurement. *Ultrasound Med. Biol.*, 19(7): 567-579, 1993.

Segers, T and M Versluis, Acoustic bubble sorting for ultrasound contrast agent enrichment. *Lab Chip*, 14(10): 1705-1714, 2014.

Seibert, J A, One hundred years of medical diagnostic imaging technology. *Health Phys.*, 69(5): 695-720, 1995.

Shapiro, E M, K Sharer, S Skrtic, and A P Koretsky, *In vivo* detection of single cells by MRI. *Magnetic resonance in medicine : official journal of the Society of Magnetic Resonance in Medicine / Society of Magnetic Resonance in Medicine*, 55(2): 242-249, 2006.

Sharma, A and U S Sharma, Liposomes in drug delivery: Progress and limitations. *Int. J. Pharm.*, 154(2): 123-140, 1997.

Sijl, J, B Dollet, M Overvelde, V Garbin, T Rozendal, N de Jong, D Lohse, and M Versluis, Subharmonic behavior of phospholipid-coated ultrasound contrast agent microbubbles. *J. Acoust. Soc. Am.*, 128(5): 3239-3252, 2010.

Sijl, J, E Gaud, P J Frinking, M Arditi, N de Jong, D Lohse, and M Versluis, Acoustic characterization of single ultrasound contrast agent microbubbles. *J. Acoust. Soc. Am.*, 124(6): 4091-4097, 2008.

Sijl, J, M Overvelde, B Dollet, V Garbin, N de Jong, D Lohse, and M Versluis, "Compression-only" behavior: a second-order nonlinear response of ultrasound contrast agent microbubbles. *J. Acoust. Soc. Am.*, 129(4): 1729-1739, 2011.

Sijl, J, H J Vos, T Rozendal, N de Jong, D Lohse, and M Versluis, Combined optical and acoustical detection of single microbubble dynamics. *J. Acoust. Soc. Am.*, 130(5): 3271-3281, 2011.

Simpson, D H, C T Chin, and P N Burns, Pulse inversion Doppler: a new method for detecting nonlinear echoes from microbubble contrast agents. *IEEE Trans Ultrason Ferroelectr Freq Control*, 46(2): 372-382, 1999.

Skachkov, I, Y Luan, A F W van der Steen, N de Jong, and K Kooiman, Targeted microbubble mediated sonoporation of endothelial cells *in vivo*. *IEEE Trans Ultrason Ferroelectr Freq Control*, in press, 2014.

Sriram, M, G A van der Marel, H L Roelen, J H van Boom, and A H Wang, Conformation of B-DNA containing O6-ethyl-G-C base pairs stabilized by minor groove binding drugs: molecular structure of d(CGC[e6G]AATTCGCG complexed with Hoechst 33258 or Hoechst 33342. *EMBO J*, 11(1): 225-232, 1992.

Stieger, S M, C F Caskey, R H Adamson, S Qin, F R Curry, E R Wisner, and K W Ferrara, Enhancement of vascular permeability with low-frequency contrast-enhanced ultrasound in the chorioallantoic membrane model. *Radiology*, 243(1): 112-121, 2007.

Stride, E, Physical principles of microbubbles for ultrasound imaging and therapy. *Cerebrovasc. Dis.*, 27 Suppl 2: 1-13, 2009.

Stride, E, K Pancholi, M J Edirisinghe, and S Samarasinghe, Increasing the nonlinear character of microbubble oscillations at low acoustic pressures. *J R Soc Interface*, 5(24): 807-811, 2008.

Stride, E and N Saffari, Microbubble ultrasound contrast agents: a review. *Proc Inst Mech Eng H*, 217(6): 429-447, 2003.

Sutton, J T, K J Haworth, G Pyne-Geithman, and C K Holland, Ultrasound-mediated drug delivery for cardiovascular disease. *Expert Opin Drug Deliv*, 10(5): 573-592, 2013.

Taylor, A, K M Wilson, P Murray, D G Fernig, and R Levy, Long-term tracking of cells using inorganic nanoparticles as contrast agents: are we there yet? *Chemical Society reviews*, 41(7): 2707-2717, 2012.

Thomas, D H, M Butler, T Anderson, M Emmer, H Vos, M Borden, E Stride, N de Jong, and V Sboros, The "quasi-stable" lipid shelled microbubble in response to consecutive ultrasound pulses. *Applied Physics Letters*, 101(7), 2012.

Thomas, D H, M Butler, N Pelekasis, T Anderson, E Stride, and V Sboros, The acoustic signature of decaying resonant phospholipid microbubbles. *Phys. Med. Biol.*, 58(3): 589-599, 2013.

Tinkov, S, C Coester, S Serba, N A Geis, H A Katus, G Winter, and R Bekeredjian, New doxorubicin-loaded phospholipid microbubbles for targeted tumor therapy: in-vivo characterization. *J Control Release*, 148(3): 368-372, 2010.

Tiukinhoy-Laing, S D, S Huang, M Klegerman, C K Holland, and D D McPherson, Ultrasound-facilitated thrombolysis using tissue-plasminogen activator-loaded echogenic liposomes. *Thromb. Res.*, 119(6): 777-784, 2007.

Tlaxca, J L, J J Rychak, P B Ernst, P R Konkalmatt, T I Shevchenko, T T Pizarro, J Rivera-Nieves, A L Klibanov, and M B Lawrence, Ultrasound-based molecular imaging and specific gene delivery to mesenteric vasculature by endothelial adhesion molecule targeted microbubbles in a mouse model of Crohn's disease. *J Control Release*, 165(3): 216-225, 2013.

Tu, J, J Guan, Y Qiu, and T J Matula, Estimating the shell parameters of SonoVue microbubbles using light scattering. *J. Acoust. Soc. Am.*, 126(6): 2954-2962, 2009.

Tu, J, J E Swalwell, D Giraud, W Cui, W Chen, and T J Matula, Microbubble sizing and shell characterization using flow cytometry. *IEEE Trans Ultrason Ferroelectr Freq Control*, 58(5): 955-963, 2011.

Unger, E C, T O Matsunaga, T McCreery, P Schumann, R Sweitzer, and R Quigley, Therapeutic applications of microbubbles. *Eur. J. Radiol.*, 42(2): 160-168, 2002.

Unger, E C, T P McCreery, R H Sweitzer, V E Caldwell, and Y Wu, Acoustically active lipospheres containing paclitaxel: a new therapeutic ultrasound contrast agent. *Invest. Radiol.*, 33(12): 886-892, 1998.

Unger, E C, T Porter, W Culp, R Labell, T Matsunaga, and R Zutshi, Therapeutic applications of lipid-coated microbubbles. *Adv Drug Deliv Rev*, 56(9): 1291-1314, 2004.

van der Meer, S M, B Dollet, M M Voormolen, C T Chin, A Bouakaz, N de Jong, M Versluis, and D Lohse, Microbubble spectroscopy of ultrasound contrast agents. *J. Acoust. Soc. Am.*, 121(1): 648-656, 2007.

van Tiel, S T, P A Wielopolski, G C Houston, G P Krestin, and M R Bernsen, Variations in labeling protocol influence incorporation, distribution and retention of iron oxide nanoparticles into human umbilical vein endothelial cells. *Contrast media & molecular imaging*, 5(5): 247-257, 2010.

van Wamel, A, K Kooiman, M Harteveld, M Emmer, F J ten Cate, M Versluis, and N de Jong, Vibrating microbubbles poking individual cells: drug transfer into cells via sonoporation. *J Control Release*, 112(2): 149-155, 2006.

Vandenbroucke, R E, I Lentacker, J Demeester, S C De Smedt, and N N Sanders, Ultrasound assisted siRNA delivery using PEG-siPlex loaded microbubbles. *J. Controlled Release*, 126(3): 265-273, 2008.

Vargas, A, M Zeisser-Labouebe, N Lange, R Gurny, and F Delie, The chick embryo and its chorioallantoic membrane (CAM) for the *in vivo* evaluation of drug delivery systems. *Adv Drug Deliv Rev*, 59(11): 1162-1176, 2007.

Versluis, M, High-speed imaging in fluids. *Experiments in Fluids*, 54(2), 2013.

Versluis, M, D E Goertz, P Palanchon, I L Heitman, S M van der Meer, B Dollet, N de Jong, and D Lohse, Microbubble shape oscillations excited through ultrasonic parametric driving. *Phys Rev E Stat Nonlin Soft Matter Phys*, 82(2 Pt 2): 026321, 2010.

Villanueva, F S, E Lu, S Bowry, S Kilic, E Tom, J Wang, J Gretton, J J Pacella, and W R Wagner, Myocardial ischemic memory imaging with molecular echocardiography. *Circulation*, 115(3): 345-352, 2007.

Viti, J, R Mori, F Guidi, M Versluis, N D Jong, and P Tortoli, Correspondence - Nonlinear oscillations of deflating bubbles. *IEEE Trans Ultrason Ferroelectr Freq Control*, 59(12): 2818-2824, 2012.

Vos, H J, B Dollet, J G Bosch, M Versluis, and N de Jong, Nonspherical vibrations of microbubbles in contact with a wall: a pilot study at low mechanical index. *Ultrasound Med. Biol.*, 34(4): 685-688, 2008.

Vos, H J, B Dollet, M Versluis, and N de Jong, Nonspherical Shape Oscillations of Coated Microbubbles in Contact with a Wall. *Ultrasound Med. Biol.*, 37(6): 935-948, 2011.

Vos, H J, F Guidi, E Boni, and P Tortoli, Method for microbubble characterization using primary radiation force. *IEEE Trans Ultrason Ferroelectr Freq Control*, 54(7): 1333-1345, 2007.

Vos, R, *Single Microbubble Imaging*. 2010, Erasmus MC: University Medical Center Rotterdam.

Wang, C, B Rallabandi, and S Hilgenfeldt, Frequency dependence and frequency control of microbubble streaming flows. *Physics of Fluids*, 25(2): 022002-022016, 2013.

Wei, K, Contrast echocardiography: applications and limitations. *Cardiol Rev*, 20(1): 25-32, 2012.

Weitz, D A, PHYSICS. Packing in the spheres. *Science*, 303(5660): 968-969, 2004.

Wen, Q, S Wan, Z Liu, S Xu, H Wang, and B Yang, Ultrasound contrast agents and ultrasound molecular imaging. *J Nanosci Nanotechnol*, 14(1): 190-209, 2014.

White, D N, Neurosonology pioneers. *Ultrasound Med. Biol.*, 14(7): 541-561, 1988.

Wijkstra, H, M Smeenge, J de la Rosette, S Pochon, I Tardy-Cantalupi, and F Tranquart. Targeted microbubble prostate cancer imaging with BR55. in *Abstract book 17th Eur Symp Ultrasound Contrast Imaging*(Issue), Year.

Williams, B A and C P Ordahl, Manipulation of the avian segmental plate *in vivo*. *Methods Cell Biol*, 51: 81-92, 1996.

Wilson, W D, C R Krishnamoorthy, Y H Wang, and J C Smith, Mechanism of intercalation: ion effects on the equilibrium and kinetic constants for the interaction of propidium and ethidium with DNA. *Biopolymers*, 24(10): 1941-1961, 1985.

Xie, A, T Belcik, Y Qi, T K Morgan, S A Champaneri, S Taylor, B P Davidson, Y Zhao, A L Klibanov, M A Kuliszewski, H Leong-Poi, A Ammi, and J R Lindner, Ultrasound-mediated vascular gene transfection by cavitation of endothelial-targeted cationic microbubbles. *JACC Cardiovasc Imaging*, 5(12): 1253-1262, 2012.

Yang, F, N Gu, D Chen, X Xi, D Zhang, Y Li, and J Wu, Experimental study on cell self-sealing during sonoporation. *Journal of controlled release : official journal of the Controlled Release Society*, 131(3): 205-210, 2008.

Yang, F, M Zhang, W He, P Chen, X Cai, L Yang, N Gu, and J Wu, Controlled release of Fe_3O_4 nanoparticles in encapsulated microbubbles to tumor cells via sonoporation and associated cellular bioeffects. *Small*, 7(7): 902-910, 2011.

Yoshina-Ishii, C, G P Miller, M L Kraft, E T Kool, and S G Boxer, General method for modification of liposomes for encoded assembly on supported bilayers. *J. Am. Chem. Soc.*, 127(5): 1356-1357, 2005.

Youn, H and K J Hong, *In vivo* non invasive molecular imaging for immune cell tracking in small animals. *Immune network*, 12(6): 223-229, 2012.

Yudina, A, M Lepetit-Coiffe, and C T Moonen, Evaluation of the temporal window for drug delivery following ultrasound-mediated membrane permeability enhancement. *Molecular imaging and biology : MIB : the official publication of the Academy of Molecular Imaging*, 13(2): 239-249, 2011.

Zheng, H, P A Dayton, C Caskey, S Zhao, S Qin, and K W Ferrara, Ultrasound-driven microbubble oscillation and translation within small phantom vessels. *Ultrasound Med. Biol.*, 33(12): 1978-1987, 2007.

Summary

Lipid-coated ultrasound contrast agent (UCA) microbubbles have been proposed as a therapeutic tool for drug-delivery applications. Drug molecules can be embedded within, surrounding, or attached to the lipid membrane. Under the application of ultrasound, mechanical forces caused by cavitation of the microbubble can cause local release the drugs and optimally deliver the drugs into the target tissue. One of the moieties we investigated was to conjugate liposomes to the microbubble surface by covalent thiol-maleimide linkages. This liposome-loaded microbubble can serve as an effective drug-delivery vehicle, i.e., to deliver highly-active therapeutic agents with a minimum influence on the untargeted healthy tissue during the transport, and be administered with a higher concentration to the target area. Echogenic liposomes (ELIP), another novel drug delivery vehicle, are thought to contain an aqueous core, allowing drug-loading, and also encapsulate a gas bubble, making them sensitive to ultrasound. It is our prime interest in this thesis to investigate the acoustic vibrational response and the drug release process as a function of ultrasound parameters (e.g., the pressure and the pulse length), for various drug delivery agents mentioned above. This is an essential step to achieve ultrasound-controlled drug delivery using these agents.

The first part of this thesis (**Chapter 2-5**) focuses on the acoustical and optical characterization of microbubble contrast agents, including lipid-shelled microbubbles, liposome-loaded microbubbles and echogenic liposomes. The investigated parameters are the lipid shell encapsulation properties, the bubble size, and the nonlinear oscillation dynamics. Novel techniques and systems were developed to achieve optical recordings of microbubble vibrational responses at a high time-resolution and over a pro-longed time duration (up to 1 ms). **Chapter 2** describes optical characterization of single liposome-loaded microbubbles based on a spectroscopy technique using the Brandaris 128 ultra-high speed camera. Lipid-shelled microbubbles without loading were used as a reference. The experimental data showed nearly the same shell elasticity for the loaded and unloaded bubbles but the shell viscosity was higher for loaded bubbles. A higher pressure threshold for the bubble vibrations was also observed for loaded bubbles.

In **Chapter 3** an optical characterization method is presented based on the use of the impulse response to characterize the interfacial shell viscosity of individual ELIP exposed to a broadband acoustic impulse excitation. Radius versus time response was

measured optically based on a single recording acquired using the Brandaris 128 ultra-high speed camera. A decrease of the apparent shell viscosity with increasing dilatation rate was observed, a nonlinear behavior which has been reported in other studies of lipid-shelled UCAs and is consistent with rheological shear-thinning.

Chapter 4 presents a new imaging mode for Brandaris 128 camera, facilitating high speed imaging during small time windows (segments) equally distributed over a relatively large time span. This mode overcomes to some degree the limited recording duration of ultra-fast framing cameras (> 10 MHz), and provides detailed information about the response of microbubbles exposed to long ultrasound pulses (> 100 cycles).

In **Chapter 5** a new system was developed by combining simultaneous optical sizing and sensitive acoustical characterization to study quantitatively the nonlinear dynamics of single freely-floating bubbles under prolonged ultrasound exposure. A coaxial-flow device was used to isolate individual microbubbles and to direct the bubble flow to the confocal region of ultrasound transducers and a high-resolution microscope objective. The data showed agreement with numerical simulations based on the shell-buckling model by Marmottant et al. The newly developed system can continuously measure bubble populations reproducibly, and thus provides a simple and efficient approach for *in vitro* characterization of contrast agent microbubbles.

The second part of this thesis (**Chapter 6 to 9**) illustrates the lipid shell materials shedding from microbubbles/liposome-loaded bubbles – a process which is triggered by the application of ultrasound. High-speed fluorescence imaging was applied for real-time monitoring of the detachment and the transport of the lipids from both the top and side view relative to a membrane. Lipid shedding behavior of individual microbubbles was optically characterized from the top view on a time scale of nanoseconds to microseconds in **Chapter 6**. Lipid detachment was observed within the first few cycles of ultrasound. Subsequently, the detached lipids were transported by the surrounding flow field, either parallel to the focal plane (in-plane shedding), or in a trajectory perpendicular to the focal plane (out-of-plane shedding). A threshold for lipid shedding under ultrasound excitation was found for a relative bubble oscillation amplitude higher than 30%, monitored by a ultra-high speed imaging camera running at 10 Mfps.

In **Chapter 7** and **Chapter 8**, we performed multi-modal studies to optically characterize shedding behavior of liposome-loaded microbubbles. The same techniques applied in **Chapter 6** were used. The data was supplemented with the observation of the bubble dissolution for hundreds of milliseconds after the shedding event. No significant difference in the threshold for shedding was found between lipids and liposomes. After the sonication, we observed an instantaneous bubble dissolution, which may be related to bubble fragmentation (up to 30% of the initial bubble size). Subsequent slower dissolution was followed over hundreds of

milliseconds until a final stabilization was reached. Additionally, we found that the occurrence of lipid/liposome shedding and the occurrence of instantaneous/long dissolution were highly correlated. A similar threshold value (around 30% of the relative amplitude of oscillation) was required to trigger these events. This suggests that the acoustic parameters used in this study may support future applications of combined imaging and drug delivery.

A completely new angle to observe lipid shedding behavior is given by **Chapter 9**. In this study, the side view ultra-high-speed bright field imaging and high speed fluorescence imaging technique was applied to reveal the details of non-spherical bubble oscillations relative to the detachment and transport of the phospholipids initially coating the microbubble. A model based on the Rayleigh-Plesset equation is established that demonstrates how the lipids locally oversaturate in the region of the bubble in contact with a rigid supporting membrane. The theoretical quantification agrees well with the experimental observations. Three regimes of shedding dynamics (mechanisms) were illustrated: lipid oversaturation, pinch off of daughter bubble fragments, and jetting. Bubble jetting resulted in an increase in the material deposited on the supporting membrane. From a clinical perspective, this regime can facilitate the transport of therapeutic agents towards the targeted cells instead of into the blood stream, opening promising possibilities for pushing further the current limitations of drug delivery with microbubbles.

The final part of this thesis (**Chapter 10 and 11**) involves parametric and mechanistic studies of drug-delivery applications using microbubbles both *in vitro* and *in vivo*. In **Chapter 10**, a parametric *in vitro* study was performed for ultrasound contrast agent-mediated superparamagnetic iron oxide (SPIO)-labeling of Human umbilical vein endothelial cells at low mechanical index (MI). The optimal ultrasound parameters were 40 kPa at 1 MHz, 10,000 cycles, 20 Hz pulse repetition frequency, applied for 30 seconds just before SPIO addition. This technique shows great potential for safe labeling of endothelial cells with SPIO for MRI tracking. In **Chapter 11** sonoporation of endothelial cells by targeted microbubbles was demonstrated for the first time *in vivo*, based on a chicken embryo model. Sonoporation was studied by intravital microscopy using the model drug propidium iodide (PI). Efficiency of PI uptake depended on the local targeted microbubble concentration and increased up to 80% for clusters of 10-16 targeted microbubbles.

With the various progresses in understanding the acoustic behavior of contrast agents *in vitro* and *in vivo* outlined in this thesis, we made an essential step closer to clinical realization of contrast-mediated ultrasound-controlled drug delivery. We also found excellent opportunities in acquiring in-depth knowledge of bubble acoustic response and bubble-cell interactions from a different angle.

Samenvatting

Recent onderzoek heeft de potentie laten zien van contrastmiddelen, zogenaamde microbellen, die met behulp van ultrageluid –lokaal medicijnen af kunnen geven. Deze medicijnen kunnen in het membraan van de microbellen ingebed worden of aan de buitenkant aan het membraan gelinkt worden. Met behulp van ultrageluid kan cavitatie van de microbel geïnduceerd worden. Wanneer dit op de plek van het zieke weefsel gedaan wordt kunnen medicijnen effectiever afgegeven worden. Een van de recente ontwikkelingen is het conjugeren van liposomen aan het oppervlak van de bel met behulp van thiol-maleimide bindingen. Deze zogenaamde liposoom geladen microbellen kunnen dienen als een effectief transport voor medicijnen. Het grote voordeel is dat zeer actieve en agressieve medicijnen binnenin de liposomen door het lichaam vervoerd worden, waardoor slechts geringe schade optreedt in gezond weefsel en de concentratie op de doellocatie lokaal hoger is dan met bijvoorbeeld intraveneuze toediening. Behalve gekoppeld aan een microbel kunnen liposomen op zich ook gebruikt worden om lokaal medicijnen af te geven, bijvoorbeeld in de vorm van echogene liposomen (ELIP). Deze zouden een waterige kern hebben waar hydrofiele medicijnen in vervoerd kunnen worden, maar daarnaast bevat het liposoom ook een luchtbel. Deze luchtbel zorgt ervoor dat ELIP gevoelig zijn voor ultrageluid. Het belangrijkste onderzoeksdoel in dit proefschrift is het bestuderen van de akoestische oscillatierespons en het medicijnafgifteproces onder invloed van ultrageluid. Om dit te bereiken bestuderen we belangrijke ultrageluid parameters, zoals druk en lengte van de geluidspuls, om de verschillende contrastmiddelen die hierboven genoemd zijn te karakteriseren. Deze stap is essentieel om het medicijnafgifteproces met ultrageluid te kunnen controleren.

Het eerste deel van dit proefschrift (**Hoofdstuk 2-5**) richt zich op de akoestische en optische karakterisering van microbellen als ultrageluidcontrastmiddel, waaronder lipidengecoate microbellen, liposoom geladen microbellen en echogene liposomen (ELIP). De belangrijkste parameters die we onderzocht hebben zijn de eigenschappen van de lipidencoating, de belgrootte en de niet-lineaire oscillaties. Met het gebruik van nieuwe technieken konden we de oscillaties van microbellen gedurende een periode van maximaal 1 ms met een hoge tijdsresolutie waarnemen. In **hoofdstuk 2** karakteriseren we individuele liposoom geladen bellen met de Brandaris 128 ultrahogesnelheidscamera door middel van spectroscopie. Hierbij hebben we lipidengecoate bellen zonder liposomen gebruikt als referentiekader. Uit deze

experimenten bleek dat de elasticiteit van de belschil niet veranderd wanneer er liposomen aan de bel gekoppeld zijn, terwijl de viscositeit voor de liposoom geladen bellen hoger was. Een ander belangrijk verschil is de druk waarbij de belvibraties startten: deze was hoger voor de liposoom geladen bellen

In **hoofdstuk 3** beschrijven we een nieuwe optische methode om de viscositeit van ELIP te karakteriseren aan de hand van de natuurlijke uitdoving van de akoestische impuls excitatie. De Brandaris 128 ultrahogesnelheidscamera is ook hier gebruikt om de oscillatie van een enkele bel gedurende een bepaalde tijd op te nemen. De belangrijkste bevinding van deze studie was de afname van de viscositeit bij een toename van de dilatatiesnelheid. Dit is een vorm van niet-lineair gedrag dat eerder beschreven is voor lipidengecoate contrastmiddelen en staat bekend als rheologisch dunner worden van de schil als gevolg van toenemende schuifspanning.

Hoofdstuk 4 handelt over een nieuwe opname modus voor de Brandaris 128 camera, die voorziet in hoge snelheidsopnamen van korte duur (zg. segmenten) die op hun beurt weer gelijkelijk verdeeld zijn over een grotere tijdspanne. Met deze modus wordt het beperkte tijdbereik van dit type ultrasnelle camera's (> 10 MHz) omzeild en kan men gedetailleerde informatie verkrijgen over de responsie van microbellen die langdurig zijn blootgesteld aan ultrageluid pulsen (meer dan 100 perioden).

In **Hoofdstuk 5** wordt de ontwikkeling van een nieuw systeem beschreven dat gelijktijdig zowel de optische als akoestische eigenschappen van individuele vrij bewegende microbellen kan meten. Dit is gedaan om kwantitatief de niet lineaire eigenschappen tijdens langdurige ultrageluid excitatie van deze bellen te karakteriseren. Een coaxiale stromingskamer is gebruikt om individuele bellen te isoleren en deze te richten op het confocale gebied van het optische en akoestische meetsysteem. De op deze manier verkregen meetdata komt grotendeels overeen met de numerieke simulaties gebaseerd op het "shell-buckling" model van Marmottant e.a. Dit nieuw ontwikkelde systeem kan op een simpel en efficiënte manier grote bellen populaties karakteriseren grote bellen populaties karakteriseren.

Het tweede deel van dit proefschrift (**hoofdstuk 6 tot 9**) behandeld de door ultrageluid geïnitieerde lipidenverspreiding afkomstig van de microbelschil. Hoge snelheid fluorescentie opnamen zijn gebruikt om om het loslaten en verspreiden van de lipiden te bestuderen. Het lipiden verspreidingsgedrag van individuele bellen is optisch vastgelegd op een tijdschaal die reikt van nanoseconden tot aan microseconden.

In hoofstuk 6 is het loslaat mechanisme van de lipiden bestudeerd in de eerste periodes van de ultrageluid excitatie. Het daarop volgende transport van de lipiden veroorzaakt door omringende stromingsveld vindt plaats in 2 richtingen: parallel aan het optische vlak en loodrecht daarop (uit vlak verspreiding). De drempelwaarde voor lipiden verspreiding geïnduceerd door ultrageluid werd daarbij vastgesteld op een

relatieve oscillatie amplitude hoger dan 30%. Dit alles werd uitgevoerd met behulp van ultra hoge snelheidsopnamen met een beeldfrequentie van 10 miljoen beelden per seconde.

In **hoofdstuk 7 en 8** zijn multimodale studies uitgevoerd met als doel het verspreidingsgedrag van liposomen geladen bellen optisch te karakteriseren. Hierbij zijn de dezelfde technieken gebruikt als beschreven in **hoofdstuk 6**. De verkregen data is daarbij aangevuld met de waarnemingen over het deflatieproces van de microbellen in de daarop volgende honderden van milliseconden. Daarbij is er geen significant verschil te zien in de drempelwaarde waarop verspreiding van lipiden en liposomen begint. Daarnaast is er een snelle deflatie waargenomen bij microbellen waarvan een afname tot 30% van de oorspronkelijke beldiameter optrad, direct na ultrageluid excitatie. Uiteindelijk neemt de diameter geleidelijk af in enkele honderden milliseconden tot een stabiele situatie wordt bereikt. De verspreiding van lipiden en liposomen en microbeldestructie hangen direct met elkaar samen. De vergelijkbare drempelwaarden tussen deze processen leveren voldoende aanknopingspunten op om deze microbellen zowel als contrastmiddel en als medicijndrager te gebruiken.

Een compleet nieuwe invalshoek in de studie naar het lipiden verspreidingsgedrag wordt beschreven in **hoofdstuk 9**. In deze studie is de verspreiding parallel aan de wand gefilmd met een ultrahoge snelheidscamera en de verspreiding loodrecht op de wand met een hoge snelheid fluorescentie camera. Dit is gedaan om de details van de niet sferische oscillaties in relatie tot het loslaten en verspreiden van de phospholipiden laag van de microbellen bloot te leggen. Er is een simulatie model gebouwd, gebaseerd op de Rayleigh-Plesset vergelijking, dat aantoont hoe lipiden lokaal oververzadigen in de regio waar de microbel in contact is met een dragend stijf membraam. De theoretische uitkomst van het model komt goed overeen met de experimentele data. Er wordt hierbij onderscheid gemaakt tussen drie regimes van lipiden verspreidingsmechanismen: Lipiden oververzadiging, het afsplitsen van z.g. dochterbel fragmenten en stralen ofwel 'jetting'. Het microbel spuiten/stralen lipiden materiaal af op het dragende membraam. Vanuit klinisch perspectief is dit regime interessant om de lokale afgifte van medicatie te stimuleren en afgifte in bloedbaan te beperken. Dit biedt mogelijkheden om de huidige beperkingen van medicijnafgifte met behulp van microbellen op te heffen.

Het laatste deel van dit proefschrift (**hoofdstuk 10 en 11**) gaat over parametrische en mechanistische studies met betrekking tot medicijnafgifte gebruikmakende van microbellen. In **hoofdstuk 10** is een parametrische *in vitro* studie uitgevoerd naar het met ultrageluid contrastmiddel ondersteund labelen van humane navelstreng endotheelcellen met superparamagnetisch ijzeroxide (SPIO) bij lage ultrageluidsdruk. De optimale ultrageluid parameters hiervoor zijn pulsen van 1

MHz, 10.000 perioden lang bij een druk van 40kPa en een herhaal frequentie van 20Hz. Deze ultrageluid therapie wordt uitgevoerd 30s voor de daadwerkelijke SPIO toediening. Deze techniek biedt grote mogelijkheden om op een veilige manier endotheelcellen te labelen met SPIO als MRI contrastmiddel.

Hoofdstuk 11 gaat over de eerste *in vivo* sonoporatie van endotheelcellen met gemarkeerde microbellen in een kippenembryo. De sonoporatie werd bestudeerd met intravitale microscopie met het test medicijn propidium iodide (PI). De PI opname is tot 80% verbeterd, afhankelijk van de cluster grootte (10-16 bellen) en de concentratie van de gemarkeerde bellen.

Met de nieuwe inzichten verkregen door het bovengenoemde onderzoek over de akoestische eigenschappen van ultrageluid contrastmiddelen is er een essentiële stap gezet voor de klinische toepassing van ultrageluid geinitieerde lokale medicijnafgifte. Daarnaast is er belangrijke kennis opgedaan over de akoestische eigenschappen van microbellen en heeft het een andere kijk opgeleverd over de interactie van deze bellen met cellen.

Acknowledgements

The best things in life are unseen. This is totally true when describing the ultrasound wave and those marvelous micro-scaled bubbles, which have accompanied the last four and half years of my PhD research. However, it is the invisible input and contributions of many amazing people that have made this work finally visible, and published as this book – *Ultrasound-triggered drug release from vibrating microbubbles*.

First of all I would like to thank my promoters, Prof. dr.ir. Nico de Jong, Prof. dr. ir. Ton van der Steen and Prof. dr. Michel Versluis. With your guidance, support and encouragement, I was able to learn many things during the past few years. Nico, you introduced me into the ultrasound and microbubble field. I am really lucky to have you as my supervisor and mentor. Your professional knowledge and personality had considerable influence on me, and I believe this influence will be life-long. Experimental works require a lot of trial and error. You always gave me freedom to try out under your guidance. With your patience and trust, my confidence has been built up and my professional skills have been fully developed. Ton, I appreciate your generous guidance and support throughout my study. You always appear when I came across difficulties, and pointed out a way. You are a great example of our lab, and I am really proud that I have you as my mentor. Michel, thank you for providing me the valuable opportunities to visit Physics of Fluids group constantly for experiments and discussions. Besides your scientific supervision, you also taught me how to clearly and precisely interpret the scientific results, both in oral presentations and in writing. Your intelligence and tireless working ethic have inspired my continuous efforts.

My PhD is part of the EU FP7 project Sonodrugs, which supported the first two years of this work. With the close collaborations built up within the project, I was able to generate multiple core chapters even after the project was ended. I especially want to thank Heleen Dewitte and Dr. Ine Lentacker from Ghent University, Belgium, for generous and continuous supply of the microbubble samples throughout my research. For the last two years of my research, I worked closely with Physics of Fluids Group at University of Twente. I appreciate my lab-mates over there – Erik Gelderblom, Guillaume Lajoinie and Tim Segers, thank you for sharing your experimental skills and knowledge. For all lipid shedding experiments, we made remarkable progresses from the beginning of zero, until we had a complete view of the lipid shedding events in the

end. These works would never have been accomplished without your efforts. Guillaume, I really appreciate your kind arrangements and warm help when I visited the lab every time. The intense experimental works and active discussions became all memorable. You are passionate, curious and talented, and undoubtedly you will be a very professional paranimph.

As a foreign PhD student living far away from family, I always feel at home with my fabulous lab-mates and colleagues at Biomedical Engineering. Tom and Ilya, I really enjoyed the time in the lab with your accompany throughout these years. We experienced adventures in the lab together, and shared both frustrating and exciting moments. We constantly encouraged each other with “Op hoop van zegen”, and having broodje kaas daily for lunch. Tom, I was always encouraged by your initiative and persistence; Ilya, you are fearless and your unique point of view often impressed me. Thank you both for being my great lab-mates as well as good friends. I will keep all those precious memories in mind: our discussions, coffee breaks, drinks, dinners, conference meetings, and the defense. I look forward to our reunion in the future. I would like to thank Robert and Frits, for all the technical support (often late in the evening for experiments, and sometimes even in weekends). I really appreciate those nice conversations and warm encouragements. Robert, thank you for your care and help which made me survive lots of challenges during PhD studies. Your brilliant ideas and warm hearted support made daily work inspiring and a fun time. You are not only a great colleague but also a precious friend. Frits, thank you for sharing your knowledge of various areas: research methods, image processing, programming, history and culture, etc. I have learned a lot from your analytical thinking. I would also like to thank Rik for valuable remarks and contributions on the lipid shedding paper, which finally became a nice “dough” after two years of “massage”. I want to thank Guillaume for transferring the knowledge on the acoustical camera without reservation so that I was able to continue this work as my last study of PhD work. Hans, I appreciate your valuable discussions, which solved a key problem on the acoustical camera chapter. I want to thank Tom for your contribution to my thesis, from the Dutch title to Samenvatting. I appreciate Verya and Alex for being the best climbing teachers ever, and for your philosophical advice. I also want to thank Jacopo, Deep, Zeynettin, Pieter and Klazina, thank you all for helpful discussions. My research was also greatly facilitated with the help of Michiel and Geert, who have helped me with the design and building of the experimental setups. I gratefully thank the kind help from Mieke, Gracia, Rita and Gerard. My thanks also go to Gijs, Min, Tianshi, Muthu, Jovana and Sophinese.

I like to thank the guidance from lab-mates who already graduated: Paul and Telli. I am grateful for Paul’s discussions and encouragement every time when we meet on conferences. Telli, you are a special friend to me. You are an intelligent girl who is

maybe 500 years old, and gave me lots of courage when I just started my PhD study. I really enjoyed the time we have spent together and hope that I will soon realize the trip visiting you and Enrico in Lille.

During my PhD study I was able to travel to lots of conferences, and got to know very talented people working in the same area. I would like to thank Dr. Alfred Yu, for your valuable comments on my research. I learned a lot and was inspired by having discussions with you. I like to thank Chao, Ling and Chessy. It was very nice to know you and I really cherish our friendship.

I will never forget a precious friend on the 23rd floor, Roy, though I will never have a chance to invite him to my defense. He taught me how to cherish – to spend more time with people you love. I will always keep in mind what he said: "Take time to smell the flowers."

I shall leave the final thanks to my beloved and my family, who have been a source of unending support.

Jason, thank you for caring, sharing and being by my side. I am really grateful that I was able to get to know you. You are disciplined but creative and initiative in generating new ideas; you are a patient listener but active in discussions and sharing your knowledge with people around you. You are a real scientist and I am very proud of you. Thank you for your unconditional support. Gary and Elaine, Darren and Tiffany, it was my great pleasure to meet you all, a lovely family. Thank you for your warm encouragement to me.

I like to appreciate my grandparents, my parents and my extended family back in China. It was your care and love that have driven me through every step of the way, from Gothenburg seven years ago to Rotterdam at this moment. I am really lucky to have you all. My dear parents, thank you for the determination and the sacrifice you have made in your life, so that I had the courage to start this fantastic journey, and experienced the best things in life.

亲爱的外公外婆，我的所有家人，比利时的亲人，我的朋友们，从七年前的瑞典到今天的鹿特丹，一路走来，你们的支持和关怀是我最大的动力。谨以此书献给你们。亲爱的爸爸妈妈，我今天的成绩归功于你们的养育和为我的成长所作出的牺牲，我爱你们。

List of publications

PATENT

Cao ZN, **Luan Y**, Shen L, Wang ZZ, "Eye movement desensitization and reprocess therapeutic equipment", Southeast University, China, CN 100589850C, 2010.

THESIS

Luan Y, Ultrasound-triggered drug release from vibrating microbubbles, PhD thesis, Erasmus University Rotterdam, the Netherlands, 2014.

Luan Y, Modelling of heat distribution in human skin caused by laser irradiation, M.S. Thesis, M.S. Thesis, Chalmers University of Technology, Sweden, 2007.

PEER-REVIEWED PAPERS

Skachkov I, **Luan Y**, van der Steen AFW, de Jong N, Kooiman K, Targeted microbubble mediated sonoporation of endothelial cells *in vivo*, IEEE Trans Ultrason Ferro electr Freq Control 2014 (accepted).

Luan Y, Lajoinie G, Gelderblom EC, Skachkov I, van der Steen AFW, Vos H, Versluis M, and de Jong N, Lipid shedding from single oscillating microbubbles. Ultrasound in medicine & biology 2014;40:1834-46.

Shpak O, Kokhuis TJA, **Luan Y**, Lohse D, de Jong N, Fowlkes B, Fabiilli M, Versluis M. Ultrafast dynamics of the acoustic vaporization of phase-change microdroplets. The Journal of the Acoustical Society of America 2013;134:1610-21.

Gelderblom EC, Vos HJ, Mastik F, Faez T, **Luan Y**, Kokhuis TJA, van der Steen AFW, Lohse D, de Jong N, Versluis M. Brandaris 128 ultra-high-speed imaging facility: 10 years of operation, updates, and enhanced features. The Review of scientific instruments 2012;83:103706.

Luan Y, Faez T, Gelderblom E, Skachkov I, Geers B, Lentacker I, van der Steen AF, Versluis M, de Jong N. Acoustical Properties of Individual Liposome-Loaded Microbubbles. Ultrasound in medicine & biology 2012;38:2174-85.

CONFERENCE PAPERS

Luan Y, Renaud G, Raymond JL, Segers T, Beurskens RHSH, Mastik F, Kokhuis TJA, Guillaume PRL, Versluis M, van der Steen AFW and de Jong N, Nonlinear dynamics of

single freely-floating microbubbles under prolonged insonation, - A combined optical sizing and ultra-fast acoustical characterization study. Ultrasonics Symposium IEEE International 2014 (submitted).

Luan Y, Lajoinie G, Gelderblom E, Skachkov I, Dewitte H, Lentacker I, van Rooij T, Vos H, van der Steen AFW, Versluis M, de Jong N. Liposome shedding from a vibrating microbubble on nanoseconds timescale. Ultrasonics Symposium IEEE International 2013;57-60.

van Rooij T, **Luan Y**, Renaud G, van der Steen AFW, de Jong N, Kooiman K. Acoustical response of DSPC versus DPPC lipid-coated microbubbles. Ultrasonics Symposium IEEE International 2013;310-3.

Shpak O, Stricker L, Kokhuis T, **Luan Y**, Fowlkes JB, Fabiilli M, Lohse D, de Jong N, Versluis M. Ultrafast dynamics of the acoustic vaporization of phase-change microdroplets. Acoustics 2013;19.

Luan Y, Gelderblom E, Lajoinie G, Skachkov I, Dewitte H, Geers B, Lentacker I, van der Steen AFW, Versluis M, de Jong N. Characterizing ultrasound-controlled drug release by high-speed fluorescence imaging. Ultrasonics Symposium IEEE International 2012;1-4.

Luan Y, Kokhuis TJA, Mastik F, Beurskens RHSH, Versluis M, De Jong N. Segmented high speed imaging of vibrating microbubbles during long ultrasound pulses. Ultrasonics Symposium IEEE International 2012;1343-6.

Skachkov I, **Luan Y**, van Tiel S, van der Steen AFW, Kooiman K, Bernsen M, De Jong N. Ultrasound contrast agents mediated cell labeling for MRI tracking. Ultrasonics Symposium IEEE International 2012;2278-81.

Luan Y, Faez T, Gelderblom E, Skachkov I, Geers B, Lentacker I, van der Steen AFW, Michel V and de Jong N. Optical characterization of inidividual liposome-loaded microbubbles. Joural of Acoustic Society of America. 131 , 3248 (2012).

Luan Y, Faez T, Skachkov I, Gelderblom E, Geers B, Lentacker I, van der Steen AFW, Versluis M, de Jong N. Optical characterization of individual liposome-loaded microbubbles. Ultrasonics Symposium IEEE International 2011;1890-3.

Skachkov I, Kooiman K, **Luan Y**, van der Steen AFW, de Jong N. Sonoporation of endothelial cells *in vivo*. Ultrasonics Symposium IEEE International 2011;1467-9.

POSTER AND ORAL PRESENTATIONS WITH ABSTRACTS

Luan Y, Renaud G, Raymond JL, Segers T, Beurskens RHSH, Mastik F, Kokhuis TJA, Guillaume P.R. L, Versluis M, van der Steen AFW and de Jong N, Nonlinear dynamics of single freely-floating microbubbles under prolonged insonation, - A combined optical sizing and ultra-fast acoustical characterization study. Poster, Ultrasonics Symposium IEEE International, Chicago, 2014.

Luan Y, Renaud G, Raymond JL, Segers T, Beurskens R, Kokhuis TJA, van der Steen AFW, Versluis M, de Jong N. Stable non-linear dynamics of free-floating lipid-coated microbubbles. Oral and poster, 167th Meeting of the Acoustic Society of America, Providence, 2014.

van Rooij T, **Luan Y**, Renaud G, van der Steen AFW, de Jong N and Kooiman K. Response to ultrasound of two types of lipid-coated microbubbles observed with a high-speed optical camera. Oral and poster, 167th Meeting of the Acoustic Society of America, Providence, 2014.

Raymond JL, **Luan Y**, van Rooij T, Huang S, McPherson DD, de Jong N and Holland CK. Estimation of damping coefficient based on the impulse response of echogenic liposomes. Oral and poster, 167th Meeting of the Acoustic Society of America, Providence, 2014.

Luan Y, Renaud G, Kokhuis T, Raymond JL, van der Steen AFW, de Jong N. Stable non-linear dynamics of free-floating lipid-coated microbubbles. Poster, The 19th European Symposium on Ultrasound Contrast Imaging, Rotterdam, 2014.

Raymond JL, **Luan Y**, van Rooij T, Huang SL, McPherson DD, de Jong N, Holland CK. Impulse Response of Echogenic Liposomes. Poster, The 19th European Symposium on Ultrasound Contrast Imaging, Rotterdam, 2014.

Harfield CJ, **Luan Y**, Ovenden NC, de Jong N and Stride E, Theoretical and Experimental Observations of Lipid Shedding, Poster,The 19th European symposium on Ultrasound Contrast Imaging, Rotterdam, 2014.

van Rooij T, **Luan Y**, Renaud G, van der Steen AFW, de Jong N, Kooiman K, Influence of DSPC versus DPPC on acoustical responses of lipid-coated microbubbles, Poster, The 19th European Symposium on Ultrasound Contrast Imaging, Rotterdam, 2014.

Luan Y, Lajoinie G, Gelderblom E, Skachkov I, Dewitte H, Lentacker I, van Rooij T, Vos H, van der Steen T, Versluis M, de Jong N. Liposome shedding from a vibrating microbubble on nanoseconds timescale. Oral, Ultrasonics Symposium IEEE International, Prague, 2013.

Luan Y, Gelderblom EC, Lajoinie G, Skachkov I, Dewitte H, Geers B, Lentacker I, van der Steen AFW, Versluis M, de Jong N, Time-resolved ultrasound-triggered release from a liposome-loaded microbubble, Oral, 18th European Symposium on Ultrasound Contrast Imaging, Rotterdam, 2013.

van Rooij T**, Luan Y**, Renaud G, van der Steen AFW, de Jong N, Kooiman K. Acoustical response of DSPC versus DPPC lipid-coated microbubbles. Poster, Ultrasonics Symposium IEEE International, Prague, 2013.

Skachkov I, **Luan Y**, van Tiel S, van der Steen AFW, Kooiman K, Bernsen M, de Jong N, Ultrasound contrast agents mediated cell labeling for MRI tracking, Poster, 18th European Symposium on Ultrasound Contrast Imaging, Rotterdam, 2013.

Luan Y, Faez T, Gelderblom EC, Skachkov I, Geers B, Lentacker I, van der Steen AFW, Versluis M and de Jong N, Optical characterization of individual liposome-loaded microbubbles, Oral, The Acoustics 2012 Conference, Hong Kong, 2012.

Luan Y, Faez T, van der Steen AFW, Geers B, Dewitte H, Lentacker I, Gelderblom EC, Versluis M, de Jong N, Characteristics of liposome-loaded microbubbles for therapeutic use, Oral, 12th International Symposium on Therapeutic Ultrasound, Heidelberg, Germany, 2012.

Luan Y, Faez T, Gelderblom EC, Skachkov I, Geers B, Lentacker I, van der Steen AFW, Versluis M and de Jong N, Optical characterization of individual liposome-loaded microbubbles, Oral, Acoustic Waves for the Control of Microfluidics Flows Workshop, Leiden, 2012.

Luan Y, Gelderblom E, Lajoinie G, Skachkov I, Dewitte H, Geers B, Lentacker I, van der Steen T, Versluis M, de Jong N. Characterizing ultrasound-controlled drug release by high-speed fluorescence imaging. Oral, Ultrasonics Symposium IEEE International, Dresden, 2012.

Gelderblom ED, **Luan Y**, Dewitte H, Geers B, Lentacker I, van der Steen AFW, de Jong N, Versluis M, High-speed fluorescence imaging of the US-triggered release from liposome-loaded microbubbles, Oral, 17th European Symposium on Ultrasound Contrast Imaging, 2012, Rotterdam

Kokhuis TJA, **Luan Y**, Mastik F, Beurskens RHSH, Versluis M, de Jong N. Segmented high speed imaging of vibrating microbubbles during long ultrasound pulses. Poster, Ultrasonics Symposium IEEE International, Dresden, 2012.

Skachkov I, **Luan Y**, van Tiel S, van der Steen T, Kooiman K, Bernsen M, de Jong N. Ultrasound contrast agents mediated cell labeling for MRI tracking. Poster, Ultrasonics Symposium IEEE International 2012;2278-81, Dresden, 2012.

Luan Y, Faez T, Skachkov I, Gelderblom EC, Geers B, Lentacker I, van der Steen T, Versluis M, de Jong N. Optical characterization of individual liposome-loaded microbubbles. Oral and poster, Ultrasonics Symposium IEEE International, Orlando, 2011.

Luan Y, Faez T, Skachkov I, de Jong N, Optical Characterization of Individual Liposome Loaded Microbubbles, Poster, 16th European Symposium on Ultrasound Contrast Imaging, Rotterdam, 2011.

Skachkov I, Kooiman K, **Luan Y**, van der Steen T, de Jong N. Sonoporation of endothelial cells *in vivo*. Poster, Ultrasonics Symposium IEEE International;1467-9, Orlando, 2011.

PhD portfolio

Courses	Year	ECTS
Nonlinear Acoustics and Harmonic Imaging (IEEE, Dresden, Germany)	2012	0.15
contrast agents: theory and experiments (IEEE, Orlando, USA)	2011	0.15
Ultrasound imaging systems: from principles to implementation (IEEE, Orlando, USA)	2011	0.15
Animal Imaging Workshop by AMIE (MolMed)	2011	1.5
Cardiovascular Imaging and Diagnostics (COEUR)	2010	1.5

Presentations	Year	ECTS
IEEE International Ultrasonic Symposium (Chicago, USA, poster)	2014	0.5
Oral presentation at University of Cincinnati	2014	1.0
167th Meeting of the Acoustical Society of America, (Providence, USA, poster + oral)	2014	1.5
Academic Expo, BCF Career Event (Amsterdam, the Netherlands, poster + oral)	2014	1.5
The 19th European Symposium on Ultrasound Contrast Imaging (Rotterdam, the Netherlands, poster)	2014	0.5
IEEE International Ultrasonic Symposium (Prague, Czech Republic, oral)	2013	1.0
The 18th European Symposium on Ultrasound Contrast Imaging (Rotterdam, the Netherlands, oral)	2013	1.0
IEEE International Ultrasonics Symposium (Dresden, Germany, posters + oral)	2012	1.5

12th International Symposium on Therapeutic Ultrasound, (Heidelberg, Germany, oral)	2012	1.0
The Acoustics 2012 Conference (Hong Kong, China, oral)	2012	1.0
Acoustic waves for the control of microfluidics flows (Leiden, the Netherlands, oral)	2012	1.0
IEEE International Ultrasonic Symposium (Orlando, USA, poster+oral)	2011	1.5
The 16th European Symposium on Ultrasound Contrast Imaging (Rotterdam, the Netherlands, poster)	2011	0.5
EU FP7 project Sonodrugs workshop (London, UK, oral)	2011	1.0
EU FP7 project Sonodrugs workshop (Paris, France, oral)	2010	1.0

International conferences	**Year**	**ECTS**
IEEE International Ultrasonic Symposium (Chicago, USA)	2014	0.9
167th Meeting of the Acoustic Society of America (Providence, USA)	2014	1.5
The 19th European Symposium on Ultrasound Contrast Imaging (Rotterdam, the Netherlands)	2014	0.6
IEEE International Ultrasonic Symposium (Prague, Czech Republic)	2013	1.2
The 18th European Symposium on Ultrasound Contrast Imaging (Rotterdam, the Netherlands)	2013	0.6
IEEE International Ultrasonic Symposium (Dresden, Germany)	2012	0.9
12th International Symposium on Therapeutic Ultrasound, (Heidelberg, Germany)	2012	0.9
The Acoustics 2012 Conference (Hong Kong, China)	2012	1.5
The 17th European Symposium on Ultrasound Contrast Imaging (Rotterdam, the Netherlands)	2012	0.6
IEEE International Ultrasonic Symposium (Orlando, USA)	2011	0.9
The 16th European Symposium on Ultrasound Contrast Imaging (Rotterdam, the Netherlands)	2011	0.6

Seminars and workshops	**Year**	**ECTS**
MedTechWest 2014	2014	0.4
EU FP7 project Sonodrugs workshop (Rotterdam, the Netherlands)	2012	0.6
Acoustic waves for the control of microfluidics flows (Leiden, the Netherlands, oral)	2012	0.9
EU FP7 project Sonodrugs workshop (London, UK,)	2011	0.9
Spring Meeting of the Dutch Society for Medical Ultrasound, Delft, the Netherlands	2011	0.3
EU FP7 project Sonodrugs workshop (Paris, France)	2010	0.9
EU FP7 project Sonodrugs workshop (Eindhoven, the Netherlands)	2010	0.6
	Total	33.75

A note about the author

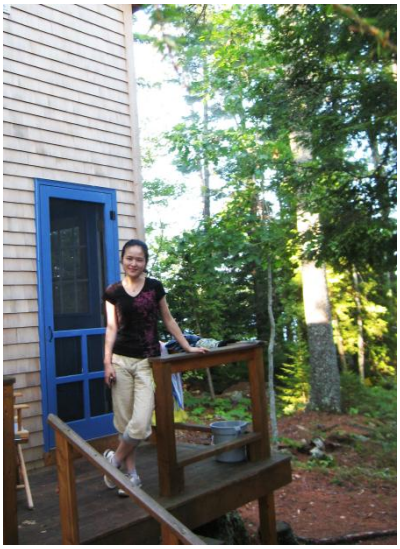

Ying Luan was born on April 8th, 1985, in Nanjing, China. She received her secondary education at No. 13 Middle School in Nanjing between 1997 and 2003. In 2003, she started her university study majored in Biomedical Engineering, Southeast University, China. During the third and the fourth year of her undergraduate study, she started to work on anticancer drug delivery research in National Key Laboratory in Southeast University. In 2007 she obtained her bachelor degree and continued her master study in Biomedical Engineering at Chalmers University, Gothenburg, Sweden. The work of her master thesis entitled "Estimation of thermal distribution in human skin under laser therapy" was conducted at Philips Research in Eindhoven, the Netherlands. Since 2010 she started her doctoral research at Department of Biomedical Engineering, Erasmus Medical Center, under the guidance of Prof. dr. ir. Nico de Jong, Prof. dr. ir. Ton van der Steen and Prof. dr. Michel Versluis. Her research focuses on acoustical responses of contrast agent microbubbles for the application of ultrasound-mediated drug delivery.

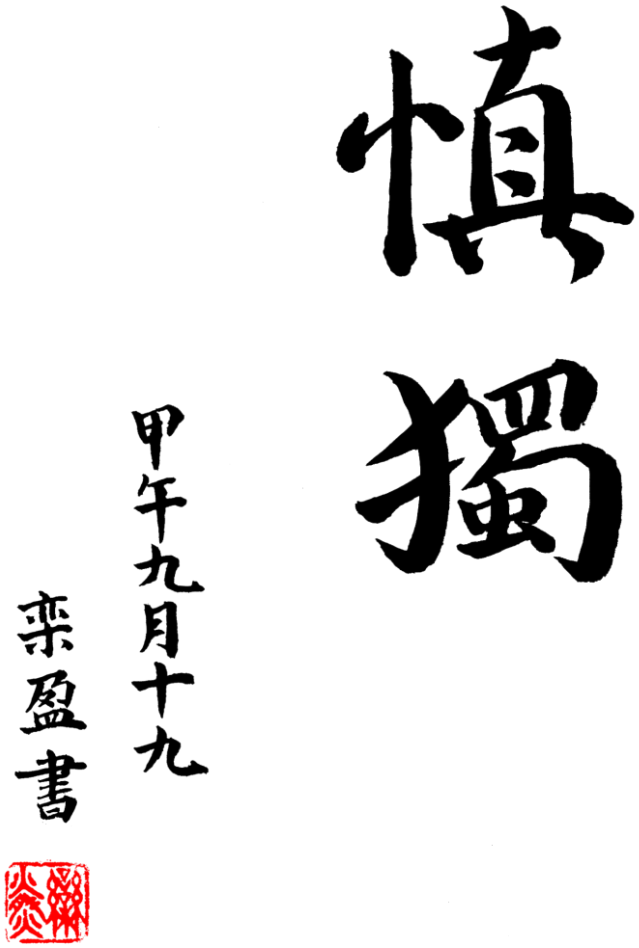

Shendu is an important term of the traditional Chinese Confusion. The most prevalent understanding of *Shendu* is the cautiousness when a person is alone. There are new interpretations which involve the inner desire to challenge; to return to nature and live a simple life. In general, the doctrine of *Shendu* focuses on self-cultivation without the presence/aid of others in Confusion classics.